UNIVERSIDADE FEDERAL DE PELOTAS

Programa de Pós-Graduação em Ciências e Engenharia de Materiais

Tese de Doutorado

INFLUÊNCIA DO INTEMPERISMO EM FILMES FINOS DE CEO2 E CEO2:V2O5 E ESTUDO DE BIOGÉIS SUSTENTÁVEIS PARA APLICAÇÃO EM DISPOSITIVOS ELETROCRÔMICOS

RAPHAEL DORNELES CALDEIRA BALBONI

Pelotas, 2022

RAPHAEL DORNELES CALDEIRA BALBONI

“INFLUÊNCIA DO INTEMPERISMO EM FILMES FINOS DE CEO2 E CEO2:V2O5 E ESTUDO DE BIOGÉIS SUSTENTÁVEIS PARA APLICAÇÃO EM DISPOSITIVOS ELETROCRÔMICOS”

Tese apresentada ao Programa de Pós-Graduação em Ciência e Engenharia de Materiais da Universidade Federal de Pelotas, como requisito à obtenção do título de Doutor em Ciência e Engenharia de Materiais.

Orientador: Prof. Dr. Robson Andreazza
Coorientador: Prof. Dr. César O. Avellaneda

Pelotas, 2022

Universidade Federal de Pelotas / Sistema de Bibliotecas
Catalogação na Publicação

B173i Balboni, Raphael Dorneles Caldeira

Influência do intemperismo em filmes finos de CeO_2 e CeO_2:V_2O_5 e estudo de biogéis sustentáveis para aplicação em dispositivos eletrocrômicos / Raphael Dorneles Caldeira Balboni ; Robson Andreazza, orientador ; Cesar Antonio Oropesa Avellanda, coorientador. — Pelotas, 2022.

141 f. : il.

Tese (Doutorado) — Programa de Pós-Graduação em Ciência e Engenharia de Materiais, Centro de Desenvolvimento Tecnológico, Universidade Federal de Pelotas, 2022.

1. Eletrocromismo. 2. Dispositivo eletrocrômico. 3. Contra-eletrodo. 4. Eletrólito. 5. Acetato de celulose. I. Andreazza, Robson, orient. II. Avellanda, Cesar Antonio Oropesa, coorient. III. Título.

CDD : 620.11063

Elaborada por Maria Inez Figueiredo Figas Machado CRB: 10/1612

Raphael Dorneles Caldeira Balboni

Influência Do Intemperismo Em Filmes Finos De CeO2 E CeO2:V2O5 E Estudo De Biogéis Sustentáveis Para Aplicação Em Dispositivos Eletrocrômicos

Tese aprovada, como requisito parcial, para obtenção do grau de Doutor em Ciências e Engenharia de Materiais, Programa de Pós-Graduação em Ciência e Engenharia de Materiais, Centro de Desenvolvimento Tecnológico, Universidade Federal de Pelotas.

Data da Defesa: 13 de maio de 2022.

Banca examinadora:

Prof. Dr. Robson Andreazza (Orientador)
Doutor em Ciência do Solo pela UFRGS

Prof. Dr. César O. Avellaneda (Coorientador)
Doutor em Ciência e Engenharia de Materiais pela USP

Prof. Dr. Cristiane Wienke Raubach
Doutor em Química pela UFSCar

Prof. Dr. José Henrique Alano
Doutor em Ciência e Engenharia de Materiais pela UFSCar

Prof. Dr. Angel Gabriel Fernandez Diaz-Carralero
Doutor em Ciencia de Materiales pela Universidad Complutense Madrid

---

Prof. Dr. Neftali Lenin Villarreal Carreno (Suplente)
Doutor em Química pela UFSCar

Dr. Guilherme Kurz Maron (Suplente)
Doutor em Ciência e Engenharia de Materiais pela UFPel


QUEM FAZ CIÊNCIA DEVE SER CURIOSO, DUVIDAR, ESTUDAR, DESCOBRIR.
CIÊNCIA PRODUZ CONHECIMENTO...
...O CONHECIMENTO DESTRÓI MITOS.
Assembleia UFSC Alexandre Beck 29/01/18

Resumo

BALBONI, Raphael Dorneles Caldeira. **“INFLUÊNCIA DO INTEMPERISMO EM FILMES FINOS DE CEO2 E CEO2:V2O5 E ESTUDO DE BIOGÉIS SUSTENTÁVEIS PARA APLICAÇÃO EM DISPOSITIVOS ELETROCRÔMICOS”** Tese (Doutorado em Ciências e Engenharia de Materiais) - Programa de Pós-Graduação em Ciências e Engenharia de Materiais, Centro de Desenvolvimento Tecnológico, Universidade Federal de Pelotas, Pelotas, 2022.

Estudos vêm sendo realizados visando a diminuição do alto consumo de energia atual, a otimização energética e a diminuição do impacto ambiental consequente deste problema. Uma vertente de estudo é a utilização de materiais eletrocrômicos na confecção de janelas inteligentes, e neste trabalho são estudadas duas diferentes camadas deste dispositivo. Primeiramente foi realizado um estudo relacionado à influência do intemperismo e da temperatura nas propriedades eletroquímicas e morfológicas de filmes finos de CeO_2 e CeO_2:V_2O_5 para utilização como contra-eletrodo. A camada referente ao eletrólito também foi estudada através do preparo e caracterização de géis poliméricos à base de acetato de celulose, polímero escolhido por apresentar aspectos sustentáveis e ser menos poluente. Para o estudo dos filmes, estes foram preparados pelo processo sol-gel, obtidos pela técnica *spin coating* e expostos à simulação de condições climáticas através de uma câmara de intemperismo acelerado. Para a confecção do gel, utilizou-se o acetato de celulose como polímero, o carbonato de propileno como solvente e o perclorato de lítio como fonte de prótons, com diferentes proporções e concentrações. Através das análises eletroquímicas, foi possível observar que após a simulação de 900 dias de exposição, ambos os filmes apresentaram um decréscimo na densidade de carga, com o filme dopado mantendo valores promissores para a aplicação proposta. Os filmes confirmaram o processo de difusão do transporte de massa através da análise de espectroscopia de impedância eletroquímica, além de uma maior uniformidade na sua superfície, confirmada pelas análises de AFM e MEV. Em relação aos géis, é possível afirmar que o gel contendo 10% em massa de acetato de celulose e 1,4 M de $LiClO_4$ foi o que se mostrou mais promissor, apresentando condutividade na ordem de $2{,}3 \times 10^{-4}$ $S.cm^{-1}$. Todos os géis testados apresentaram uma voltametria cíclica com a forma esperada à diferentes velocidades de varredura, além de manter uma estabilidade após 400 ciclos de análise, demonstrando um pequeno decréscimo na área do voltamograma. O gel demonstrou também uma transparência na faixa de 85% na faixa de comprimento de onda entre 300 e 800 nm e significante perda de massa entre 150 e 250 °C, através das análises de espectroscopia UV-Vis e termogravimetria, respectivamente.

Palavras-chave: eletrocromismo, eletrólitos poliméricos, acetato de celulose, filme fino, CeO_2:V_2O_5

Abstract

BALBONI, Raphael Dorneles Caldeira. **“INFLUENCE OF WEATHERING ON CEO2 AND CEO2:V2O5 THIN FILMS AND STUDY OF SUSTAINABLE BIOGELS FOR APPLICATION IN ELECTROCHROME DEVICES”** Thesis (PhD in Materials Science and Engineering) - Graduate Program in Materials Sciences and Engineering, Center for Technological Development, Federal University of Pelotas, Pelotas, 2022.

Studies have been carried out to reduce the current high energy consumption, aiming energy optimization and reduction of the environmental impact resulting from this problem. One alternative is the use of electrochromic materials in the production of smart windows, and in this work, two different layers of this device are studied. First, a study related to the influence of weathering and temperature on the electrochemical and morphological properties of thin films of CeO_2 and CeO_2:V_2O_5 for use as a counter electrode was carried out. The layer referring to the electrolyte was also studied through the preparation and characterization of polymeric gels based on cellulose acetate, a polymer chosen for presenting sustainable aspects and being less polluting. For the study of the films, they were prepared by the sol-gel process, obtained by the spin coating technique and exposed to the simulation of climatic conditions through an accelerated weathering chamber. To produce the gel, cellulose acetate was used as a polymer, propylene carbonate as a solvent and lithium perchlorate as a source of protons, with different proportions and concentrations. Through the electrochemical analysis, it was possible to observe that after the simulation of 900 days of exposure, both films showed a decrease in charge density, with the doped film maintaining promising values for the proposed application. The films confirmed the mass transport diffusion process through electrochemical impedance spectroscopy analysis, in addition to a greater uniformity on its surface, confirmed by AFM and SEM analyses. Regarding the gels, it is possible to state that the gel containing 10% by mass of cellulose acetate and 1.4 M of $LiClO_4$ was the most promising, presenting conductivity in the order of $2.3x10^{-4}$ $S.cm^{-1}$. All tested gels showed a cyclic voltammetry with the expected shape at different scan rates, in addition to maintaining stability after 400 analysis cycles, demonstrating a small decrease in the voltammogram area. The gel also demonstrated a transparency close to 85% in the wavelength range between 300 and 800 nm and significant mass loss between 150 and 250 °C, through UV-Vis spectroscopy and thermogravimetry analyses, respectively.

Keywords: electrochromism, polymer electrolyte, cellulose acetate, thin film, CeO_2:V_2O_5

Lista de Figuras

ARTIGO 01

ARTIGO 02

ARTIGO 03

ARTIGO 04

Lista de Tabelas

ARTIGO 01

ARTIGO 01

ARTIGO 03

Lista de abreviaturas, símbolos e siglas

CRT	Cathode ray tube - Tubo de raios catódicos
DRX	Difração de raios-X
DSC	Differential scanning calorimeter – Calorimetria exploratória diferencial
EIA	Estudo de impacto ambiental
EIE	Espectroscopia de impedância eletroquímica
EPE	Empresa de pesquisa energética
FTO	Fluorine doped tin oxide – Óxido de estanho dopado com fluor
H^+	Íon hidrogênio
Hz	Hertz
ITO	Indium doped tin oxide – Óxido de estanho dopado com índio
LCD	Liquid crystal display – Display de cristal líquido
LED	Light emitting diode – Diodo emissor de luz
Li^+	Íon lítio
MEV	Microscopia eletrônica de varredura
MFA	Microscopia de força atômica
mV	milivolt
nm	nanômetro
TGA	Thermogravimetricanalysis - Termogravimetria
TWh	terawatt-hora
UV	Ultravioleta
UV-Vis	Ultravioleta-visível
WO_3	Óxido de tungstênio (VI)

Sumário

1 Introdução

O consumo de energia tem um cenário cada vez mais alarmante, muito devido à estimativa do crescimento populacional e da corrida industrial e econômica atual. Assim, têm se tornado cada vez mais comuns estudos relacionados à eficiência energética, que pode ser definida como uma relação entre a quantidade de energia destinada à execução de certa atividade e a energia disponibilizada para a realização de tal atividade. Ela busca a utilização de energia da forma mais econômica e racional possível, mantendo o nível de conforto e qualidade de vida.

O aumento da eficiência energética está ligado a duas soluções: um aumento na parcela de energias renováveis utilizadas – energia eólica, solar e hídrica – e/ou à diminuição do consumo de energia. Como a tendência de energia demandada é cada vez maior, uma forma para que este consumo diminua é o desenvolvimento de novas tecnologias que otimizem a utilização dos recursos ofertados. O principal destino desta energia e as classes que apresentam maior taxa de crescimento de consumo são atualmente a classe residencial e comercial. É possível afirmar que, tanto em uma classe quanto na outra, uma grande parcela destina-se ao aquecimento e resfriamento do ambiente, além da iluminação artificial (EIA, 2012; OMRANY; MARSONO, 2016).

As fachadas das construções sem elementos de proteção solar tornam-se fatores comuns e relacionados aos altos valores de taxa de consumo. Uma solução é o desenvolvimento de uma tecnologia que ajude a controlar a climatização e iluminação excessiva, como exemplo os vidros eletrocrômicos, materiais que possuem características de mudança de coloração quando submetidos a um estímulo elétrico, podendo desta forma barrar a passagem de luz e/ou calor conforme desejado (YANG; SUN; MAI, 2016). Assim, com a utilização de fachadas cobertas de vidros eletrocrômicos ao invés dos vidros convencionais, é possível obter um controle maior da incidência de luz e calor sobre os prédios, sem perda de calor no inverno e/ou ganho de calor excessivo no verão. Tais fatores levam à uma diminuição no uso de climatizadores e gera uma queda de consumo energético.

O dispositivo eletrocrômico é formado por diferentes camadas com diferentes funções eletroquímicas, sendo o contra eletrodo responsável pelo armazenamento de íons e equilíbrio das cargas que se intercalam durante o processo de

coloração/descoloração, enquanto o eletrólito é a camada responsável pela condução dos íons entre o eletrodo de trabalho e o contra eletrodo.

Em relação ao contra-eletrodo, é desejado que o material escolhido para utilização como filme fino apresente propriedades específicas como boa capacidade de armazenamento de carga, transparência no processo de intercalação e estabilidade eletroquímica. Um material promissor para este uso é o dióxido de cério (CeO_2) (CAI; WANG; LEE, 2016), que apresenta algumas destas propriedades desejadas, e que pode ter suas desvantagens complementadas pela dopagem com o pentóxido de vanádio (V_2O_5) (MOURA et al., 2018). Um fator importante a ser considerado destes dispositivos é a necessidade de manter suas propriedades após longos períodos de exposição, o que abre demanda para um estudo relacionado à influência do intemperismo e da variação de temperatura nas propriedades eletroquímicas destes filmes (TONG et al., 2017).

O eletrólito, quando apresentado na forma de gel, apresenta vantagens como maior segurança e facilidade no processamento. Assim, muito estudos apresentam opções de eletrólitos géis poliméricos a base de polímeros, como exemplo poliacrilonitrila (PAN), polivinilpirrolidona (PVP), polietilenoglicol (PEG) e poli (álcool vinílico) (PVA) (DOS SANTOS, 2011; LIU et al., 2022b; RASIA, 2014). Para este trabalho, foi priorizada a utilização de um material eco-friendly e assim optou-se por trabalhar com um biogel sustentável à base de acetato de celulose, uma vez que este é transparente, incolor e proveniente de matriz natural, o que o torna menos danoso ao ambiente em seu descarte. O material em questão apresenta aplicações como imobilização de enzimas (YANEVA et al., 2018) e utilização como membranas e filtros (KAISER; STARK; GRASS, 2017), podendo ser obtido através da acetilação de diferentes fontes de celulose como polpa de árvore (ALVES et al., 2019) e subprodutos agrícolas (MOSTAFA et al., 2018).

Desta forma, o trabalho propõe uma análise da influência do intemperismo nas propriedades eletroquímicas e morfológicas de filmes finos de CeO_2 e CeO_2:V_2O_5, além de realizar um estudo mais amplo e completo de géis poliméricos à base de acetato de celulose em relação ao estabelecido na literatura, realizando caracterizações eletroquímicas, estruturais, térmicas e ópticas, reforçando o potencial de ambos os materiais estudados para a aplicação proposta e

apresentando uma promissora alternativa para utilização em dispositivos eletrocrômicos, visando o aumento da eficiência energética.

2 Objetivos

2.1 Objetivo geral

O objetivo geral deste trabalho foi realizar um estudo da influência do intemperismo e da temperatura nas propriedades de filmes finos de CeO_2 e CeO_2:V_2O_5 para utilização como contra-eletrodo, além de produzir um gel sustentável à base de acetato de celulose para utilização como eletrólito polimérico.

2.2 Objetivos específicos

- ✓ Preparar a solução de CeO_2 e CeO_2:V_2O_5 pelo método sol-gel;
- ✓ Preparar os filmes de CeO_2 e CeO_2:V_2O_5 pela técnica de *spin coating*, a fim de se obter filmes finos uniformes e com boa reprodutibilidade;
- ✓ Realizar a caracterização eletroquímica, morfológica e estrutural dos filmes finos pré e pós exposição, a fim de analisar a resistência das propriedades dos filmes ao processo de exposição ao intemperismo;
- ✓ Realizar a caracterização eletroquímica dos filmes finos em função da variação de temperatura através das análises de voltametria cíclica, cronoamperometria/ cronocoulometria e espectroscopia de impedância eletroquímica, a fim de avaliar os efeitos da temperatura nas suas propriedades;
- ✓ Produzir um gel polimérico sustentável à base de acetato de celulose para utilização como eletrólito em dispositivos eletrocrômicos;
- ✓ Caracterizar os géis poliméricos eletroquimicamente através de:
  - o Medidas de impedância eletroquímica (EIE) com o objetivo de estudar o comportamento de difusão e a condutividade do gel;
  - o Medidas de voltametria cíclica (VC) com o objetivo de realizar uma varredura potencial do gel;
  - o Medidas de voltametria cíclica (VC) a longo prazo com o objetivo de estudar a estabilidade cíclica do gel.
- ✓ Caracterizar os géis poliméricos estruturalmente através de:
  - o Medidas de difração de raios-X (DRX) com o objetivo de estudar a estrutura cristalina do gel;

- Medidas de espectroscopia no infravermelho por transformada de Fourier (FTIR) com o objetivo de estudar a energia absorvida pelo gel na região do infravermelho.

✓ Caracterizar os géis poliméricos termicamente através de:

- Medidas de termogravimetria (TG) com o objetivo de estudar a perda de massa do gel em temperaturas variadas.

✓ Caracterizar os géis poliméricos opticamente através de:

- Medidas de espectroscopia na região do Ultravioleta-Visível com o objetivo de estudar a interação da luz na região UV-Vis com o gel.

3 Revisão da literatura

3.1 Cosumo Energético

Os níveis de consumo energético mundial crescem a cada ano. Conforme ocorre o aumento da população, aumenta-se também a demanda de recursos e energia. Outros fatores como a disputa econômica e industrial mundial, a tecnologia mais avançada e os padrões de conforto exigidos atualmente ajudam a aumentar esta demanda.

Dentre os maiores consumidores, encontram-se no topo a China e em segundo lugar os EUA. O consumo energético combinado destes dois países equivale a mais de 40% do consumo mundial, que no ano de 2019, alcançou valores superiores a 21.000 TWh. Estes valores equivalem aproximadamente a 5.000 e 4.000 TWh, respectivamente (IEA, 2019). O Brasil terminou o ano em questão entre os 10 maiores consumidores de energia no mundo, com 482TWh, valores equivalentes a 2,3% de toda energia consumida mundialmente (Figura 1) (EPE, 2020; IEA, 2019).

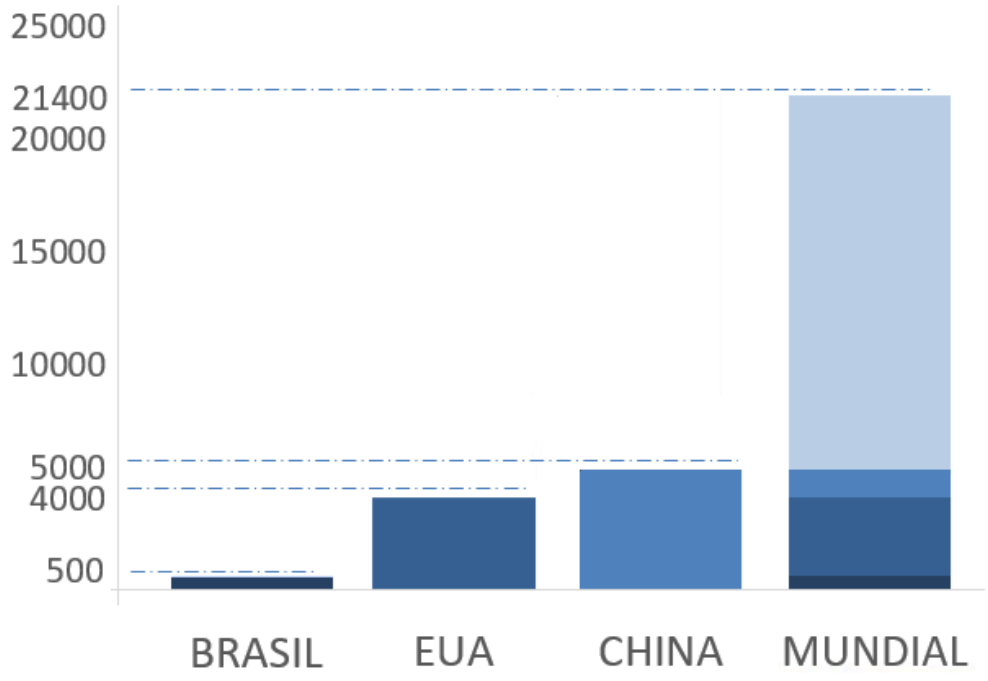

Figura 1 – Consumo de energia elétrica no ano de 2019
Fonte: International Energy Agency - IEA, 2019. - Adaptado

Estima-se que no intervalo de 20 anos (entre 2010 e 2030), ocorra um aumento constante destes valores, com um crescimento de 2,6 %/ano à nível mundial e 4,28 %/ano à nível nacional, segundo estudo realizado traçando a projeção de consumo energético realizada pelo Plano Nacional de Energia (PNE 2030), conforme ilustra a Figura 2 (EPE, 2020).

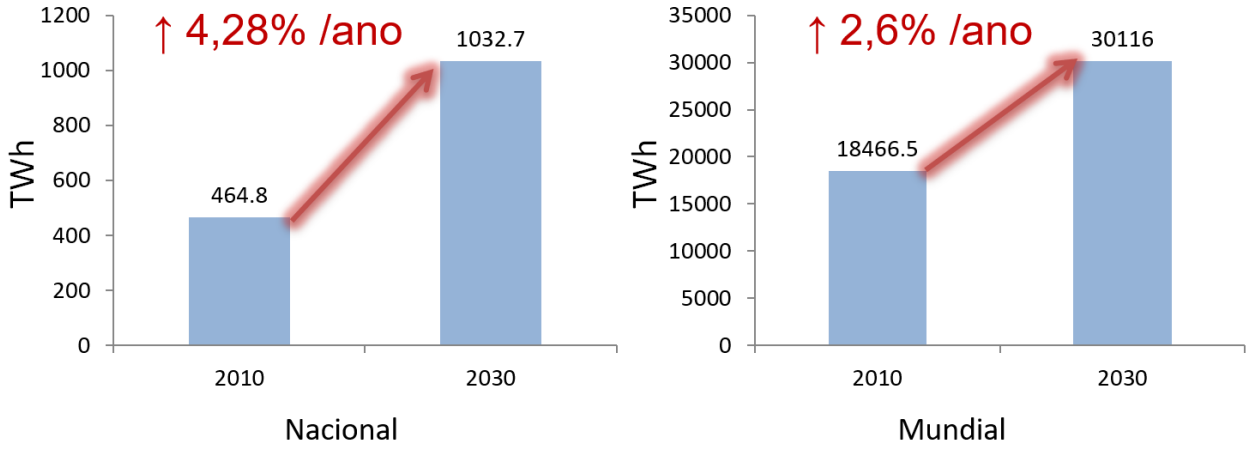

Figura 2 – Projeção de consumo energético
Fonte: EPE, 2020 - Adaptado

Na década passada, muitos estudos foram realizados acerca da utilização de energias renováveis em detrimento do uso de energias fósseis, devido ao fato de que grande parte da energia consumida ainda vem de fontes não renováveis. Em 2006, de toda energia utilizada mundialmente, 81% se originaram de combustíveis fósseis, entre eles, o carvão, o gás e o petróleo, principalmente (LUCON; GOLDEMBER, 2009).

3.1.1 Consumo energético em edificações

Um detalhamento da análise energética mostra que as classes com maior taxa de crescimento são as classes comercial e residencial, apresentando variações próximas à +4% no biênio 2018-2019. A classe industrial ainda possui a maior taxa de consumo, embora apresente valores decrescentes nos últimos anos (EPE, 2020). Estudos mais detalhados acerca deste consumo e do destino desta energia vêm sendo realizados principalmente nos EUA, e dados mostram que nos últimos anos, um valor equivalente a 73% de toda a energia gasta no país foi destinado apenas para consumo em edifícios (DEFOREST et al., 2017).

Especificando-se ainda mais estes dados, detalharam-se quais os destinos da energia gasta nos edifícios. Apenas com o objetivo de aquecimento e resfriamento, designa-se 35% da energia total gasta. Este valor equivale a aproximadamente 20% de toda energia consumida (EIA, 2012).

Além dos gastos destinados ao conforto térmico como aquecedores, ventiladores e condicionadores de ar, há ainda um gasto elevado relacionado à iluminação interna dos edifícios. Um fator comum entre estas altas taxas de consumo são as fachadas de edifícios e construções sem a utilização de elementos de proteção solar. Assim, destaca-se a importância de pesquisas nesta área com o intuito de desenvolver dispositivos que auxiliem a diminuir tais gastos, oferecendo um maior controle sobre as propriedades ópticas e térmicas dos vidros e janelas (OMRANY; MARSONO, 2016).

Dependendo de fatores como incidência de luz e posição dos prédios, o uso de alguns destes dispositivos pode gerar uma economia que gira entre 48 e 67 % (LEE; CLAYBAUGH; LAFRANCE, 2012).

3.1.2 Construções sustentáveis

Considerando os dados obtidos de diversos estudos realizados em relação aos altos índices de consumo energético, evidencia-se ainda mais o desenvolvimento sustentável como uma pauta e discussão pertinente. Este tema pode ser definido como o desenvolvimento que “satisfaz as necessidades do presente sem comprometer a possibilidade das gerações futuras satisfazerem suas próprias necessidades” (BRUNDLAND, 1987).

A partir desta definição, propõe-se a busca do equilíbrio entre a quantidade de recursos naturais disponíveis e os níveis de desenvolvimento. Este deve acontecer de forma que não prejudique a integridade do ambiente natural, tanto a curto como a longo prazo. Outro fator importante é manter o equilíbrio entre as dimensões econômica, social e ambiental, pois somente assim ocorrerá o desenvolvimento sustentável.Atualmente, o fator econômico tem sido priorizado enquanto o fator ambiental é neglicendiado.

E assim surgiu o conceito de “construção sustentável”, termo proposto por Kibert em 1994 e anteriormente discutido na conferência Rio-92. Este conceito discute a produção de construções adaptadas tanto aos seus utilizadores quanto ao

meio, causando menos dano ambiental e, assim, aumentando as oportunidades para as gerações futuras (KIBERT, 1994).

Dentro do que se entende como construção sustentável, alguns pontos são prioridades a serem seguidas, dentre eles, pode-se citar (MATEUS, 2004):

- Maximização da durabilidade das contruções
- Planejamento da conservação e manutenção das construções
- Utilização de materiais eco-eficientes
- Minimização da produção de resíduos
- Economia de energia e água.

Desta forma, quanto mais sustentável forem as construções, menos energia será demandada, logo, menores serão os danos ao ambiente, uma vez que grande parte da energia consumida é proveniente de combustíveis fósseis e este consumo gera um esgotamento de recursos naturais, além de uma grande quantidade de poluentes (ANSER et al., 2020).

3.2 Eletrocromismo

Materiais que possuem a capacidade de mudar a sua coloração devido a um estímulo externo são chamados de materiais cromógenos. Estes estímulos podem vir de diferentes fontes, como mudança de temperatura no meio (termocromismo), mudança de pressão (barocromismo), exposição à luz visível ou ultravioleta (fotocromismo) e potencial elétrico (eletrocromismo). Assim, o eletrocromismo pode ser definido como o fenômeno responsável pela mudança de coloração de certos materiais quando expostos a uma aplicação de corrente ou potencial elétrico (PATHAK et al., 2020).

O fenômeno da mudança de coloração ocorre uma vez que as moléculas cromógenas presentes no material absorvem a perturbação elétrica, e como resposta, acabam tendo suas propriedades ópticas alteradas. Tanto a perturbação quanto a resposta estão associadas à estrutura do material, que tende a ser amorfa e porosa, apresentando uma condutividade iônica e facilitando a difusão iônica (MOSER et al., 2016).

Entre as propriedades ópticas do material, podemos citar a absorção, a transmissão e a reflexão em alguns materiais específicos. Em função da aplicação

de corrente ou potencial, íons são inseridos na estrutura do material e os espectros de absorção e emissão do material, em alguns casos, podem sofrer um deslocamento de até centenas de angstroms (QUINTANILHA et al., 2014).

Estas mudanças nas propriedades ópticas são responsáveis pela mudança da coloração do material. O material pode ser considerado eletrocrômico se apresentar mudança de coloração reversível durante uma reação de oxidação/redução. Em outras palavras, o material sai da sua coloração natural ao ser submetido a uma corrente, e ao se inverter esta corrente, o material volta a sua coloração inicial (WEY et al., 2017).

Algumas propriedades intensivas do material como estequiometria, cristalinidade e composição química influenciam diretamente nas cores e na mudança de coloração. Durante o processo, o material pode assumir uma coloração a partir do transparente e/ou apresentar mais de um estado colorido, ocorrendo assim uma variação na coloração do material (VELEVSKA et al., 2017).

O primeiro registro de um fenômeno eletrocrômico data de 1704, quando Diesbach notou que a oxidação do ferro fazia com que o material mudasse de transparente para azul, e assim descobriu o azul da Prússia (hexacianoferrato (II) de ferro (III)) (MASTURAH BINTI FAKHRUDDIN et al., 2022). Já em 1815, Berzelius relatou que o óxido de tungstênio assumia uma coloração também azulada quando o mesmo era esquentado com hidrogênio atmosférico (SHAKHNOV; VLASOV; TOKAREV, 2016). Apesar destes relatos, o primeiro material estudado como sendo eletrocrômico data de 1951, quando Brimm et al. (1951) utilizou o bronze de sódio-tungstênio (Na_xWO_3) em uma célula eletroquímica. Após uma década de estudos sobre o tema, Platt (1961) cunhou o termo eletrocromismo, que passou a ser utilizado desde então.

3.3 Dispositivos Eletrocrômicos

Os primeiros dispositivos eletrocrômicos surgiram no final da década de 60, como pesquisador Deb, utilizando o tungstênio como material eletrocrômico e a aplicação do campo elétrico gerou uma mudança de coloração azulada nos filmes inicialmente transparentes, como esperado. Ao se inverter o campo elétrico, ocorreu a descoloração do filme, comprovando a teoria do eletrocromismo (DEB, 1969).

Ao se construir um dispositivo eletrocrômico completo, primeiramente é importante que haja um estudo aprofundado dos materiais cromógenos a serem utilizados. A coloração destes materiais ocorre apenas nas camadas eletrocrômicas, e o aumento ou diminuição da transparência do dispositivo depende da natureza eletrocrômica do material (GÖKDEMIR et al., 2014).

Outra função dos dispositivos, além da mudança de coloração marcante no espectro visível, é a modulação de energia multiespectral, trabalhando em regiões no infravermelho próximo, infravermelho térmico e micro-ondas. Assim, pode-se afirmar que os dispositivos podem trabalhar com dois modos de operação diferentes, absortivo/transmissivo ou absortivo/reflexivo (JAROSZ et al., 2019).

Após estudos e tentativas de aprimoramento dos dispositivos eletrocrômicos, foram buscadas formas de se utilizar os mesmos visando economia e otimização de produtos. Assim, estes dispositivos foram aos poucos substituindo o uso de monitores, tanto de CRT (raios catódicos) quanto de LCD (cristal líquido) e LED (diodos emissores de luz). Alguns dos motivos desta substituição são vantagens como custo reduzido, cores combinadas e facilidade na montagem dos dispositivos (XIONG et al., 2019).

Estes custos mais baixos decorrentes da utilização de dispositivos eletrocrômicos estão ligados ao menor consumo de energia destes em relação a outras tecnologias como LCD e LED. Estes dispositivos consomem pouca energia para produzir imagens e estas, uma vez formadas, requerem pouca ou nenhuma energia adicional para manter a mesma. Outro fator que gera menos gasto nestes dispositivos é a possibilidade de se produzir produtos com grandes áreas (YANG; SUN; MAI, 2016). Estudos recentes demonstraram a possibilidade de se trabalhar com áreas de deposição superiores a 100 cm^2 sem perda de resposta ou de funcionalidade, facilitando o processo para obtenção de materiais para aplicação em grandes áreas (SINGH et al., 2017).

3.3.1 Estrutura e funcionamento de dispositivos eletrocrômicos

O dispositivo eletrocrômico possui uma estrutura simples formada basicamente por cinco camadas distintas: uma camada eletrocrômica (filme eletrocrômico), uma camada condutora de íons (eletrólito), uma camada que armazena íons (contra-eletrodo), um condutor eletrônico transparente e uma camada

de vidro, sendo que estas 2 últimas aparecem em ambas as extremidades do dispositivo (DEFOREST et al., 2017).

Na montagem do dispositivo, os dois condutores eletrônicos transparentes ficam nas extremidades, separados pelas outras três camadas, em forma de sanduíche, como mostra a Figura 3. Estes condutores podem ser compostos de óxido de estanho dopado com flúor (FTO: SnO_2:F) ou com índio (ITO: In_2O_3:Sn) e estão depositados em substratos geralmente feitos de vidro ou plástico.

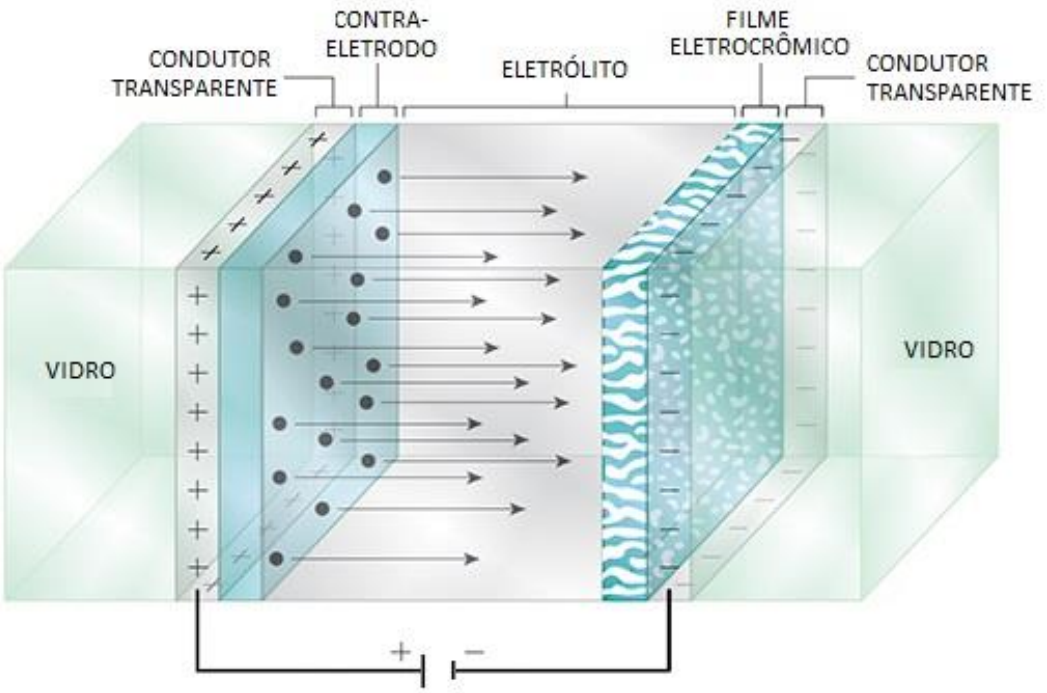

Figura 3–Camadas de um dispositivo eletrocrômico
Fonte: MORTIMER, 2013 - Adaptado

A principal camada é o eletrodo primário, ou eletrodo de trabalho. Este é propriamente o filme eletrocrômico e é aquele que sofre a mudança de cor devido à intercalação/troca de espécie iônica, seja Li^+ ou H^+. O eletrodo secundário é o contra-eletrodo, camada com a função de armazenar íons. Este pode aumentar o contraste óptico e fornecer um estado colorido extra, se necessário. Quando ocorre a coloração do filme devido à troca iônica, o contra-eletrodo é a camada responsável por equilibrar essas cargas trocadas, sejam por inserção ou extração (SHEN; OSTERHOLM; REYNOLDS, 2015).

A terceira camada é o eletrólito, onde deve possuir características como: capacidade de condução iônica, alto coeficiente de difusão (valor que representa a propensão do soluto de se movimentar em um solvente), rápida cinética eletroquímica (movimento de espécies ativas) e baixa condutividade eletrônica. O eletrólito fica entre os eletrodos primário e secundário e é o responsável pelo transporte das cargas durante a troca iônica (PORTO et al., 2020).

O modo de operação do dispositivo baseia-se em uma troca simples de cargas entre as diferentes camadas citadas devido à aplicação de um potencial elétrico. Ao ocorrer a inserção de cargas no filme, muda-se o estado de oxidação do filme eletrocrômico e com isso ocorre a mudança de cor (BALBONI et al., 2018).

O dispositivo abre também a possibilidade de se trabalhar em três estágios. Além dos dois estágios já discutidos, colorido e descolorido, há também a possibilidade de se criar um estado intermediário entre estes, no qual a voltagem é reduzida a um estado intermediário, permitindo assim a passagem da luz natural, porém, bloqueando a passagem do calor e possibilitando a utilização do dispositivo em diferentes estações e com diferentes propósitos, de acordo com a necessidade (YANG; SUN; MAI, 2016).

Independente da aplicação e do modo de operação desejado para o dispositivo, este baseia-se no mesmo conceito e modo de funcionamento. Inicialmente, o dispositivo encontra-se sem potencial aplicado e no seu estado descolorido. Os íons de Li^+ encontram-se todos no contra-eletrodo e não há nenhuma reação eletrocrômica envolvida no sistema, assim permitindo a passagem tanto da luz quanto do calor através do dispositivo, como se pode ver na Figura 4-(a).

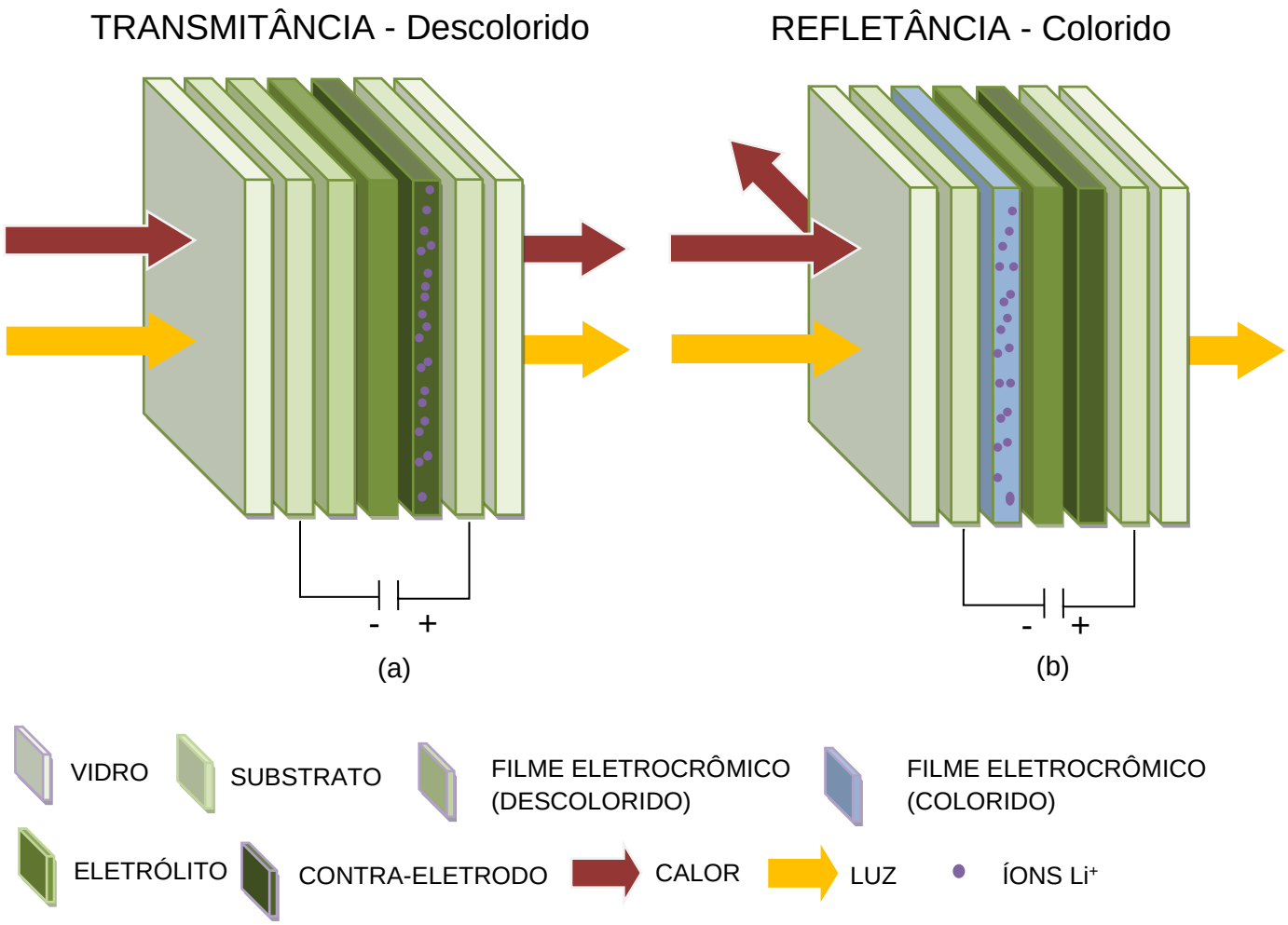

Figura 4 – Estrutura de um dispositivo eletrocrômico
Fonte: Adaptado de GRANQVIST (1998).

Quando se aplica tensão negativa sobre o filme eletrocrômico, ocorre então a reação eletrocrômica e os íons que inicialmente se encontravam no contra-eletrodo migram para o filme eletrocrômico, a fim de balancear a carga deste, conforme a equação abaixo, onde se utiliza o exemplo do óxido de tungstênio como filme eletrocrômico (GRANQVIST; HULTAKER, 2002):

$$I^+ + WO_3 + xe^- \leftrightarrow I_xWO_3$$

Após ocorrer a reação de redução, o filme que recebe os íons do contra-eletrodo assume uma coloração e cessa a transmitância, passando a refletir o calor e não mais o transmitindo, conforme mostra a Figura 4-(b). Os dispositivos devem apresentar uma reversibilidade desta reação, isto é, ao cessar o potencial, ou

invertê-lo, ocorre a oxidação do filme e os íons depositados neste retornam ao contra-eletrodo, uma vez que esta camada agora é quem possui o potencial negativo. Esta reação implica na volta da transparência da camada, logo, transmitância de todo o dispositivo (YANG; SUN; MAI, 2016).

Os íons do reservatório podem ser de hidrogênio ou lítio, sendo este segundo o mais utilizado devido à sua maior estabilidade. Usualmente se opta por trabalhar com estes íons específicos devido aos seus raios iônicos menores em relação a outros elementos da família 1A, onde encontram-se elementos com elevada eletropositividade (KITAZAWA et al., 2017).

3.3.2 Materiais eletrocrômicos e suas propriedades

A utilização dos dispositivos está associada a algumas propriedades específicas dos materiais. Dentre estas propriedades, pode-se citar o tempo de resposta, que é o tempo necessário para que ocorra a reação e subsequente mudança de pelo menos 95% da absorbância do material, podendo variar de segundos a minutos (MA et al., 2018).

Outras propriedades importantes relacionadas aos dispositivos são a memória óptica, tempo que as mudanças ópticas do estado colorido perduram após a cessão da voltagem e também a eficiência eletrocrômica, que faz uma relação entre a quantidade de carga que é injetada no material e a variação de cor que é produzida a partir desta inserção (LIU et al., 2018).

Os materiais eletrocrômicos são divididos em dois grupos em relação ao tipo de reação que ocorre com estes. Os materiais eletrocrômicos catódicos são aqueles nos quais a transmitância muda a partir da inserção de íons (resultado da redução), enquanto os materiais eletrocrômicos anódicos têm essa mudança devido à extração de íons (resultado da oxidação). A tendência é a utilização do material catódico como filme eletrocrômico e do material anódico como contra-eletrodo (camada de armazenamento de íon), uma vez que este trabalha com a extração de íons, a fim de se aumentar a eficiência do dispositivo (SHIM et al., 2017).

Quando ocorre a utilização de materiais que apresentam mudança de coloração em ambas as camadas, pode-se chamar de janela eletrocrômica complementar. Esta é basicamente a combinação do estado colorido reduzido de um material eletrocrômico catódico com o estado colorido oxidado de um material

eletrocrômico anódico, proporcionando assim um aumento na intensidade de absorção de luz e diminuição na passagem de luz solar, além de um aumento no contraste eletrocrômico (KORTZ et al., 2019).

Nesta combinação de materiais complementares, a oxidação de uma camada ocorre simultaneamente à redução da outra camada, e os estados coloridos/descoloridos são coincidentes durante a reação. Este processo complementar se dá através da seguinte reação:

$$MeO_n(transparente) + xI^+ + xe^- \leftrightarrow IxMeO_n\ (colorido)$$

Onde:

Me = metal, I^+ = íon (H^+ ou Li^+), e^- = elétron, *n* = varia conforme o óxido

3.3.3 Funcionalidade de um dispositivo eletrocrômico

Por possuírem diversas características favoráveis à sua utilização, os dispositivos eletrocrômicos possuem diversas áreas de aplicação e os materiais utilizados e suas propriedades é que irão definir a aplicação destes. Por sua vez, a finalidade de aplicação do dispositivo é que irá determinar o modo de funcionalidade do mesmo. Esta relação entre a aplicação e o modo de operação de cada dispositivo está representada na Figura 5.

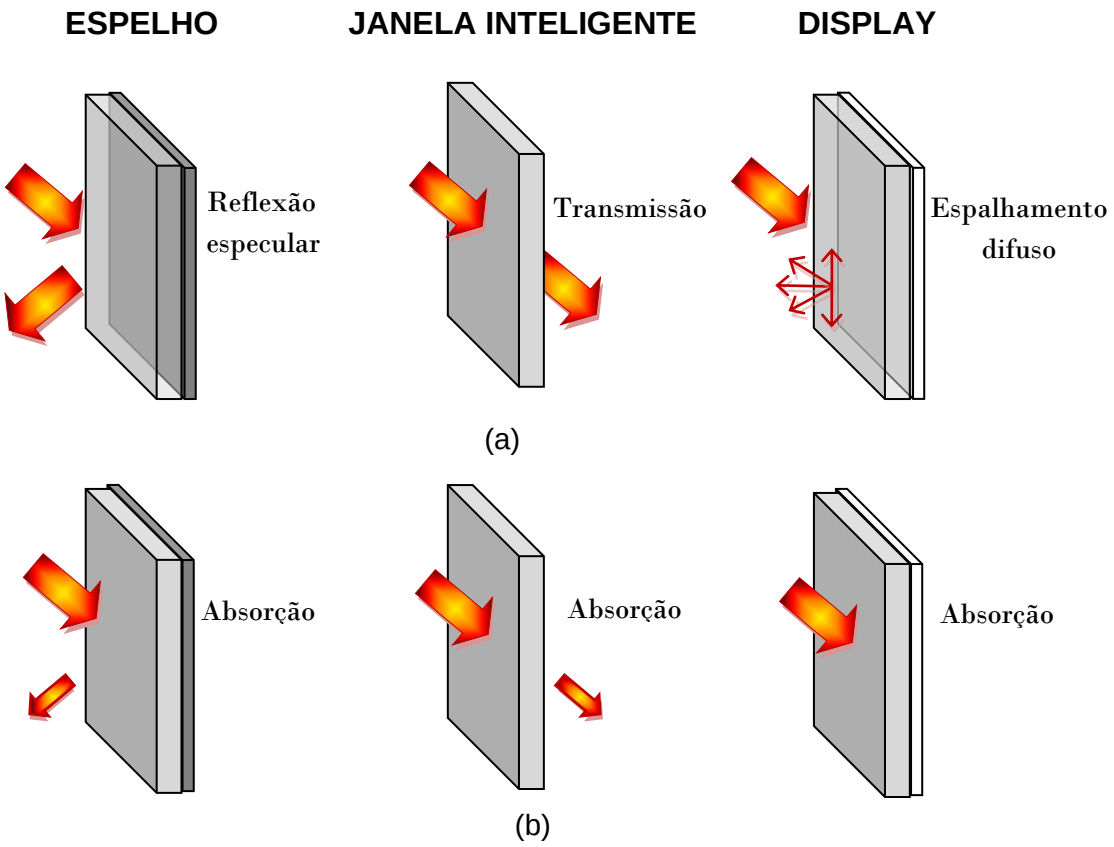

Figura 5– Funcionalidade de dispositivos eletrocrômicos em dois momentos: (a) potencial não aplicado; (b) potencial aplicado
Fonte: GRANQVIST, 1998 – Adaptado

Um dos modos de operação do dispositivo é atenuando a intensidade de luz a ser refletida. Este é utilizado quando se trabalha com espelhos eletrocrômicos, onde a luz não pode ser totalmente bloqueada, porém, ela não é refletida com sua intensidade total. Os espelhos eletrocrômicos são mais comumente utilizados na indústria automobilística, pois oferece maior segurança ao motorista em diversas condições de luminosidade, uma vez que não ofusca a visão (CHANG-JIAN et al., 2018).

No caso da utilização dos dispositivos para janelas inteligentes, o dispositivo funciona modulando ou diminuindo a intensidade da transmissão, tanto da luz visível quanto da infravermelha, assim, diminuindo o consumo energético relacionado às lâmpadas e climatizadores, ajudando nos gastos relacionados ao conforto térmico e também visual.

O terceiro modo de funcionamento dos dispositivos é ligado ao efeito de memória do dispositivo e se dá de forma semelhante ao funcionamento do espelho eletrocrômico, porém a reflexão neste caso ocorre de forma difusa, fazendo com que o material varie a cor observada. Esta variação pode perdurar mesmo após o fornecimento de potência ser cessado. Esta característica faz com que o material seja apropriado para utilização em painéis eletrônicos indicativos, como displays. Quando aplicado na confecção de displays, estes dispositivos apresentam ainda a possibilidade de se trabalhar com diferentes materiais, uma vez que os mesmos podem ser curvos além de planos (ONOZATO; CHO; OHTA, 2020).

A estrutura e disposição das camadas para dispositivos que funcionam de modo absortivo/transmissivo é a mesma dos dispositivos absortivo/reflexivo, porém, ao se trabalhar com reflexão, é possível adicionar uma camada refletiva permeável à íons entre a camada ativa e a camada responsável pelo balanço de cargas, assim o contra-eletrodo fica fora do campo de visão e a eficiência da reflexão do dispositivo é potencializada (KNOTT et al., 2012).

3.3.4 Janelas Inteligentes

O termo “janela inteligente” foi cunhado apenas em 1985, referindo-se a janelas que possuem características eletrocrômicas, isto é, janelas que podem mudar sua transmitância sob diferentes voltagens. Pode receber também o nome de janela eletrocrômica (SVENSSON; GRANQVIST, 1985).

O uso destas janelas passou a ser mais comum após estudos mostrarem que o gasto total de energia ligada a conforto térmico em edifícios chega à faixa entre 20 e 40 %, sendo que boa parcela deste consumo está relacionada a aparelhos climatizadores (KAMALISARVESTANI et al., 2013). Desta forma, a ideia de diminuir os gastos com consumo de energia aliado ao uso sustentável da energia fez com que o recurso das janelas eletrocrômicas fosse explorado. Estas poderiam ser utilizadas para modificar a incidência da luz do sol em uma peça específica ou até mesmo em todo um edifício ou construção, assim economizando energia e evitando poluição visual (ZHU; WANG, 2019).

Estudos já mostraram que há uma diminuição considerável nos gastos quando há a utilização deste recurso, porém, essa variação tem ligação com alguns fatores importantes, como o tipo, a orientação e localização da construção em

questão. Uma vez que esta economia está ligada ao uso de ar-condicionado, pode-se afirmar que quanto mais quente e maior a incidência do sol sobre o edifício, maior também será esta economia (TAVARES et al., 2014).

Este controle, tanto da passagem de radiação solar quanto da modulação da luz visível e infravermelha, além de diminuir o uso de climatizadores, também permite uma vista para o exterior do edifício, uma vez que dispensa a utilização de cortinas ou persianas, que teriam a finalidade de minimizar a incidência de luz. Como os dispositivos eletrocrômicos trabalham com mudança de cor, os mesmos podem ser utilizados na arquitetura também para fins estéticos (DI CARLO et al., 2018).

Todas estas vantagens fizeram com que o uso das janelas se difundisse e fosse utilizada, além da indústria automobilística, construção civil e arquitetura, que já fazem uso a mais tempo, em outras indústrias como a empresa aérea Boeing, que passou a utilizar vidros eletrocrômicos em uma de suas linhas de aviões. As janelas são 25% maiores que as usuais e permitem aos passageiros modularem a transparência em cinco estágios diferentes (YANG; SUN; MAI, 2016).

3.4 Contra-eletrodo

Os materiais utilizados nos dispositivos eletrocrômicos podem ser classificados em duas principais categorias: óxidos de metal de transição em materiais inorgânicos e polímeros condutores em materiais orgânicos. Quando se trabalha com materiais inorgânicos, uma técnica de deposição mais sofisticada é requerida com alta temperatura ou vácuo, o que aumenta o custo do processo. Podem ainda apresentar baixas velocidades de troca de coloração do dispositivo depois de montado e pouca versatilidade de ajuste de cores (WANG et al., 2020).

Uma destas camadas, o contra-eletrodo ou eletrodo secundário, é constituída de um filme fino formado por um material com propriedade de armazenamento (reservatório) de íons, podendo ou não ser um material eletrocrômico (ISLAM; BARILE, 2019). Tem como função fornecer o equilíbrio de cargas intercaladas durante o processo de coloração/descoloração do dispositivo eletrocrômico. Assim, o material deve possuir coeficiente de difusão, capacidade de armazenamento de íons e estabilidade eletroquímica comparáveis às da camada referente ao filme eletrocrômico, com o fim de equilibrar as reações de inserção/extração.

Para utilização como camada de contra-eletrodo, preferencialmente são utilizados materiais como óxidos de metais de transição, por apresentarem interessantes propriedades eletroquímicas, como exemplo a tolerância para trabalhar com eletrólitos alcalinos e grande capacidade de armazenamento de carga (WU et al., 2018).

3.4.1 CeO_2 como contra-eletrodo

Dentre os óxidos de metal estudados como eletrocrômicos, o CeO_2 apresenta propriedades eletrocrômicas interessantes – boa capacidade de inserção/extração de íons de lítio e alta transparência óptica na região visível – e vem sendo estudado desde o início da década de 90. Entretanto, o material apresenta uma taxa de reação mais lenta comparada a outros materiais, o qualificando para ser utilizado apenas como contra-eletrodo (JITTIARPORN et al., 2017). Ao se realizar estudos focados para esta aplicação, foram demonstradas características como transmitância de 80% e, para análises com vários ciclos, razão de densidade de carga próxima a 1,0, porém com uma queda na sua capacidade de armazenamento de carga (AVELLANEDA; BULHÕES, 2008).

Com essa investigação, concluiu-se que o óxido deveria ser dopado com outro material a fim de potencializar suas características para tal aplicação, uma vez que a substituição dos átomos de Ce por átomos com menor raio atômico irá aumentar o tamanho de seus poros, favorecendo o processo de condução dos íons Li^+ (SIM; PAWLICKA, 2020).

3.4.2 V_2O_5 como contra-eletrodo

Uma alternativa interessante para essa dopagem é o pentóxido de vanádio (V_2O_5), composto com alto potencial de utilização nestes dispositivos. Estudos deste material para aplicação em dispositivos eletrocrômicos revelaram sua superfície porosa, o que permite a fácil inserção de íons de lítio, característica que favorece o armazenamento de carga (LIN; TSAI; CHEN, 2008).

Estudos mais a fundo confirmaram esta alta capacidade de armazenamento de carga, com um processo de inserção/extração altamente reversível e processo de inserção de carga rápido. Esta capacidade de armazenamento, porém não se

mostrou estável a longo prazo, com uma queda na sua capacidade de litiação após diversos ciclos aplicados. Em relação às características ópticas do material, por possuir uma coloração amarelada característica, apresenta uma baixa transmissão visível, tornando-se mais transparente durante o processo de inserção de íons lítio (LOI et al., 2019).

Um estudo focado em determinar a eficiência eletrocrômica do material concluiu que este apresenta valores relativamente baixos em relação a outros óxidos, o que sugere a utilização do mesmo combinado com outros óxidos, equilibrando as vantagens e desvantagens de cada um dos materiais (AVELLANEDA; BERTON; BULHÕES, 2006).

3.4.3 CeO_2:V_2O_5 como contra-eletrodo

Desta forma, foram testados e estudados filmes finos de óxidos de cério dopados com óxidos de vanádio, esperando que o material resultante apresente as propriedades eletrocrômicas de cada um destes óxidos. Estes estudos demonstraram uma transmitância aproximada de 88%, valores acima dos demonstrados pelos filmes compostos pelos óxidos não combinados (PICARDI et al., 1999). Em outro estudo, verificou-se que após a combinação dos óxidos, houve um aumento na estabilidade eletroquímica, além da capacidade de armazenamento de carga (OREL; LAVRENCIC-STANGAR; PIHLAR, 1999). Essa melhora pode ser explicada pela condutividade tipo-p, que ocorre pela inserção de átomos com deficiência de um elétron na estrutura cristalina, facilitando a entrada de um íon nesta lacuna formada (WENDLING, 2011).

Através destes estudos, foi comprovada a eficiência da dopagem dos materiais, uma vez que incorpora a alta transparência em ambos os estados proporcionada pelo óxido de cério com a grande capacidade de armazenamento de carga proporcionada pelo pentóxido de vanádio, tornando-os assim complementares quando combinados.

3.5 Eletrólitos Poliméricos

Ao se trabalhar com eletrólitos, uma vertente bastante promissora são os polímeros condutores, uma vez que requerem um baixo custo no processo de

deposição, podendo ser feitas a temperatura ambiente. Estes tendem a apresentar alta eficiência de coloração e uma rápida troca de coloração (YUKSEL et al., 2017). Outra grande vantagem da utilização destes materiais em relação à utilização de óxidos é o seu processo de degradação, especialmente quando se trabalha com biopolímeros ou polímeros naturais.

Existem basicamente dois métodos para o preparo destes polímeros condutores: polimerização química e eletroquímica (ZHANG et al., 2019b). A partir da polimerização química, utilizam-se oxidantes químicos, resultando na formação de um material mais volumoso precipitado a partir da reação. Este envolve imersão de um substrato sólido na solução contendo o monômero e oxidante correspondente. A polimerização eletroquímica implica em uma oxidação eletroquímica do monômero correspondente em um eletrodo, o qual é seguido pela precipitação do polímero em uma superfície (ZHANG; DONG; HU, 2018).

A escolha do material certo para ser utilizado na camada certa durante a montagem de um dispositivo fará toda a diferença nos resultados finais e na eficiência do mesmo. Uma das camadas dos dispositivos a ser estudada é o eletrólito e este pode apresentar diferentes composições, que variam em função da funcionalidade buscada no dispositivo.

Grande parte dos eletrólitos são formados por solventes e sais que ionizam para fornecer os íons necessários ao sistema. Estes podem ser divididos em três classes: líquidos, sólidos inorgânicos e poliméricos. Os primeiros estudos de eletrólitos levavam a utilização de eletrólitos líquidos. Estes são soluções de sais, geralmente de lítio, em solventes orgânicos apróticos. Podem ser utilizados líquidos como carbonato de propileno, carbonato de etileno ou dimetilcarbonato para dissolver os sais de lítio (CANNAVALE et al., 2016).

Entretanto, eletrólitos líquidos tendem a reagir com os eletrodos, o que leva à uma diminuição no tempo de vida útil da célula, uma propriedade determinante na fabricação de dispositivos. Estes também exigem um maior custo para a montagem do dispositivo, uma vez que sua estrutura deve prevenir vazamentos. Ambas as desvantagens citadas podem ser determinantes na escolha pela não utilização de eletrólitos líquidos, uma vez que também apresentam riscos em termos de segurança (JIN et al., 2018).

A fim de substituir e descobrir uma forma de amenizar estes problemas foram estudadas novas formas de se trabalhar com eletrólitos. Os primeiros materiais utilizados foram os eletrólitos de géis poliméricos. Estes são basicamente materiais poliméricos que possuem uma adição significante de plastificante. Por apresentar bastante vantagens, foram adaptadas para sistemas eletroquímicos como baterias íon-lítio e aplicações eletrocrômicas (SUN et al., 2016).

Algumas destas vantagens apresentadas em relação aos eletrólitos líquidos são a facilidade no processamento, a vasta gama de temperatura de trabalho, a boa aderência das outras duas camadas do dispositivo que estão em contato com esta e a segurança contra possíveis choques e vazamentos, aumentando assim a estabilidade da célula em longo prazo (SENEVIRATHNE; SENEVIRATNE; ILEPERUMA, 2018).

O eletrólito deve apresentar a capacidade de doar elétrons, possuir uma longa durabilidade cíclica dentro da faixa de temperatura a que o dispositivo poderá ser submetido, estabilidade química e eletroquímica dentro da faixa de potencial com que se deseja trabalhar, um baixo custo, visto que esta é uma das principais vantagens do uso destes eletrólitos, e uma transparência óptica, principal característica das janelas inteligentes. Em relação à condutividade iônica, buscam-se valores semelhantes à de eletrólitos líquidos. Idealmente, esta condutividade deve estar na ordem de 10^{-4} $S.cm^{-1}$ (CHOLANT et al., 2020a).

Estes eletrólitos poliméricos têm como principal desvantagem a dificuldade de se manter uma estabilidade química e eletroquímica, por isso é importante que haja um estudo do polímero certo para uso e da possível dopagem do mesmo (CHOLANT et al., 2020b). Diversos estudos com diferentes materiais podem ser encontrados relatados na literatura, entre eles podem-se citar alguns polímeros sintéticos como PEO (MATHELA et al., 2022), poli (ácido acrílico) (PAA) (WANG; YAO; NIU, 2020), polimetilmetacrilato (PMMA) (LEE et al., 2020), poli (fluoreto de vinilideno) (PVDF) (LIU et al., 2022a) e poliacrilonitrila (PAN) (LIU et al., 2022a), além de materiais baseados em biopolímeros como goma arábica (CHOLANT et al., 2020a), goma xantana (CALDEIRA et al., 2018), pectina (MUTHUKRISHNAN et al., 2019) e celulose (MONISHA et al., 2017).

3.5.1 Fonte de íons

Uma das principais características desejadas em um eletrólito é a sua capacidade de conduzir íons entre os eletrodos. Assim, na confecção do mesmo, uma parcela importante é o material responsável pela condução iônica. Em polímeros, a condutividade iônica é basicamente a movimentação dos íons ao longo da matriz polimérica (MANJUNATHA et al., 2018).

Diferentemente do que se pensava inicialmente, o transporte iônico nos eletrólitos poliméricos ocorre na fase amorfa da matriz polimérica, e não na fase cristalina (UTPALLA et al., 2019).

Alguns fatores são determinantes para que o material apresente uma boa condução iônica, entre eles, pode-se citar (AHMAD, 2015):

- Concentração das espécies iônicas condutoras;
- Tipo de portador de carga (anódico ou catódico);
- Mobilidade dos portadores de carga;
- Temperatura.

Solvatação é o fenômeno responsável pelo transporte iônico. Os cátions provenientes da dissociação do sal coordenam-se com doares de elétrons capazes de solvatá-los, podendo estes ser da mesma cadeia ou então de cadeias poliméricas diferentes (ONG et al., 2015).

Um dos fatores que facilitam esta inserção e a movimentação dos cátions na rede polimérica é o pequeno tamanho destes, por isso geralmente são utilizados Li^+ (ARYA; SHARMA, 2017). Além de ser um doador que apresenta pequeno raio atômico, o Li^+ também apresenta relativa estabilidade química, diferentemente do H^+, por exemplo, que apesar de possuir um raio atômico menor, é suscetível a reações ao receber carga (SHAHI; ARUNAN, 2014). Por outro lado, utilização do lítio apresenta a desvantagem da questão socioambiental, uma vez que desafios surgem em relação ao descarte deste material, principalmente relacionado à utilização de baterias a base de lítio. Apesar da legislação brasileira compreender a remediação deste problema através da Política Nacional dos Resíduos Sólidos, o descarte e coleta destes materiais ainda configuram um desafio a ser resolvido. Desta forma, é importante sempre equilibrar os benefícios da utilização do lítio como precursor de íons com as desvantagens do mesmo, sempre prezando pela utilização de uma quantidade otimizada do material, a fim de gerar menos impacto ambiental.

A relação entre a condução iônica e a concentração do portador de carga adicionado ao eletrólito existe, mas não é diretamente proporcional. Diferentes fatores estão ligados ao aumento na condução. A presença do sal dissolvido na matriz polimérica faz com que a condutividade aumente devido à adição de portadores de carga. Porém, conforme se adiciona mais sal ao material, os possíveis "locais de hospedagem" do polímero começam a ficar indisponíveis. Quando ocorre um aumento excessivo nesta concentração de sal, o número de íons que podem interagir entre si também aumenta, levando a uma maior ocorrência de agregados iônicos e diminuição das espécies portadoras de carga efetivamente. Isto acaba levando a uma perda de mobilidade, o que significa uma diminuição da condutividade (POOSAPATI et al., 2019).

Assim, não basta apenas adicionar sal ao polímero esperando um aumento da condutividade. A concentração do sal ideal deve ser encontrada com objetivo de maximizar esta capacidade de condução do material. O objetivo é achar o valor máximo de sal que pode ser adicionado, sem que ocorram interações do tipo íon-íon (SMIATEK; HEUER; WINTER, 2018). Em alguns estudos realizados utilizando $LiClO_4$, este efeito causado pela saturação de sal é demonstrado e pode ser explicado pela presença de um grande número de agregados de múltiplos íons Li^+ e ClO_4^- no sistema eletrolítico (NGAMAROONCHOTE; CHOTSUWAN, 2016).

3.5.2 Plastificantes

Além de adicionar o sal ao polímero e estudar a concentração ótima deste, há outra forma de melhorar este material, que é adicionando um plastificante. Este material, ao mudar a organização molecular da rede polimérica, acaba aumentando o volume livre desta rede. Com mais espaço livre, os íons encontram mais caminhos e sua mobilidade aumenta. Com a mobilidade maior, a condutividade iônica do material aumenta (HAN et al., 2019).

Os plastificantes trabalham através da separação das cargas complexadas do polímero, o que promove uma dissociação do sal. Com isso, pode-se adicionar mais sal ao material, uma vez que a presença do plastificante diminui a chance de pares iônicos serem formados e, consequentemente, uma saturação de cargas ocorrer (LI, 2018).

Os materiais que possuem adição de um plastificante sofrem uma diminuição de suas atrações intermoleculares entre cadeias poliméricas, isso faz com que o mesmo mostre alterações em suas propriedades físicas e mecânicas, aumentando sua flexibilidade, capacidade de trabalho e mobilidade de cargas (LAU; KAHAR; YUSRINA, 2021).

Outras propriedades que sofrem alterações são a diminuição da resistência mecânica, o módulo de elasticidade, a cristalinidade e a temperatura de transição vítrea.

Na escolha do plastificante, devem-se levar em conta fatores como a eficiência na mudança das propriedades desejadas, a otimização dos efeitos sobre as propriedades naturais do polímero, a capacidade de se misturar ao polímero de forma uniforme e de permanecer na massa polimérica durante todo o tempo de vida útil do material (COSTA et al., 2017). Pode-se citar como exemplos de plastificantes: carbonato de etileno, carbonato de propileno, carbonato de dietila e gama-butirolactona (SUBBU et al., 2016).

3.5.3 Polímeros

Ao se trabalhar com eletrólitos poliméricos, a escolha mais importante é o próprio polímero a ser utilizado, uma vez que a compatibilidade e a sinergia deste com a fonte de íons e com o plastificante escolhidos será determinante para as propriedades finais do eletrólito obtido.

O termo polímero pode ser dividido em duas partes: meros, que são as unidades de repetição e poli, por estas unidades se repetirem muitas vezes, enquanto uma molécula formada por uma única unidade de repetição é denominada monômero. Quando é formada uma macromolécula a partir da repetição (geralmente dezenas de milhares de vezes) deste mero através de ligações covalentes, esta recebe a denominação de polímero (LIU et al., 2020).

Inicialmente tratados como isolantes elétricos, os polímeros passaram a ser estudados como condutores por acaso, porém, logo se mostraram promissores para utilização nesta área. Estes polímeros ainda apresentam a capacidade de dissolver sais inorgânicos, logo, gerando cargas e promovendo a condutividade iônica (MEDEIROS et al., 2012).

O fato de eletrólitos necessitarem de características específicas fez com que se passasse a estudar maneiras de modificar propriedades específicas dos polímeros envolvidos nesta confecção, sejam através de processos físicos ou de processos químicos. Buscam-se principalmente membranas que possibilitem a adesão entre as camadas de dispositivos, sejam de vidro ou metal, além de propriedades ópticas e mecânicas interessantes para uso (BALAKRISHNAN et al., 2021).

Quando os polímeros são obtidos através de modificações ou são produzidos completamente de forma artificial, passam a ser chamados de polímeros sintéticos. Estes surgem a partir de reações de polimerização, onde o monômero é unido a outro monômero, e assim sucessivamente, até obter-se uma grande cadeia polimérica (TIAN et al., 2012).

Apresentam uma estrutura mais simples, com pesos moleculares mais baixos e são mais estáveis termicamente. Possuem várias propriedades mecânicas a serem observadas e podem ser classificados basicamente em: plásticos, tecidos, elastômeros e silicones (ZHANG et al., 2019a).

3.5.4 Biopolímeros

Biopolímeros ou polímeros naturais são uma classe de materiais que se apresentam naturalmente, com sua formação ocorrendo durante o ciclo de crescimento de organismos vivos, não necessitando de uma sintetização ou intervenção (UPADHYE et al., 2022). Estes se dão como borrachas, polissacarídeos e proteínas. Possuem uma menor estabilidade quando submetidos a temperaturas altas e por serem naturais, apresentam baixa toxicidade, baixo custo e um caráter ecológico (DETSI et al., 2020).

A propriedade biodegradável destes polímeros se caracteriza pela mudança na estrutura química causada por atividade biológica, e se torna relevante pelo menor tempo necessário para degradação do material e pela menor quantidade de resíduos, uma vez que o plástico sintético degrada estes em plásticos menores, tornando o processo mais lento (MARIANO-TORRES; LÓPEZ-MARURE; DOMIGUEZ-SÁNCHEZ, 2015). Outro fator que reforça o apelo pela utilização dos biopolímeros é sua fonte de matriz renovável, uma vez que políticas de

desenvolvimento são cada vez mais fortes em relação à limitação crescente da disponibilidade de matéria-prima fóssil.

Possuem as características de solubilidade em água, podendo emulsificar óleos e modificar superfícies, além de possuir altas viscosidades. Tudo isso os qualificam para utilização na indústria de tintas, indústria têxtil e de cosméticos (BABU; O'CONNOR; SEERAM, 2013).

Os polímeros naturais vêm recebendo bastante atenção na área eletrônica, principalmente na confecção de eletrólitos e na utilização destes para a melhoria de outros eletrólitos, muito pelo fato de apresentarem pares de elétrons livres e interagiram com sais inorgânicos (KUMAR; RANWA; KUMAR, 2019).

Desta forma, tanto os polímeros naturais quanto os sintéticos apresentam vantagens e desvantagens importantes, e a escolha pelo uso de um ou outro está condicionada à aplicação final deste e às propriedades desejadas. Uma saída para chegar ao produto desejado é a utilização de ambos estados poliméricos, obtendo-se assim o chamado polímero biomodificado (GERMERSHAUS et al., 2015).

3.5.4.1 Acetato de Celulose

Um dos exemplos de polímeros biomodificados muito utilizados no mercado é o acetato de celulose. Este é um derivado da celulose e possui importância na utilização em fibras, plásticos e filtro para cigarro.

A celulose é um polímero natural linear semicristalino, com regiões cristalinas e regiões amorfas, com alta massa molecular e com a unidade repetitiva sendo formada de unidades glicosídicas (SHARMA et al., 2019). Sua estrutura pode ser vista na Figura 6. Possui características específicas que lhe proporcionam papel importante na formação de fibras, como a possibilidade de uma elongação da cadeia polimérica e uma formação que o induz a uma menor energia (JAUHARI et al., 2019).

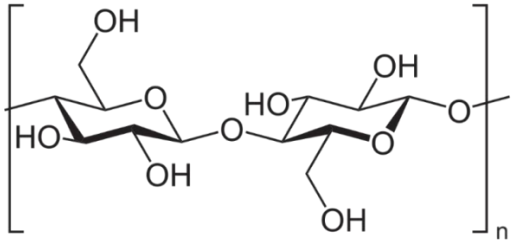

Figura 6–Estrutura da celulose
Fonte: Adaptado de SENNA (2011)

Apesar de ser abundante na natureza e possuir caráter renovável, o tornando um polímero sustentável, a utilização do mesmo na indústria é limitado, uma vez que este apresenta dificuldades de interação com outros precursores. Visando melhorar este fator, começou-se a testar formas de modificar a superfície do polímero através de reações químicas (ABUSHAMMALA; MAO, 2019).

Uma destas modificações é feita através da acetilação da celulose, seja pelo método heterogêneo ou pelo homogêneo. Em ambos os métodos, a reação da celulose ocorre através de uma mistura com ácido acético e anidrido acético, na presença de um ácido (sulfúrico ou perclórico) como catalisador. Na acetilação homogênea, a celulose se solubiliza no meio reacional, causando mudanças na morfologia de suas fibras, uma vez que ocorre o rompimento das interações entre cadeias adjacentes. Já na acetilação heterogênea (ou processo fibroso), devido à presença do agente não inchante (tolueno), o acetato permanece insolúvel, não ocorrendo assim mudanças significativas na morfologia das fibras (QUINTANA et al., 2018). Nesta reação, substituem-se os grupos hidroxila das unidades de glicose por grupos acetila (Figura 7). Assim, as cadeias tornam-se mais hidrofóbicas, as interações intermoleculares tornam-se menos intensas e pode-se provocar a dissolução devido ao rompimento destas interações, permitindo ao material uma dissolução em solventes convencionais (SENNA, 2011).

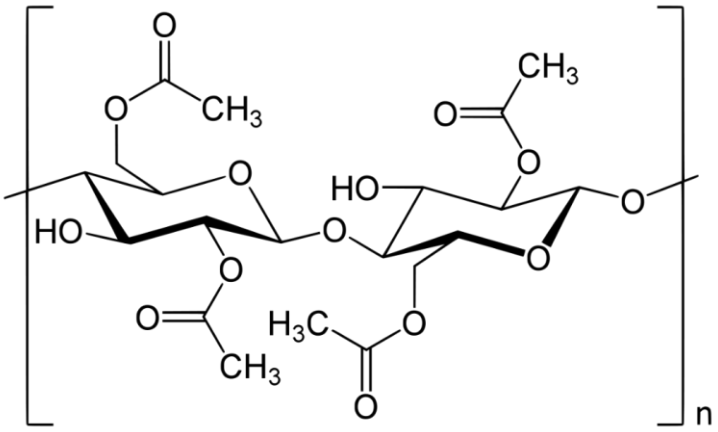

Figura 7–Estrutura do acetato de celulose
Fonte: Adaptado de CERQUEIRA et al., (2010)

O acetato de celulose resultante gera então um polímero neutro, a baixo custo e com capacidade de formar filmes transparentes (CERQUEIRA et al., 2010). A utilização do acetato de celulose tem por principal foco de utilização o preparo de membranas, isto é, filmes que permitem uma seletividade e permeabilidade em relação a íons. Outras áreas de interesse são na incorporação de polímeros condutores, podendo ser utilizado em dispositivos eletrônicos e eletrocrômicos (AKBARZADEH; SHOCKRAVI; VATANPOUR, 2021).

3.6 Intemperismo

Dispositivos eletrocrômicos como janelas inteligentes são usualmente utilizados no exterior de prédios e construções. Assim, além de apresentar boas propriedades eletroquímicas e eletrocrômicas, como transparência, armazenamento de íons, condutividade e estabilidade, é essencial que estes materiais apresentem uma boa performance a longo prazo, mantendo um grande *serviceability*, termo cunhado pelo American Society for Testing and Materials (ASTM, 1996), e que está relacionado à capacidade de um material ser utilizado sem perder sua manutenção ao longo de um período de tempo, ou seja, manter a capacidade de desempenhar sua função (CZANDERNA et al., 1999). Pela exposição à fatores climáticos como luz solar, vento e umidade, estes dispositivos estão sujeitos a terem sua durabilidade reduzida ao longo do tempo, o que torna tão necessário um entendimento sobre a influência destas condições no comportamento eletroquímico e morfológico dos filmes a longo prazo.

Pela dificuldade imposta experimentalmente para a realização deste tipo de estudo, uma alternativa viável é a utilização de câmaras simuladoras de intemperismo, como exemplo a Figura 8. Estas são câmaras que expõem um material a condições próximas ao intemperismo natural causado por fatores climáticos, utilizando tecnologias análogas aos naturais. Para tal, faz-se uso de lâmpadas fluorescentes para simular a radiação ultravioleta da luz solar, condensação forçada para simular umidade oriunda de chuva e orvalho, e aquecedores para simular variações de temperatura.

Figura 8– Câmara de intemperismo acelerado
Fonte: https://www.q-lab.com/

Apesar da importância destes testes, existem variáveis relacionadas ao tipo de função a ser desempenhada e às condições relacionadas a essa função, havendo, portanto, regras e padrões específicos para cada câmara. A utilização e programação da câmara utilizada está relacionada diretamente ao tipo de exposição desejada e ao tipo de material a ser estudado. Usualmente, as câmaras são programadas com normas específicas para os diferentes tipos de materiais: plásticos, revestimentos, materiais automotivos, materiais de cobertura, madeira e materiais de revestimento com exposição de alta irradiância, sendo este último o mais apropriado para testes em filmes finos utilizados em dispositivos eletrocrômicos.

Partindo desta determinação, a ASTM (American Society for Testing and Materials) fornece padrões específicos para tal simulação, como a designação G

154-06 – *Standard Practice for Operating Fluorescent Ultraviolet (UV) Lamp Apparatus for Exposure of Nonmetallic Materials*, Ciclo 6, que visa adequar os parâmetros da câmara à materiais usados para revestimento e com alta taxa de exposição. Este ciclo específico utiliza uma lâmpada UVA-340 com uma irradiância típica de 1,55 $W.m^{-2}.nm^{-1}$ em comprimento de onda aproximado de 340 nm, assim, cada dia de exposição na câmara equivale a 12 dias de exposição à condições externas (ASTM, 2006). As especificações de cada ciclo estão descritas na Tabela 1.

Tabela1– Parâmetros de diferentes ciclos programáveis para simulação de intemperismo

Ciclo	**Lâmpada**	**Irradiação Típica**	**Comprimento de onda aproximado**	**Ciclo de exposição**
1	UVA-340	0,89 $W.m^{-2}.nm^{-1}$	340 nm	8 h UV - 60 (± 3) °C 4 h Condensação - 50 (± 3) °C
2	UVB-313	0,71 $W.m^{-2}.nm^{-1}$	310 nm	4 h UV - 60 (± 3) °C 4 h Condensação - 50 (± 3) °C
3	UVB-313	0,49 $W.m^{-2}.nm^{-1}$	310 nm	8 h UV - 70 (± 3) °C 4 h Condensação - 50 (± 3) °C
4	UVA-340	1,55 $W.m^{-2}.nm^{-1}$	340 nm	8 h UV - 70 (± 3) °C 4 h Condensação - 50 (± 3) °C
5	UVB-313	0,62 $W.m^{-2}.nm^{-1}$	310 nm	20 h UV - 80 (± 3) °C 4 h Condensação - 50 (± 3) °C
6	UVA-340	1,55 $W.m^{-2}.nm^{-1}$	340 nm	8 h UV - 60 (± 3) °C 4 h Condensação - 50 (± 3) °C
7	UVA-340	1,55 $W.m^{-2}.nm^{-1}$	340 nm	8 h UV - 60 (± 3) °C 0,25 h spray de água 3,75 h Condensação - 50 (± 3) °C
8	UVB-313	28 $W.m^{-2}$	270 a 700 nm	8 h UV - 70 (± 3) °C 4 h Condensação - 50 (± 3) °C

Fonte: ASTM, 2006 - Adaptado

4 Artigos

Os resultados e metodologias referentes ao desenvolvimento do presente trabalho estão descritos conforme os artigos produzidos durante o período de pesquisa e são apresentados a seguir. Dos artigos desenvolvidos, 2 foram publicados e são relacionados ao estudo dos filmes finos como contra-eletrodo, 1 artigo a ser publicado foi produzido relacionado ao estudo de eletrólitos géis poliméricos e 1 artigo publicado é referente ao Período Sanduíche realizado na University of Surrey através da bolsa CAPES-PRInt.

4.1 Artigo 1

O artigo intitulado “**Electrochemical, UV–Vis, and microscopical characteristics of sol–gel CeO2:V2O5 thin film**” é apresentado conforme publicado na Revista Journal of Materials Science: Materials in Electronics, ISSN: 0957-4522, classificação A2 na área de Materiais.

Journal of Materials Science: Materials in Electronics (2018) 29:16911–16920
https://doi.org/10.1007/s10854-018-9786-5

Electrochemical, UV–Vis, and microscopical characteristics of sol–gel CeO_2:V_2O_5 thin film

R. D. C. Balboni[1] · R. M. J. Lemos[2] · E. A. Moura[3] · C. M. Cholant[1] · C. F. Azevedo[2] · I. M. Caldeira[1] · A. Gündel[4] · W. H. Flores[4] · A. Pawlicka[5] · C. O. Avellaneda[1]

Received: 18 April 2018 / Accepted: 30 July 2018 / Published online: 9 August 2018

Abstract

Cerium dioxide (CeO_2) and cerium dioxide doped with vanadium pentoxide (CeO_2:V_2O_5) were synthesized from sol–gel precursors and deposited by spin coating on a conductive glass substrate (FTO). The films with different concentration of dopant and number of deposited layers were studied throughout cyclic voltammetry (CV), chronoamperometry/chronocoulometry, atomic force microscopy (AFM), scanning electron microscopy (SEM), and UV–Vis spectroscopy. The best value of charge density of 18.9 mC cm^{-2} was obtained for CeO_2 doped with 15 mol% of V_2O_5 film. The chemical diffusion coefficient of lithium ions into CeO_2 was 1.73×10^{-12} and CeO_2:V_2O_5 15 mol% 6.75×10^{-13} cm^2 s^{-1}. This film presented 79% of transparency in UV–Vis and 5% color change under ± 1.3 V of applied potentials. Structural analyses revealed its homogeneous surface and the root mean-squared roughness (RMS) value of 9.42 nm. Based on the obtained results, CeO_2 doped with 15 mol% V_2O_5 film is a promising thin coating for the use in electrochromic devices as a passive counter-electrode.

1 Introduction

Cerium dioxide (CeO_2) thin films have a property of being electrochemically active but optically passive [1, 2]. Therefore, they have been studied in the last 20 years as materials for passive electrodes, mainly counter-electrode, in electrochemical devices. For example, in electrochromic devices the counter-electrode thin films have a function of storing ions. During the process of coloration/discoloration of these devices occurs a charge exchange in the electrochromic film layer, and the counter-electrode is responsible for compensation of these charges [3]. CeO_2 thin films have high optical transparency in the visible region and a structure with large pores and no cracks that allows easy passage of ions during their intercalation and deintercalation [4]. From the other hand, CeO_2 thin films have a slowest reaction rate when compared to other materials [5, 6]. Moreover, cerium dioxide films present a decrease of the ion storage capacity over

✉ C. O. Avellaneda
cesaravellaneda@gmail.com

R. D. C. Balboni
raphael.balboni@gmail.com

R. M. J. Lemos
rafaela.mjl@gmail.com

E. A. Moura
blackmoura2@gmail.com

C. M. Cholant
camila_scholant@hotmail.com

I. M. Caldeira
izabel_mc@hotmail.com

A. Gündel
gundel@gmail.com

W. H. Flores
wladimir.flores@unipampa.edu.br

A. Pawlicka
agnieszka@iqsc.usp.br

[1] Centro de Desenvolvimento Tecnológico - CDTec, Universidade Federal de Pelotas, Rua Gomes Carneiro 1, Centro, Pelotas, RS 96010-610, Brazil

[2] Centro de Ciências Químicas, Farmacêuticas e de Alimentos - CCQFA, Universidade Federal de Pelotas, Campus Capão do Leão, Pelotas, RS 96160-000, Brazil

[3] Departamento de Física, Centro Politécnico, Universidade Federal do Paraná, C.P. 19044, Curitiba, PR 81531-990, Brazil

[4] Universidade Federal do Pampa, Rua Travessa 45 No. 1650, Bagé, RS 96413-170, Brazil

[5] IQSC-USP, Av. Trabalhador Sãocarlense 400, São Carlos, SP 13566-590, Brazil

time, a common problem with transition metal oxides [7]. Therefore, seeking to enhance electrochemical properties of CeO_2 Baudry et al. [8] have proposed its doping with TiO_2, which resulted in more electrochemically stable films. After that, other modifications of CeO_2 films were developed, and among them Krasovec et al. [9] have reported on doping cerium dioxide films with vanadium pentoxide by the sol–gel route. They have obtained tetragonal crystal structure, determined by X-ray diffraction, that acted as ion storage material. Moreover, the small color changes (color efficiency of about 0.1–0.5 cm^2 C^{-1}) qualified it to be applied as counter electrode in electrochromic devices. Masetti et al. [6] have studied mixed cerium–vanadium oxides obtained by radio reactive frequency sputtering. As the main result, they have registered 30 mC cm^{-2} of lithium ions inserted charge and a total charge of 60 mC cm^{-2} during a reversible electrochemical cycling in the 1–5 V potential range versus Li. They did not observe any degradation, but probably due to the 1:1 of CeO_2 to V_2O_5 ratio in target powders there was a color change from yellow to transparent. Malini and Sanjeeviraja have also reported on vanadium–cerium mixed oxides, deposited by radio frequency magnetron sputtering in a pure argon atmosphere and using CeO_2 to V_2O_5 target compositions of 1:1 and 1:2 [10]. They have shown that this material is a good electrode for electrochromic devices because of its passive optical behavior and good charge capacity. More recently, aiming to advance on understanding ceria-based materials, Bishop et al. [11] have studied chemical expansion and oxygen non-stoichiometry behavior of 10 mol% gadolinium doped cerium oxide and undoped ceria as a function of partial pressure of oxygen at 800 °C. As a conclusion, they stated that cerium-based oxides display considerable chemical expansions, which must be considered for their use in electrochemical devices such as solid oxide fuel cells and ceramic oxygen generators. More recently, Temerk and Ibrahim have studied glassy carbon paste electrode modified with indium doped CeO_2 [12] and boron doped CeO_2 nanoparticles [13] for selective and sensitive electrochemical detection of uric acid (UA). The authors have shown that modified electrode of indium (In) doped CeO_2 had better catalytic activity toward the detection of uric acid than the undoped CeO_2 electrode. Additionally, both In and B modified electrodes showed very good selectivity for electrochemical determination of UA. In summary, obtained sensor revealed fast response, high sensitivity, and acceptable reproducibility.

Aiming to advance on studies of CeO_2 doped materials, vanadium pentoxide (V_2O_5) was chosen because of its high capacity of ion storage and a reversible coloration in the visible spectrum range under insertion of lithium ions [14]. Besides this, V_2O_5 is known as material that undergoes semiconductor–metal phase transition at 257 °C and also changes its optical properties when doped with lithium, molybdenum or tungsten [15]. The present study focuses on new, cerium–vanadium mixed oxides thin films and the possibility of their applications in modern electronics. To show the advantage of this new material, CeO_2:V_2O_5 films were synthesized, by sol–gel method, with different concentrations of dopant and had different number of deposited layers. All these films were analyzed by cyclic voltammetry and chronoamperometry/chronocoulometry, and after choosing the best film, in terms of electrochemical performance, there were performed more electrochemical, morphologic, and optical-electrochemical analyses.

1 Experimental

1.1 Preparation of the sols and thin films

To obtain cerium-based sol, 0.56 g of cerium chloride heptahydrate ($CeCl_3 \cdot 7H_2O$; Sigma-Aldrich), 0.58 g of citric acid ($C_6H_8O_7$; Synth), and 10 mL of ethyl alcohol (C_2H_6O; Synth) were maintained under stirring for 30 min. To obtain cerium–vanadium-based sol, 5, 10, 15, 20, and 25 mol% of vanadium isopropoxide ($OV(OCH(CH_3)_2)_3$; Alfa Aesar) was added to cerium-based sol and the resulting solution was stirred for 10 min.

Thin films were deposited by spin-coating technique (Chemat Technology Spin-Coater KW-4A) on a FTO (fluorine tin oxide; Pilkington) conductive glass substrate. A first spin cycle was at 500 rpm for 3 s and a second at 2000 rpm for 30 s. Immediately after the deposition, the films were submitted to a heat treatment at 450 °C for 30 min for each deposited layer.

1.2 Characterization of thin films

Electrochemical measurements were done in an electrochemical cell with three electrodes, where a working electrode was a CeO_2:V_2O_5 film, a reference electrode was a silver wire, and a counter-electrode was a platinum foil of 1 cm^2. The electrolyte was a 0.1 mol L^{-1} lithium perchlorate ($LiClO_4$; Vetec) dissolved in propylene carbonate (PC; Sigma-Aldrich). These measurements were controlled by potentiostat/galvanostat Autolab PGSTAT 302N.

The morphological properties were studied with the atomic force microscopy (AFM; Agilent Technologies 5500) and scanning electron microscopy (SEM; JOEL JSM-6610LV) equipment.

The optical measurements were done with Cary 100 UV–Vis spectrometer (Agilent Technologies), operating in a wavelength range between 320 and 800 nm.

X-ray diffraction patterns were collected from X-ray diffractometer (Rigaku Ultima IV diffractometer), operating with a radiation source of CuKα (λ = 1.5406 Å). The applied

voltage was of 40 kV, a current of 20 mA, a 2θ scan range of 20°–70°, and scanning speed of 2° min^{-1}.

1 Results and discussion

The influence of V_2O_5 on the charge capacity of the CeO_2 film was studied by potentiostatic step and the obtained results are depicted in Fig. 1a. Chronocoulometric measurements were performed at a potential of − 1.25 V (intercalation) and + 1.25 V (deintercalation) applied during 60 s to the film composed of five layers. Figure 1a shows that an increase of the amount of dopant leads to an increase of the charge density of CeO_2:V_2O_5, reaching a maximum value of 17.6 (± 1) mC cm^{-2} for CeO_2 film with 15 mol% of V_2O_5. Masetti et al. [6] have registered the charge density of about 30 mC cm^{-2} for the films obtained by reactive radio frequency sputtering and having as a targets mixed powder of CeO_2:V_2O_5 with ratio of 1:1. In the present study, higher quantity of V_2O_5 promotes a decrease of the charge density, which may mean a possible saturation of the dopant as observed for films of NiO:V_2O_5 [16]. The influence of number of layers on the charge density of CeO_2 and CeO_2 with 15 mol% V_2O_5 films is shown in Fig. 1b. This figure shows that the best charge density response of 18.9 (± 1) mC cm^{-2} is obtained with five layers CeO_2 film doped with 15 mol% of V_2O_5, and the best value among the undoped CeO_2 film is of 7.5 mC cm^{-2} for the one with three layers (Fig. 1b). From this figure it is clearly seen that not only the film composition but also the number of film layers impact on the charge density values of the CeO_2 doped films as in CeO_2/SnO_2 thin films [17]. Similar behavior was already observed for V_2O_5 thin films doped with Nb_2O_5 [18]. This is probably due to increased resistance of semi-conductor film, which is a result of increased thickness.

Aiming to verify the behavior of the electroactive species, thin films of CeO_2 and CeO_2:V_2O_5 15 mol% were subjected to impedance analyses under applied different potentials. The Nyquist curves are plotted in Fig. 2 and consist mainly of linear region associated with Warburg diffusion. The straight lines have a slop close to 45°, especially for the applied lower potentials, and this behavior is more consistent for the samples doped with V_2O_5. This is an indication that the mass transport of the oxidized/reduced species in both films is given by diffusion [19].

Figure 3 shows cyclic voltammograms of CeO_2 and CeO_2:V_2O_5 films with different dopant concentrations; all the films are composed of five layers. At the first look, these voltammograms are different of the ones published by other authors [6, 10], which can be due to the different methods used to obtain the films and because they have different structures. In present study, the applied cathodic and anodic potentials were of − 1.3 and + 1.3 V, respectively, and the scan rate was 50 mV s^{-1}. CeO_2 film doped with 15 mol% of V_2O_5 presents a larger area than the other ones, which means a better electrochemical performance, i.e., an easy way to ion charge transfer process [20]. Moreover, there is a large anodic peak, with maximum at − 0.5 V, for pure CeO_2 thin film that corresponds to extraction of ions, but the cathodic peak is absent [2]. The addition of vanadium pentoxide to CeO_2 thin film promotes an increase of current density and shift of anodic peak to more positive values. For example, the anodic peak maximum of CeO_2:V_2O_5 thin film with 5 mol% of V_2O_5 is observed at − 0.25 V and with 15 mol% at − 0.15 V. Anodic peaks of films with 10 and 20 mol% of V_2O_5 are more pronounced and have maxima at 0.05 V.

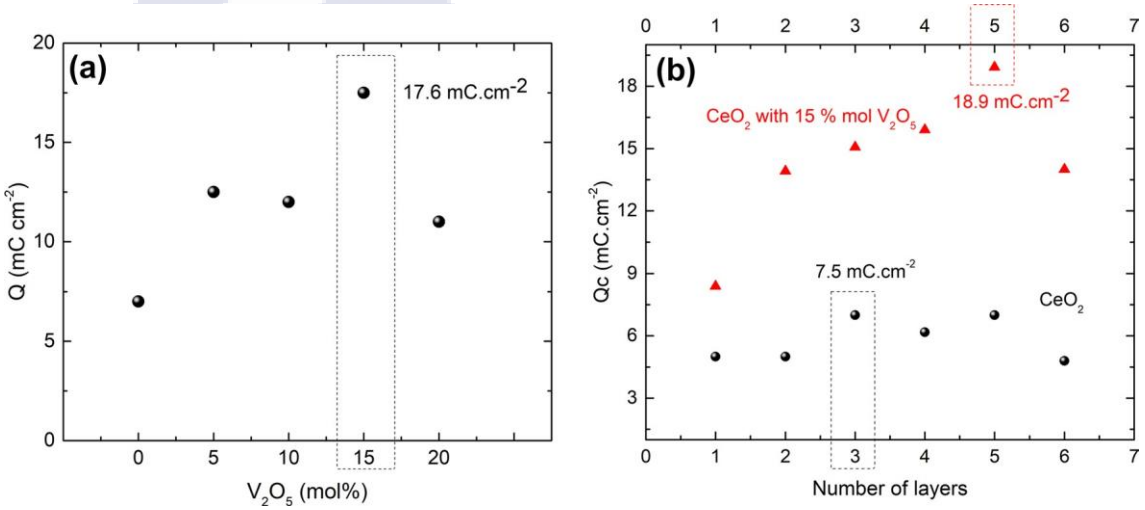

Fig. 1 Charge density of the thin films as a function of **a** concentration of V_2O_5 as dopant for a five layers' thin film and **b** number of deposited layers for CeO_2 and CeO_2:V_2O_5 with 15 mol% films

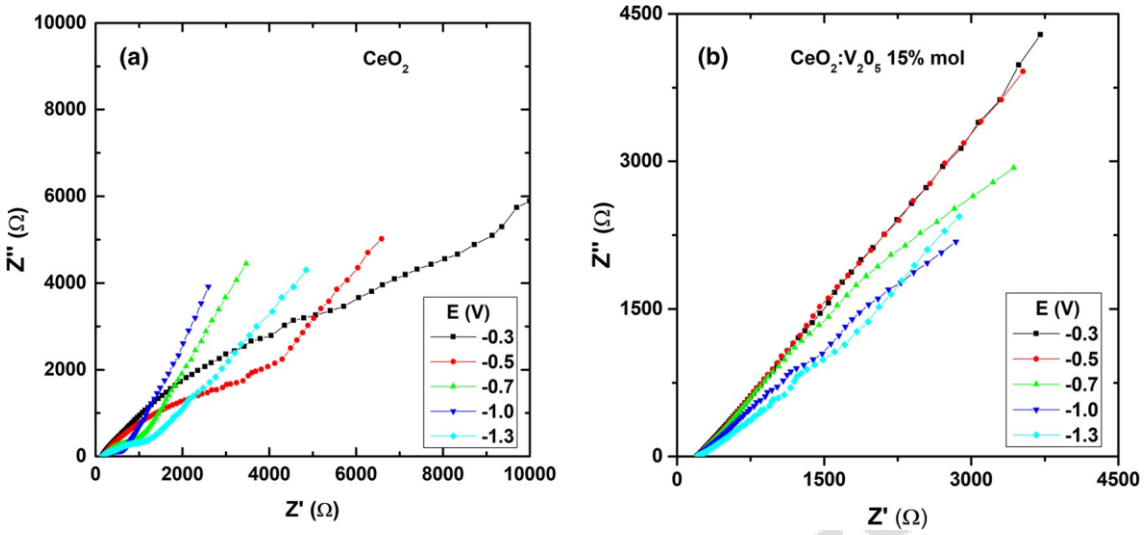

Fig. 2 Nyquist plots of CeO_2 (**a**) and CeO_2:V_2O_5 15 mol% (**b**) thin films at different applied potentials

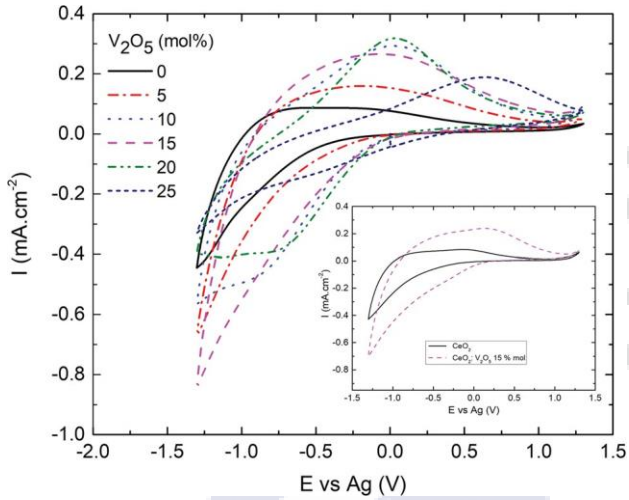

Fig. 3 Cyclic voltammetry of CeO_2:V_2O_5 films as a function of V_2O_5 concentration (mol%). Comparison of CeO_2 and CeO_2:V_2O_5 voltammograms in inset

This shift of anodic peak can be due to either some change in film resistance, as already observed for NiO_x thin films [21], or the influence of V_2O_5 on electrochemical behavior of CeO_2:V_2O_5 because of similar V_2O_5 voltammogram [22]. These only two films also show cathodic peaks centered at − 0.8 and − 0.6 V, which is very similar to the results obtained for CeO_2–TiO_2 [23] and CeO_2–TiO_2–ZrO_2 [24] thin films obtained by sol–gel method. Other films display only increase of cathodic currents as a function of increase of V_2O_5 doping, resembling to films of Nb_2O_5–TiO_2 [25] or Nb_2O_5, Nb_2O_5:Li^+:V_2O_5, and Nb_2O_5:Li^+ [26].

A comparison of cyclic voltammograms of undoped and 15 mol% V_2O_5 doped CeO_2 films reveals an increase of the cathodic current, starting at the potential near to − 0.50 V, for the undoped film (Fig. 3 inset). In the anodic direction of the scan, there is a large wave with a small peak maximum at −0.25 V and current density of 0.08 mA cm^{-2}, after which the current density decreases and begins increasing again at the potential of − 1.3 V. For the doped film, this increase of the cathodic current values occurs at the potential of 0 V and reaches a maximum value of anodic current at the potential of 0.15 V. There is an anodic peak with current density equal to 0.24 mA cm^{-2}. The difference between both voltammograms consists in their area, peaks and the current density values. The increase of the voltammogram area of the doped film relative to the undoped film means that the chemical structure of the film offers an easier way for the ion charge transfer process [20]. Both, the cathodic and the anodic, peaks are related to the reduction and oxidation of the compounds, respectively. In this specific case, the cathodic peaks suggest the reduction from Ce^{4+} to Ce^{3+} as well as the reduction of V^{5+} to V^{4+}. On the other hand, the anodic peaks represent the opposite phenomenon, i.e., the oxidation of Ce^{3+} to Ce^{4+} and V^{4+} to V^{5+} [27].

In order to study Li^+ diffusivity in films of CeO_2 (Fig. 4a) and CeO_2–V_2O_5 (Fig. 4b), the samples were subjected to cyclic voltammetry measurements at different scan rates of 2, 5, 10, 20, 30, 40, 50, and 100 mV s^{-1}. In Fig. 4a, b the anodic peaks and cathodic current maxima (at − 1.3 V) and their separation increase with increasing scan rate. Randles–Sevcik equation (Eq. 1), which describes the relationship between the peak current (i_p) and square root of the scan rate ($v^{1/2}$) [28], is then applied to determine the chemical diffusion coefficient of the Li^+ ion in CeO_2 and CeO_2:V_2O_5 films.

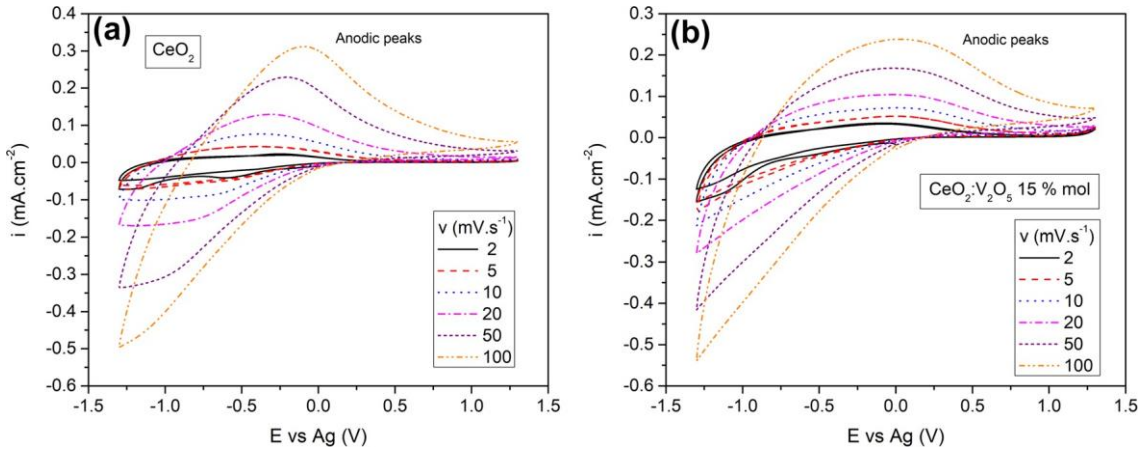

Fig. 4 Second cycle of the cyclic voltammetries for CeO_2 and CeO_2:V_2O_5 with 15 mol% films at different scan rates

$$i_p = 2.72 \times 10^5 \times n^{3/2} \times A \times D^{1/2} \times C_0 \times v^{1/2}, \quad (1)$$

where i_p is a peak current (A cm^{-2}), n is the number of transferred electrons, A is the electrode area (cm^2), D is the diffusion coefficient (cm^2 s^{-1}), C_0 is the concentration (mol cm^{-3}), and v is the scan rate (V s^{-1}). Furthermore, i_p increases with $v^{1/2}$ and is directly proportional to concentration. This relationship becomes particularly important in the study of electrode mechanisms. The ratio of i_{pa} to i_{pc} (anodic and cathodic peak currents, respectively) should be close to one; however, chemical reactions coupled to the electrode process can significantly alter the ratio of peak currents. Moreover, in present study most of voltammograms have only an increase of the cathodic current instead of peaks, so the values of i_{pa} versus maximum of cathodic current densities, that are of about 0.8 for CeO_2 and 0.4 for CeO_2:V_2O_5 15 mol%, are not totally exact. To obtain chemical diffusion coefficient of lithium ions a plot of normalized peak current values as a function of the square root of the scan rate ($v^{1/2}$) of CeO_2 and CeO_2:V_2O_5 films is shown in Fig. 5a, b, respectively. The obtained values are of 1.73×10^{-12} and 6.75×10^{-13} cm^2 s^{-1} for CeO_2 and CeO_2:V_2O_5 15 mol%, respectively. Pinar Gokdemir et al. [2] have found $D_{Li}^{+} = 8.74 \times 10^{-20}$ cm^2 s^{-1} for CeO_2 sol–gel films annealed at 450 °C. Malini et al. [10] have found values of $D_{H}^{+} = 10^{-10}$ to 10^{-14} cm^2 s^{-1} for V–Ce mixed oxide thin films (prepared from 1:1 and 1:2 oxides power molar ratio and different RF sputtering conditions). Value of $D_{Li}^{+} = 1.66 \times 10^{-13}$ cm^2 s^{-1} was found for CeO_2–TiO_2 sol–gel film [29].

CeO_2 and CeO_2:V_2O_5 films were also analyzed by chronoamperometry (Fig. 6a) and chronocoulometry (Fig. 6b) techniques. After 60 s of applied − 1.3 V potential, CeO_2 film reaches the current density of 1.83 mA cm^{-2}. At the same conditions, CeO_2 with 15 mol % of V_2O_5 film reaches 6 mA cm^{-2} (Fig. 6a). This result allow us to affirm that the charge insertion/extraction in the doped film is faster than in undoped one, and this can be explained by the higher

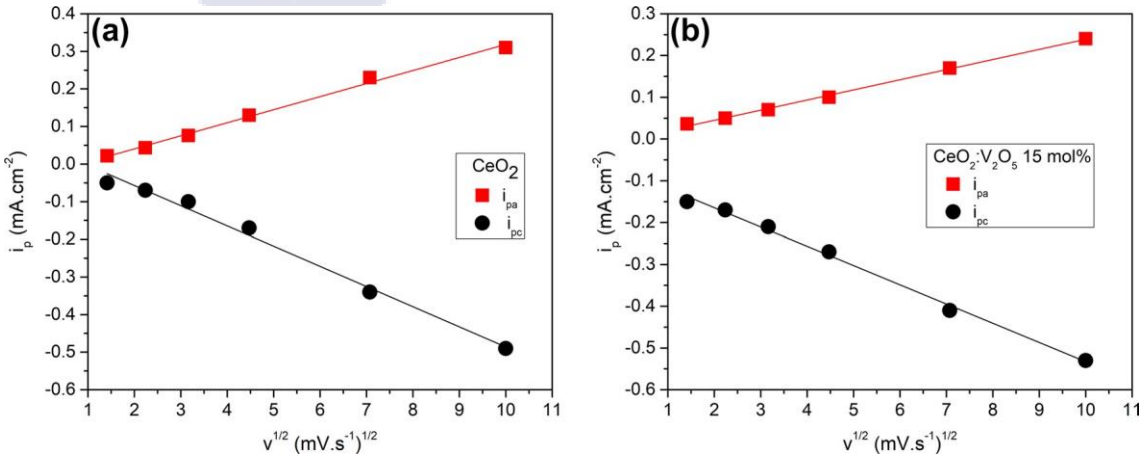

Fig. 5 **a** Chronoamperometry and **b** chronocoulometry of CeO_2 and CeO_2:V_2O_5 with 15 mol% films. Applied potentials of − 1.3 to + 1.3 V

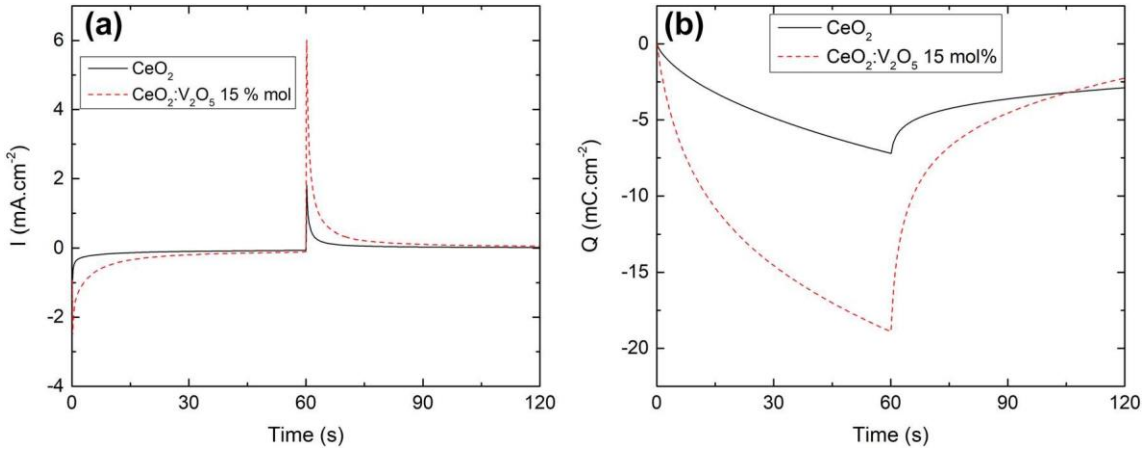

Fig. 6 Normalized peaks current versus square root of the scan rate ($v^{1/2}$) of CeO_2 and CeO_2:V_2O_5 with 15 mol% films

conductivity of the doped film, as observed in CeO_2–ZrO_2 [30]. Figure 6b shows the chronocoulometry results of both films. In the first 60 s occurs a charge insertion of 7.5 and 18.9 mC cm^{-2} for undoped and doped film, respectively. After the potential inversion to + 1.3 V, the inserted charge is now extracted. From the undoped film there is extracted 5.7 mC cm^{-2}, which represents 80% of the inserted charge. From the doped film, this extraction reaches 16.7 mC cm^{-2} and represents 88% of the inserted charge. Consequently, the doped film has better reversibility of the redox process when compared to undoped one, and the charge inserted values are almost twice of the value of 8 mC cm^{-2} (for 30 s of applied potential) obtained for CeO_2–TiO_2–ZrO_2 [24].

UV–Vis spectra were taken to study the variation of the transmittance and/or coloration of the undoped and doped films. For this comparison, the measurements occurred in three different moments. Initially, the transmittance was measured for an unpolarized film, i.e., after the deposition and before any potential application. Then, the measure was taken immediately after the polarization of the film by applying potential of − 1.3 V for 60 s, so the ions were already inserted into the film. Finally, the measure was done after depolarization of the film at + 1.3 V for 60 s, i.e., soon after all inserted ions were extracted. The spectra collected at these three moments for CeO_2 and CeO_2:V_2O_5 15 mol% films are shown in Fig. 7. The three spectra of the undoped CeO_2 film (Fig. 7a) overlap in 450–800 nm range. This means that independent on CeO_2 film polarization state its transmittance is the same in visible range [24]. Consequently, the insertion of Li^+ ions in the film is not sufficient to modify its coloration, which confirms that CeO_2 is not chromogenic material [31]. The small difference in transmittance of the film in as deposited and after application of ± 1.3 V, in 320–450 nm range, can be due to lattice accommodation under Li ions insertion. The maximum transmittance value of this film is ~90%. UV–Vis spectra of CeO_2:V_2O_5 15 mol% film (Fig. 7b) reveal that the film is less transparent than undoped one because its transmittance

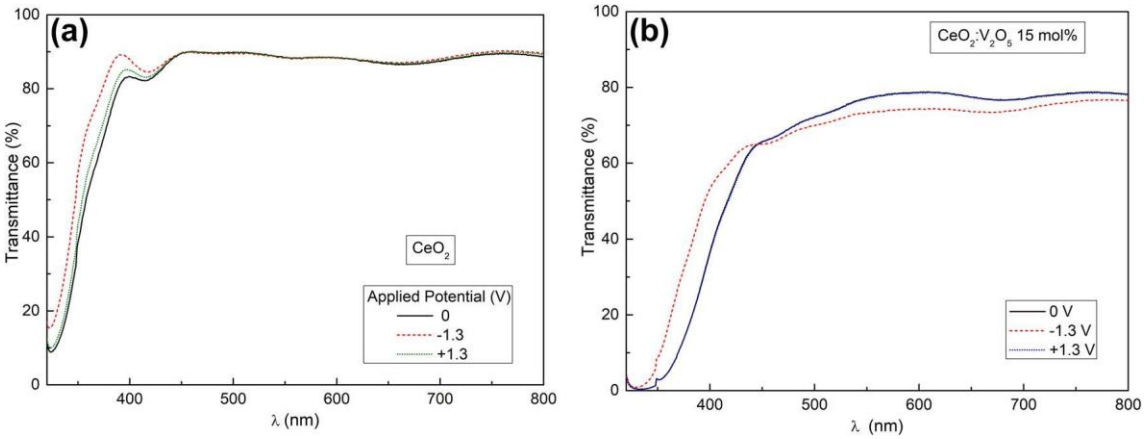

Fig. 7 UV–Vis spectra of **a** CeO_2 and **b** CeO_2:V_2O_5 with 15 mol% films in as deposited and after applied potentials of ± 1.3 V

reach ~ 79% in the visible range. Moreover, differently from Krasovec et al. [9] there is a small change between polarized and depolarized state in the visible range. When the ions are inserted into the film, after the cathodic potential application, the film becomes slightly colored, which is evidenced by 5% of transmittance decrease at 600 nm, reaching a value of 74% [6]. After the depolarization, the result of transmittance returns to the original value of 79% at 600 nm (both spectra, at 0 and + 1.3 V, are completely overlapped in 320–800 nm range). This means that this small coloration change is due to the insertion of ions, and this process is reversible because the transmittance recovers its initial value after depolarization. This characterizes the film as poor but reversible electrochromic material and indicates its use as a passive counter-electrode [32].

The morphology of the films was studied through AFM technique aiming to obtain information about the surface and roughness of the films [33]. Figure 8 shows a 3D image of three samples: the substrate FTO (Fig. 8a), the undoped film (CeO_2, Fig. 8b), and the doped film (CeO_2:V_2O_5 15 mol%, Fig. 8c). The dimensions of the images are 1 µm × 1 µm. FTO substrate presents irregularities with many pores and a uniform porosity of its structure (Fig. 8a). CeO_2 (Fig. 7b) and CeO_2:V_2O_5 (Fig. 8c) samples are more homogeneous than pure FTO, but they still have some pores in their structures. This homogeneity is related to the efficiency of the deposition technique. The root mean-squared (RMS) roughness values of the samples are of 13.8, 18.9, and 9.42 nm for FTO, CeO_2, and CeO_2 with 15 mol% V_2O_5, respectively. The highest roughness of CeO_2 film is probably due to the formation of clusters during the deposition. This did not happen when the CeO_2 with 15 mol% V_2O_5 was deposited, which resulted in lowest RMS value, when compared to the undoped film [33]. All this data suggest that CeO_2 with 15 mol% V_2O_5 film presents higher potential for application in electrochromic devices due to its high homogeneity and low roughness [34].

Aiming to confirm the data obtained by AFM a scanning electron microscopy (SEM) analysis was performed. Figure 9 presents the results of FTO, CeO_2, and CeO_2 with 15 mol% V_2O_5 samples with a magnification of ×7000. SEM picture of FTO (Fig. 9a) presents some irregularities and some few points that are due to its irregular surface. CeO_2 film (Fig. 9b) presents some highlighted points, which can be related to irregularities in the film surface. Surface of CeO_2 with 15 mol% V_2O_5 film (Fig. 9c) is free of cracks, attesting its good surface homogeneity. Again, this homogeneity confirms excellent CeO_2:V_2O_5 morphology, making it promissory for electrochemical devices application [32].

The X-ray diffraction patterns of the thin films of CeO_2 (undoped) and CeO_2 doped with 15 mol% of V_2O_5 are shown in Fig. 10. Cerium dioxide presents a fluorite structure with cubic coordination [35]. The crystallographic planes (111), (200), and (220) correspond to CeO_2 (JCPDS No. 34-0394), where the plan (111) is the preferential orientation. No peaks of vanadium or derivatives of vanadium oxides are observed in CeO_2 with 15 mol% V_2O_5 diffractogram, indicating its probable amorphous state. Table 1 lists estimated values of crystallites sizes calculated by the Debye–Scherrer equation

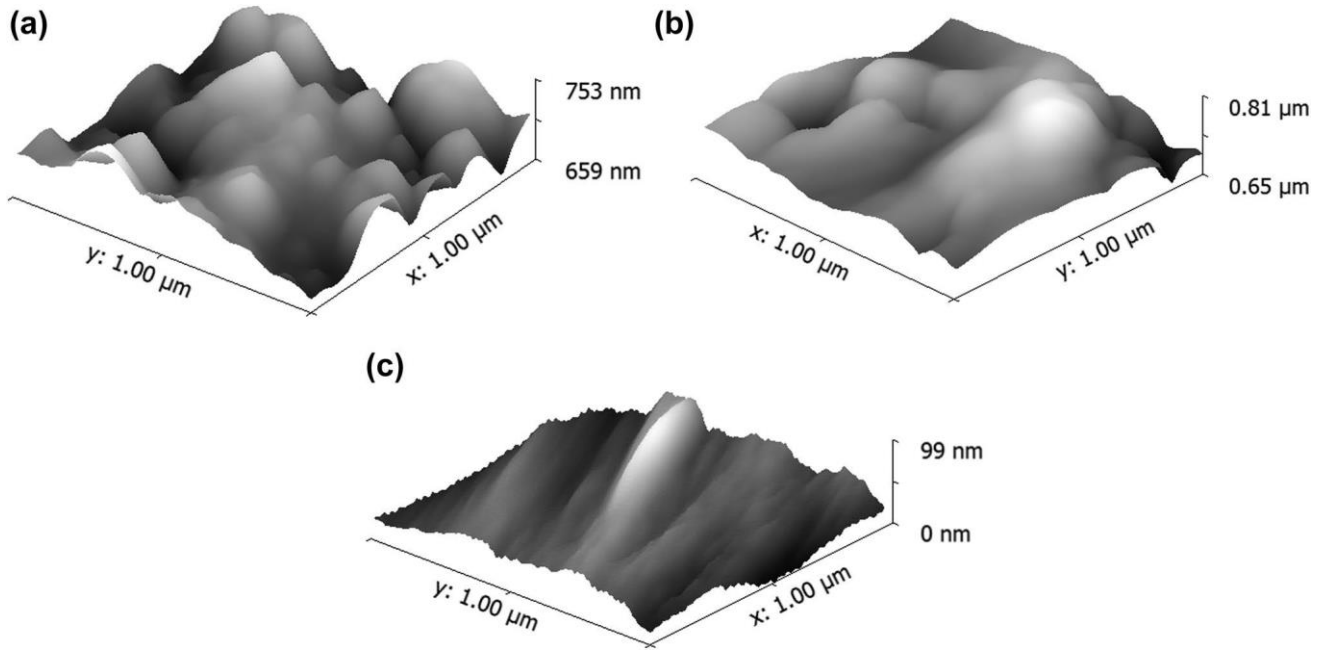

Fig. 8 AFM pictures scanned on 1 µm × 1 µm area of **a** FTO, **b** CeO_2, and **c** CeO_2:V_2O_5 with 15 mol% films

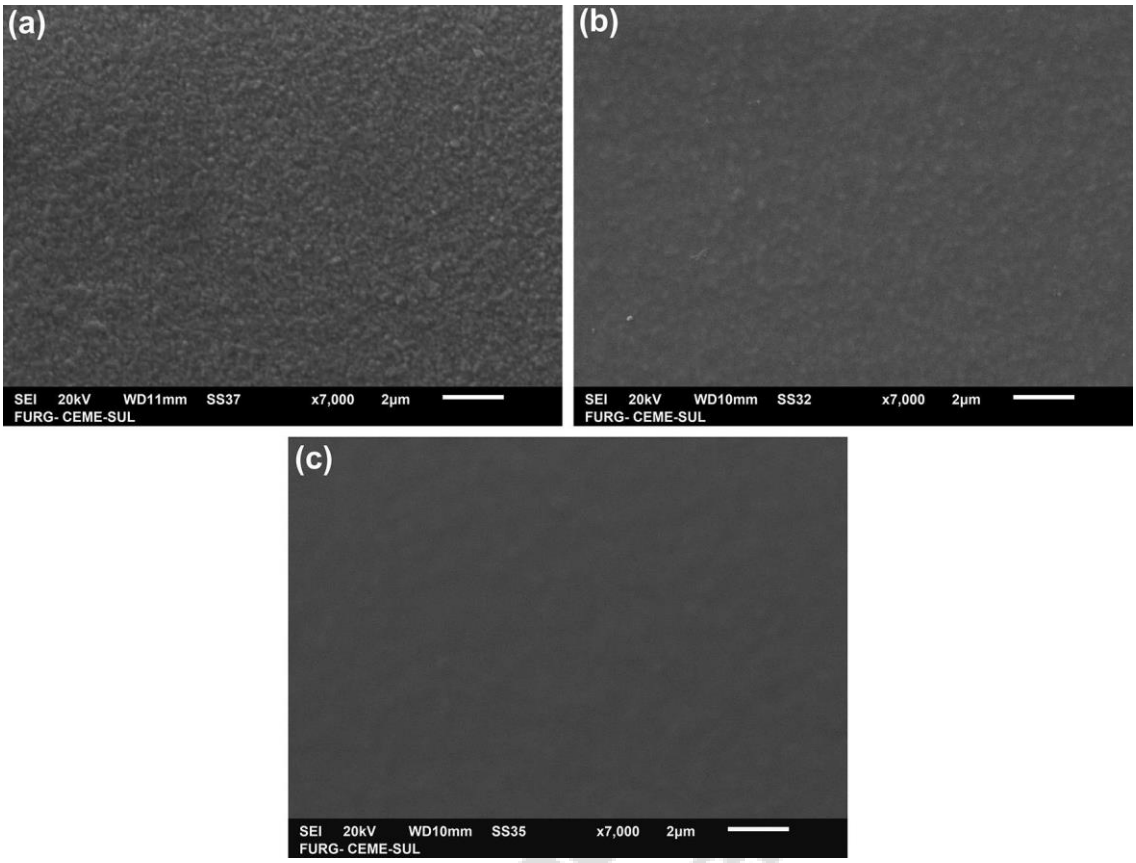

Fig. 9 SEM pictures of **a** FTO, **b** CeO_2, and **c** CeO_2:V_2O_5 with 15 mol% films

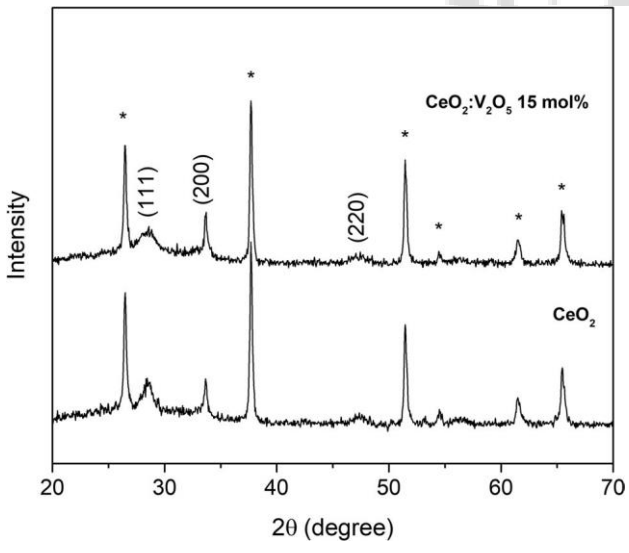

Fig. 10 X-ray patterns of CeO_2 and CeO_2:V_2O_5 15 mol% thin films treated at 450 °C for 30 min; peaks with asterisk are related to FTO

[18], which is based on the full width at half maximum (FWHM) of the diffraction peak (111) of the CeO_2 and is given in Eq. 2.

Table 1 Structural parameters of CeO_2 and CeO_2 with 15 mol% V_2O_5 thin films

Thin flim	FWHM (°)	Crystallite size (nm)	Interplanar distance (nm)	Position at 2θ (°)
CeO_2	1.04	8.11	3.07	28.57
CeO_2 with 15 mol% V_2O_5	1.97	4.09	3.16	28.40

$$D = \frac{k\lambda}{\beta \cos\theta} \tag{2}$$

where D is the crystallite size, k is a constant (0.94), λ is the radiation wavelength (1.5406 Å), β is the full width at half maximum (FWHM) at (111) peak, and θ is the Bragg angle.

V_2O_5 influence on CeO_2 structure is observed by a decrease of crystallite size from 8.11 to 4.09 nm and by the increase in the interplanar distance, caused by a small shift of (111) peak at low angles in 2θ. This may justify the higher charge density of 17.5 mC cm^{-2} of CeO_2 with 15 mol% V_2O_5 film when compared to 7 mC cm^{-2} registered for CeO_2 film (Fig. 6b). Therefore, the doping of CeO_2 with V_2O_5 shows a significant change in the structural properties,

providing an increase in the charge density and allowing the use of this material as a counter electrode in electrochromic devices. There were not found characteristic peaks of V_2O_5 atoms, which may mean that these atoms must be displaced from normal positions of the crystalline lattice to empty locations or adjacent atomic space of the CeO_2 structure likely to replace hydrogen or cerium atoms.

4 Conclusions

Thin films of CeO_2 and CeO_2 doped with different concentrations of V_2O_5 and having different numbers of deposited layers were synthesized and characterized by electrochemical, optical, microscopical, and structural analyses. A comparison between samples of CeO_2 doped with different quantities of V_2O_5 pointed that film, composed of five layers and doped with 15 mol% of V_2O_5, presented the best electrochemical responses, so this film was studied more deeply. The results of this film have always been compared to the undoped film with three deposited layers, which was the best configuration for the undoped film. The cyclic voltammetry analyses revealed that CeO_2 film reached a maximum value of anodic current of 0.08 mA cm^{-2} at about −0.25 V, while CeO_2 with 15 mol% V_2O_5 film presented a maximum value of anodic peak current of 0.24 mA cm^{-2} at about −0.15 V. 60 s of −1.3 V of applied potential resulted in a charge insertion of 7.5 and 18.9 mC cm^{-2} with reversibility of 80 and 88% for undoped and doped film, respectively. 79% of transparency in UV–Vis was registered for CeO_2 with 15 mol% V_2O_5 film, which also revealed 5% color change, decreasing its transmittance to 74% after Li^+ ions insertion into the film. AFM and SEM showed an irregular surface with a large number of pores and an uniform porosity of FTO substrate. The undoped film presented pores too, but its surface was homogeneous. The CeO_2 with 15 mol% V_2O_5 film presented an even more homogeneous surface that was totally free of cracks and irregularities. The root mean-squared (RMS) roughness values were of 13.8, 18.9, and 9.42 nm for FTO, CeO_2, and CeO_2 with 15 mol% V_2O_5 films, respectively. Finally, the doping of the CeO_2 with V_2O_5 improved both electrochemical and morphological properties of the film. In summary, CeO_2 with 15 mol% V_2O_5 film showed to be promising thin coating for the use in electrochromic devices as a passive counter-electrode.

Acknowledgements The authors are indebted to FAPERGS (Grant 12/2239-9) and Capes for the financial support given to this research.

References

1. S.-Y. Zheng, A. Andersson-Fäldt, B. Stjerna, C. Granqvist, Optical properties of sputter-deposited cerium oxyfluoride thin films. Appl. Opt. **32**(31), 6303–6309 (1993). https://doi.org/10.1364/AO.32.006303
2. F. Pinar Gokdemir, A. Evrim Saatci, O. Özdemir, B. Keskin, K. Kutlu, Structural, optical and electrochromic properties of cerium dioxide thin films prepared by sol–gel dip coating method. Mater. Sci. Semicond. Process. **38**, 300–305 (2015). https://doi.org/10.1016/j.mssp.2014.08.037
3. D.E. Shen, A.M. Österholm, J.R. Reynolds, Out of sight but not out of mind: the role of counter electrodes in polymer-based solid-state electrochromic devices. J. Mater. Chem. C **3**(37), 9715–9725 (2015). https://doi.org/10.1039/C5TC01964H
4. A. Bhosale, P. Shinde, N. Tarwal, R. Pawar, P. Kadam, P. Patil, Synthesis and characterization of highly stable optically passive CeO_2–ZrO_2 counter electrode. Electrochim. Acta **55**(6), 1900–1906 (2010). https://doi.org/10.1016/j.electacta.2009.11.005
5. E. Bêche, P. Charvin, D. Perarnau, S. Abanades, G. Flamant, Ce 3d XPS investigation of cerium oxides and mixed cerium oxide (CexTiyOz). Surf. Interface Anal. **40**(3-4), 264–267 (2008). https://doi.org/10.1002/sia.2686
6. E. Masetti, F. Varsano, F. Decker, Sputter-deposited cerium vanadium mixed oxide as counter-electrode for electrochromic devices. Electrochim. Acta **44**(18), 3117–3119 (1999). https://doi.org/10.1016/S0013-4686(99)00028-6
7. S. Bakardjieva, P. Bezdička, T. Grygar, P. Vorm, Reductive dissolution of microparticulate manganese oxides. J. Solid State Electrochem. **4**(6), 306–313 (2000). https://doi.org/10.1007/s100089900104
8. P. Baudry, A. Rodrigues, M.A. Aegerter, L. Bulhoes, Dip-coated TiO_2-CeO_2 films as transparent counter-electrode for transmissive electrochromic devices. J. Non-Cryst. Solids **121**(1–3), 319–322 (1990). https://doi.org/10.1016/0022-3093(90)90151-B
9. U.O. Krasovec, B. Orel, R. Reisfeld, Electrochromism of $CeVO_4$ and Ce/V-Oxide Ion-Storage Films Prepared by the Sol-Gel Route. Electrochem. Solid-State Lett. **1**(2), 104–106 (1998). https://doi.org/10.1149/1.1390652
10. D.R. Malini, C. Sanjeeviraja, H^+-intercalation electrochemical/electrochromic properties of V-Ce mixed oxide thin films. Int. J. Electrochem. Sci. **8**, 1349–1365 (2013).
11. S. Bishop, K. Duncan, E. Wachsman, Defect equilibria and chemical expansion in non-stoichiometric undoped and gadolinium-doped cerium oxide. Electrochim. Acta **54**(5), 1436–1443 (2009). https://doi.org/10.1016/j.electacta.2008.09.026
12. Y. Temerk, H. Ibrahim, A new sensor based on In doped CeO_2 nanoparticles modified glassy carbon paste electrode for sensitive determination of uric acid in biological fluids. Sens. Actuators B **224**, 868–877 (2016). https://doi.org/10.1016/j.snb.2015.11.029
13. H. Ibrahim, Y. Temerk, Sensitive electrochemical sensor for simultaneous determination of uric acid and xanthine in human biological fluids based on the nano-boron doped ceria modified glassy carbon paste electrode. J. Electroanal. Chem. **780**, 176–186 (2016). https://doi.org/10.1016/j.jelechem.2016.09.016
14. A. Almoabadi, S. Badilescu, V.-V. Truong, M. Alsawafta, V. Stancovski, T. Sharma, R. Brüning, Electrochromic and electrical properties of layered and tubular vanadium pentoxide thin films. In: Photonics North, 2015 (IEEE, 2015), pp. 1–8
15. E.E. Chain, Optical properties of vanadium dioxide and vanadium pentoxide thin films. Appl. Opt. **30**(19), 2782–2787 (1991)
16. C.F. Azevedo, R.D.C. Balboni, C.M. Cholant, E.A. Moura, R.M.J. Lemos, A. Pawlicka, A. Gündel, W.H. Flores, M. Pereira, C.O. Avellaneda, New thin films of NiO doped with V_2O_5 for electrochromic applications. J. Phys. Chem. Solids **110**, 30–35 (2017). https://doi.org/10.1016/j.jpcs.2017.05.021
17. Z.C. Orel, B. Orel, Ion storage properties of CeO_2 and mixed CeO_2/SnO_2 coatings. J. Mater. Sci. **30**(9), 2284–2290 (1995). https://doi.org/10.1007/bf01184574

18. T.M. Westphal, C.M. Cholant, C.F. Azevedo, E.A. Moura, D.L. da Silva, R.M.J. Lemos, A. Pawlicka, A. Gündel, W.H. Flores, C.O. Avellaneda, Influence of the Nb_2O_5 doping on the electrochemical properties of V_2O_5 thin films. J. Electroanal. Chem. **790**, 50–56 (2017). https://doi.org/10.1016/j.jelechem.2017.02.014
19. L.A.d. Carvalho, A.R.d. Andrade, P.R. Bueno, Espectroscopia de impedância eletroquímica aplicada ao estudo das reações heterogêneas em ânodos dimensionalmente estáveis. Quím. Nova **29**(4), 796–804 (2006). https://doi.org/10.1590/S0100-40422006000400029
20. C. Patil, N. Tarwal, P. Jadhav, P. Shinde, H. Deshmukh, M. Karanjkar, A. Moholkar, M. Gang, J. Kim, P. Patil, Electrochromic performance of the mixed V_2O_5–WO_3 thin films synthesized by pulsed spray pyrolysis technique. Curr. Appl. Phys. **14**(3), 389–395 (2014). https://doi.org/10.1016/j.cap.2013.12.014
21. X. Xie, C. Gao, X. Du, G. Zhu, W. Xie, P. Liu, Z. Tang, Improved optical and electrochromic properties of niox films by low-temperature spin-coating method based on NiOx nanoparticles. Materials **11**(5), 760 (2018)
22. C. Cholant, T. Westphal, R. Balboni, E. Moura, A. Gündel, W. Flores, A. Pawlicka, C. Avellaneda, Thin films of V_2O_5/MoO_3 and their applications in electrochromism. J. Solid State Electrochem. **21**(5), 1509–1515 (2017). https://doi.org/10.1007/s10008-016-3491-1
23. C.O. Avellaneda, A. Pawlicka, Preparation of transparent CeO_2-TiO_2 coatings for electrochromic devices. Thin Solid Films **335**(1–2), 245–248 (1998). https://doi.org/10.1016/S0040-6090(98)00965-1
24. C.O. Avellaneda, L.O.S. Bulhoes, A. Pawlicka, The CeO_2-TiO_2-ZrO_2 sol-gel film: a counter-electrode for electrochromic devices. Thin Solid Films **471**(1–2), 100–104 (2005). https://doi.org/10.1016/j.tsf.2004.04.039
25. E. Da Costa, C.O. Avellaneda, A. Pawlicka: Alternative Nb_2O_5-TiO_2 thin films for electrochromic devices. J. Mater. Sci. 36(6), 1407–1410 (2001). https://doi.org/10.1023/A:1017576125092
26. G.F. Azevedo, R.M.J. Lemos, J. Andrade, K.R.L. Castagno, A. Gundel, C.M. Cholant, C.F. Azevedo, A. Pawlicka, C.O. Avellaneda, Influence of Li^+: V_2O_5 doping on Nb_2O_5 thin films electrochemical performance. Mol. Cryst. Liq. Cryst. **655**(1), 71–78 (2017). https://doi.org/10.1080/15421406.2017.1361296
27. D.S. Dalavi, R.S. Devan, R.S. Patil, Y.-R. Ma, P.S. Patil, Electrochromic performance of sol–gel deposited NiO thin film. Mater. Lett. **90**, 60–63 (2013). https://doi.org/10.1016/j.matlet.2012.08.108
28. P. Scherrer: Bestimmung der Größe und der inneren Struktur von Kolloidteilchen mittels Röntgenstrahlen, vol. 1918. Nachrichten von der Gesellschaft der Wissenschaften zu Göttingen, Mathematisch-Physikalische Klasse (1918). Weidmannsche Buchhandlung, Berlin (1918)
29. C.O. Avellaneda, A. Pawlicka, Lithium intercalation in CeO_2-TiO_2 thin film. Mol. Cryst. Liq. Cryst. **415**, 221–227 (2004). https://doi.org/10.1080/15421400490482060
30. J.-H. Lee, S. Yoon, B.-K. Kim, H.-W. Lee, H. Song, Electrical conductivity and defect structure of CeO_2-ZrO_2 mixed oxide. J. Mater. Sci. **37**(6), 1165–1171 (2002). https://doi.org/10.1023/A:1014363304942
31. M.A. Aegerter, Sol-gel chromogenic materials and devices, in *Optical and Electronic Phenomena in Sol-Gel Glasses and Modern Application*, ed. by C.K. Jorgensen, R. Reisfeld (Springer, Berlin, 1996), pp. 149–194
32. C.O. Avellaneda, M.A. Berton, L.O. Bulhoes, Optical and electrochemical properties of CeO_2 thin film prepared by an alkoxide route. Sol. Energy Mater. Sol. Cells **92**(2), 240–244 (2008). https://doi.org/10.1016/j.solmat.2007.03.035
33. D. Johnson, S. Al Malek, B. Al-Rashdi, N. Hilal, Atomic force microscopy of nanofiltration membranes: effect of imaging mode and environment. J. Membr. Sci. **389**, 486–498 (2012). https://doi.org/10.1016/j.memsci.2011.11.023
34. J. Andrade, I. Cesarino, R. Zhang, J. Kanicki, A. Pawlicka, Properties of electrodeposited WO_3 thin films. Mol. Cryst. Liq. Cryst. A **604**, 71–83 (2014). https://doi.org/10.1080/15421406.2014.968030
35. S. Domingues, T. Pereira, A. Florentino, A. Cavalheiro, M. Saeki, Caracterização estrutural da cerâmica $Ti_x(Sm_{0,2}Ce_{0,8})_{1-x}O_{2-delta}$ pelo método de Rietveld. Cerâmica **53**, 205–211 (2007). https://doi.org/10.1590/S0366-69132007000200016

4.2 Artigo 2

O artigo intitulado “**Influence of Weathering and Temperature On the Electrochemical and Microscopical Characteristics of CeO2 and CeO2:V2O5 Sol-Gel Thin Films**” é apresentado conforme publicado na Revista Materials Research Bulletin, ISSN: 0025-5408, classificação A2 na área de Materiais.

Materials Research Bulletin 142 (2021) 111432

Contents lists available at ScienceDirect

Materials Research Bulletin

journal homepage: www.elsevier.com/locate/matresbu

Influence of weathering and temperature on the electrochemical and micr

Raphael D.C. Balboni [a], Camila M. Cholant [a], Luana U. Krüger [a], Elton A. Moura [b],Guilherme K. Maron [a], Wladimir H. Flores [c], André Gündel [c], Darci A. Gatto [a], Agnieszka Pawlicka [d], Cesar A.O. Avellaneda [a], Robson Andreazza [a,*]

[a] Centro de Desenvolvimento Tecnológico, Universidade Federal de Pelotas, Rua Gomes Carneiro, 1, Centro, Pelotas, RS 96010-610, Brazil
[b] Setor de Ciências Exatas, Universidade Federal do Paraná, R. Cel. Francisco Heráclito dos Santos, 100, Jardim das Américas, Curitiba, PR 81531-980, Brazil
[c] Campus Bagé, Universidade Federal de Pampa, Rua Maria A.G. de Godoy n° 1650, Bagé, RS 96413-170, Brazil
[d] IQSC-USP, Av. Trabalhador Sãocarlense 400, São Carlos, SP 13566-590, Brazil

ARTICLE INFO

Keywords:
Thin films
Oxides
Sol-gel chemistry
Impedance spectroscopy
Electrochemical properties

ABSTRACT

Thin films of cerium dioxide (CeO_2) and cerium dioxide doped with vanadium pentoxide (CeO_2:V_2O_5) were prepared through sol-gel route and spin coating deposition, for use as smart materials. This work evaluated films that underwent a weathering process in an accelerated weathering test chamber and the changes in their properties. The influence of the temperature was also studied electrochemically. Regarding the weathering process, there were variations in the charge insertion capacity during the investigated period. However, at the end of the 900 simulated days, the CeO_2:V_2O_5 presented interesting values. For the EIS analyses, the curve (Nyquist plot) remained about 45° inclination, suggesting a diffusional process. The morphological and structural analyses demonstrated that by doping the film, occurs a reduction on the degradation, although the structure showed no changes. For different temperatures, the film becomes more resistive as the temperature increases. The chronocoulometry showed that the charge insertion capacity increases with temperature.

1. Introduction

Different technologies have been created in order to obtain a better control on the temperature and lighting for residential and commercial buildings, aiming to reduce electricity costs related to the use of air conditioners and/or artificial lighting. Among these technologies, smart windows are devices that emerge as excellent alternatives, mainly due to the characteristic of changing coloration as desired, consequently reducing the transmission of light and radiation due to redox reactions of the chemical species involved. [1] These devices are based on a property called electrochromism, which is characterized by the reversible change of color in response to an applied external potential. This device consists of 3 main parts: a working electrode, a counter electrode and an electrolyte. [2] The counter electrode is a layer that has the function of storing ions, operating as an ion reservoir. After the charge shift process on the working electrode layer (electrochromic film) that happens due to oxidation/reduction reactions and lead to the device coloration/decoloration, the counter electrode causes a charge compensation in order to maintain the electrical balance. [3] Some specific properties are desired for the counter electrode layer, such as ion storage capacity, transparency in the intercalation process and electrochemical stability. A promising electrochemically active material that can provide good stability as well as good transparency in the visible region is cerium dioxide (CeO_2). [4] Additionally, the CeO_2 structure favors the passage of ions because it has large pores with absence of cracks. [5] On the other hand, its limited ion storage capacity leads to the need of using another material as dopant to improve the reaction rate. Thus, a material that could complement these properties was sought, and vanadium pentoxide (V_2O_5) was used, since it has excellent electrochemical properties in cathodic and anodic state. This material has a great capacity of storing lithium ions (Li^+), because of its orthorhombic layered structure, besides the fact that it presents both types of coloration, cathodic and anodic. The disadvantage of using vanadium pentoxide (V_2O_5) is the unwanted coloring that may occur during the lithium intercalation. [6] For this type of device, besides good electrochemical and electrochromic properties, such as transparency, ion

* Corresponding author.
E-mail address: robsonandreazza@yahoo.com.br (R. Andreazza).

https://doi.org/10.1016/j.materresbull.2021.111432
Received 5 April 2021; Received in revised form 22 May 2021; Accepted 3 June 2021
Available online 7 June 2021
0025-5408/

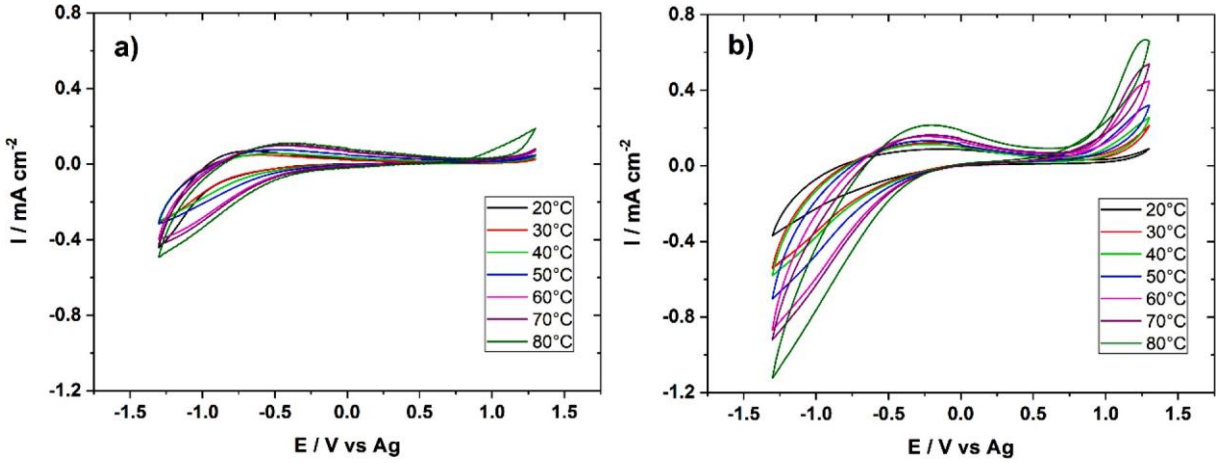

Fig. 1. Voltammogram of the thin films as a function of temperature: **a)** CeO_2; **b)** CeO_2:V_2O_5.

storage, conductivity and stability, it is also important to present good durability, a property that is related to the ability of a material to be used without losing its serviceability over a period of time, i.e., keeping its capability to perform its function. [7] Electrochromic windows are subject to climatic factors such as sunlight, wind and moisture, all factors that can affect its durability. Therefore, for materials that need to have durability and be long lasting, specific tests must be performed. In this sense, acceleration tests are very important, although they are not consolidated and have variables related to the type of function to be performed and the conditions related to this function. [8] The aim on this type of study is to compare results before and after some specific condition. Thus, the present study aims to evaluate the effects on the properties of thin films of CeO_2 and CeO_2:V_2O_5 under two different conditions, temperature variation and weathering exposure. Both films were prepared by the sol-gel technique and the long term electrochemical and morphological behavior of the films were studied using an accelerated weathering method. The materials were first analyzed and then exposed to a test chamber that simulates natural conditions such as UV radiation, rain and humidity for a specific period of time in an accelerated way. New analyses were performed at some periods of time, after 15 days of exposure in the chamber (time corresponding to 6 months of natural exposure) until the total period, equivalent to 2.5 years. Another condition used to evaluate the durability of the films was the temperature, by performing electrochemical analyses in the range of 20 to 80 °C, with 10 °C steps.

1. Experimental

1.1. Preparation of the thin films

The sol of cerium oxide was prepared by stirring cerium chloride heptahydrate ($CeCl_3 . 7H_2O$; Sigma-Aldrich), citric acid ($C_6H_8O_7$; Synth) and ethyl alcohol for 30 min, obtaining a 0.15 mol.L^{-1} solution. Then, 15% mol of vanadium isopropoxide ($OV(OCH(CH_3)_2)_3$; Sigma-Aldrich) was added and stirred for further 10 min to obtain cerium-vanadium-based sol. The deposition of the sols to obtain the thin films was done by the spin-coating technique (Chemat Technology Spin-Coater KW-4A) in a fluorine tin oxide (FTO) conductive glass substrate (Pilkington) under the following conditions: 500 rpm (3 s) and 2000 rpm (30 s). Finally, the film was subjected to a heat treatment in an oven at 450 °C during 30 min for each deposited layer, with the objective of adhering the film layer to the substrate and eliminating any impurities therein. The optimized number of layers for each film in terms of electrochemical properties is 3 for the undoped film and 5 for the doped film, according to a previous study that presented thickness values of 92 and 300 nm respectively. [9]

1.2. Weathering process

For the weathering experiments, a Climate Aging Chamber UV Accelerated Weathering Tester (Wuxi DHS Testing Equipment Technology Co., Ltd.) was used to simulate the exposure of the materials to the environment. The weathering effects were examined by exposing the samples to weathering conditions, such as: sunlight ultraviolet radiation (provided by fluorescent lamps); moisture, like rain and dew (provided by forced condensation); and temperature variations (controlled by heaters), in cycles where the incidence is equivalent to the exposure in external environments, and proportional to the time course in the chamber. The study was based on the standard provided by the ASTM (American Society for Testing and Materials), designation G 154–06, Standard Practice for Operating Fluorescent Ultraviolet (UV) Lamp Apparatus for Exposure of Nonmetallic Materials, and the chosen cycle according to this standard was the Cycle 6, which is indicated for coatings. This cycle uses an UVA-340 lamp with a typical irradiance of 1.55 W m^{-2} nm^{-1} at approximate wavelength of 340 nm. Each sample was subjected to 8 h of UV exposure at 60 °C followed by a 4 h of condensation at 50 °C. In this cycle, each day of exposure in the chamber is equivalent to 12 days of exposure to external conditions. Therefore, the materials remained in the chamber for 15 days to simulate 180 days (6 months) of exposure. At the end of each cycle, the samples were removed from the chamber and the electrochemical analyses were repeated, in order to have a detailed monitoring regarding the effects of exposure on the material properties. In this way, the initial analyses (pre-weathering), were determined as day 0, and the further analyses were performed in the simulated days equivalent to 180, 360, 720 and 900 days of exposure.

For the electrochemical measurements as a function of the temperature, the electrochemical cell was maintained in a heated water bath and a thermocouple was connected to the stainless-steel electrode, in order to allow the direct control of the electrode's temperature.

1.3. Characterization of the films

The thin films were electrochemically, structurally and morphologically characterized. The electrochemical measurements were carried out in a three-electrode electrochemical cell. The film of CeO_2:V_2O_5 was used as a working electrode, a platinum foil of 1 cm^2 as a counter electrode, and a silver wire as a reference electrode. As electrolyte, a solution of propylene carbonate (PC; Sigma-Aldrich) with 0.1 M lithium perchlorate ($LiClO_4$; Vetec) was used. Under these conditions, cyclic voltammetry and chronocoulometry tests were performed on a potentiostat/galvanostat Autolab PGSTAT 302 N, and the electrochemical impedance spectroscopy on a potentiostat/galvanostat IVIUM

Table 1
Values of the potential peaks and anodic currents for the respective temperatures of the thin films of CeO_2 and CeO_2:V_2O_5.

Temperature Thin film		20 °C	30 °C	40 °C	50 °C	60 °C	70 °C	80 °C
CeO_2	I_a (mA/cm^{2})	0.068	0.047	0.056	0.075	0.098	0.101	0.111
	E (V vs Ag)	—0.697	—0.647	—0.535	—0.508	—0.448	—0.434	—0.404
CeO_2:V_2O_5	I_a (mA/cm^{2})	0.088	0.123	0.114	0.132	0.155	0.164	0.213
	E (V vs Ag)	—0.216	—0.196	—0.193	—0.208	—0.213	—0.211	—0.212

I_a: anodic current; E: potential.

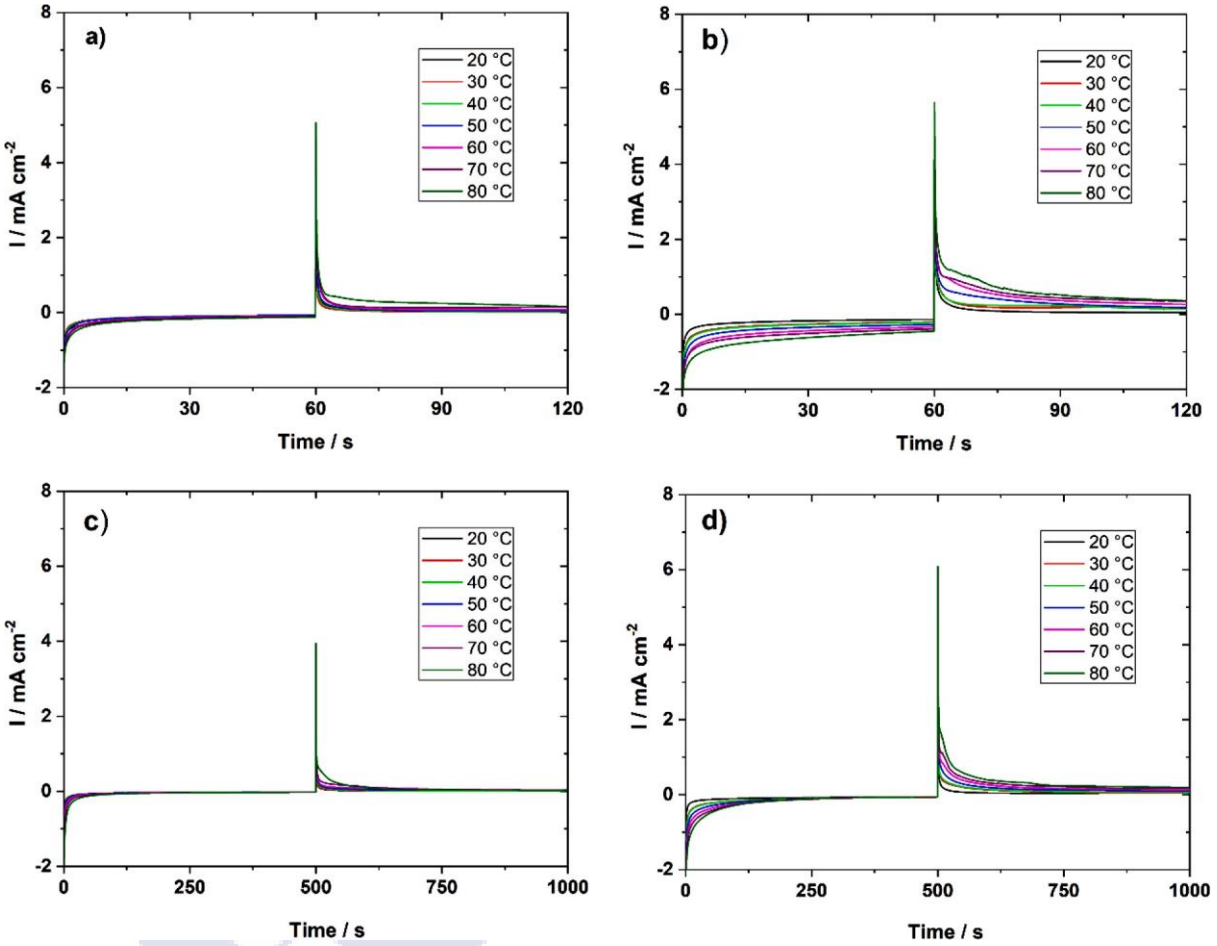

Fig. 2. Chronoamperometry curves of the thin films as a function of temperature: **a)** CeO_2 with 60 s insertion/extraction; **b)** CeO_2:V_2O_5 with 60 s insertion/extraction; **c)** CeO_2 with 500 s insertion/extraction; **d)** CeO_2:V_2O_5 with 500 s insertion/extraction.

CompactStat.h. The morphological characteristics of the materials were examined by an atomic force microscopy (AFM; Agilent Technologies 5500) and a scanning electron microscopy (SEM; JOEL JSM-6610LV before weathering and TESCAN VEGA3 after weathering). The structure of the thin films was studied by X-ray diffraction using a Rigaku Ultima IV diffractometer with Bragg-Brentano geometry at room temperature operating under the following operating conditions: 40 kV and 20 mA, CuKa radiation (λ =1,5419 Å), range of 2q from 20 º to 85 º, steps of 0.05 º and 2 s of time of integration.

1. Results and discussion

For the electrochemical analyses, a cathodic and anodic potential of —1.3 and +1.3 V was used with a scan rate of 50 mV s^{-1}. The potential application time was 60 and 500 s, to understand the charge deposition capacity of the material in the short and long term. For the electrochemical impedance spectroscopy, a signal with 10 mV of amplitude was used in a frequency range from 10^{-1} to 10^{6} Hz.

1.1. Influence of the temperature

Fig. 1 shows the cyclic voltammetry of the CeO_2 and CeO_2:V_2O_5 thin films as a function of the temperature, varying from 20 to 80 °C. Through the voltammograms, it is possible to analyze the processes of oxidation and reduction of the films, as well as electrochemical behaviors. [10]

For both films, it is possible to observe the presence of a well-defined anodic peak, associated with the extraction process of Li^+ ions, due to the oxidation reaction of the involved species. [9,11] It is also possible to observe that the presence of the dopant promoted an increase of the current density (Fig. 1b), as well as in the area of the voltammetry curve, suggesting that the doped film has a greater ion storage capacity. Regarding the influence of the temperature in the results, there is a relationship between the increase in temperature and an increase in the

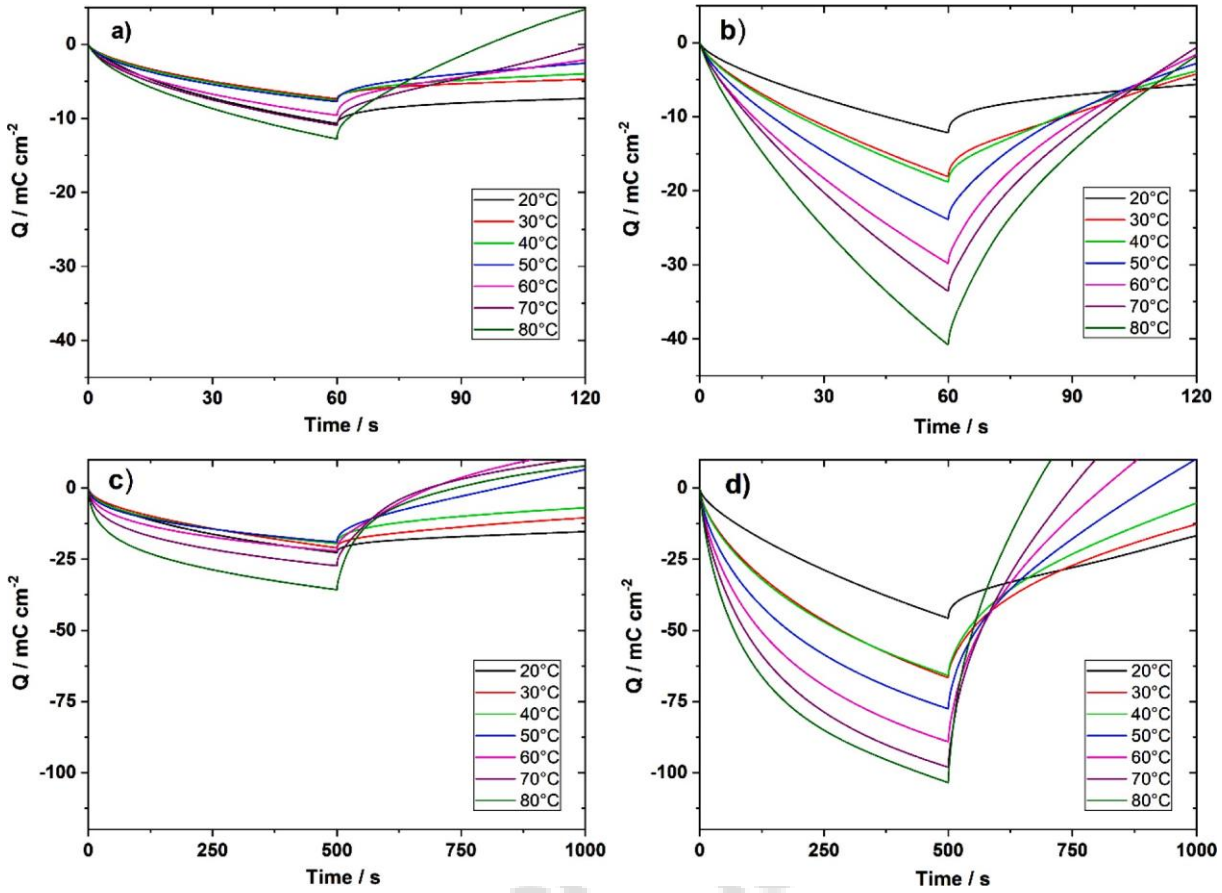

Fig. 3. Chronocoulometry curves of the thin films as a function of temperature: **a)** CeO_2 with 60 s insertion/extraction; **b)** CeO_2:V_2O_5 with 60 s insertion/extraction; **c)** CeO_2 with 500 s insertion/extraction; **d)** CeO_2:V_2O_5 with 500 s insertion/extraction.

current density, besides a displacement of the anodic peaks to more positive potential values, as Table 1 shows. This behavior can be explained by the presence of the dopant, which has the characteristic of enhancing this property, and by the thickness of the film that increases with the number of layers. [12]

Through the chronoamperometry technique using the predetermined parameters, it was possible to analyze the response time of the insertion/extraction processes of Li^+ ions in thin films of CeO_2 and CeO_2:V_2O_5 as a function of the temperature. As the application time increases, the current response over time becomes slower (as shown in Fig. 2). When heating the system, it is possible to note that the response time became slower, especially for the doped film, which can be explained by the concentration and structure of the film that has a greater number of layers in its structure compared to the undoped film. [6]

The chronocoulometry curves were obtained through the integration of the chronoamperometry curves and present the amount of charge inserted/extracted in the films (Fig. 3). The results evidenced a relationship between the ability of insertion/extraction and the increase in temperature, since the property was improved for both materials, especially for the doped film. It is important to highlight that during the process of insertion of Li^+ ions, it was observed that the CeO_2:V_2O_5 film acquired a bluish coloration, and during the process of extraction of Li^+ ions, the film returned to its original coloration, while no noticeable color change was observed for the CeO_2 film during the processes. This color change is reported in the literature and represents a variation in the transmittance equivalent to 4% at a wavelength of 633 nm[9] and occurs due to the existence of chromogens molecules that modify their optical properties in response to an electrical stimulus. [13]

Fig. 4 presents the results of charge density of the films, extracted from the chronocoulometry analyses. As expected, the addition of V_2O_5 into the CeO_2 matrix increases the charge density for both application times, similar to the influence caused by the increase in the temperature. Thus, from 50 °C, for both application times, an electrochemical reversibility behavior was observed, with all the inserted charge being extracted. [12] The increase in the charge density for the CeO_2:V_2O_5 thin films can be justified by the influence of V_2O_5 in the CeO_2 structure, which causes a decrease in the crystallite size and an increase in the interplanar distance. [9,14–16] The influence of the crystallite size on the charge density can be explained by higher number of surface defects, higher active surface area, shorter paths for ion diffusion and/or a greater ratio of surface area to volume. [17–19]

Based on the impedance measurements, the charge transport processes (high frequency regions, of 10^5 Hz) and mass transport processes (low frequency regions, of 10^{-1} Hz) were investigated (Fig. 5). The results revealed straight lines inclined towards the real axis, representing the behavior of the electrolyte-electrode double layer capacitance. Furthermore, the Nyquist plots showed that, as the temperature increases, the resistance decreases, resulting in an improvement in ion conductivity, which can be attributed to a greater ion movement at higher temperatures.

The ion conduction might also be facilitated by the vibrational movements of the main and side chains of CeO_2 and CeO_2:V_2O_5 films, which becomes more intense as the temperature increases. The increase of the vibration amplitude approaches the coordination sites and allows the Li^+ ions to jump from an occupied to an unoccupied site, with less energy required. [20] The difusional behavior becomes more evidenced with the increase of ionic conductivity, which is related to the decrease in diffusion resistance. The Nyquist spectra in Fig. 5 shows the decrease in resistance with the increase in temperature, having a linear Warburg

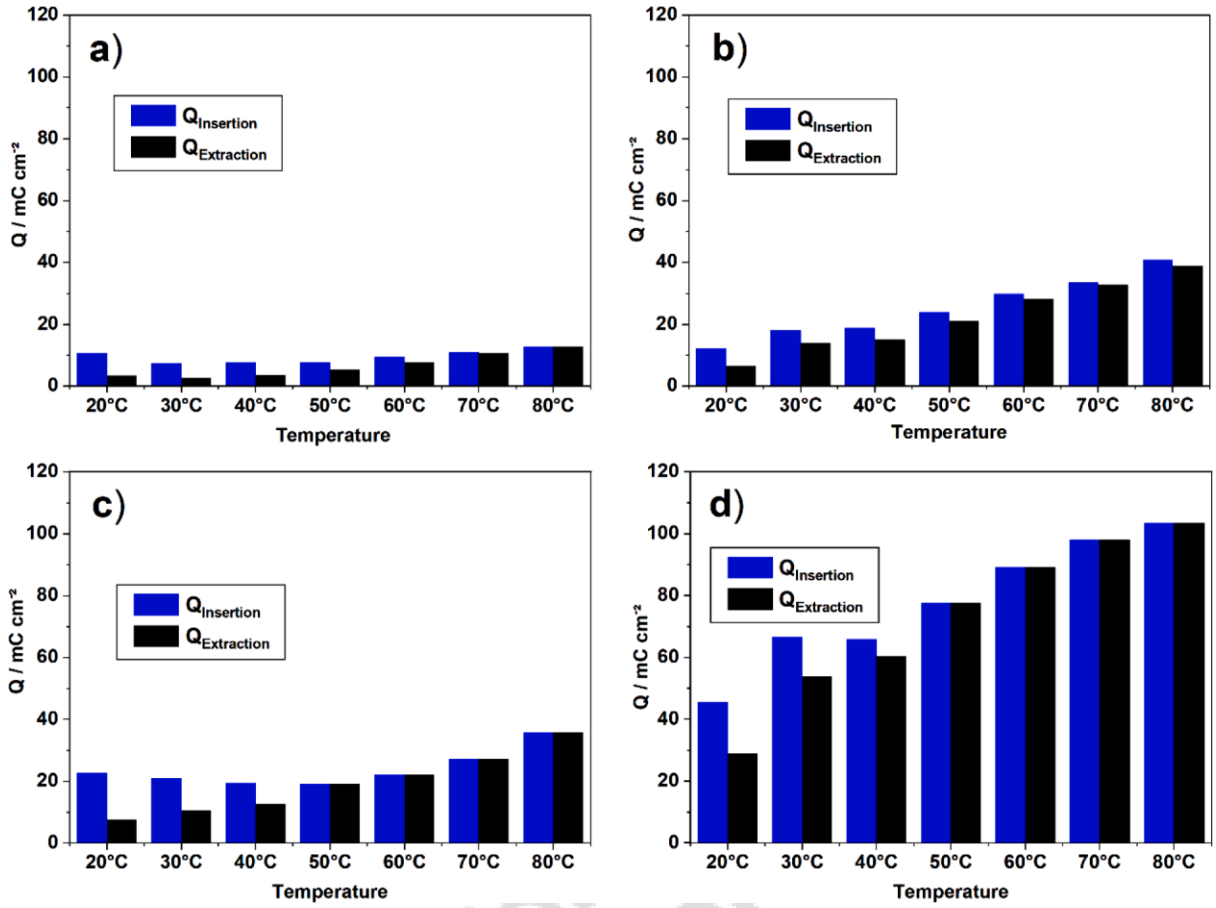

Fig. 4. Charge density of the thin films as a function of temperature: **a)** CeO_2 with 60 s insertion/extraction; **b)** CeO_2:V_2O_5 with 60 s insertion/extraction; **c)** CeO_2 with 500 s insertion/extraction; **d)** CeO_2:V_2O_5 with 500 s insertion/extraction.

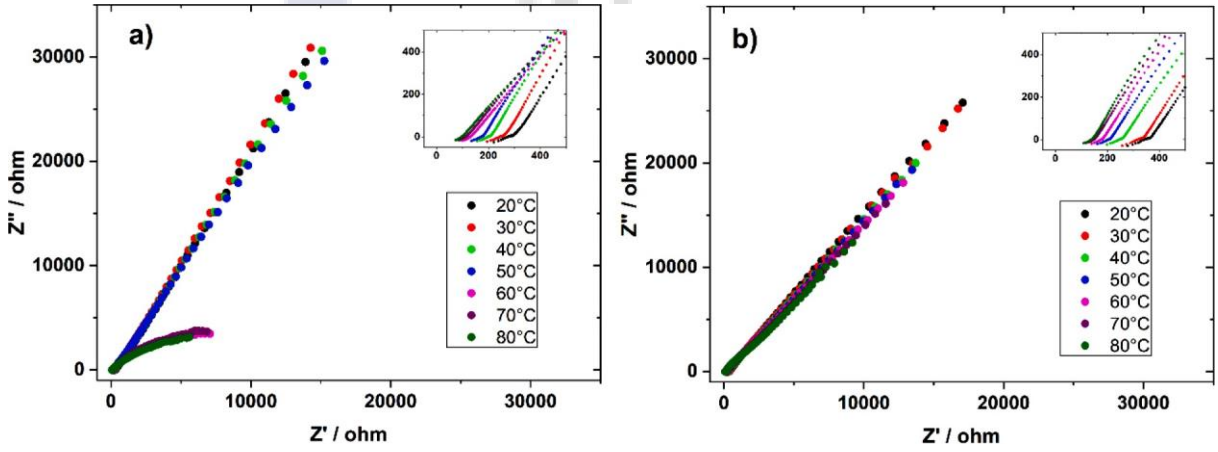

Fig. 5. Nyquist diagram of the thin films as a function of temperature: **a)** CeO_2; **b)** CeO_2:V_2O_5.

region with a more defined 45° angle, suggesting a diffusion process at low frequencies, which consists in electron transport phenomena being faster than mass transport phenomena.

The conductivity behavior profile, that is, the behavior of the electrical conductivity along the frequency, for the CeO_2 and CeO_2:V_2O_5 films through temperature variation showed two defined regions, a high-frequency region between 10^5 and 10^3 Hz, represented by a plateau, which is correlated with the domain of conductivity not dependent on frequency; and a region of low-frequency, characterized by a dispersion of Li^+ ions and an increase in the frequency-dependent conductivity, which is related to the electrode polarization phenomena (Fig. 6). Also, it is noted that the doped films showed an increase in the ionic conductivity, which tends to increase as a function of the temperature variation, due to the domain of the kinetic system of the charge/electron transportation. Thus, the CeO_2 film evidenced low results of ionic conductivity (Fig. 6a and Table S-1), which can be attributed to the low concentration of oxygen vacancies. [21]

However, the ionic conductivity increased for the doped film

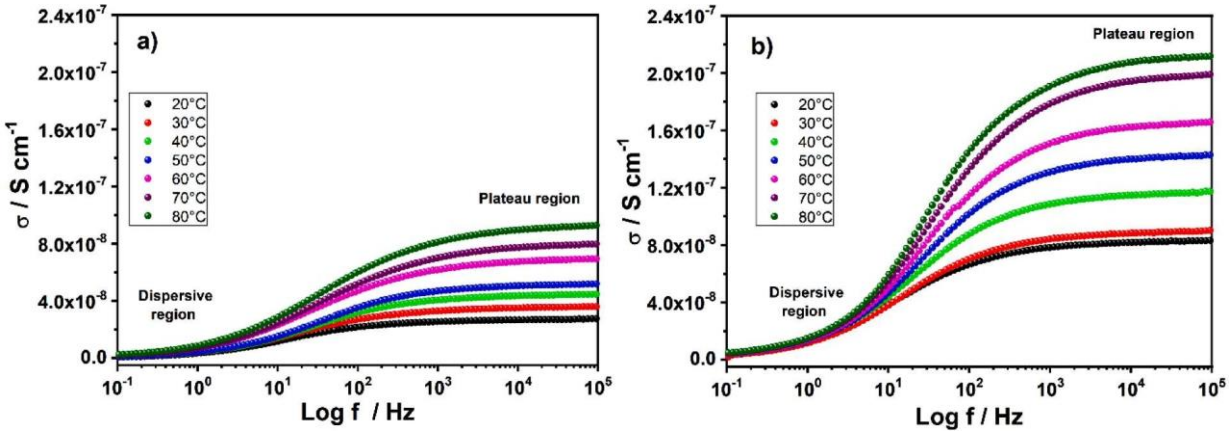

Fig. 6. Conductivity profile of the thin films as a function of temperature: **a)** CeO_2; **b)** CeO_2:V_2O_5.

(Fig. 6b), as shown in Table S-2, which can be attributed to the contribution of the V_2O_5 cations of less divalent or trivalent valence. In previous studies, where the CeO_2 is doped with a bivalent oxide, like CeO_2/ZnO, the Ce (IV) atoms of the host network are replaced by bivalent cations, and an oxygen vacancy is formed to compensate the charge created, facilitating the O^- ions diffusion and increasing the ionic conductivity. [22] By the formation of the oxygen vacancy, the reduction of two neighboring ions from Ce^{4+} to Ce^{3+} occurs, so this increase in the concentration of oxygen vacancies and in its mobility with a bivalent dopant can increase the ionic conductivity. [23] The conductivity values were obtained with Eq (1):

$$\sigma = l/R_p S \quad (1)$$

where σ is the ionic conductivity; l is the thickness of the film; R_P is the resistance, determined by the Nyquist plot in the intersection of the semicircle with the Z' (imaginary axis); and S is the superficial area of the film.

The phase angle (0) of the thin films is presented in Figure S-1, allowing the analysis of the capacitive and resistive behavior as a function of frequency. A predominantly resistive behavior in the high frequency region was noted for both films, with the phase angle tending to zero ($0 = 0°$). In the low frequency region, a predominance of the capacitive behavior was observed, as indicated by the phase angle values, which increased to 63.7° and 56.8° for CeO_2 and CeO_2:V_2O_5 films, respectively, at temperature of 20 °C. Besides that, it was observed that the increase in the temperature resulted in a decrease in phase angle, to 32.6° and 54.2° for CeO_2 and CeO_2:V_2O_5, respectively, at temperature of 80 °C, contributing to the decrease of the capacitive behavior, and consequently, increasing the ionic conductivity. The phase angle values for the thin films at different temperatures can be verified in Tables S-1 and S-2. [24]

The Bode diagram presents the impedance module |Z| versus the frequency log, where it showed a decrease in the impedance module |Z| as the temperature increased. A similar behavior was observed for the tests carried out as a function of the frequency (Figure S-2). The capacitive behavior profiles for both the CeO_2 and CeO_2:V_2O_5 thin films evidenced that the capacitive behavior tends to decrease as the temperature increases (Figure S-3). Thus, it was clearly noted that the capacitive behavior decreases with the doping of V_2O_5, contributing to an increase in ionic conductivity, which can be explained by the replacement of Ce^{4+} in the lattice structure for dopant cations, leading to an increase in the concentration of oxygen vacancies, a process that tends to occur at low doping concentrations. [22] The capacitance values were obtained through Eq (2):

$$C = 1/R_p\omega \quad (2)$$

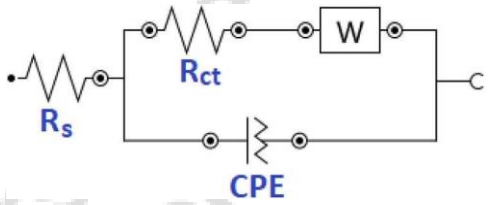

Fig. 7. Model of the proposed equivalent circuit for the thin films [R(RQW)].

where C is the capacitance, R_p is the resistance, and ω is the angular frequency.

The application of equivalent circuits fitted the impedance results obtained for the CeO_2 and CeO_2:V_2O_5 thin films; simulation in the NOVA 2.1 software was based on similarities between the behavior of the electrochemical cell and the electrical circuit composed of resistors, a constant phase element, and a Warburg diffusional element (Fig. 7).

In the circuit, the first resistor is related to the electrolyte solution (Rs), the second resistor (Rct) represents the end of the arc and is in parallel with a constant phase element (CPE) that represents the charge transfer in the film, where there is the capacitance formed by the double layer of the electrode/film. Lastly, there is the Warburg impedance element (Zw), that is the Faraday impedance and represents the mass transfer (diffusional process) in the interface electrode/film + electrolyte. A comparison between experimental and fitted Nyquist and Bode diagrams is presented in Figure S-4.3.2 Influence of weathering

3.1.1. *Electrochemical properties*

The analyses of the films that were subjected to the accelerated weathering process are shown below. In order to increase the reliability of the results, since studies with accelerated tests do not have consolidated processes, all materials were analyzed in duplicate. Fig. 8 presents the CeO_2 and CeO_2:V_2O_5 voltammograms for different simulated days.

The scale of the current axis was fixed for both voltammograms for better comparison between both films. The CV area of the doped film (Fig. 8b) is significantly greater, which was expected, since its chemical structure facilitates the ion charge transfer process. Both materials presented cathodic peaks (related to reduction) and anodic peaks (related to oxidation). For both films, the anodic peak occurs at −0.50 V. However, a significant difference between the values of current density was obtained, achieving 0.05 mA/cm^2 and 0.18 mA/cm^2 for CeO_2 and CeO_2:V_2O_5, respectively. This suggests that the doped material has a higher amount of free charge carriers flowing through the same cross section at the same applied potential, as expected according to the literature. [9]

Concerning the weathering effect, it was noted that even if there

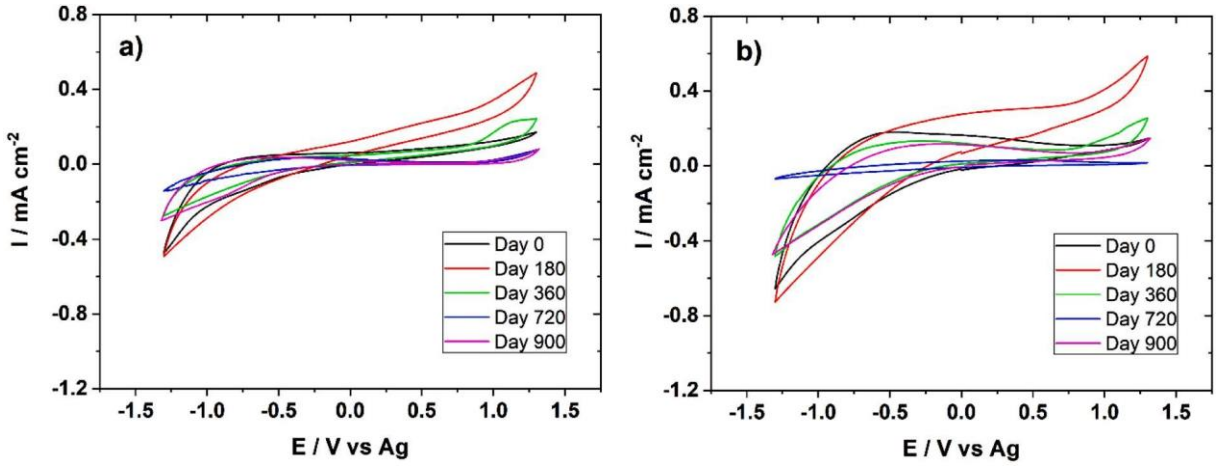

Fig. 8. Voltammogram of the films: a) CeO_2; b) CeO_2:V2O_5.

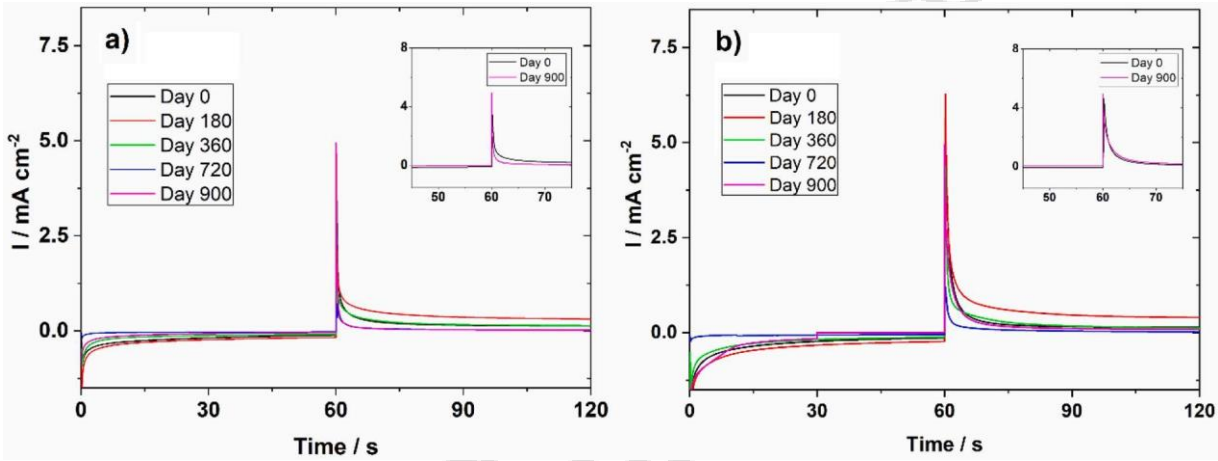

Fig. 9. Chronoamperometry of the films with 60 s: a) CeO_2; b) CeO_2:V2O_5.

were some variations during the process, especially in the 180th day, the difference between the initial and the final analyses was very small and not significant.

Fig. 9 shows the chronoamperometry for 60 s for both films. As can be seen in the insets, the CeO_2 film exhibits a variation in the results, and after the 900 days, the charge insertion/extraction occurred faster. For the film containing V_2O_5, this variation is nearly insignificant. In both cases, this process was optimized in the presence of dopant in the films due to its higher conductivity.

The chronocoulometry of the films was performed for 60 s as standard, and for 500 s to study the ability of the materials to insert/extract charges in the long-term (Fig. 10). The film containing V_2O_5 presented higher values of inserted charges for both tests, since the capacity to store ions is an important characteristic of the dopant. It was noted that after the initial analyses, the material tended to show some variation in this ability. Although the variation was not uniform, it occurred consistently in all analyses, and after 900 days of simulated weathering, it is possible to affirm that storage capacity decreases for both films, especially for the CeO_2 film, either for short- or long-term analyses.

To better understand these values of charge insertion, a charge density study was performed (Fig. 11). The behavior and the influence of the weathering through the time course was quite similar for both materials and for both potential application times.

The CeO_2:V_2O_5 film showed better results for all tested scenarios, continuously allowing more charge to be inserted when compared to the CeO_2 film. It also showed a decrease in the capacity of insertion compared to the one presented in the beginning of the process, but the results are still promising, confirming that it can be used for this purpose in the long term.

The EIS was performed for both materials, and the Nyquist plot shows the linear region of the Warburg diffusion (Fig. 12). Both films presented curves with angulation of about 45°, an expected value for this type of material and caused by the current limitation in the material due to a resistance. [25] This behavior indicates that the mass transport of the oxidized/reduced species occurs through diffusion. For the measurements over time, the values of conductivity decreased slightly, indicating an increase in the resistance of the films, which can be attributed to limited ions movements. For post weathering measurements, the angulation of the curve of the CeO_2 film got closer to 45°, while for the CeO_2:V_2O_5 film, the angulation remained close to 45° for both analyses (pre- and post-weathering). In both cases, the curve tended to be closer to 45° throughout the analysis, suggesting a diffusion process at low frequencies.

3.1.2. *Morphological and structural properties*

The surface morphology of the films before and after weathering was investigated through SEM and AFM. The SEM images of CeO_2 and CeO_2:V_2O_5 before weathering (Fig. 13a and b) exhibited compact and regular surfaces. For the CeO_2 film, some irregularities were noticed, while for the CeO_2:V_2O_5 film, a highly homogeneous surface in all extension was observed, which confirms that the film was well adhered to the FTO substrate. [26] The SEM images after weathering (Fig. 13c and d)

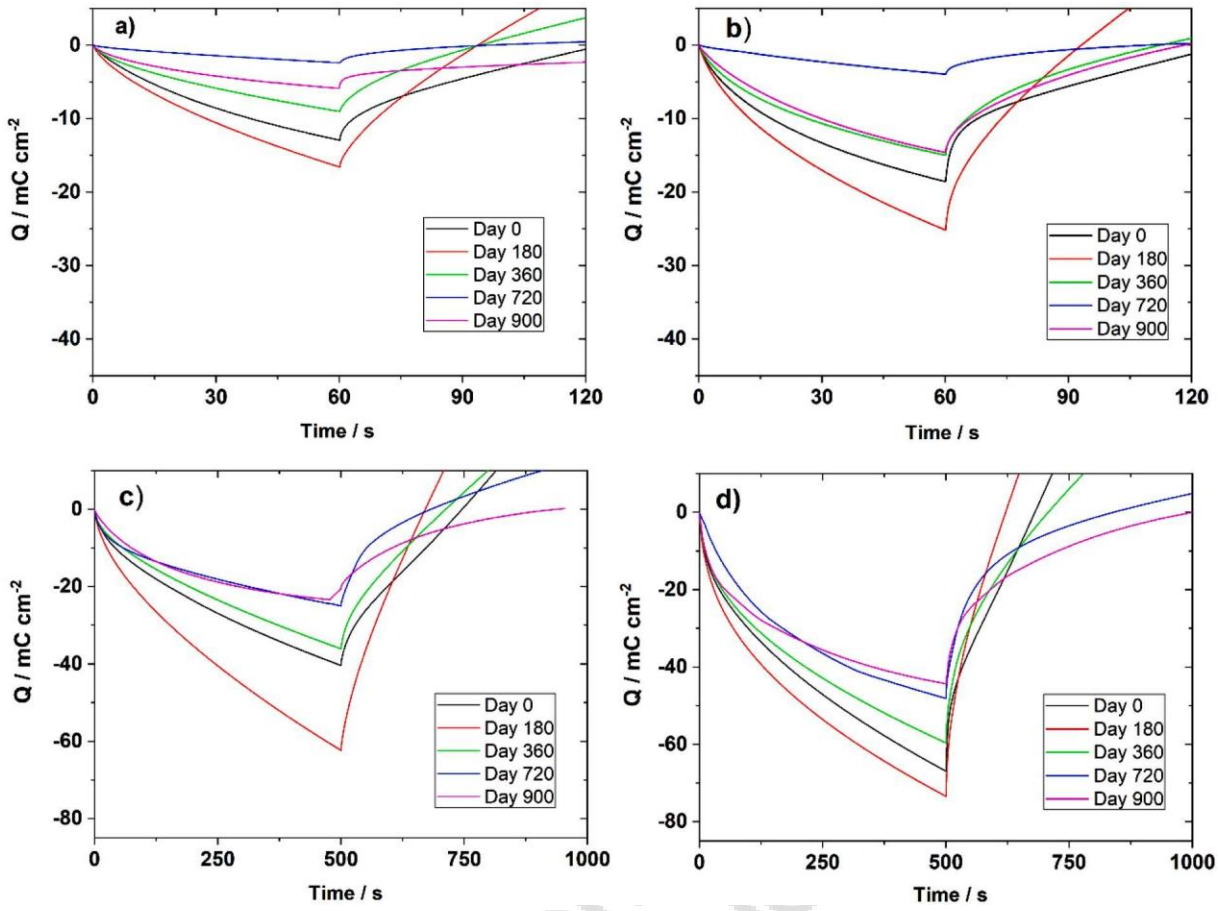

Fig. 10. Chronocoulometry of the films: **a)** CeO_2 with 60 s; **b)** CeO_2:V_2O_5 with 60 s; **c)** CeO_2 with 500 s; **d)** CeO_2:V_2O_5 with 500 s.

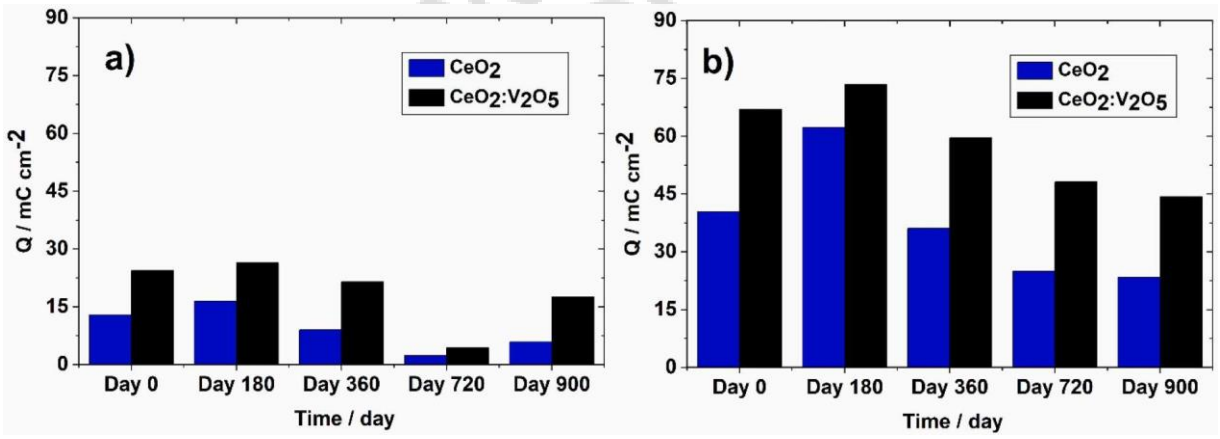

Fig. 11. Charge density of both films with potential application time of: a) 60 s; b) 500 s.

exhibited significant differences between the two samples. The CeO_2 film surface presented higher degradation, with increased porosity and the presence of cracks along the entire surface. The CeO_2:V_2O_5 sample presented a predominantly smooth surface with no significant cracks, confirming that the presence of V_2O_5 improved the resistance and reduced film degradation.

The surface topography of both the CeO_2 and CeO_2:V_2O_5 films were studied through AFM (Fig. 14). The results corroborated the SEM images, with the CeO_2 films presenting a more irregular surface, while the CeO_2:V_2O_5 revealed higher homogeneity. The root mean-squared (RMS) roughness values of the samples were 59.3 and 22.3 nm for CeO_2 and CeO_2:V_2O_5, respectively. It suggests a better deposition efficiency for the film containing V_2O_5. The weathering process resulted in the degradation of both films (Fig. 14c and d). Nevertheless, the defects were more pronounced in the CeO_2 film, whereas the CeO_2:V_2O_5 had a better response, displaying a more uniform surface, which is fundamental for films applied in electrochromic devices. [9,27]

The structure of the films was studied through X-Ray Diffraction, and the XRD patterns of CeO_2 and CeO_2:V_2O_5 films before and after weathering are shown in Fig. 15. The identification of FTO plans is also shown in the figure, which works as an internal standard to identify the position of the film peaks. In all analyses, CeO_2 films were

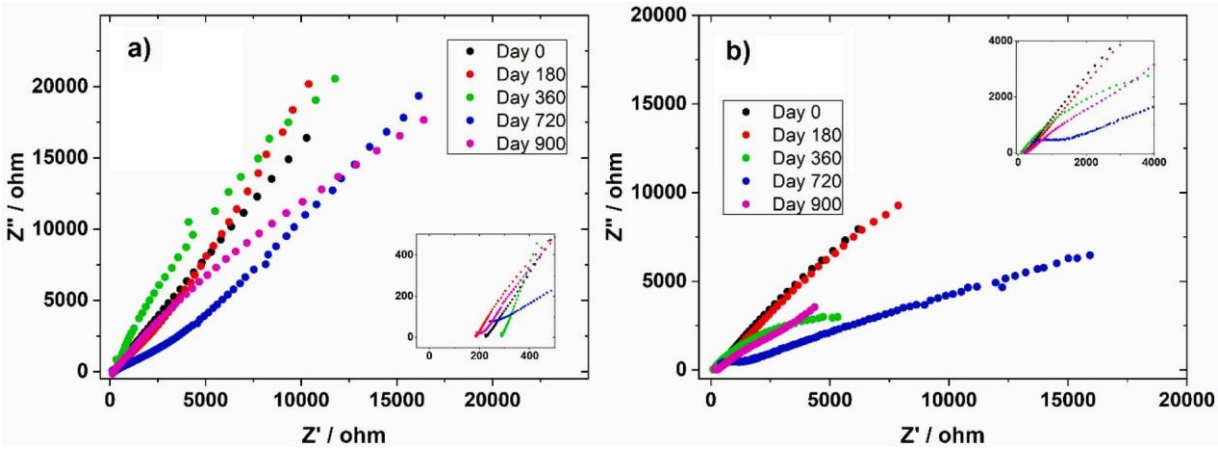

Fig. 12. Nyquist diagram of the thin films: **a)** CeO_2; **b)** CeO_2:V_2O_5.

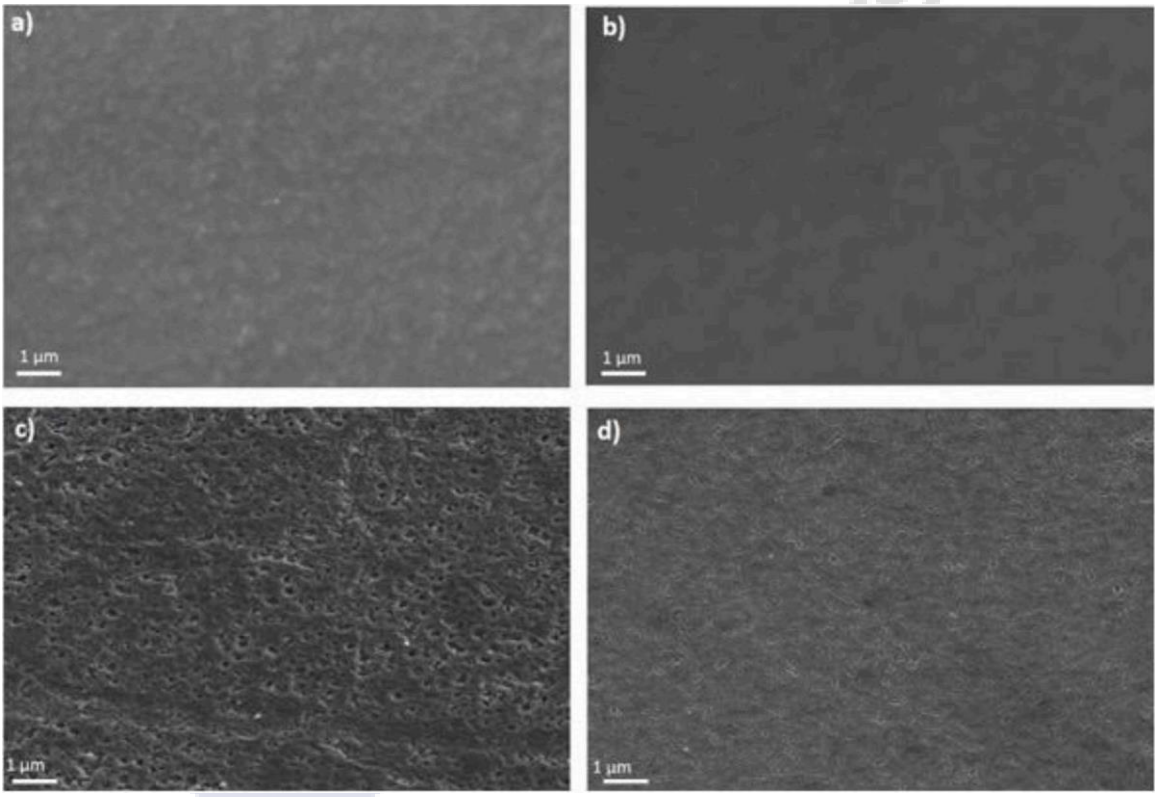

Fig. 13. Scanning Electron Microscopy of the films: **a)** CeO_2 pre weathering; **b)** CeO_2:V_2O_5 pre weathering; **c)** CeO_2 post weathering; **d)** CeO_2:V_2O_5 post weathering.

polycrystalline, and diffraction peaks of cerium dioxide were observed at 28°, 33°, 47° and 56°, related to the (111), (200), (220) and (311) crystallographic planes, respectively, corresponding to the cubic fluorite structure of CeO_2 (JCPDS No. 34–0394). [9,28] As expected, the insertion of V_2O_5 in the CeO_2 films presented a small displacement of the CeO_2 peaks, indicating a doping behavior of this material in the CeO_2 structure. The inset in the figure shows the effect of the presence of V_2O_5 in the thin films, with the increase in full width at half maximum of the CeO_2 (111) peak. No peaks of the V_2O_5 were observed, which can be explained by the low amount of dopant. Regarding the effect of the weathering process on the structure of the films, no significant differences were noticed, corroborating the AFM and SEM results, confirming that their crystalline structures were not altered after the degradation.

4. Conclusions

Thin films of CeO_2 and CeO_2 doped with V_2O_5 were prepared and tested under two different conditions: temperature (in a range from 20 to 80 °C) and weathering (in the equivalent days of 0, 180, 360, 720 and 900). Firstly, the influence of the temperature on the electrochemical properties of the films showed that an increase in temperature led to an increase in current density, as well as a displacement of the peaks. Through the chronoamperometry/ chronocoulometry technique, it was noticed that the response time became slower with increasing temperatures. However, the ability to insert ions in the layer improved, from 10 to 12 mC cm^{-2} and 12 to 40 mC cm^{-2} for CeO_2 and CeO_2:V_2O_5 films, respectively, for 60 s of applied potential. From the impedance, it was observed that the increase in temperature caused a decrease in resistance, favoring ion conductivity in both films. For the films that were

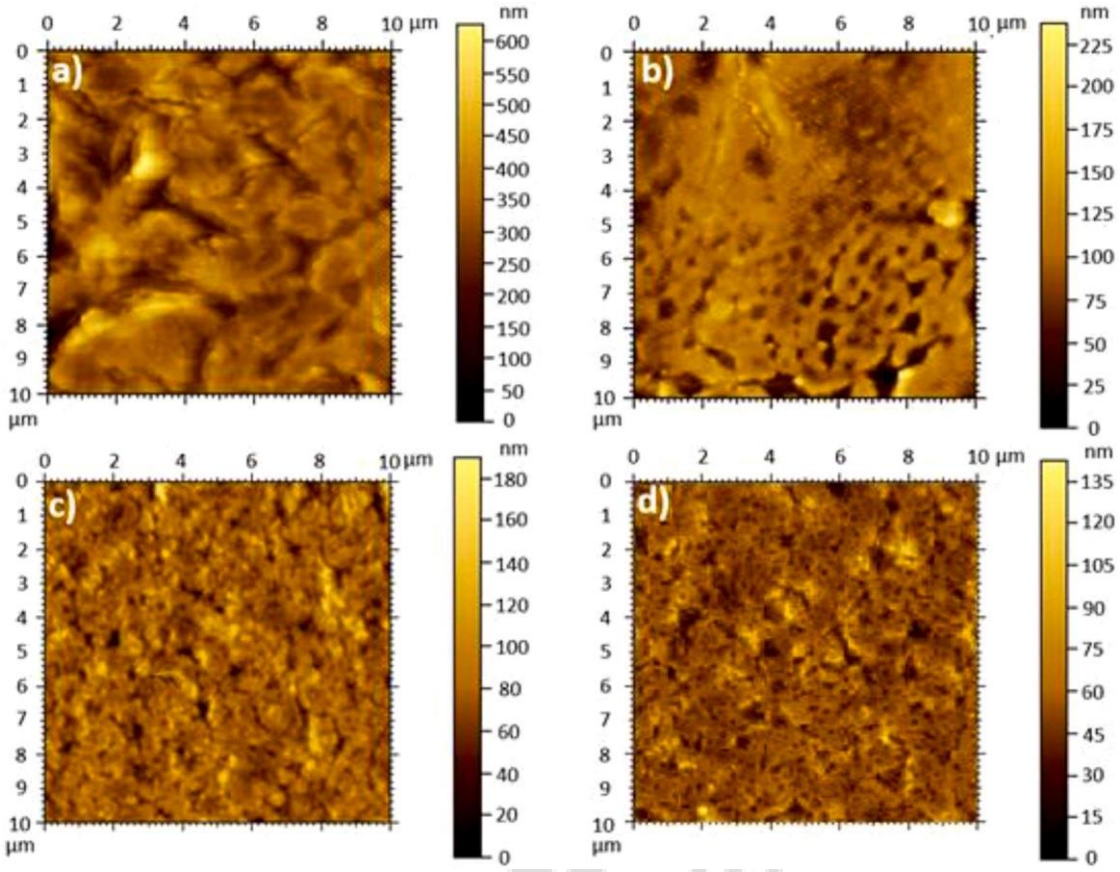

Fig. 14. Atomic Force Microscopy of the films: **a)** CeO_2 pre weathering; **b)** CeO_2:V_2O_5 pre weathering; **c)** CeO_2 post weathering; **d)** CeO_2:V_2O_5 post weathering.

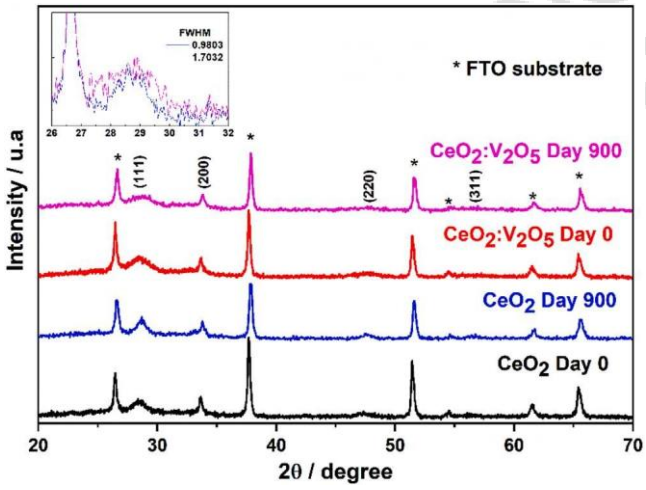

Fig. 15. X-Ray Diffraction of the CeO_2 films pre- and post-weathering and CeO_2:V_2O_5 films pre- and post-weathering.

subjected to the weathering process, in addition to electrochemical tests, morphological and structural tests were performed. Both films exhibited cyclic voltammetry profiles containing cathodic and anodic peaks, however, the CeO_2:V_2O_5 film presented a greater area than the CeO_2 film, and after the 900th day of incubation, both films presented non-significant differences. Thus, the presence of the dopant makes the insertion process faster, as shown in the chronoamperometry. Regarding the weathering, a significant difference in response time was noticed only for the CeO_2 film, which presented a faster process of insertion. The chronocoulometry showed that the CeO_2:V_2O_5 film allows more charge to be inserted in all possible scenarios, confirming the efficiency of the doping process. After the 900 days, the storage capacity decreased but still presented promising results. According to the EIS, the diffusion process of mass transport was confirmed, since the Nyquist plot presented curves with angulation close to 45°, which remained even after the weathering process. Through AFM and SEM, the CeO_2 film presented higher degradation, an increased porosity and the presence of cracks after the weathering process, while the CeO_2:V_2O_5 presented a more uniform and smoother surface. The DRX showed no changes in the films structure after the period of weathering exposure. Finally, it is possible to affirm that the material continues performing and presenting promising properties after 2.5 years of exposure to the weathering, important characteristic for this type of material and its proposed application.

Supporting information

Electrochemical impedance spectroscopy parameters and resistances of CeO2 and CeO2:V2O5 thin films; phase angle calculated by electrochemical impedance spectroscopy versus frequency log as a function of temperature for CeO2 and CeO2:V2O5 thin films; bode diagram by electrochemical impedance spectroscopy as a function of temperature for CeO2 and CeO2:V2O5 thin films; capacitance calculated by electrochemical impedance spectroscopy as a function of temperature for CeO2 and CeO2:V2O5 thin films; experimental and fitted curves for Nyquist and Bode diagram of CeO2 and CeO2:V2O5 thin films.

Declaration of Competing Interest

The authors declare that they have no known competing financial interests or personal relationships that could have appeared to influence the work reported in this paper.

Acknowledgements

The authors are indebted to FAPERGS (grant 12/2239–9), CNPq (grant 201820/2014–5) and CAPES for the financial support given to this research. The publication of this paper was partially supported by PRPPGI/UFPel and CAPES.

Author Statement

Raphael D. C. Balboni, Conceptualization; Writing - Original Draft
Camila M. Cholant, Methodology
Luana U. Krüger, Methodology
Elton A. Moura, Methodology
Guilherme K. Maron, Methodology
Wladimir H. Flores, Resources
André Gündel, Resources
Darci A. Gatto, Data Curation
Agnieszka Pawlicka, Resources
Cesar A. O. Avellaneda, Conceptualization; Resources; Writing - Original Draft; Supervision
Robson Andreazza; Conceptualization; Resources; Supervision

Supplementary materials

Supplementary material associated with this article can be found, in the online version, at doi:10.1016/j.materresbull.2021.111432.

References

[1] R.S. de Oliveira, F.S. Semaan, E.A. Ponzio, Janelas Eletrocrômicas: uma nova era em eficiência energética, Rev. Virtual Química. 7 (2015) 336–356.
[2] Y. Nishikitani, T. Asano, S. Uchida, T. Kubo, Thermal and optical behavior of electrochromic windows fabricated with carbon-based counterelectrode, Electrochim. Acta. 44 (1999) 3211–3217.
[3] C.G. Granqvist, A. Azens, A. Hjelm, L. Kullman, G.A. Niklasson, D. Rönnow, M. S. Mattsson, M. Veszelei, G. Vaivars, Recent advances in electrochromics for smart windows applications, Sol. Energy. 63 (1998) 199–216.
[4] B. Elidrissi, M. Addou, M. Regragui, C. Monty, A. Bougrine, A. Kachouane, Structural and optical properties of CeO2 thin films prepared by spray pyrolysis, Thin Solid Films 379 (2000) 23–27.
[5] A.K. Bhosale, P.S. Shinde, N.L. Tarwal, R.C. Pawar, P.M. Kadam, P.S. Patil, Synthesis and characterization of highly stable optically passive CeO2–ZrO2 counter electrode, Electrochim. Acta. 55 (2010) 1900–1906.
[6] E.A. Moura, C.M. Cholant, R.D.C. Balboni, T.M. Westphal, R.M.J. Lemos, C. F. Azevedo, A. Gündel, W.H. Flores, J.A. Gomez, F. Ely, A. Pawlicka, C. O. Avellaneda, Electrochemical properties of thin films of V <inf>2</inf>O <inf>5</inf>doped with TiO <inf>2</inf>, J. Phys. Chem. Solids. (2018) 119, https://doi.org/10.1016/j.jpcs.2018.03.023.
[7] A.W. Czanderna, D.K. Benson, G.J. Jorgensen, J.-.G. Zhang, C.E. Tracy, S.K. Deb, Durability issues and service lifetime prediction of electrochromic windows for buildings applications, Sol. Energy Mater. Sol. Cells. 56 (1999) 419–436.
[8] T. Kubo, T. Shinada, Y. Kobayashi, H. Imafuku, T. Toya, S. Akita, Y. Nishikitani, H. Watanabe, Current state of the art for NOC-AGC electrochromic windows for architectural and automotive applications, Solid State Ionics 165 (2003) 209–216.
[9] R.D.C. Balboni, R.M.J. Lemos, E.A. Moura, C.M. Cholant, C.F. Azevedo, I. M. Caldeira, A. Gündel, W.H. Flores, A. Pawlicka, C.O. Avellaneda, Electrochemical, UV–Vis, and microscopical characteristics of sol–gel CeO<inf>2</inf>:V<inf>2</inf>O<inf>5</inf>thin film, J. Mater. Sci. Mater. Electron. 29 (2018), https://doi.org/10.1007/s10854-018-9786-5.
[10] D.S. Dalavi, R.S. Devan, R.S. Patil, Y.-.R. Ma, P.S. Patil, Electrochromic performance of sol–gel deposited NiO thin film, Mater. Lett. 90 (2013) 60–63.
[11] C.O. Avellaneda, M.A.C. Berton, L.O.S. Bulhões, Optical and electrochemical properties of CeO2 thin film prepared by an alkoxide route, Sol. Energy Mater. Sol. Cells. 92 (2008) 240–244.
[12] C.M. Cholant, C.F. Azevedo, I. Caldeira, R.D.C. Balboni, E.A. Moura, T. M. Westphal, A. Pawlicka, M.A.C. Berton, J.A. Gomez, C.O. Avellaneda, Li+ ions diffusion coefficient in V<inf>2</inf>O<inf>5</inf>:MoO<inf>3</inf>Sol-Gel films, Mol. Cryst. Liq. Cryst. 655 (2017), https://doi.org/10.1080/15421406.2017.1360712.
[13] C.M. Lampert, C.-.G. Granqvist, Large-area chromogenics: Materials and Devices For Transmittance Control, SPIE, 1990.
[14] J.P. Gomilsek, I.K. Skofic, N. Bukovec, A. Kodre, X-Ray absorption study of CeO2 and Ce/V mixed oxide thin films obtained by sol–gel deposition, Thin Solid Films 446 (2004) 117–123.
[15] F. Varsano, F. Decker, E. Masetti, Thin film counterelectrodes with high Li charge capacity for electrochromic windows, Mol. Mater. Funct. Polym. (2001) 83–95.
[16] D.S. Dalavi, A.K. Bhosale, R.S. Desai, P.S. Patil, Energy efficient electrochromic smart windows based on highly stable CeO2-V2O5 optically passive counter electrode, Mater. Today Proc. (2020).
[17] J. Yin, E.S. Takeuchi, K.J. Takeuchi, A.C. Marschilok, Synthetic control of manganese birnessite: impact of crystallite size on Li, Na, and Mg based electrochemistry, Inorganica Chim. Acta. 453 (2016) 230–237.
[18] J. Yin, A.B. Brady, E.S. Takeuchi, A.C. Marschilok, K.J. Takeuchi, Magnesium-ion battery-relevant electrochemistry of MgMn 2 O 4: crystallite size effects and the notable role of electrolyte water content, Chem. Commun. 53 (2017) 3665–3668.
[19] K.J. Takeuchi, S.Z. Yau, A. Subramanian, A.C. Marschilok, E.S. Takeuchi, The electrochemistry of silver Hollandite nanorods, AgxMn8O16: enhancement of electrochemical battery performance via dimensional and compositional control, J. Electrochem. Soc. 160 (2013) A3090.
[20] A. Jin, W. Chen, Q. Zhu, Y. Yang, V.L. Volkov, G.S. Zakharova, Structural and electrochromic properties of molybdenum doped vanadium pentoxide thin films by sol–gel and hydrothermal synthesis, Thin Solid Films 517 (2009) 2023–2028.
[21] I.C. Amaechi, A.C. Nwanya, D. Obi, S.C. Ezugwu, A.E. Udounwa, A.B.C. Ekwealor, R.U. Osuji, M. Maaza, F.I. Ezema, Structural characterization and electrochemical properties of cerium–vanadium (Ce–V) mixed oxide films synthesized by chemical route, Ceram. Int. 42 (2016) 3518–3524.
[22] S. Rehman, H. Kim, M.F. Khan, J.-.H. Hur, A.D. Lee, D. Kim, Tuning of ionic mobility to improve the resistive switching behavior of Zn-doped CeO 2, Sci. Rep. 9 (2019) 1–10.
[23] A.K. Lucid, P.R.L. Keating, J.P. Allen, G.W. Watson, Structure and reducibility of CeO2 doped with trivalent cations, J. Phys. Chem. C. 120 (2016) 23430–23440.
[24] P. Mannu, M. Palanisamy, G. Bangaru, S. Ramakrishnan, A. Kandasami, P. Kumar, Temperature-dependent AC conductivity and dielectric and impedance properties of ternary In–Te–Se nanocomposite thin films, Appl. Phys. A. 125 (2019) 458.
[25] L.A. de Carvalho, A.R. de Andrade, P.R. Bueno, Espectroscopia de impedância eletroquímica aplicada ao estudo das reações heterogeneas em ânodos dimensionalmente estáveis, Quim. Nova. 29 (2006) 796–804.
[26] I. Manouchehri, D. Mehrparvar, R. Moradian, K. Gholami, T. Osati, Investigation of structural and optical properties of copper doped NiO thin films deposited by RF magnetron reactive sputtering, Optik (Stuttg) 127 (2016) 8124–8129.
[27] T.M. Westphal, C.M. Cholant, C.F. Azevedo, E.A. Moura, D.L. da Silva, R.M. J. Lemos, A. Pawlicka, A. Gündel, W.H. Flores, C.O. Avellaneda, Influence of the Nb2O5 doping on the electrochemical properties of V2O5 thin films, J. Electroanal. Chem. 790 (2017) 50–56.
[28] S. Domingues, T.J. Pereira, A.O. Florentino, A.A. Cavalheiro, M.J. Saeki, Structural study of Ti x (Sm0. 2Ce0. 8) 1-xO2-delta ceramic by the Rietveld method, Cerâmica 53 (2007) 205–211.

4.3 Artigo 3

O artigo intitulado “**Sustainable Biogels Based On Cellulose Acetate For Application In Electrochromic Devices**” é apresentado conforme preparado para submissão na Revista Carbohydrate Polymers, ISSN: 0144-8617, classificação A1 na área de Materiais.

Sustainable Biogels Based On Cellulose Acetate For Application In Electrochromic Devices

Raphael D. C. Balboni[1], Camila M. Cholant[1], Rafaela M. J. Lemos[1], Lucas S. Rodrigues[1], Cesar A. O. Avellaneda[1], Robson Andreazza[1]

[1] Centro de Desenvolvimento Tecnológico, Universidade Federal de Pelotas, Rua Gomes Carneiro, 1, Centro, Pelotas, RS 96010-610, Brazil

ABSTRACT

In this study, an easy and low-cost production method of a cellulose acetate-based gel polymer containing lithium perchlorate and propylene carbonate is described, as well as the investigation of its properties for possible application as an electrolyte in electrochemical devices. Cellulose acetate is a biopolymer originated from natural matrix, colorless and transparent, as confirmed by the UV-Vis spectroscopy, presenting 85% transparency in visible spectrum. The gels were prepared and tested at different concentrations and proportions to optimize their properties. The gel containing 10% by mass of cellulose acetate and 1.4 M of $LiClO_4$ was the most promising, presenting conductivity of $2.3x10^{-4}$ $S.cm^{-1}$ at 25 °C and $3.0x10^{-4}$ $S.cm^{-1}$ at 80 °C, an ideal shape of cyclic voltammetry curves and stability after 400 cycles. Its morphological and structural properties have also been investigated through thermogravimetry, XRD and FTIR, and have demonstrated suitable characteristics for the proposed application.

1. INTRODUCTION

As the future of humanity moves towards reducing the carbon footprint through new technologies, current research is aimed at developing greener and more environmentally friendly devices that help with the energy issue. [1] Studies report that more than 70% of the energy consumed is destined for buildings, of which 35% are used for air conditioning, [2] due to the flow of heat and light that demand compensation through heating/cooling systems. [3] Thus, devices that offer greater control over the optical and thermal properties of glass and windows have been studied, helping to reduce expenses related to electricity and lighting. [4,5] An example of these devices are smart windows, a device that allows this modulation through an external electrical stimulus. [6,7]

Smart windows work from the electrochromic properties of their constituent materials, which are structured in layers with different functions. One of these layers, the electrolyte, has the function of transporting charges during the ion exchange that occurs in response to the applied potential, and needs to present characteristics such as ionic conduction capacity, high diffusion coefficient and rapid electrochemical kinetics. [8] By choosing to use gel electrolytes rather than liquid electrolytes, advantages such as ease of handling, safety and lower cost to assembly are obtained, in addition to preventing leakage and reactions between the electrolyte and the electrodes, thus increasing device lifespan. [9,10]

When working with gel electrolytes, its ionic conduction capacity must be evaluated, as it should present values similar to those of liquid electrolytes, ideally on the order of 10^{-4} $S.cm^{-1}$ or higher. [11] In polymer gel electrolytes, for example, it is important to add a material responsible for providing ions that will be moved along the amorphous phase of the polymer matrix. [12,13] A material commonly used as an ion source are salts containing Li^{+}, as this ion has a small atomic radius and relative chemical stability. [14,15] However, the amount of lithium added to the material needs to be optimized, equalizing the advantages of its use with the socio-environmental disadvantage – related to its disposal. Furthermore, an excessive increase in the salt concentration in the polymer matrix can lead to a decrease in ionic mobility and a consequent decrease in conductivity, due to ion-ion interactions that lead to a greater occurrence of ionic aggregates and a decrease in charge carrier species. [16,17]

For polymer gel electrolytes, compatibility and synergy between polymer and ion source are required to optimize the desired properties. Initially treated as electrical insulators, polymers soon showed promise as conductors for use in electrochemical devices, mainly due

to their ability to dissolve inorganic salts, generating charges and promoting ionic conductivity. [18] Other important characteristics are the optical properties, the viscosity – since adhesion between the layers of the device is expected – and the chemical and electrochemical stability – which tend to be inferior compared to liquid electrolytes, requiring a long-term stability assessment. [19]

Aiming to obtain more sustainable materials, several studies opt for the use of electrolytes based on biopolymers, a class of materials with a renewable matrix that occurs naturally, without the need for synthesis in its formation. [20] In addition to the ecological character, they also have advantages such as water solubility, low toxicity, and low cost, however, presenting lower stability when subjected to high temperatures. [21] To obtain a material with optimized properties, it is interesting to use both polymeric states – natural and synthetic. [22] Cellulose acetate is an example of these modified natural polymers, being a derivative of cellulose, a linear semi-crystalline natural polymer – having crystalline and amorphous regions – and of high molecular mass, with its structure illustrated in Figure 1a. [23] Despite being abundant in nature and renewable, its use is limited by the difficulty of interacting with other precursors. A possible process that aims to modify the surface of the polymer is through the acetylation of cellulose, where the hydroxyl groups of the glucose units are replaced by acetyl groups, resulting in the structure illustrated in Figure 1b.

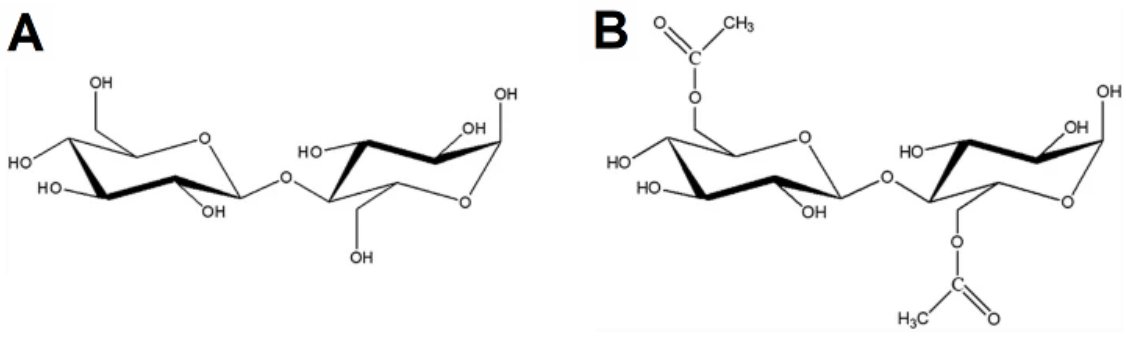

Figure 1 Structural formula of: a) cellulose, b) cellulose acetate. [24]

This modification allows the material to dissolve in conventional solvents, generating a low-cost neutral polymer, capable of forming transparent films, which can be used as

membranes – allowing selectivity and permeability in relation to ions – or as conductive polymers – in electronic and electrochromic devices. [25]

2. EXPERIMENTAL

2.1 Preparation of the gels

To prepare the polymer gel, the amount of lithium perchlorate ($LiClO_4$) (Dinâmica Química Contemporânea) was first fixed at 0.8M and different amounts of cellulose acetate (CA) (Sigma-Aldrich) were added (6–14 wt%) to investigate the influence of the polymer on the viscosity and conductivity of the gels. After analyzing the results obtained, the concentration of cellulose acetate was set at 10% and different amounts of the salt (0.4–1.8 M) were added. The methodology used was the same for all gels, with the addition of the polymer and the salt to the propylene carbonate (PC) (Sigma-Aldrich) and magnetic stirring for 8 hours with heating at 100 °C until complete dissolution. The list of gels and their concentrations can be found in Table 1.

Table 1 Composition of the different produced gels.

GEL	**A**	**B**	**C**	**D**	**E**	**F**	**G**	**H**	**I**	**J**	**K**	**L**	**M**
[CA] (m/m)	6	8	10	12	14	10	10	10	10	10	10	10	10
[$LiClO_4$] (mol.L^{-1})	0.8	0.8	0.8	0.8	0.8	0.4	0.6	0.8	1.0	1.2	1.4	1.6	1.8

* CA = Cellulose Acetate; $LiClO_4$ = Lithium Perchlorate

2.3 Characterization of the gels

The electrochemical impedance spectroscopy measurements were performed using a potentiostat (IVIUM – Compactstat), operating in the frequency range from 10^6 to 10^{-1} and potential amplitude of 10 mV. The gel sample was tested in a Teflon® electrochemical cell containing two circular stainless-steel electrodes – 1 cm in diameter and 0.3 cm apart – as current collectors, as shown in Figure 2a,b. The measurements were performed in triplicate and the results presented are the average values. For the EIS analysis with temperature

variation, measurements were carried out at 25, 30, 40, 50, 60, 70 and 80 °C using a homemade temperature-controlled oven with a thermocouple connected to the electrochemical cell, allowing direct temperature reading, as shown in Figure 2c. Cyclic voltammetry was performed in another potentiostat (Metrohm Autolab, PGSTAT302 N).

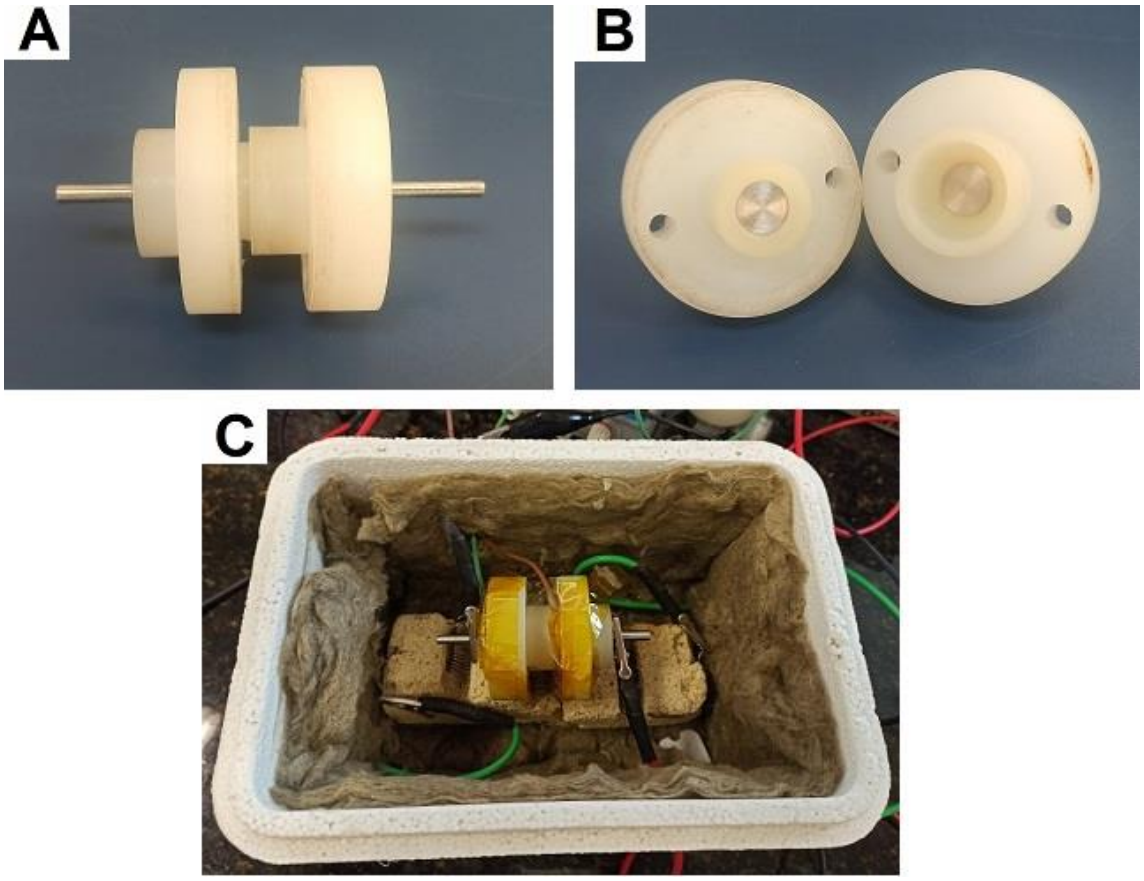

Figure 2 a, b) electrochemical cell containing two circular stainless-steel electrodes as current collectors; c) homemade temperature-controlled oven with a thermocouple connected to the electrochemical cell.

The structure of the gels was studied through X-ray diffraction, carried out in an XRD6000 Diffractometer (SHIMADZU), with CuKa radiation, voltage of 30 kV, current of 30 mA and variation of the scanning angle (2θ) from 10 to 80° at room temperature. The FTIR was performed with the IRPrestige-21 spectrometer (SHIMADZU), in the range of 700–4000 cm^{-1}. The transparency of the gels was investigated by UV-Vis Spectrophotometry using a HR2000 + ES Spectrometer (Ocean Insight) in the range of 25-800 nm. For thermal

analysis, TG 209 F1 Iris Thermogravimetric Analyzer (NETZSCH Group) was used, and the samples were heated from 30 to 600 °C at 10 °C min^{-1}.

3. RESULTS AND DISCUSSION

3.1 Electrochemical characterization

The electrochemical characterization of the gels was initially evaluated by cyclic voltammetry (CV). First, the analysis was performed in different potential windows to investigate the behavior of the gels as a function of the applied voltage. The results are shown in Figure S1, and it is possible to observe that the optimized potential window is from -0.75 V to +0.75 V, where the voltammogram presented a more regular and rectangular shape.

CV was then performed for all gels in the optimized potential window with a scan rate of 50 $mV.s^{-1}$, and Figure 3 shows the voltammogram for samples with different amount of cellulose acetate (Figure 3a) and lithium perchlorate (Figure 3b). For all measurements, a rectangular profile was presented, with no cathodic and anodic peaks and a symmetrical current-potential response, which indicates the good electrochemical performance. [26] It is also possible to observe a slight difference in the voltammogram area for different gel compositions. Then, CV was performed for all gels at 10, 20, 50 and 100 $mV.s^{-1}$ to verify the electrochemical performance of the electrolytes at different scan rates. Figure 3c shows the voltammogram of the gel containing 10 wt% of CA and 1.4M of $LiClO_4$ (Gel K), where is possible to observe the maintenance of behavior and shape (even with a smaller area at lower scan rates). Figure S2 shows voltammograms of gels with different polymer and salt contents as a function of scan rate, and the good performance is observed in all scenarios.

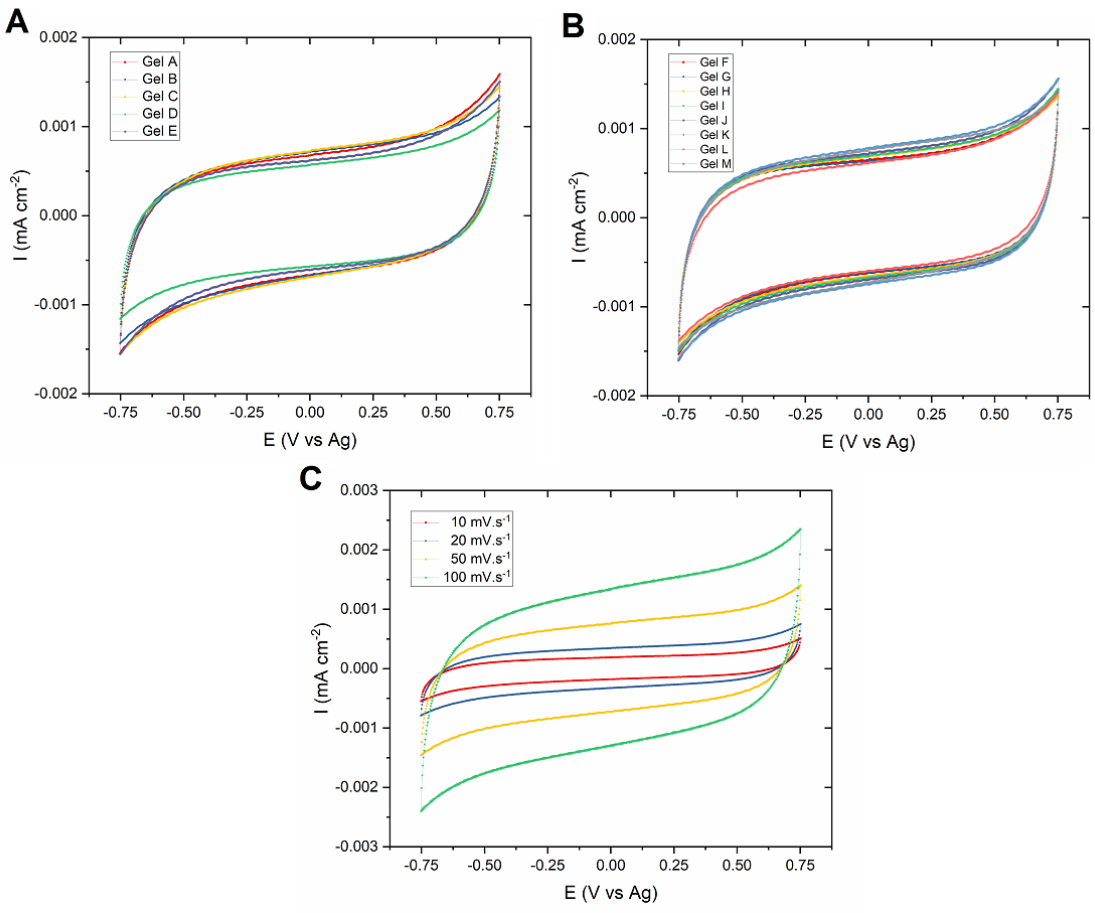

Figure 3 Cyclic voltammetry curves of gels with different amounts of: a) cellulose acetate (6-14 wt%), b) lithium perchlorate (0.4-1.8M); c) CV curves of Gel K at different scan rates.

To assess the long-term stability of the electrolytes, cyclic voltammetry analyzes were performed and Figure 4 shows the voltammogram over 400 cycles of applied potential for samples with different amounts of cellulose acetate (Figure 4a) and lithium perchlorate (Figure 4b). For all gels, the rectangular profile was maintained, no peaks were presented, and the shape remained symmetrical. Figure 4c shows the voltammogram over 400 cycles of the gel containing 10 wt% of CA and 1.4M of $LiClO_4$ (Gel K), being possible to observe a small decrease in the voltammogram area from cycle 2 to cycle 100. From cycle 100 onwards, the area of the curves did not change, showing the same performance up to cycle 400, which suggests the great cyclic stability of the electrolyte and qualifies it for use in long-term devices. Voltammograms over 400 cycles of gels with different polymer and salt contents are shown in Figure S3, and the behavior was maintained for all gel compositions.

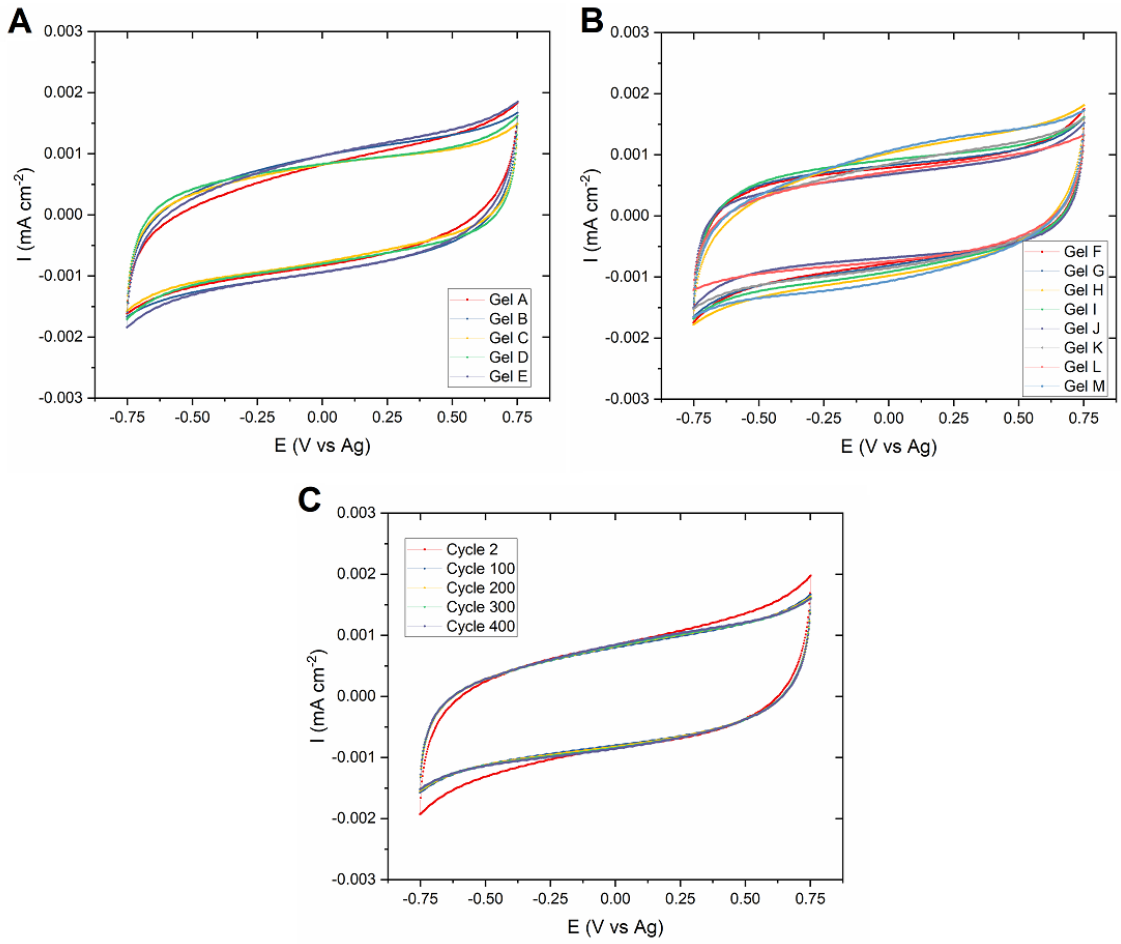

Figure 4 Cyclic voltammetry curves over 400 cycles of gels with different amounts of: a) cellulose acetate (6-14 wt%), b) lithium perchlorate (0.4-1.8M); c) CV curves of Gel K at cycle 2, 100, 200, 300 and 400.

Electrochemical impedance spectroscopy was performed to investigate the conductivity and diffusion of the gels, and Figure 5 shows the Nyquist plot obtained. The absence of a well-defined semicircle at high frequencies may indicate a limited contribution of the capacitive component, suggesting a diffusion process, an idea supported by the angle close to 45° of the straight line as seen in Figure 5 insets. Since the lines do not start at zero ohms, a resistance between the electrode and the electrolyte is also implied. [27,28]

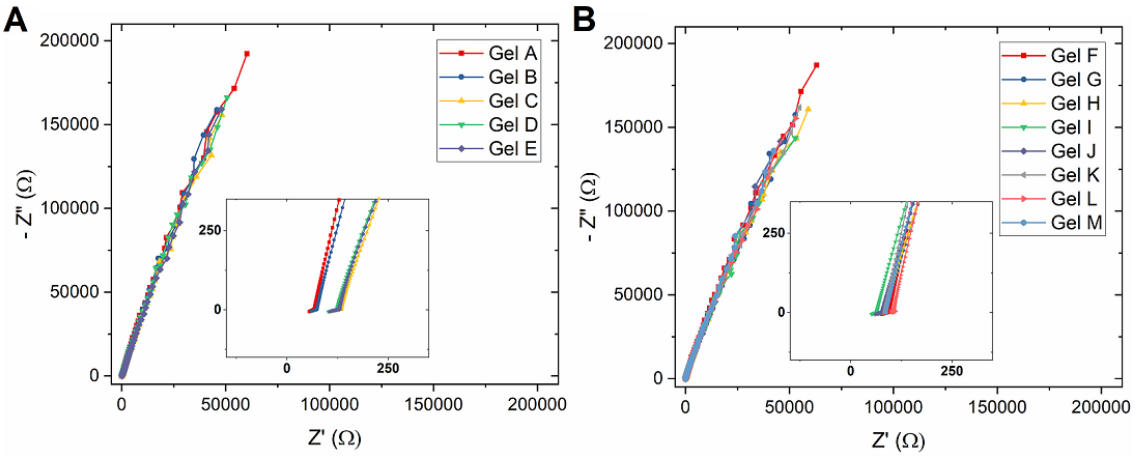

Figure 5 EIS curves of gels with different amounts of: a) cellulose acetate (6-14 wt%), b) lithium perchlorate (0.4-1.8M).

Through the EIS analysis, it was possible to investigate the ionic conductivity using Equation 1:

$$\sigma = \frac{L}{R_b \mathrm{X}\, A} \tag{1}$$

where σ is the ionic conductivity, R_b is the bulk electrical resistance, A is the contact area between the electrolyte and the electrodes, and l is the distance between them.

First, the influence of the amount of cellulose acetate on ionic conductivity was investigated. As can be seen in Figure 6a, the increase in cellulose acetate led to an increase in ionic conductivity. The sample that presented the highest ionic conductivity was the sample containing 14 wt% of the polymer (Gel E), however, the gel presented high viscosity, a property not suitable for the proposed application, as it can make it difficult to inject the electrolyte into the device. [29]

The samples containing 10 and 12 wt% (Gels C and D) presented a non-significant difference in their ionic conductivity, suggesting the use of the one with the smallest amount of material. Then, the influence of the salt was studied and different amounts of $LiClO_4$ were added to the gel containing 10 wt% of the polymer. Figure 6b shows the relationship between the parameters, as the conductivity increases almost proportionally with the addition of $LiClO_4$, with the greatest increment occurring from the 1.2M sample (Gel J) to the 1.4M

sample (Gel K), which delivered an ionic conductivity of $2.3x10^{-4}$ $S.cm^{-1}$. This conductivity is consistent with other polymer electrolytes reported in the literature, such as based on xanthan gum-PVA (1.97×10^{-4} $S.cm^{-1}$) [30], Guar gum (1.46×10^{-4} $S.cm^{-1}$) [31] and Chitosan:Methylcellulose (1.93×10^{-4} $S.cm^{-1}$) [32].

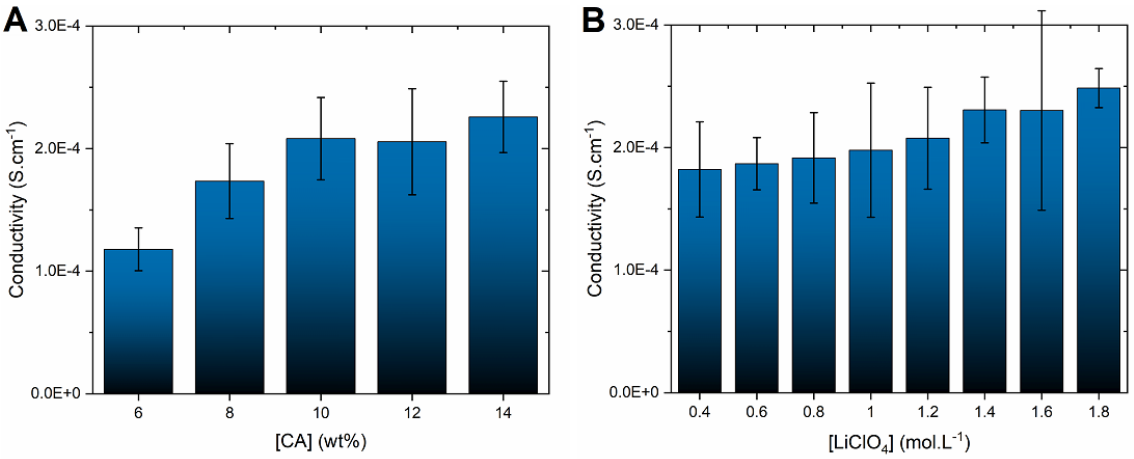

Figure 6 Ionic conductivity of gels with different amounts of: a) cellulose acetate (6-14 wt%), b) lithium perchlorate (0.4-1.8M).

Among all the tested electrolytes, the one containing 1.8M of $LiClO_4$ presented the highest ionic conductivity, and this increase can be explained by the higher quantity of charge carriers and mobile ions, as the $LiClO_4$ dissociation provides free ClO_4^- and Li^+ ions, favoring the conduction process. [11,29] As we aim to develop a green and sustainable electrolyte, the amount of lithium added to the gel is a determining factor to consider. Therefore, the electrolyte containing 1.8M of $LiClO_4$ (Gel M) presents an increase in the conductivity in relation to the other electrolytes, however, this difference does not compensate in proportion to the amount of lithium perchlorate added, as this material can generate an environmental impact at high concentrations. Lithium, when used in charge/discharge systems, can become electrically isolated and present some instability after some cycles, becoming electrochemically inactive, but still chemically reactive due to its high surface area, resulting in possible internal short and thermal runaway. When forming lithium perchlorate, due to the oxidation state of chlorine (VII), can present itself as a strong oxidant and end up generating strong reactions with organic species. [33,34]

EIS analyzes at different temperatures were performed and the dependence of the ionic conductivity of the gels over temperatures from 25 to 80 °C is shown in Figure 7, where the conductivity logarithm was plotted against the inverse of the temperature for a better understanding. The results show that the conductivity varies with temperature, but in a non-linear way. The graphs were divided into three regions, I, II and III, which correspond to the temperature ranges 25-30, 30-70 and 70-80 °C, respectively. First, the identification of the three regions suggests that the ionic transport mechanism is complex, occurring both by ionic jumps and by segmental movement of the polymer. [35] This may be associated with the gel-like texture, which has a high viscosity and denser structure in terms of polymer chains. [36] Furthermore, it may suggest a phase transition of cellulose acetate, [37] which is a semicrystalline polymer according to XRD.

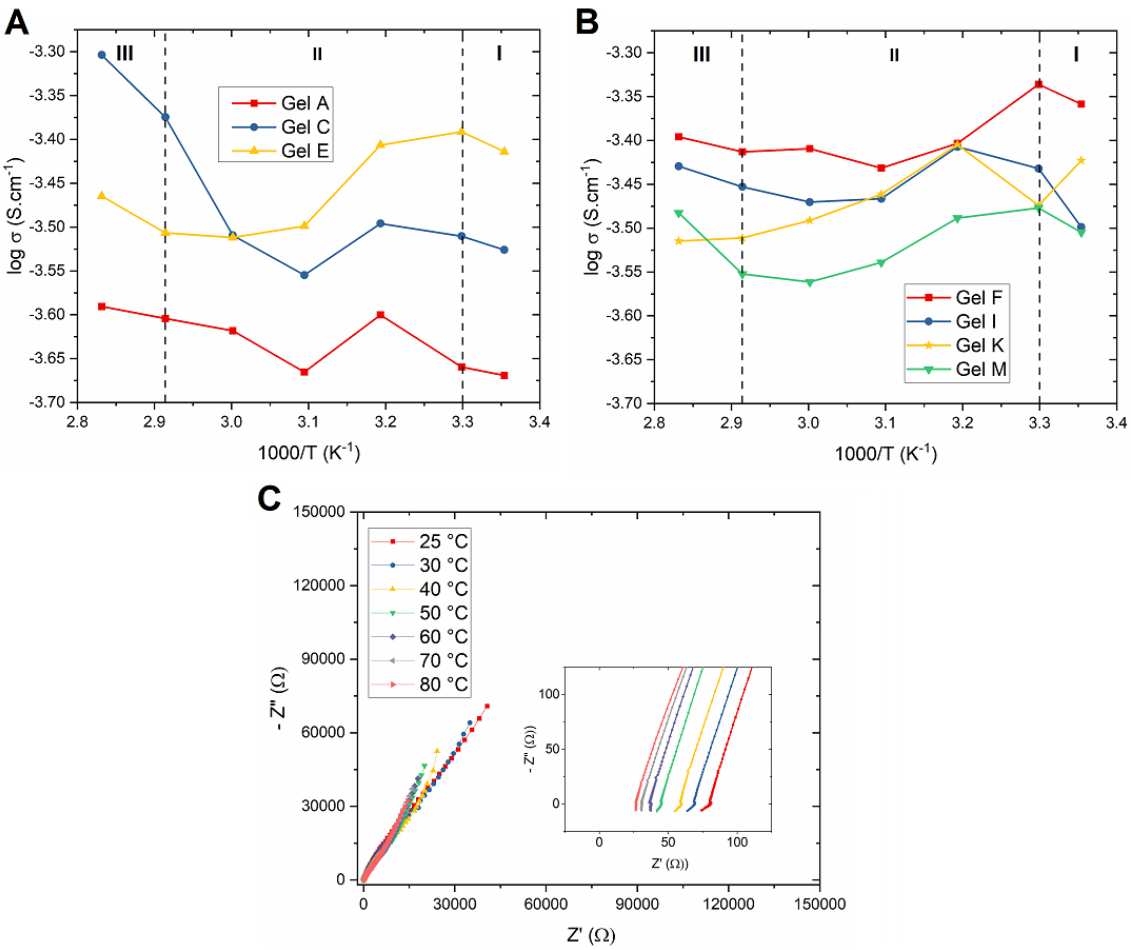

Figure 7 Ionic conductivity over temperature of gels with different amounts of: a) cellulose acetate (6-14 wt%), b) lithium perchlorate (0.4-1.8M); c) EIS curves of Gel K from 25 to 80 °C.

In regions I and III, it is possible to observe an increase in conductivity for most samples, which can be explained by an increase of the diffusibility that facilitates the transport of the ions in the polymer. [38] Region II presents a variable behavior with a predominance of a decrease in conductivity with increasing temperature. This can be explained by the high glass temperature (Tg) of the electrolyte, an intrinsic characteristic of the cellulose acetate. At lower temperatures, the polymer structure becomes more rigid, making segmental dynamics difficult. In some reported works, the presence of salt can increase Tg, depending on the amount added. [39] Furthermore, the breaking of cellulose acetate bonds due to the high entropy condition can also influence the reduction of ionic conductivity. [40] Figure 7c shows the Nyquist plot of the sample containing 1.4M of $LiClO_4$ (Gel K), where it is possible to observe in the inset that the resistance between the electrode and the electrolyte decreases as the straight lines shift towards zero at high frequencies as the temperature increases, corroborating the influence of temperature in ionic conductivity. Figure S4 shows the Nyquist plot of gels with different polymer and salt contents at different temperatures, which corroborates the behavior presented by the Gel K.

3.2 Optical characterization

An important characteristic of the electrolytes in some electrochemical devices is their transparency. An intrinsic property of most electrolytes based on natural polymers is that they tend to form transparent gels/membranes. That said, Figure 8 shows the optical transmittance spectra for cellulose acetate-based electrolytes in the range of 250–800 nm. It is possible to observe small differences in transmittance as a function of the amount of polymer, as the gel with the highest cellulose acetate content presents highest transmittance. For different amounts of $LiClO_4$, the difference is almost negligible over the entire wavelength range. After 500 nm, the transmittance varies between 82 and 85% for all tested gels, a non-significant difference.

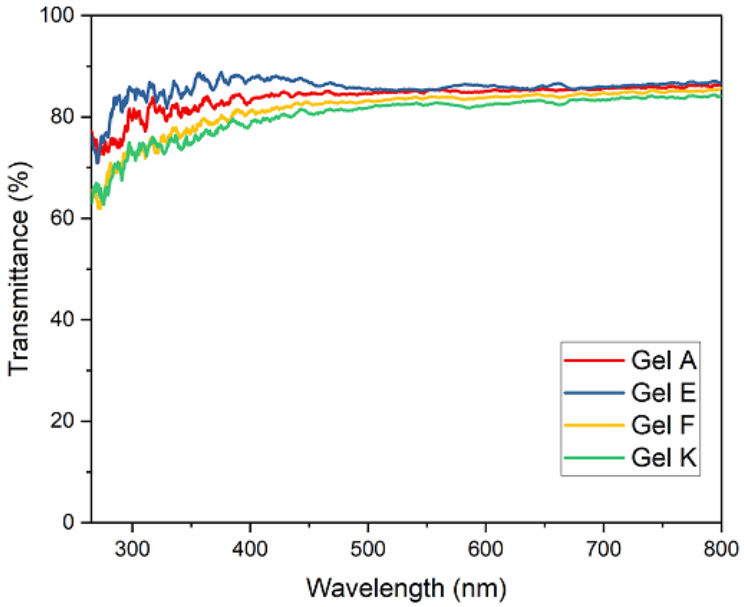

Figure 8 Ultraviolet–visible transmittance spectra of gels with different amounts of cellulose acetate and lithium perchlorate.

3.3 Thermal characterization

To better understand the thermal stability of the cellulose acetate based gels, thermogravimetric analyzes were performed and the thermal behavior of the electrolytes is shown in Figure 9. The first stage of thermal degradation occurred at temperatures up to 100 °C and only 5% of mass loss occurred, which can be attributed to the loss of free water and/or moisture evaporation. The second stage starts at 150 °C, where a massive mass loss begins to occur and, up to 250 °C, 90% of the initial mass is lost for all gels, due to their degradation. Above 250 °C, degradation continues at a low rate, remaining only material residues. Regarding the different amounts of materials added to the gels, it is possible to observe that the mass loss of the gel containing less polymer occurs faster. The sample containing 6 wt% of cellulose acetate (Gel A) presented a mass loss of 80% at 200 °C, while the one containing 14 wt% (Gel E) presented the same loss mass only at 240 °C. For different amounts of salt, a small increase in stability is shown for the one containing 1.4M of $LiClO_4$ (Gel K) when compared to the one with 0.4M (Gel F). However, as the thermograms are similar, it suggests that there are no significant changes in the electrolyte structures and that the lithium perchlorate does not act as a catalyst in the decomposition of gels.

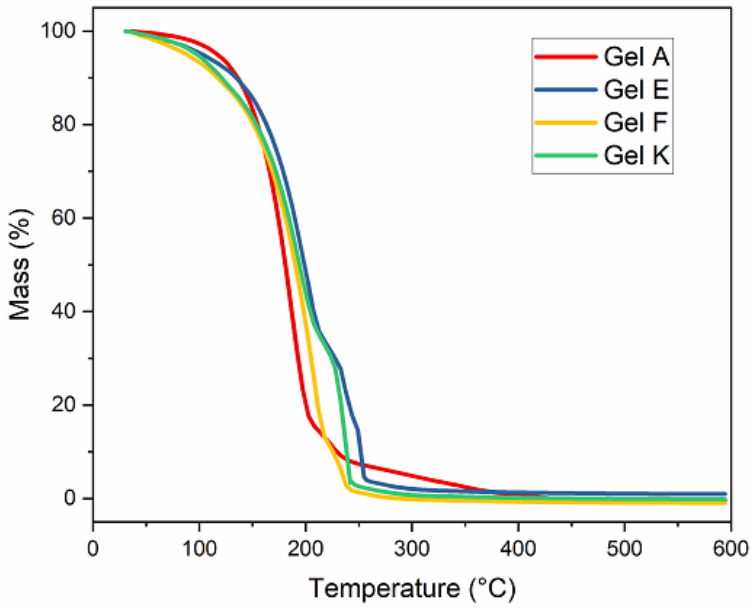

Figure 9 Thermogravimetric analysis of gels with different amounts of cellulose acetate and lithium perchlorate.

3.4 Structural characterization

XRD measurements were performed for electrolytes containing two different amounts of cellulose acetate and lithium perchlorate to investigate the influence of these materials on the structure of the gels at room temperature. Figure 10 shows the XRD patterns of the tested gels, where it is possible to infer that the gels are composed of a combination of amorphous and crystalline phases, which makes them semi-crystalline in nature. A broad halo related to the semi-crystalline nature of cellulose acetate can be observed from $2\theta=23°$ to $2\theta=27°$, which is in agreement with the literature. [39,41] Regarding the different amounts of cellulose acetate, the addition of the polymer content does not generate a significant difference in broadness and relative intensity. In terms of salt addition, the gel with the lowest amount of lithium perchlorate shows a slight increase in peak intensity, which may infer a higher crystallinity, suggesting that the increase in salt amount leads to an increase in the amorphous character. [39] XRD patterns do not present peaks corresponding to $LiClO_4$, which indicates complete dissociation of the salt in the cellulose acetate matrix. [42] As there are no significant changes in the XRD patterns, it is possible to state that there are no significant changes in the structure of the electrolytes, predominating the amorphous character, which may produce greater diffusivity and higher ionic conductivity, as the ions easily migrate into the polymer. [26]

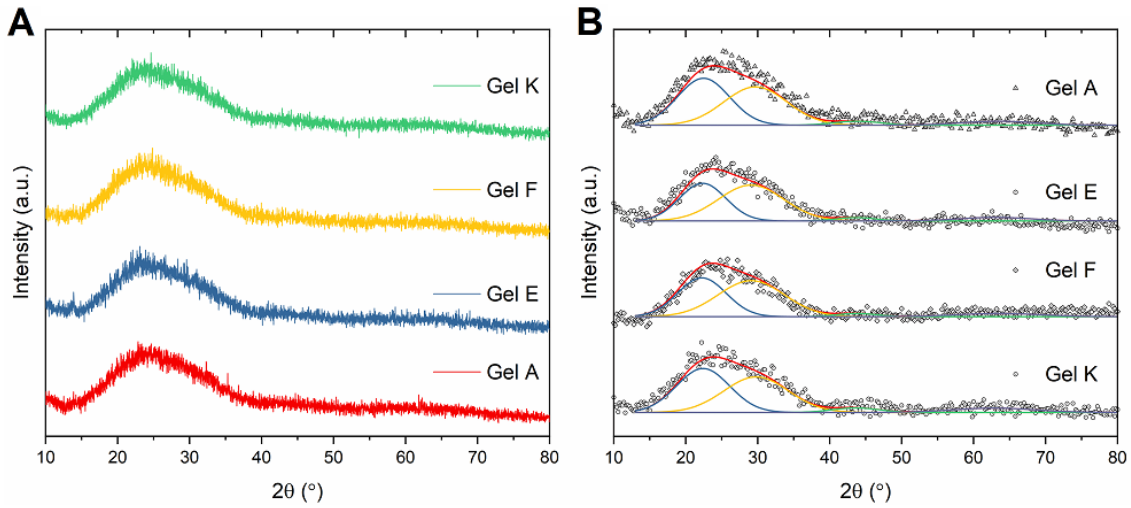

Figure 10 a) Diffractograms of gels with different amounts of cellulose acetate and lithium perchlorate; b) deconvolution of the diffractograms presented in (a).

FTIR was performed to analyze the functional groups and the interaction between the gel constituents. Figure 11 shows the FTIR spectra of cellulose acetate gels with different polymer and salt amounts. To investigate the influence of cellulose acetate, the amount of salt was fixed and gels with three different polymer concentration were tested – gels A,C and E (6, 10 and 14 wt%). The influence of lithium perchlorate was studied by fixing the amount of polymer and varying the salt concentration – gels I, K and M (1.0, 1.4 and 1.8 M).

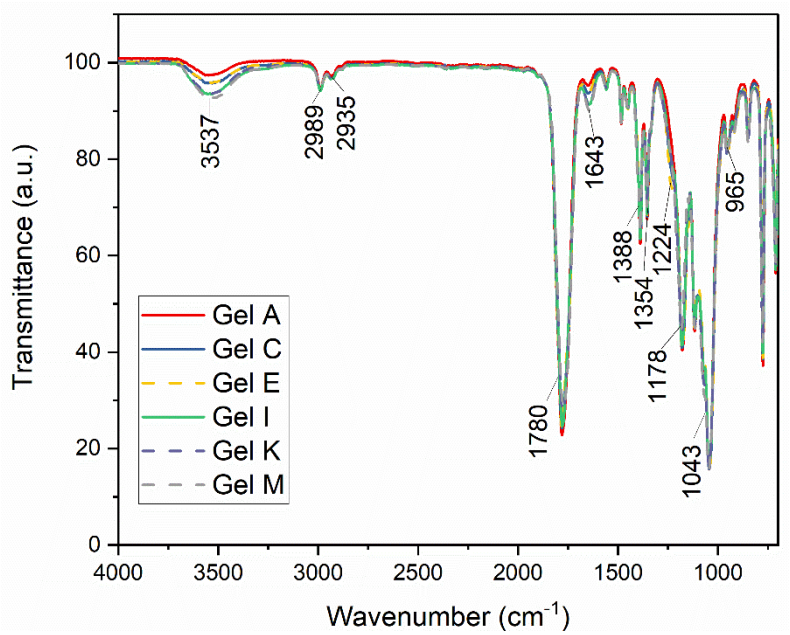

Figure 11 Fourier transform infrared spectroscopy (FTIR) spectra of gels with different amounts of cellulose acetate and lithium perchlorate.

Through the FTIR specters, it was possible to identify characteristic peaks of cellulose acetate and carbonate groups of propylene carbonate – used as solvent – which owns similar organic functional groups and are presented in Table 2. The main absorption peaks of cellulose acetate are 3537 corresponding to O-H stretching, 1780 corresponding to C=O symmetric stretching and 1224–1043 cm^{-1}, both as a result of overlapping single peaks, referent to the C–O stretching. [43] With the exception of the O–H peak, the other peaks have the contribution of the propylene carbonate, being the characteristic band of carbonate group appearing at 1178 cm^{-1} and corresponding to the O–C–O group, also overlapped with 1224 cm^{-1} peak. [44]

Table 2 Fourier transform infrared spectroscopy (FTIR) assignments of cellulose acetate gels

Wavenumber (cm^{-1})	Assignments
3537	O—H stretching
2989	C—H stretching symmetric
2935	C—H stretching
1780	C=O symmetric stretching
1643	C—C ring
1388	C—H bending
1354	C—H assymmetric
1224	C—O stretching
1178	O—C—O assymmetric
1043	C—O—C stretching
965	C—H bending and CH_2 rocking

The increase of cellulose acetate concentration caused a small variation in peak intensities. The O–H band presents greater intensity for Gels C and E due to the high number of functional groups, whereas the Gel A presents greater intensity in the O–C–O peak, which is the largest amount of propylene carbonate. In Gels I, K and M, the increase in the amount of Li^+ ions led to a decrease in peak intensity at 1780 cm^{-1}, suggesting a greater interaction of the ions with the carbonyl group. A decrease in the peak attributed to the carbonate group was also observed, indicating the possibility of interaction between Li^+ ions and propylene carbonate. [40,45]

4. CONCLUSIONS

Gel polymer electrolytes with different concentrations of cellulose acetate and lithium perchlorate were produced and analyzed electrochemically, structurally, thermally and optically. The gel that presented the best results was the gel containing 10 wt% of cellulose

acetate and 1.4M of $LiClO_4$, with conductivity values in the order of $2.3x10^{-4}$ $S.cm^{-1}$ at 25 °C and $3.0x10^{-4}$ $S.cm^{-1}$ at 80 °C. Through cyclic voltammetry, a stability analysis was performed, and the gel proved to be stable after 400 scanning cycles, presenting a small decrease in the voltammogram area. The gel showed a transparency close to 85% by UV-Vis spectroscopy and a significant mass loss between 150 and 250 °C by thermogravimetry. The gel showed a semicrystalline structure through XRD and characteristic peaks of cellulose acetate and of the carbonate group of propylene carbonate. Thus, it is possible to affirm that the mentioned gel is a promising electrolyte to be used in electrochromic devices.

SUPPORTING INFORMATION

The online version contains supplementary material available.

ACKNOWLEDGEMENTS

The authors would like to thank the support of National Council for Scientific and Technological Development (CNPq, grant 201820/2014-5) and Research Support Foundation of the State of Rio Grande do Sul (FAPERGS, grant 12/2239-9; grant 19/2551-0001974-2) for the financial support given to this research. This study was financed in part by the Coordenação de Aperfeiçoamento de Pessoal de Nível Superior – Brasil (CAPES) – Finance code 001.

REFERENCES

[1] R.D.C. Balboni, G.K. Maron, M.G. Masteghin, M.O. Tas, L.S. Rodrigues, V. Gehrke, J.H. Alano, R. Andreazza, N.L. V Carreño, S.R.P. Silva, An easy to assemble PDMS/CNTs/PANI flexible supercapacitor with high energy-to-power density, Nanoscale. (2022).

[2] N. DeForest, A. Shehabi, S. Selkowitz, D.J. Milliron, A comparative energy analysis of three electrochromic glazing technologies in commercial and residential buildings, Appl. Energy. 192 (2017) 95–109.

[3] C.F. Azevedo, R.D.C. Balboni, C.M. Cholant, E.A. Moura, R.M.J. Lemos, A. Pawlicka, A. Gündel, W.H. Flores, M. Pereira, C.O. Avellaneda, New thin films of NiO doped with V<inf>2</inf>O<inf>5</inf> for electrochromic applications, J. Phys. Chem. Solids. 110 (2017). https://doi.org/10.1016/j.jpcs.2017.05.021.

[4] H. Omrany, A.K. Marsono, Optimization of building energy performance through passive design strategies, Br. J. Appl. Sci. Technol. 13 (2016) 1–16.

[5] R.D.C. Balboni, C.M. Cholant, L.U. Krüger, E.A. Moura, G.K. Maron, W.H. Flores, A. Gündel, D.A. Gatto, A. Pawlicka, C.A.O. Avellaneda, Influence of weathering and temperature on the electrochemical and microscopical characteristics of CeO2 and CeO2: V2O5 sol-gel thin films, Mater. Res. Bull. 142 (2021) 111432.

[6] H. Zhu, L. Wang, Smart window based on Cu7S4/hydrogel composites with fast photothermal response, Sol. Energy Mater. Sol. Cells. 202 (2019) 110109.

[7] E.A. Moura, C.M. Cholant, R.D.C. Balboni, T.M. Westphal, R.M.J. Lemos, C.F. Azevedo, A. Gündel, W.H. Flores, J.A. Gomez, F. Ely, A. Pawlicka, C.O. Avellaneda, Electrochemical properties of thin films of V <inf>2</inf> O <inf>5</inf> doped with TiO <inf>2</inf>, J. Phys. Chem. Solids. 119 (2018). https://doi.org/10.1016/j.jpcs.2018.03.023.

[8] F. Chen, Y. Ren, J. Guo, F. Yan, Thermo-and electro-dual responsive poly (ionic liquid) electrolyte based smart windows, Chem. Commun. 53 (2017) 1595–1598.

[9] C.M. Cholant, M.P. Rodrigues, L.L. Peres, R.D.C. Balboni, L.U. Krüger, D.N. Placido, W.H. Flores, A. Gündel, A. Pawlicka, C.O. Avellaneda, Study of the conductivity of solid polymeric electrolyte based on PVA/GA blend with addition of acetic acid, J. Solid State Electrochem. 24 (2020) 1867–1875.

[10] A.M.C. Senevirathne, V.A. Seneviratne, O.A. Ileperuma, Use of fumed silica nanoparticles to attain polymer free novel quasi-solid state electrolyte for high-efficiency dye-sensitized solar cells, Sol. Energy. 159 (2018) 531–537.

[11] C.M. Cholant, L.U. Krüger, R.D.C. Balboni, M.P. Rodrigues, F.C. Tavares, L.L. Peres, W.H. Flores, A. Gündel, A. Pawlicka, C.O. Avellaneda, Synthesis and characterization of solid polymer electrolyte based on poly(vinyl alcohol)/gum Arabic/LiClO<inf>4</inf>, Ionics (Kiel). 26 (2020). https://doi.org/10.1007/s11581-

019-03433-3.

[12] H. Manjunatha, R. Damle, K. Pravin, G.N. Kumaraswamy, Modification in the transport and morphological properties of solid polymer electrolyte system by low-energy ion irradiation, Ionics (Kiel). 24 (2018) 3027–3037.

[13] P. Utpalla, S.K. Sharma, K. Sudarshan, M. Sahu, P.K. Pujari, Investigation of the free volume characteristics of PEO based solid state polymer electrolyte by means of positron annihilation spectroscopy, Solid State Ionics. 339 (2019) 114990.

[14] A. Arya, A.L. Sharma, Polymer electrolytes for lithium ion batteries: a critical study, Ionics (Kiel). 23 (2017) 497–540.

[15] A. Shahi, E. Arunan, Hydrogen bonding, halogen bonding and lithium bonding: an atoms in molecules and natural bond orbital perspective towards conservation of total bond order, inter-and intra-molecular bonding, Phys. Chem. Chem. Phys. 16 (2014) 22935–22952.

[16] A. Poosapati, K. Negrete, N. Jang, L. Hu, Y. Lan, D. Madan, Wood cellulose-based thin gel electrolyte with enhanced ionic conductivity, MRS Commun. 9 (2019) 1015–1021.

[17] J. Smiatek, A. Heuer, M. Winter, Properties of ion complexes and their impact on charge transport in organic solvent-based electrolyte solutions for lithium batteries: insights from a theoretical perspective, Batteries. 4 (2018) 62.

[18] U. Ali, K.J.B.A. Karim, N.A. Buang, A review of the properties and applications of poly (methyl methacrylate)(PMMA), Polym. Rev. 55 (2015) 678–705.

[19] N. Balakrishnan, J.D. Joyner, N.S. Jishnu, A. Das, M.J. Jabeen Fatima, R. Prasanth, Electrospun polyacrylonitrile (PAN)-based polymer gel electrolytes for lithium-ion batteries, in: Electrospinning Adv. Energy Storage Appl., Springer, 2021: pp. 121–152.

[20] M.C. Upadhye, M.C. Kuchekar, R.R. Pujari, N.U. Sable, Biopolymers: A comprehensive review, (2022).

[21] A. Detsi, E. Kavetsou, I. Kostopoulou, I. Pitterou, A.R.N. Pontillo, A. Tzani, P. Christodoulou, A. Siliachli, P. Zoumpoulakis, Nanosystems for the encapsulation of natural products: The case of chitosan biopolymer as a matrix, Pharmaceutics. 12

(2020) 669.

[22] O. Germershaus, T. Lühmann, J.-C. Rybak, J. Ritzer, L. Meinel, Application of natural and semi-synthetic polymers for the delivery of sensitive drugs, Int. Mater. Rev. 60 (2015) 101–131.

[23] A. Sharma, S. Nagarkar, S. Thakre, G. Kumaraswamy, Structure–property relations in regenerated cellulose fibers: comparison of fibers manufactured using viscose and lyocell processes, Cellulose. 26 (2019) 3655–3669.

[24] D.T. Reis, I.H.S. Ribeiro, D.H. Pereira, DFT study of the application of polymers cellulose and cellulose acetate for adsorption of metal ions (Cd2+, Cu2+ and Cr3+) potentially toxic, Polym. Bull. 77 (2020) 3443–3456.

[25] E. Akbarzadeh, A. Shockravi, V. Vatanpour, High performance compatible thiazole-based polymeric blend cellulose acetate membrane as selective CO2 absorbent and molecular sieve, Carbohydr. Polym. 252 (2021) 117215.

[26] R.D. Knuth, F.A. Knuth, G.K. Maron, R.D.C. Balboni, M.L. Moreira, C.W. Raubach, P.L.G. Jardim, N.L. V Carreno, C.O. Avellaneda, E.C. Moreira, Development of xanthan gum-based solid polymer electrolytes with addition of expanded graphite nanosheets, J. Appl. Polym. Sci. (n.d.) 52400.

[27] F.C. Tavares, D.S. Dörr, A. Pawlicka, C. Oropesa Avellaneda, Microbial origin xanthan gum-based solid polymer electrolytes, J. Appl. Polym. Sci. 135 (2018) 46229.

[28] J.R. Andrade, E. Raphael, A. Pawlicka, Plasticized pectin-based gel electrolytes, Electrochim. Acta. 54 (2009) 6479–6483.

[29] A. Ngamaroonchote, C. Chotsuwan, Performance and reliability of cellulose acetate-based gel electrolyte for electrochromic devices, J. Appl. Electrochem. 46 (2016) 575–582.

[30] I. Caldeira, A. Lüdtke, F. Tavares, C. Cholant, R. Balboni, W.H. Flores, A. Galio, A. Pawlicka, C.O. Avellaneda, Ecologically friendly xanthan gum-PVA matrix for solid polymeric electrolytes, Ionics (Kiel). 24 (2018). https://doi.org/10.1007/s11581-017-2223-6.

[31] A. Gunasekaran, A. Sorrentino, A.M. Asiri, S. Anandan, Guar gum-based polymer gel

electrolyte for dye-sensitized solar cell applications, Sol. Energy. 208 (2020) 160–165.

[32] S.B. Aziz, M.H. Hamsan, R.M. Abdullah, R.T. Abdulwahid, M.A. Brza, A.S. Marif, M.F.Z. Kadir, Protonic EDLC cell based on chitosan (CS): Methylcellulose (MC) solid polymer blend electrolytes, Ionics (Kiel). 26 (2020) 1829–1840.

[33] D. Lisbona, T. Snee, A review of hazards associated with primary lithium and lithium-ion batteries, Process Saf. Environ. Prot. 89 (2011) 434–442.

[34] K. Xu, Nonaqueous liquid electrolytes for lithium-based rechargeable batteries, Chem. Rev. 104 (2004) 4303–4418.

[35] J. Shi, Y. Yang, H. Shao, Co-polymerization and blending based PEO/PMMA/P(VDF-HFP) gel polymer electrolyte for rechargeable lithium metal batteries, J. Memb. Sci. 547 (2018) 1–10. https://doi.org/10.1016/j.memsci.2017.10.033.

[36] C. Chotsuwan, S. Boonrungsiman, U. Asawapirom, K. Jiramitmongkon, T. Jiemsakul, A. Ngamaroonchote, T. Rattanaamron, Highly viscous composite gel electrolyte based on cellulose acetate and nanoparticles, J. Electroanal. Chem. 828 (2018) 91–96. https://doi.org/10.1016/j.jelechem.2018.09.038.

[37] N.A. Johari, T.I.T. Kudin, A.M.M. Ali, M.Z.A. Yahya, Electrochemical studies of composite cellulose acetate-based polymer gel electrolytes for proton batteries, Proc. Natl. Acad. Sci. India Sect. A - Phys. Sci. 82 (2012) 49–52. https://doi.org/10.1007/s40010-012-0005-0.

[38] C.M. Cholant, M.P. Rodrigues, R.D.C. Balboni, L.U. Krüger, R.M.J. Lemos, D.F. Lopes, A. Pawlicka, C.O. Avellaneda, Study of the effect of LiClO4 concentration on the ionic transport of solid polymer electrolyte based on poly (vinyl alcohol)/gum Arabic, Ionics (Kiel). (2022) 1–15.

[39] S. Monisha, S. Selvasekarapandian, T. Mathavan, A. Milton Franklin Benial, S. Manoharan, S. Karthikeyan, Preparation and characterization of biopolymer electrolyte based on cellulose acetate for potential applications in energy storage devices, J. Mater. Sci. Mater. Electron. 27 (2016) 9314–9324. https://doi.org/10.1007/s10854-016-4971-x.

[40] S. Borah, M. Deka, Effect of silica nanofiber dispersion on electrochemical properties

of cellulose acetate composite gel electrolytes, Mater. Chem. Phys. 252 (2020) 123218. https://doi.org/10.1016/j.matchemphys.2020.123218.

[41] S. Ramesh, R. Shanti, E. Morris, Characterization of conducting cellulose acetate based polymer electrolytes doped with “green” ionic mixture, Carbohydr. Polym. 91 (2013) 14–21.

[42] P. Perumal, P.C. Selvin, S. Selvasekarapandian, P. Sivaraj, K.P. Abhilash, V. Moniha, R.M. Devi, Plasticizer incorporated, novel eco-friendly bio-polymer based solid bio-membrane for electrochemical clean energy applications, Polym. Degrad. Stab. 159 (2019) 43–53.

[43] L. Sampathkumar, P. Christopher Selvin, S. Selvasekarapandian, P. Perumal, R. Chitra, M. Muthukrishnan, Synthesis and characterization of biopolymer electrolyte based on tamarind seed polysaccharide, lithium perchlorate and ethylene carbonate for electrochemical applications, Ionics (Kiel). 25 (2019) 1067–1082. https://doi.org/10.1007/s11581-019-02857-1.

[44] M. Liu, S. Zhang, G. Li, C. Wang, B. Li, M. Li, Y. Wang, H. Ming, Y. Wen, J. Qiu, J. Chen, P. Zhao, A cross-linked gel polymer electrolyte employing cellulose acetate matrix and layered boron nitride filler prepared via in situ thermal polymerization, J. Power Sources. 484 (2021) 229235. https://doi.org/10.1016/j.jpowsour.2020.229235.

[45] M. Mahalakshmi, S. Selvanayagam, S. Selvasekarapandian, V. Moniha, R. Manjuladevi, P. Sangeetha, Characterization of biopolymer electrolytes based on cellulose acetate with magnesium perchlorate (Mg(ClO4)2) for energy storage devices, J. Sci. Adv. Mater. Devices. 4 (2019) 276–284. https://doi.org/10.1016/j.jsamd.2019.04.006.

4.4 Artigo 4

O artigo intitulado “**An easy to assemble PDMS/CNTs/PANI flexible supercapacitor with high energy-to-power density**” é apresentado conforme publicado na Revista Nanoscale, ISSN: 2040-3364, classificação A1 na área de Materiais. O artigo é referente ao trabalho desenvolvido durante o período de Doutorado Sanduíche na University of Surrey.

Nanoscale

PAPER

View Article Online
View Journal

Cite this: DOI: 10.1039/d1nr06914d

An easy to assemble PDMS/CNTs/PANI flexible supercapacitor with high energy-to-power density†

Raphael D. C. Balboni,[a] Guilherme K. Maron,[a] Mateus G. Masteghin,[b] Mehmet O. Tas,[b] Lucas S. Rodrigues,[a] Veridiana Gehrke,[a] José H. Alano,[c] Robson Andreazza,[a] Neftali L. V. Carreño[a] and S. Ravi P. Silva *[b]

Received 19th October 2021,
Accepted 9th January 2022

DOI: 10.1039/d1nr06914d

rsc.li/nanoscale

The fabrication of a flexible supercapacitor with state-of-the-art performance is described, based on a facile and low-cost fabrication method that encompasses aligned carbon nanotube arrays (ACNTA)-polyaniline/polydimethylsiloxane electrodes (ACNTA-PANI/PDMS). The ACNTA were partially embedded in PDMS to ensure excellent adhesion and integration whilst PANI was electrodeposited on its surface to improve energy storage properties. The supercapacitor structure and morphology were investigated by Raman spectroscopy and scanning electron microscopy (SEM), respectively. The energy storage properties of the electrodes were evaluated in two and three-electrode configurations. The maximum value of specific capacitance was 408 mF cm^{-2} (265 F g^{-1}) at 1 mA cm^{-2}, and a high energy density of 20 μW h cm^{-2} (25.5 W h kg^{-1}) was achieved at a power density of 100 μW cm^{-2} (126.6 W kg^{-1}) for a symmetric two-electrode device. The device showed a good capacitance retention of 76% after 5000 cycles and was able to maintain 80% of its electrochemical properties while being measured at different bending angles, demonstrating excellent mechanical agility performance under extreme conditions and some of the highest carbon-based energy storage properties.

Introduction

Humankind's future depends on carbon footprint reduction by means of technological development, and at the forefront are green and environmentally friendly energy storage devices.[1] Besides, with the growing use of wearable devices there is an inevitable need for flexible, lightweight and miniaturized electrochemical energy devices, *e.g.*, lithium batteries and supercapacitors (SC).[2–7] SCs have a high power density and a long-life cyclability,[8,9] unlike batteries that involve phase changes and redox reactions with metallic ions – leading to a slow diffusion process and consequently low power density – as a result of the charge/discharge process. SC devices also exhibit fast charge–discharge capability, lightweight, safer operability and low cost,[10–12] turning them into an optimal choice when high- and rapid-cycling power is required.[13,14]

Supercapacitors usually operate in two basic modes: electrochemical double-layer capacitance (EDLC) and pseudocapacitance (PC).[12,15–18] EDLCs operate based on the electrostatic effect resulting from the charge separation occurring at the interface of the electrode surface and the electrolyte ions,[9,11,16,19] which mainly depends on the surface area of the electrodes and the electrolyte properties.[9,11,12] On the other hand, PC response to reversible redox reactions causes charge accumulation that involves the entire active material and leads to a high capacitance and energy density.[9,17,19]

Electrodes themselves are fundamental components of supercapacitors and are usually composed of either metal nitrides for their excellent electrical conductivity,[20–22] inorganic perovskite oxides and spinel ferrites due to their high energy density,[23] transition metal sulphides for presenting high ionic conductivity,[24] or carbon-based materials, such as carbon nanotubes (CNTs) due to their outstanding chemical and mechanical stability and often used as a conducting base/substrate for further electropolymerization.[25]

Therefore, the combination of PC materials with carbon nanotubes (CNTs)[25] and graphene[26] results in a material with

[a]Graduate Program in Materials Science and Engineering, Technology Development Center, Federal University of Pelotas, Pelotas, RS, 96010-000, Brazil
[b]Advanced Technology Institute, Department of Electrical and Electronic Engineering, University of Surrey, Guildford GU2 7XH, UK. E-mail: s.silva @surrey.ac.uk
[c]Graduate Program in Mechanical Engineering, School of Engineering, Federal University of Rio Grande, Rio Grande, RS, 96203-900, Brazil

† Electronic supplementary information (ESI) available. See DOI: 10.1039/d1nr06914d

an improved lifetime, fast charge/discharge, and high-power density.[9,12,16,17,27,28]

SCs that operate solely through the EDLC mechanism have some disadvantages such as limited specific capacitance and reduced energy storage capacity.[11,16] To overcome this, the incorporation of pseudocapacitive materials is frequently reported, including transition metal oxides and conductive polymers.[15,29,30] Accordingly, the use of low-cost and easily processable polyaniline (PANI) is developed as an interesting strategy due to its high electrochemical activity and high specific capacitance.[31,32] Furthermore, PANI possesses three different oxidation states (leucoemeraldine, emeraldine and pernigraniline) in which the valence change allows for energy storage, exhibiting specific anodic/cathodic peaks for each transition as observed during electrochemical analyses.[32,33] On the other hand, during continuous charge–discharge processes, PANI may suffer from volume expansion and degradation, resulting in low stability, which can be easily overcome by the incorporation of carbon-based materials.[34,35] Recent studies have shown the production of CNTs/PANI nanocomposites *via* a vacuum-assisted fabrication technique, chemical and electrochemical polymerization.[5,16] By combining polyaniline and carbon nanotubes, PANI incorporates into the open structure of the latter improving the electrolyte permeability throughout the device leading to an improved supercapacitor that stores charge *via* both EDLC and PC mechanisms.[17,32]

Several methods for the processing of CNTs for SC electrodes have been reported, *e.g.*, the deposition of a CNT dispersion on a hard substrate (current collector) through dip-coating,[36] spin-coating,[37] or drop-casting[38] to name a few. Flexibility can be achieved by mixing CNTs with a polymeric or elastomeric material. Mixing processes include infiltration of the polymer binder, mixture of nanoparticles in a polymeric matrix, or transfer of active CNTs grown on a rigid substrate to a flexible polymer substrate.[2,39] An ideal approach is the use of a green and cheap silicone-based elastomer such as the polydimethylsiloxane (PDMS). PDMS is a non-toxic polymeric organosilicon compound with good thermal and chemical stability in addition to its inherent ability to withstand high mechanical deformations.[2,40] Moreover, the easy processing and malleability allow stackings that favours the interaction between PANI and CNT, promoting a synergistic effect that leads to better stability.[41,42]

In this paper, a single deposition step and low-cost process is presented to produce environmentally friendly flexible supercapacitors, in which vertically aligned carbon nanotubes (VA-CNT) grown on Si/SiO_2 substrates through the photothermal chemical vapour deposition method (PTCVD) were transferred to a partially cured PDMS, later completing the curing and retaining CNT alignment but with added flexibility.[8,43] Then, PANI is electrodeposited on the top of EDLC elements to confer pseudocapacitive behaviour, resulting in electrodes of aligned carbon nanotubes-PANI/PDMS (ACNTA-PANI/PDMS) that delivered outstanding energy storage properties.

Results and discussion

Fig. 1a and b show top- and side-view SEM images of the as-grown VA-CNT on a Si wafer, respectively. The top-view image corresponds to a densely packed CNT "forest", while the side-view image shows an average height of 17 μm for the CNTs. The SEM image depicted in Fig. 1c was taken with an angle of 45° between the electron beam and the sample normal, allowing a more accurate measure of the CNT diameter, with which a relative frequency distribution over 300 CNTs was counted resulting in an average diameter of 14.0 nm ± 3.6 nm, as shown in Fig. 1d.

Fig. 2 shows the SEM image of the ACNTA/PDMS flexible material containing the CNTs transferred from the Si/SiO_2 wafer to the PDMS matrix. Bearing in mind the weight of the wafer applying a shear force during drop casting, it is expected that the VA-CNTs will in turn convert to horizontally aligned carbon nanotubes (HA-CNTs) as shown in the top-view SEM image of Fig. 2a. The cross-sectional SEM image shown in Fig. 2b displays two distinguished areas: a top region, showing the CNTs laying down after the casting process; and the bottom region still containing vertically aligned CNTs. The top interfacial region corresponds to the CNTs that were in contact with the Si/SiO_2 wafer and the VA-CNTs are in contact with the PDMS. The CNTs in contact with PDMS remained aligned due to densification caused by the PDMS that ascended into the CNTs by capillary forces, as highlighted in the inset of Fig. 2b, where features of the VA-CNTs can be seen embedded in the

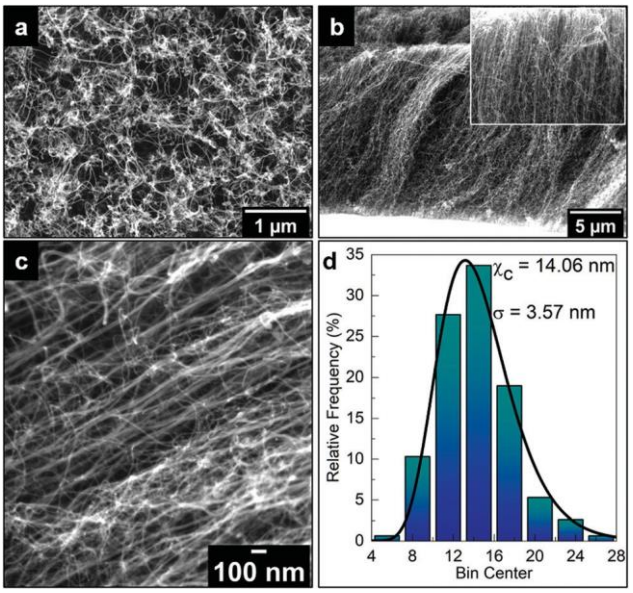

Fig. 1 Scanning electron microscopy (SEM) images of the as-grown vertically aligned carbon nanotubes (VA-CNT). (a) Top-view SEM image showing the tips of the CNT "forest". (b) Side-view SEM image of the VA-CNT showing a height of about to 17 μm. (c) 45° tilt of one of the SEM images used to measure the CNT diameter, whose relative frequency distribution is depicted in (d). (d) From the LogNormal fitting to the distribution, an average diameter of 14.0 nm ± 3.6 nm was obtained.

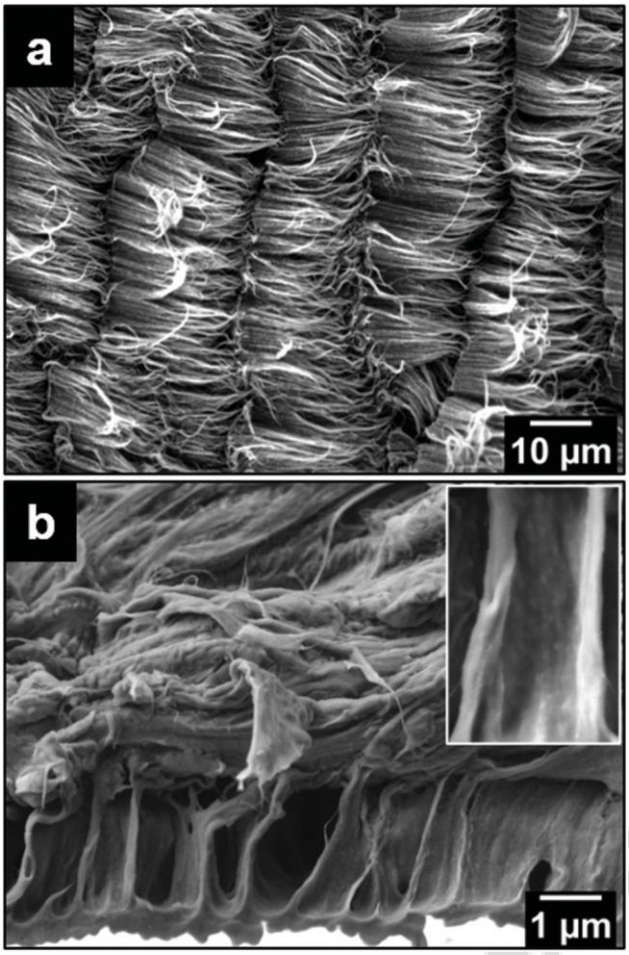

Fig. 2 (a) Top-view SEM image of the horizontally aligned carbon nanotubes (HA-CNTs) that were bent during the wafer drop casting process. (b) Cross-sectional SEM image of the **fl**exible electrode showing HA-CNTs on top of vertically aligned carbon nanotubes (VA-CNTs) densi**fi**ed when in contact with the polydimethylsiloxane (PDMS) matrix. PANI is a thin indistinguishable layer spread across the HA-CNTs/air interface.

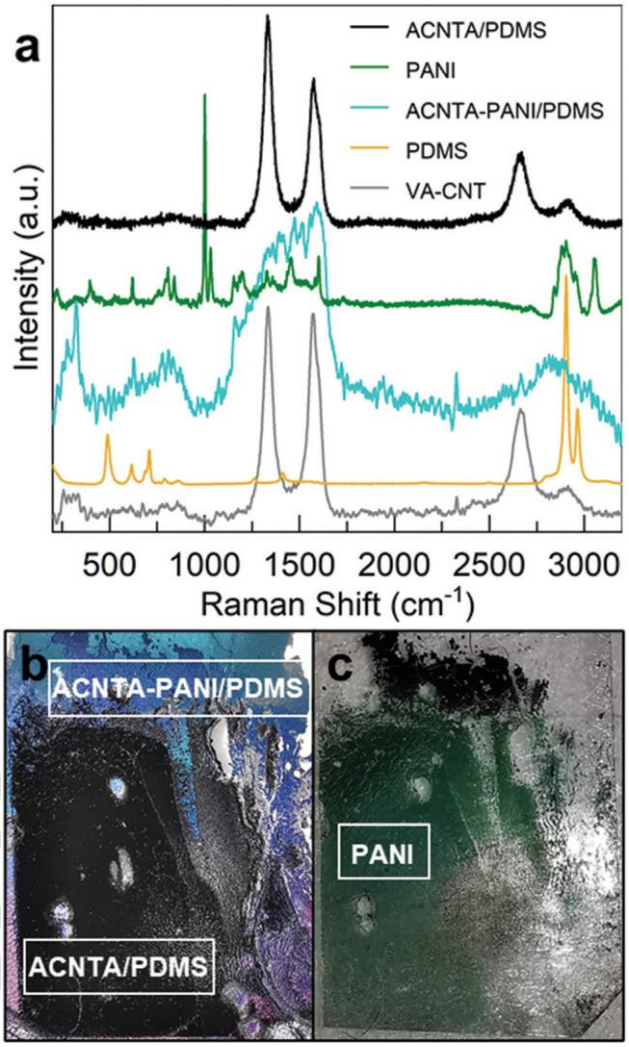

Fig. 3 (a) Raman spectra of the **fl**exible electrode (ACNTA-PANI/PDMS, represented in cyan), the horizontally aligned carbon nanotubes(HA-CNTs) underneath the PANI super**fi**cial layer (ACNTA/PDMS, black line), and the as-grown CNTs on the Si/SiO_2 wafer (CNT, in grey). The PANI and PDMS spectra were added as comparative purposes. (b) The ACNTA-PANI/PDMS label de**fi**nes the original electrode area, whilst the "ACNTA/PDMS" label identi**fi**es the HA-CNTs region underneath the PANI following the scotch-tape exfoliation. (c) PANI exfoliated from the electrode surface.

polymeric matrix (reference Fig. 1b). This effect should be very pronounced, considering both the high cross-sectional contact area and the sorptivity of CNTs.[44] The same densification should occur at a lower level in the HA-CNT region after PANI electrodeposition.

The structural evaluation of the flexible material was carried out in two steps. Firstly, the micro-Raman laser was focused on the PANI covered region of the sample (marked "ACNTA PANI/PDMS" in Fig. 3b), and next it irradiated the HA-CNTs that were underneath PANI (noted as "ACNTA/PDMS", black line, and shown in Fig. 3b). The HA-CNTs were exposed after a scotch-tape exfoliation of the superficial PANI layer, in which the latter is visible in the optical image of Fig. 3c. This approach was chosen since the overlapping Raman active peaks of PANI and the CNTs, alongside the low penetration depth of the 532 nm laser into the VA-CNTs, complicate the analysis of the peak convolution and mask the PDMS Raman active peaks from the electrode spectrum (cyan line in Fig. 3a). In addition, the strong presence of peaks related to the PANI and the lacking G′ band of the CNTs were a strong indication that electrodeposited PANI remained on the surface. The PANI Raman spectrum obtained from the material on the scotch-tape (green line) and the PDMS from the opposite surface (orange line) are presented in Fig. 3a as reference. The peaks attributed to the PANI nanostructures correspond to the out of plane ring deformation (about 410 cm^{-1}), ring deformation and silicon vibrations (520 cm^{-1}), quinonoid ring deformation (730 cm^{-1} and 763 cm^{-1}), benzenoid ring deformation (805 cm^{-1}), C–H deformation (960 cm^{-1}), in-plane bending of the C–H bonds in the semiqui-

nonoid ring (1165 cm^{-1}), stretching of the C–N (1330 cm^{-1}, 1350 cm^{-1}, 1375 cm^{-1}, and C**v**N at 1475 cm^{-1}), and N–H bending (1520 cm^{-1}).[45] Extra peaks in the PANI spectrum (green line) are from the Scotch-tape used in the exfoliation process. The typical peaks for cured PDMS are assigned to the aromatic C–H stretching (3000 cm^{-1}), CH_3 symmetric stretching (2890 cm^{-1}), Si–C symmetric stretching (710 cm^{-1}), and Si–O–Si stretching (622 cm^{-1} and 494 cm^{-1}).[46]

Raman spectroscopy is a well-known technique used to benchmark CNTs. The quality of the carbon nanotubes can be estimated based on the ratio between the D and G peaks, in which the D peak appears between 1330 and 1360 cm^{-1} and the G peak can be found at 1580 cm^{-1}, and hence the importance of having to exfoliate the PANI layer masking the peaks prior to this analysis. As shown in Fig. 3a, the as-grown VA-CNTs (grey line) presented an I_D/I_G ratio of 1.0 ± 0.4, while the I_D/I_G of the HA-CNTS underneath the PANI layer (black line) was 1.5 ± 0.3. A considerably higher D peak can be a consequence of defects, which as measured by Raman spectroscopy, is any contribution coming from lattice defects (substitution, inclusion, vacancies, or impurities) or amorphous carbon.[47] Therefore, we attribute the higher I_D/I_G ratio of the electrode to the amorphous carbon resulting from the electrodeposition of PANI or possibly to defects introduced during the bending of the CNTs during drop casting, such as kinks on the nanotubes' walls.

Contact angle measurements (refer to ESI, Fig. S1†) were performed to complement the conclusions drawn from the microscopy and spectroscopy studies. It is observed that the water droplet contact angle of 128.5° for the ACNTA-PANI/PDMS sample is higher than the value observed for ACNTA/PDMS and pure PDMS, being 125.74° and 90.55°, respectively. The lower contact angle measured for the pure PDMS was expected based on the possible hydrogen bonds occurring between water molecules and the oxygen atoms contained in the $(–SiO(CH_3)_2)_n$ monomer, and the higher value of the PDMS/CNTs is another indication that the diffusion of the PDMS was limited to the bottom half of the VA-CNTs (refer Fig. 1b). Following PANI electrodeposition, a slight and non-significant change of about 2% (within instrument experimental error)[48] in the contact angle occurred from 125.74° for the ACNTA/PDMS to 128.57° for ACNTA-PANI/PDMS, which can be explained by the PANI diffusion along the CNTs (refer Fig. 3b and c).[49,50]

Electrochemical results

The electrochemical performance of the ACNTA-PANI/PDMS electrodes was firstly investigated *via* cyclic voltammetry (CV) and galvanostatic charge/discharge (GCD) measurements with potentials ranging between −0.2 and 0.8 $V_{Ag/AgCl}$. The typical CV profiles measured in the three-electrode configuration are shown in Fig. 4a where two pairs of redox peaks were observed at approximately 0.32 V/−0.06 V and 0.55 V/0.4 V, attributed to leucoemeraldine/emeraldine and emeraldine/pernigraniline transition forms of PANI, respectively, revealing a strong pseudocapacitive behaviour. A reduction of the redox peaks whilst increasing the scan rate can be observed and related to the high-frequency charge diffusion through the inner active sites of the electrodes, minimising redox reactions during the charge and discharge processes.[10,51] Moreover, the oxidation peaks shifting positively at higher scan rates are indicative of kinetic limited systems.[52] GCD curves (Fig. 4b) exhibited a triangular profile with small deviations from linearity due to pseudocapacitive behaviour of PANI, and quicker charge/discharge with increasing applied current density is typical for SCs as a result of ready-to-transfer charge carriers between the active electrode and the electrolyte.[53,54] Fig. 4c and Fig. S2† further show the values of areal and gravimetric specific capacitances calculated from the discharge curves over current densities varying from 1 to 3 mA cm^{-2}. The values of gravimetric specific capacitances were calculated based on the mass of PANI electrodeposited on the surface of ACNTA/PDMS. The maximum values of areal and gravimetric specific capacitances were 408 mF cm^{-2} and 265 F g^{-1}, respectively, at a current density of 1 mA cm^{-2}. Such specific capacitance values are remarkable for flexible/wearable supercapacitors. A comparison of the electrochemical performance of ACNTA-PANI/PDMS measured in a three-electrode configuration with various similar materials reported in previous studies are listed in Table S1.†

To further explore the electrochemical properties of the ACNTA-PANI/PDMS electrodes as an energy storage device, a flexible symmetric two-electrode supercapacitor was fabricated (inset of Fig. 5d) and studied in an ionic liquid electrolyte. The CV curves of the ACNTA/PDMS and ACNTA-PANI/PDMS structure measured at scan rates varying between 5 and 50 mV s^{-1} in a potential range of 0–1 V are shown in Fig. S3a† and Fig. 5a, respectively. The ACNTA/PDMS device exhibited the typical rectangular shape regardless of the scan rates as expected from electrical double-layer capacitors. On the other hand, CV curves containing redox peaks from the multiple reduction and oxidation states of PANI points out the existence of a PC behaviour.[52,55] Furthermore, with the increase in the scan rate, the oxidation peaks shifted positively (in contrast to the anodic peaks) due to an increase in the internal resistance of the electrodes, deviating from the ideal shape of CV curves.[5,56] Additionally, the GCD curves of ACNTA/PDMS and ACNTA-PANI/PDMS at different current densities are shown in Fig. S3b† and Fig. 5b, respectively. Both devices displayed nearly symmetric triangular profiles, revealing high reversibility during charge/discharge processes. ACNTA/PANI presented an ideal linear profile of charge/discharge, evidencing the EDLC behaviour of the CNTs, while the ACNTA-PANI/PDMS sample showed a slight deviation in the triangular shape that confirms the presence of the already pointed-out pseudocapacitive behaviour combined with the EDLC mechanism.[5,19,55] Furthermore, Fig. 5c compares the CV curves of ACNTA/PDMS and ACNTA-PANI/PDMS devices at a scan rate of 5 mV s^{-1}. The CV area of ACNTA-PANI/PDMS is remarkably higher than that of ACNTA/PDMS and demonstrates a significant improvement in energy storage properties after PANI electropolymerization on the surface of ACNTAs. This is further confirmed, as shown in Fig. 5d comparing the GCD curves of both samples at a current density of 0.5 mA

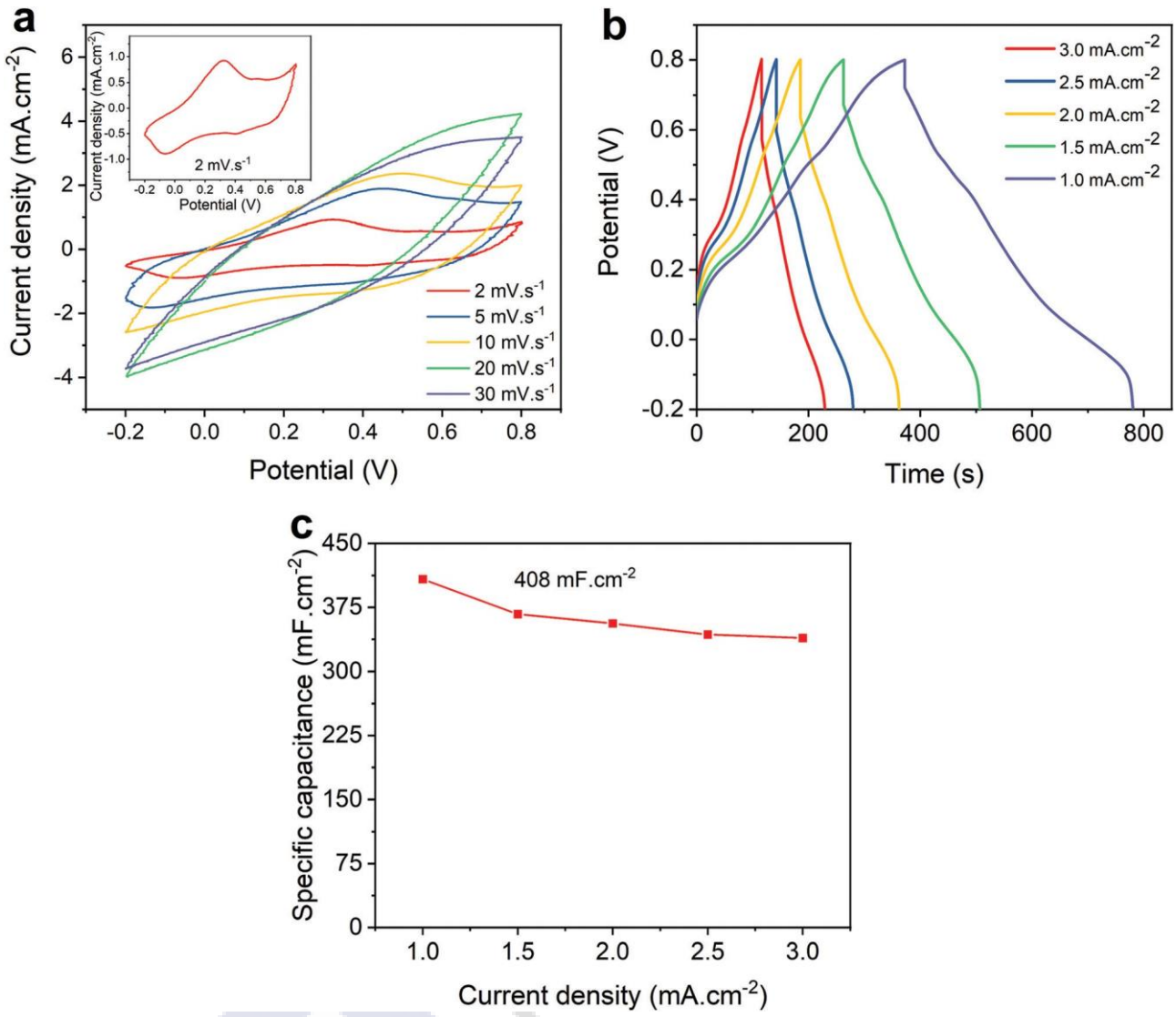

Fig. 4 Electrochemical performance of ACNTA-PANI/PDMS measured in a three-electrode configuration. (a) CV curves of the electrodes at different scan rates from 2 to 30 mV s^{-1}. The inset shows the CV curve at a scan rate of 2 mV s^{-1}. (b) GCD curves at different current densities varying from 1 to 3 mA cm^{-2}. (c) Areal specific capacitance calculated from GCD curves.

cm^{-2}, showing the larger charge/discharge time of ACNTA-PANI/PDMS at the same current density caused by higher specific capacitances obtained when PANI is present. This suggests that the presence of PANI directly electrodeposited on the surface of the aligned CNTs produces a composite that enhances the interfacial charge transfer through the electrodes and, therefore, improves the overall electrochemical performance.[51,57] The areal specific capacitances were calculated from the GDC measurements and plotted in Fig. 5e. ACNTA-PANI/PDMS delivered a maximum value of 40.6 mF cm^{-2} at 0.2 mA cm^{-2}, about 24 times higher than ACNTA/PDMS at the same current density. Once again we highligth the charge accumulation increase at the electrode/electrolyte interface due to PANI redox reactions and the synergetic effect between PANI and ACNTAs as numerous conductive pathways that allow fast ion diffusion through the electrodes.[54,55,58]

EIS measurements were further performed and Fig. 6a shows the Nyquist plot of ACNTA/PDMS and ACNTA-PANI/PDMS devices. The experimental data were adjusted to the equivalent circuit exhibited in the inset of Fig. 6a. The R_s denote the internal resistance of the electrodes, while the $C1$/$R1$ elements connected in parallel represents the electrochemical reaction impedance. The W denotes the Warburg impedance resulting from the frequency dependence of ionic diffusion through the electrode/electrolyte interface and $C2$ corresponds to the intercalation capacitance, which can be associated with the pseudocapacitance of the devices.[54,59] The parameters obtained from the equivalent electric circuit are described in detail in Table S2.† The real axis intercept values at high frequencies denote the internal resistance of the electrodes and the contact resistance between the electrodes and electrolyte (R_s).[53,60] The R_s values were 214.8 and 153.3 ohm

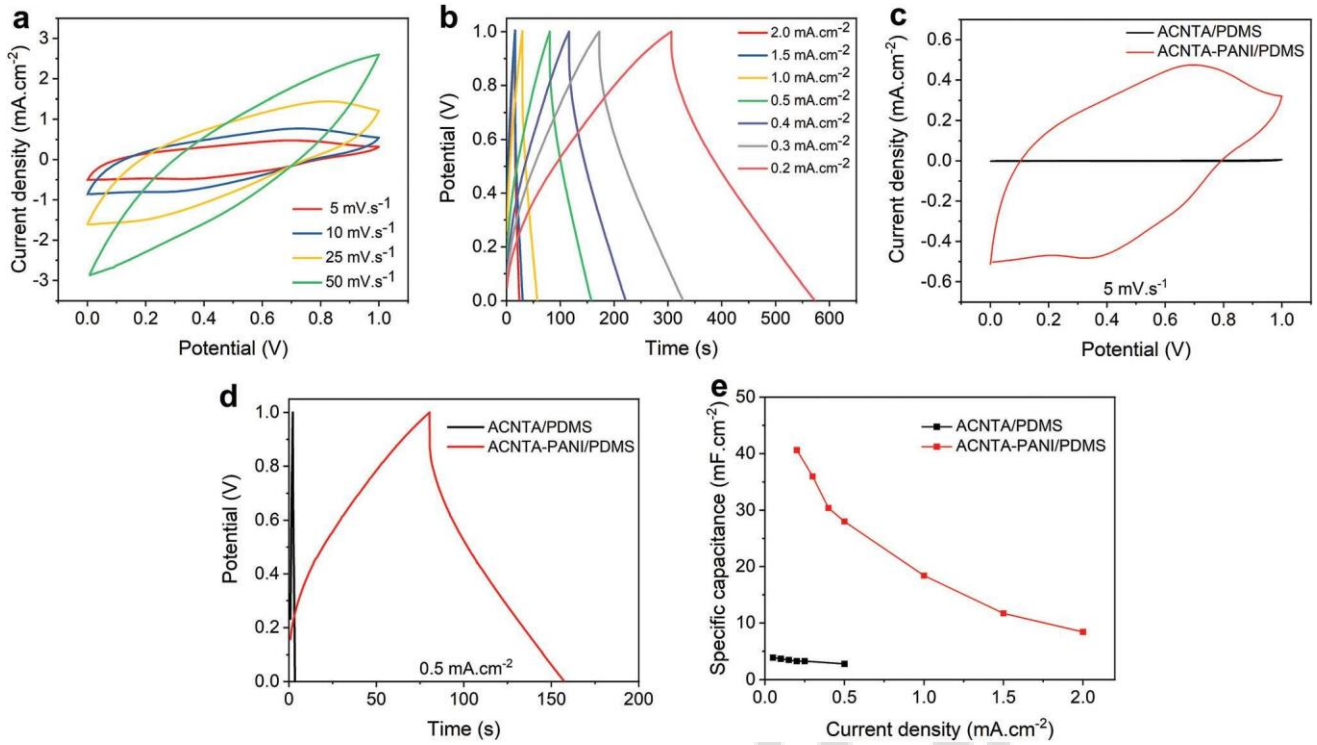

Fig. 5 Electrochemical performance of symmetric two-electrode supercapacitors. (a) CV curves of ACNTA-PANI/PDMS at scan rates varying between 5 and 50 mV s^{-1}. (b) GCD curves at different current densities. (c) CV curves of ACNTA/PDMS and ACNTA-PANI/PDMS at a scan rate of 5 mV s^{-1}. (d) GCD curves of ACNTA/PDMS and ACNTA-PANI/PDMS at 0.5 mA cm^{-2}. (e) Areal specific capacitances calculated for different current densities.

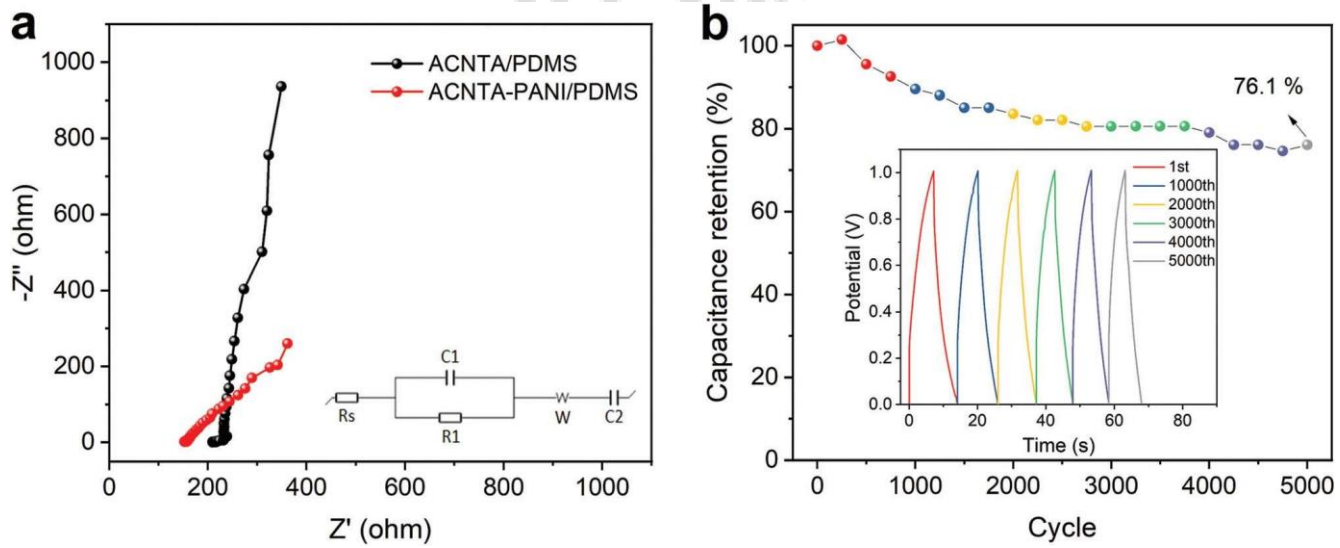

Fig. 6 Electrochemical performance of symmetric two-electrode supercapacitors. (a) EIS curve of ACNTA-PANI/PDMS at frequencies varying between 10^{-1} and 10^{5} Hz; the inset shows the equivalent circuit used for fitting the experimental data. (b) GCD stability of ACNTA-PANI/PDMS in a potential range between 0 and 1 V for 5000 cycles.

cm^{-2} for the ACNTA/PDMS and ACNTA-PANI/PDMS device, respectively, suggesting that PANI provided a good electrical network within the ACNTAs, which facilitated charge transfer through the electrodes, and consequently modified the R_s value. The $C1$ values were approximately the same for the two electrodes, 8.35 mF cm^{-2} for ACNTA-PANI/PDMS and 7.00 mF cm^{-2} for ACNTA/PDMS, indicating similar contribution of the double-layer capacitance for both samples. Furthermore, the ACNTA-PANI/PDMS electrode displayed a $R1$ value approximately 3 times smaller than ACNTA/PDMS (72.5 ohm cm^{-2}

and 209.7 ohm cm^{-2}, respectively), indicating a lower charge transfer resistance for the device containing PANI. Finally, the $C2$ values represents the contribution of the pseudocapacitance mechanism for each sample, reaching 1.04 mF cm^{-2} for ACNTA/PDMS and 20.23 mF cm^{-2} for ACNTA-PANI/PDMS, which is in good agreement with the previous results.

Long-term cycling stability (*i.e.*, capacitance retention) was evaluated after 5000 charge/discharge cycles of the ACNTA-PANI/PDMS device, as shown in Fig. 6b. The capacitance gradually increased during the first 250 cycles, suggesting an improvement of surface wettability and activation process of the electrodes.[51,61] After 5000 cycles, the capacitance retention was partially stabilized at 76.1%.

The working voltage of supercapacitors is an important parameter that controls their electrochemical properties and is directly related to the amount of energy that the device is capable of storing. Aiming to improve the energy density stored in our ACNTA-PANI/PDMS device, CV and GCD measurements were performed at a working potential of 2 V and different scan rates varying between 5 and 50 mV s^{-1}, as shown in the CV curves of Fig. 7a. The CV curves display characteristic prominent redox peaks during positive and negative sweeps, corroborating the existence of deeper reactions at wider potentials, which is a commonly reported behaviour.[62,63] Thus, a slight deviation in the CV shape is expected as the scan rate increases due to the increase in the current density. Accordingly, Fig. 7b displays the GCD profiles of the ACNTA-PANI/PDMS device at a working voltage of 2 V tested at different current densities. As observed in the CV measurements, the GCD results reveal the presence of a stronger PC behaviour of PANI appearing for wider potentials as evidenced by the distortions in the charge/discharge profiles.[5,52] A small voltage drop (*IR* drop) in the beginning of the discharge curves was noticed in all curves and attributted to the internal resistance of the electrodes. Moreover, the discharge curves exhibited two well pronounced stages with a fast linear discharge followed by a much longer discharge time as a characteristic of a PC mechanism.[2]

A Ragone plot containing the values of areal energy and power densities calculated from GCD measurements is plotted in Fig. 7c. Since the values of energy and power densities are proportional to the square of the voltage (see eqn (5) and (6) available in the ESI†), one should expect an increase in the quantity of energy stored with a broader voltage range. When measured at a potential range beetween 0 and 2 V, the ACNTA-PANI/PDMS device delivered a maximum specific

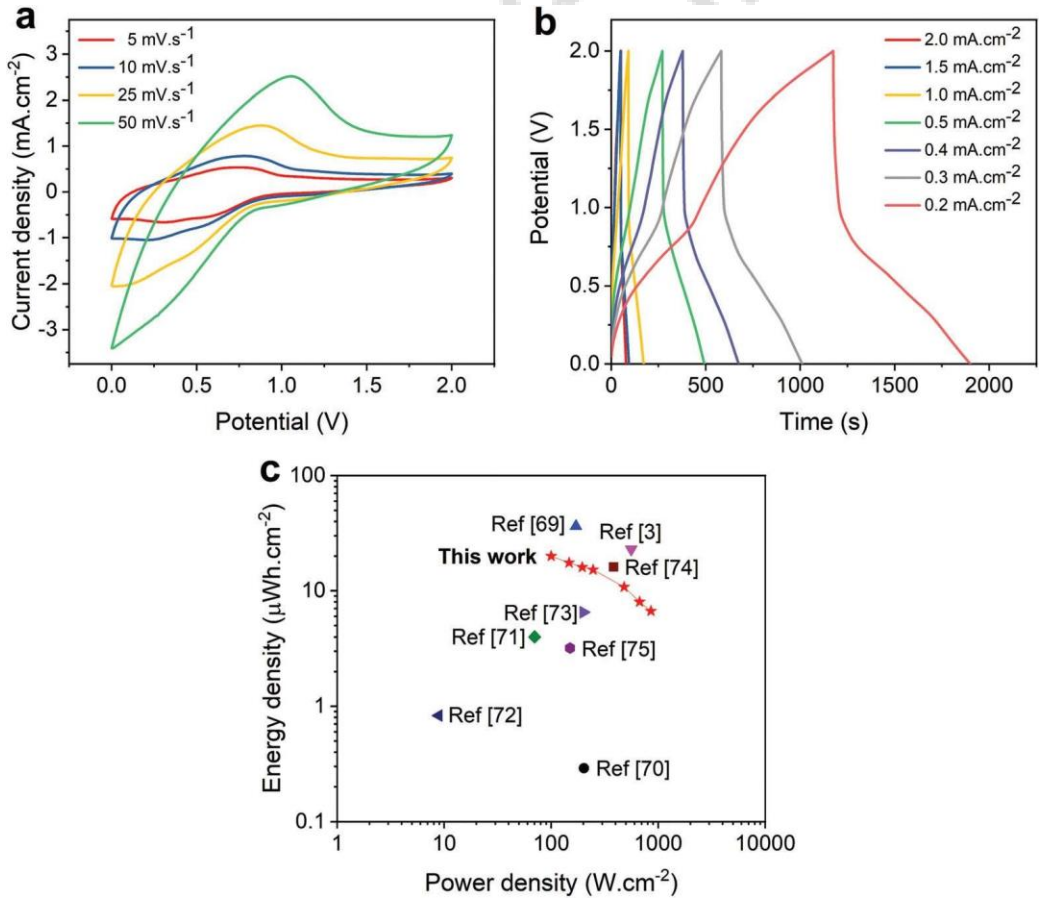

Fig. 7 Electrochemical properties of ACNTA-PANI/PDMS over different potential ranges varying from 0 to 2 V. (a) CV curves at different scan rates. (b) GCD curves at different current densities. (c) Ragone plot comparing the values of areal energy and power density of this work with similar flexible supercapacitors described in the literature.[3,69–75]

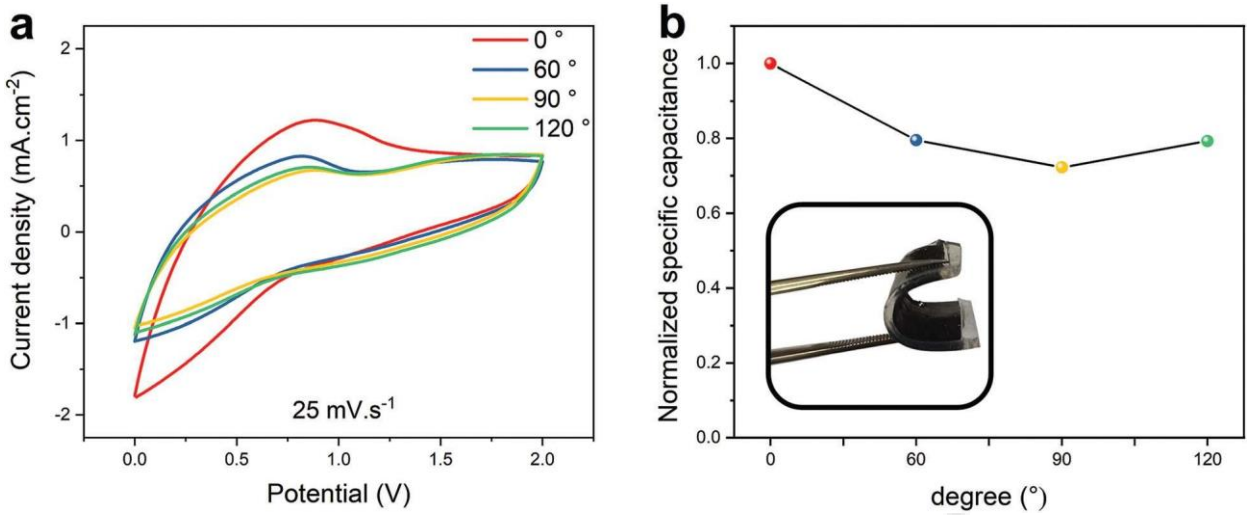

Fig. 8 Performance of the ACNTA-PANI/PDMS device under different bending angles. (a) CV curves at 25 mV s^{-1}. (b) Normalized specific capacitance calculated from the CV curves over the bent angle. The inset illustrates the flexibility of the devices under different angles.

energy density of 20 μW h cm^{-2} at a power density of 100 μW cm^{-2} but maintained an energy density of 6.7 μW h cm^{-2} when the power density increased to 856 μW cm^{-2}, revealing an excellent performance, as confirmed by the comparison with other flexible SCs (Fig. 7c). Thus, the gravimetric energy and power densities calculated based on the PANI mass are shown in the Ragone plot displayed in Fig. S4.† A high energy density of 25.5 W h kg^{-1} was obtained at a power density of 126.6 W kg^{-1}, maintaining 8.3 W h kg^{-1} when the power density increased to 1071 W kg^{-1}. All these results suggest that the high number of active sites derived from the multiple oxidation states of PANI improved the amount of charges accumulated in the electrodes.[19,31,54,64]

The flexibility of the ACNTA-PANI/PDMS device was further investigated by comparing the electrochemical performance under different bending angles. Fig. 8a displays the CV curves at a scan rate of 25 mV s^{-1} under bending angles of 0°, 60°, 90° and 120°. The CV curves presented nearly similar profiles even when the bending angle increased up to 120°, revealing that the device preserves great capacitive behaviour when deformed. The normalized specific capacitances were calculated according to the CV curves as the bending angles increased from 0° to 120°, and the results are shown in Fig. 8b. A decrease in the values of capacitance with further increase in the bending angle was observed, but a retention of 80.4% when bent to 120° confirms the viability of using ACNTA/PDMS as a platform for stretchable energy storage devices.

Conclusions

This work described the fabrication of a high-performance flexible supercapacitor based on polyaniline-coated ACNTA/PDMS. Aligned CNTs were transferred from a Si wafer to a PDMS substrate, providing a densely compacted CNT "forest" and granting thermal and chemical stability in addition to great flexibility. PANI was directly electropolymerized on the surface of the aligned CNTs, which resulted in a structure with remarkable electrochemical properties. The abundant active sites and multiple oxidation states of PANI promoted a significant enhancement in the energy storage properties of the ACNTA-PANI/PDMS electrodes, which delivered a maximum areal specific capacitance of 408 mF cm^{-2} at 1 mA cm^{-2}. Moreover, the symmetric two-electrode flexible device displayed a high energy density of 20 μW h cm^{-2} (25.5 W h kg^{-1}) at a power density of 100 μW kg^{-1} (126.6 W kg^{-1}), which is among the best reported for flexible devices. Thus, the device can maintain 80.4% of its electrochemical properties when bent at 120°. Considering the significant findings of this study, the ACNTA-PANI/PDMS electrodes are a promising candidate for future flexible electronics, presenting outstanding achievements combined with facile and low-cost fabrication with few processing steps. A truly flexible technology which will bridge the requirements of energy and power for future IoT devices is demonstrated in this paper.

Experimental

Growth of vertically aligned carbon nanotubes

Carbon nanotubes (CNTs) were deposited *via* the photothermal chemical vapour deposition method (PTCVD), as described elsewhere.[43,65,66] In brief, the PTCVD system is a complementary metal–oxide–semiconductor (CMOS) compatible, low-temperature CNT growth method which employs an optical heat source to efficiently couple the high optical energy and focus it at the catalyst front only whilst the substrate is being water cooled continuously. This allows achieving up to 300 °C temperature gradients between the catalyst front and the substrate. CNT deposition was performed on a full 4-inch

silicon (Si) wafer with 300 nm native oxide (SiO_2). A 3 nm iron (Fe^0) catalyst layer was sputtered on top of a 10 nm aluminum (Al^0) co-catalyst interlayer to prevent the catalyst from coalescence and increase the CNT density. The PTCVD system was operated at around 400–420 °C substrate temperature, measured using a bulk pyrometer.[67] The Fe^0 catalyst was activated for 5 min under 100 sccm H_2, immediately followed by 5 min growth under 100 sccm H_2 and 25 sccm (acetylene) C_2H_2 at 5 torr chamber pressure. After 5 min, C_2H_2 supply was cut-off, hydrogen (H_2) was allowed to flowing into the chamber with the optical light on for an extra minute to avoid amorphous carbon built-up on the tip of the CNTs. The chamber was cooled down to room temperature and purged twice with nitrogen (N_2) before the substrates were removed.

Preparation of ACNTA-PANI/PDMS

A schematic illustration of the processes employed during electrode fabrication is shown in Fig. S5.† A solution was prepared by mixing the polydimethylsiloxane (PDMS) base and its curing agent (Dow Chemical Company) with a mass ratio of 10 : 1, and degassed under 10^{-2} mbar for 30 min to prevent bubble formation. After holding the PDMS at 70 °C for 3 h, the vertically aligned carbon nanotubes (VA-CNT) previously grown on the Si wafer was dropcast facing the partially cured PDMS. At the end of the curing process, the Si wafer was pulled, leaving behind the aligned CNTs (ACNTA) which were then attached to the PDMS, since the adhesion of ACNTA/PDMS is stronger than that of the VA-CNTs/Si wafer. Finally, ACNTA/PDMS was coated with a layer of polyaniline *via* electropolymerization. PANI was electropolymerized on the surface of ACNTA/PDMS through cyclic voltammetry (CV) in a three-electrode configuration, using ACNTA/PDMS as the working electrode, platinum as the counter electrode and Ag/AgCl (saturated with KCl) as the reference electrode. The electrode array was submerged in a solution containing 0.5 mol L^{-1} aniline (Dinâmica Química Contemporânea) and 0.5 mol L^{-1} H_2SO_4 (Êxodo Científica). The electropolymerization was initiated with one cycle in the potential range between 0 and 1.4 $V_{Ag/AgCl}$, followed by 10 cycles in the potential range between 0 and 0.8 $V_{Ag/AgCl}$, at a scan rate of 5 mV s^{-1}. Finally, the fabricated ACNTA-PANI/PDMS electrodes were rinsed with distilled water and left to dry for 12 h.

Characterisation

The morphology of the as-grown VA-CNTs, as well as the ACNTA-PANI/PDMS flexible electrodes was analysed using a scanning electron microscope (SEM), Tescan MIRA II. The VA-CNTs on the silicon/silicon dioxide (Si/SiO_2) wafer were inspected using a 0.20 nA electron beam operated at 30 keV, ensuring a spot size lower than 3.8 nm. The diameter of the CNTs were measured using the ImageJ software and its average diameter was obtained after a LogNormal fit to the relative frequency distribution. In order to verify the alignment of the aCNTs following the casting of the Si wafer on the mildly cured PDMS, the sample was cut with a N°11 scalpel blade and mounted on a 45° tilted stub. The stage tilt (up to 35°) allowed us to verify its cross-section region and also to obtain top-view SEM images, both using a 0.20 nA electron beam accelerated at 5 keV which results in a spot size of about 8 nm. The lower energy and the in-beam secondary electron detector allowed the prevention of charging in the PDMS and to obtain more details of the material surface, respectively.

Structural characterisation was carried out using micro-Raman spectroscopy, with a laser excitation of 532 nm. The 50× objective lens and the filter resulted in a spot size of 5 μm and a power below 10 mW μm^{-2}. The ratio between the D and G peaks intensity (I_D and I_G, respectively) benchmarked the quality of the VA-CNTs before and after being converted into a capacitor electrode, and the uncertainty related to the analysis was calculated based on $I_D/I_G \times \sqrt{1/I_D + 1/I_G}$.[68]

The D and G peak intensities were obtained *via* Lorentzian curve fittings. PDMS and polyaniline (PANI) were also characterised. The wettability of the materials was checked by contact angle measurements carried out under ambient conditions using an optical tensiometer, Theta Lite TL100, where a drop of distilled water (8 μL) was dropped onto the material surface whilst recording with a digital camera. The images were analysed using Oneattension software.

Electrochemical measurements

To evaluate the electrochemical performance of the electrodes, firstly tests in three-electrode configuration were performed in H_2SO_4 1 mol L^{-1} electrolyte, with ACNTA-PANI/PDMS as the working electrode, and Pt mesh and Ag/AgCl (KCl 3 mol L^{-1}) as the counter and reference electrodes, respectively. CV and GCD measurements were conducted in the potential range between −0.2 and 0.8 $V_{Ag/AgCl}$ at various scan rates and at different current densities, respectively. To further examine the ACNTA-PANI/PDMS material, a flexible two-electrode supercapacitor was fabricated and tested in an ionic liquid electrolyte (1-butyl 3-methyl imidazolium tetrafluoroborate [BMIM][BF_4]). The device was assembled by sandwiching two ACNTA-PANI/PDMS electrodes, using quantitative filter paper (JP40, average porosity of 25 μm) as a separator. An illustration of the supercapacitor assembly is shown in Fig. S6.† CV and GCD tests were performed in a working potential range between 0 and 1 V. Electrochemical impedance spectroscopy (EIS) was performed from 0.1 to 100 000 Hz, with an amplitude of 0.005 V referred to the open circuit potential. Long-term cycling stability was assessed according to GCD in a potential range between 0 and 1 V for 5000 cycles. Tests were also performed in a wider voltage range (0–2 V) to improve the energy density stored. Furthermore, CV tests varying the bending angle (0° to 120°) were also performed, as shown in Fig. S7.† The electrochemical tests were performed in a programmable sourcemeter (Keithley – 2651A), a potentiostat (Metrohm Autolab, PGSTAT302 N) and another potentiostat (IVIUM – Compactstat). For further information on how areal and gravimetric specific capacitances, energy, and power densities were calculated, refer to the supplementary material.

Author contributions

All authors contributed significantly to the manuscript, as described: R. D. C. B., G. K. M. and M. G. M. conceived the idea, elaborated the methodology, fabricated the materials, designed and performed the experiments and wrote the paper; M. O. T. elaborated the methodology, helped with the fabrication of materials and wrote the paper; L. S. R. and V. G. contributed to the project design, collected and analyzed the data; J. H. A. and R. A. supervised the project and performed data curation; N. L. V. C. and S. R. P. S. conceived the idea and supervised the project. All authors contributed to the discussion and revised the manuscript prior to submission.

Conflicts of interest

The authors declare no conflict of interest.

Acknowledgements

We acknowledge the funding support from the Coordenação de Aperfeiçoamento de Pessoal de Nível Superior (CAPES – finance code 001/process number print 88887.310585/2018-0), Fundação de Amparo à Pesquisa do Estado do Rio Grande do Sul (Fapergs/PqG 2017 17/2551-0001157-0), Conselho Nacional de Desenvolvimento Científico e Tecnológico (CNPq) and the University of Surrey acknowledges support from the Brazilian Government FAPESP BEPE and SPRINT Programme for conducting this work.

Notes and references

1 S. R. P. Silva, *Energy Environ. Mater.*, 2021, **4**, 497–499.
2 Y. Xiao, Y. Liu, F. Liu, P. Han and G. Qin, *J. Alloys Compd.*, 2020, **813**, 152089.
3 J. Ren, R. P. Ren and Y. K. Lv, *Chem. Eng. J.*, 2018, **349**, 111–118.
4 W. Wang, L. Lu, Y. Xie, X. Mei, Y. Tang, W. Wu and R. Liang, *Appl. Surf. Sci.*, 2020, **504**, 144487.
5 D. Liu, P. Du, W. Wei, H. Wang, Q. Wang and P. Liu, *Electrochim. Acta*, 2017, **233**, 201–209.
6 J. Yu, W. Lu, S. Pei, K. Gong, L. Wang, L. Meng, Y. Huang, J. P. Smith, K. S. Booksh, Q. Li, J. H. Byun, Y. Oh, Y. Yan and T. W. Chou, *ACS Nano*, 2016, **10**, 5204–5211.
7 X. Chen, H. Lin, P. Chen, G. Guan, J. Deng and H. Peng, *Adv. Mater.*, 2014, **26**, 4444–4449.
8 R. Zhang, J. Ding, C. Liu and E. H. Yang, *ACS Appl. Energy Mater.*, 2018, **1**, 2048–2055.
9 Q. Jiang, N. Kurra, M. Alhabeb, Y. Gogotsi and H. N. Alshareef, *Adv. Energy Mater.*, 2018, **8**, 1–10.
10 H. Luo, J. Dong, Y. Zhang, G. Li, R. Guo, G. Zuo, M. Ye, Z. Wang, Z. Yang and Y. Wan, *Chem. Eng. J.*, 2018, **334**, 1148–1158.
11 W. Chen, R. B. Rakhi and H. N. Alshareef, *J. Mater. Chem. A*, 2013, **1**, 3315–3324.
12 W. Fan, C. Zhang, W. W. Tjiu, K. P. Pramoda, C. He and T. Liu, *ACS Appl. Mater. Interfaces*, 2013, **5**, 3382–3391.
13 T. Lv, Y. Yao, N. Li and T. Chen, *Angew. Chem., Int. Ed.*, 2016, **55**, 9191–9195.
14 R. Zhang, J. Ding, C. Liu and E. H. Yang, *Advanced Materials: TechConnect Briefs 2017*, 2017, **1**, 44–47.
15 M. Saghafi, M. Mahmoodian, S. A. Hosseini, A. Abdollahi and S. Mohajerzadeh, *Electrochim. Acta*, 2018, **283**, 1450–1459.
16 S. Hussain, E. Kovacevic, R. Amade, J. Berndt, C. Pattyn, A. Dias, C. Boulmer-Leborgne, M. R. Ammar and E. Bertran-Serra, *Electrochim. Acta*, 2018, **268**, 218–225.
17 V. H. R. De Souza, M. M. Oliveira and A. J. G. Zarbin, *J. Power Sources*, 2014, **260**, 34–42.
18 G. K. Maron, J. H. Alano, B. da Silveira Noremberg, L. da Silva Rodrigues, V. Stolojan, S. R. P. Silva and N. L. V. Carreño, *J. Alloys Compd.*, 2020, **836**, 155408.
19 D. D. Potphode, P. Sivaraman, S. P. Mishra and M. Patri, *Electrochim. Acta*, 2015, **155**, 402–410.
20 M.-S. Balogun, W. Qiu, W. Wang, P. Fang, X. Lu and Y. Tong, *J. Mater. Chem. A*, 2015, **3**, 1364–1387.
21 R. Adalati, A. Kumar, M. Sharma, P. Tiwari and R. Chandra, *Appl. Phys. Lett.*, 2020, **117**, 123904.
22 R. Adalati, A. Kumar, Y. Kumar and R. Chandra, *Energy Technol.*, 2020, **8**, 2000466.
23 M. I. A. Abdel Maksoud, R. A. Fahim, A. E. Shalan, M. Abd Elkodous, S. O. Olojede, A. I. Osman, C. Farrell, H. Ala'a, A. S. Awed and A. H. Ashour, *Environ. Chem. Lett.*, 2020, 1–65.
24 S. Khalid, Y. Khan, E. Ahmed, S. Nawaz, N. R. Khalid and W. Ahmed, in *Emerging Nanotechnologies for Renewable Energy*, Elsevier, 2021, pp. 407–445.
25 S. Hussain, R. Amade and E. Bertran, *Mater. Chem. Phys.*, 2014, **148**, 914–922.
26 W. K. Chee, H. N. Lim, I. Harrison, K. F. Chong, Z. Zainal, C. H. Ng and N. M. Huang, *Electrochim. Acta*, 2015, **157**, 88–94.
27 S. J. Paul, I. Sharma, I. Elizabeth, B. Gahtori, R. Manikandan, S. S. Titus, P. Chandra and B. K. Gupta, *ACS Appl. Mater. Interfaces*, 2020, **12**, 16946–16958.
28 C. Lim, Y. Shin, S. Hong, S. Lee and D. H. Kim, *Adv. Mater. Interfaces*, 2020, **7**, 1–8.
29 M. Ramadan, A. M. Abdellah, S. G. Mohamed and N. K. Allam, *Sci. Rep.*, 2018, **8**, 1–8.
30 M. Li, M. F. El-Kady, J. Y. Hwang, M. D. Kowal, K. Marsh, H. Wang, Z. Zhao and R. B. Kaner, *Nano Res.*, 2018, **11**, 2836–2846.
31 S. Y. Lee, J. Il Kim and S. J. Park, *Energy*, 2014, **78**, 298–303.
32 S. B. Yoon, E. H. Yoon and K. B. Kim, *J. Power Sources*, 2011, **196**, 10791–10797.
33 V. Mottaghitalab, B. Xi, G. M. Spinks and G. G. Wallace, *Synth. Met.*, 2006, **156**, 796–803.
34 S. R. Mangisetti, M. Kamaraj and S. Ramaprabhu, *Electrochim. Acta*, 2019, **305**, 264–277.
35 A. M. White and R. C. T. Slade, *Electrochim. Acta*, 2004, **49**, 861–865.

36 H. Zhang, Y. Liu, C. Yang, L. Xiang, Y. Hu and L. Peng, *Adv. Mater.*, 2018, **30**, 1805408.
37 D. Janas and K. K. Koziol, *Nanoscale*, 2014, **6**, 3037–3045.
38 E. J. Park, K.-D. Kim, H. S. Yoon, M.-G. Jeong, D. H. Kim, D. C. Lim, Y. H. Kim and Y. D. Kim, *RSC Adv.*, 2014, **4**, 30368–30374.
39 C. Choi, M. K. Choi, S. Liu, M. S. Kim, O. K. Park, C. Im, J. Kim, X. Qin, G. J. Lee, K. W. Cho, M. Kim, E. Joh, J. Lee, D. Son, S. H. Kwon, N. L. Jeon, Y. M. Song, N. Lu and D. H. Kim, *Nat. Commun.*, 2017, **8(1)**, **DOI: 10.1038/s41467-017-01824-6**.
40 M. Amjadi, K. U. Kyung, I. Park and M. Sitti, *Adv. Funct. Mater.*, 2016, **26**, 1678–1698.
41 M. Xue, F. Li, J. Zhu, H. Song, M. Zhang and T. Cao, *Adv. Funct. Mater.*, 2012, **22**, 1284–1290.
42 A. Khosrozadeh, G. Singh, Q. Wang, G. Luo and M. Xing, *J. Mater. Chem. A*, 2018, **6**, 21064–21077.
43 M. O. Tas, M. A. Baker, M. G. Masteghin, J. Bentz, K. Boxshall and V. Stolojan, *ACS Appl. Mater. Interfaces*, 2019, **11**, 39560–39573.
44 D. Łukawski, F. Lisiecki and A. Dudkowiak, *Fibers Polym.*, 2018, **19**, 524–530.
45 M. Trchová, Z. Morávková, M. Bláha and J. Stejskal, *Electrochim. Acta*, 2014, **122**, 28–38.
46 D. Cai, A. Neyer, R. Kuckuk and H. M. Heise, *J. Mol. Struct.*, 2010, **976**, 274–281.
47 K. Sato, R. Saito, Y. Oyama, J. Jiang, L. G. Cancado, M. A. Pimenta, A. Jorio, G. G. Samsonidze, G. Dresselhaus and M. S. Dresselhaus, *Chem. Phys. Lett.*, 2006, **427**, 117–121.
48 S. Chen, Y. Chen, X. Liu, S. Shen and X. Wang, *Int. J. Energy Clean Environ.*, 2018, **19**, 105–117.
49 J. Bae, Y. Hwang, S. J. Park, J.-H. Ha, H. J. Kim, A. Jang, J. An, C.-S. Lee and S.-H. Park, *Polymers*, 2018, **10**, 951.
50 W. Zhai, Q. Xia, K. Zhou, X. Yue, M. Ren, G. Zheng, K. Dai, C. Liu and C. Shen, *Chem. Eng. J.*, 2019, **372**, 373–382.
51 Q. Liu, S. Jing, S. Wang, H. Zhuo, L. Zhong, X. Peng and R. Sun, *J. Mater. Chem. A*, 2016, **4**, 13352–13362.
52 A. Stott, M. O. Tas, E. Y. Matsubara, M. G. Masteghin, J. M. Rosolen, R. A. Sporea and S. R. P. Silva, *Energy Environ. Mater.*, 2020, **3**, 389–397.
53 V. Gehrke, G. K. Maron, L. da Silva Rodrigues, J. H. Alano, C. M. P. de Pereira, M. O. Orlandi and N. L. V. Carreño, *Mater. Today Commun.*, 2020, 101779.
54 G. Wu, P. Tan, D. Wang, Z. Li, L. Peng, Y. Hu, C. Wang, W. Zhu, S. Chen and W. Chen, *Sci. Rep.*, 2017, **7**, 1–8.
55 H. Lin, L. Li, J. Ren, Z. Cai, L. Qiu, Z. Yang and H. Peng, *Sci. Rep.*, 2013, **3**, 1–6.
56 L. Zhang, D. Huang, N. Hu, C. Yang, M. Li, H. Wei, Z. Yang, Y. Su and Y. Zhang, *J. Power Sources*, 2017, **342**, 1–8.
57 K. Jost, D. Stenger, C. R. Perez, J. K. McDonough, K. Lian, Y. Gogotsi and G. Dion, *Energy Environ. Sci.*, 2013, **6**, 2698–2705.
58 S. A. El-Khodary, G. M. El-Enany, M. El-Okr and M. Ibrahim, *Synth. Met.*, 2017, **233**, 41–51.
59 H. Wang, J. Lin and Z. X. Shen, *J. Sci.: Adv. Mater. Devices*, 2016, **1**, 225–255.
60 T. Chen, H. Peng, M. Durstock and L. Dai, *Sci. Rep.*, 2014, **4**, 1–7.
61 K. Wang, Q. Meng, Y. Zhang, Z. Wei and M. Miao, *Adv. Mater.*, 2013, **25**, 1494–1498.
62 M. Gao, X. Wu, H. Qiu, Q. Zhang, K. Huang, S. Feng, Y. Yang, T. Wang, B. Zhao and Z. Liu, *RSC Adv.*, 2018, **8**, 20661–20668.
63 S. Lehtimäki, A. Railanmaa, J. Keskinen, M. Kujala, S. Tuukkanen and D. Lupo, *Sci. Rep.*, 2017, **7**, 1–9.
64 M. Yu, Y. Zhang, Y. Zeng, M. S. Balogun, K. Mai, Z. Zhang, X. Lu and Y. Tong, *Adv. Mater.*, 2014, **26**, 4724–4729.
65 M. Ahmad, J. V. Anguita, V. Stolojan, T. Corless, J. Chen, J. D. Carey and S. R. P. Silva, *Adv. Funct. Mater.*, 2015, **25**, 4419–4429.
66 J.-S. Chen, V. Stolojan and S. R. P. Silva, *Carbon*, 2015, **84**, 409–418.
67 M. O. Tas, M. A. Baker, V. Musaramthota, H. Uppal, M. G. Masteghin, J. Bentz, K. Boxshall and V. Stolojan, *Carbon*, 2019, **150**, 117–127.
68 M. G. Masteghin, M. Ahmad, M. O. Tas, C. T. G. Smith, V. Stolojan, D. C. Cox and S. R. P. Silva, *Appl. Phys. Lett.*, 2020, **116**, 103101.
69 X. Liang, L. Zhao, Q. Wang, Y. Ma and D. Zhang, *Nanoscale*, 2018, **10**, 22329–22334.
70 P. Avasthi, A. Kumar and V. Balakrishnan, *ACS Appl. Nano Mater.*, 2019, **2**, 1484–1495.
71 L. Li, Z. Lou, W. Han, D. Chen, K. Jiang and G. Shen, *Adv. Mater. Technol.*, 2017, **2(3)**, 1600282.
72 Y. Zhu, N. Li, T. Lv, Y. Yao, H. Peng, J. Shi, S. Cao and T. Chen, *J. Mater. Chem. A*, 2018, **6**, 941–947.
73 H. Park, C. Song, S. W. Jin, H. Lee, K. Keum, Y. H. Lee, G. Lee, Y. R. Jeong and J. S. Ha, *Nano Energy*, 2021, **83**, 105837.
74 V. K. A. Muniraj, R. Boukherroub and M. V. Shelke, *ACS Sustainable Chem. Eng.*, 2020, **8**, 6433–6441.
75 A. P. M. Udayan, O. Sadak and S. Gunasekaran, *ACS Appl. Energy Mater.*, 2020, **3**, 12368–12377.

5 Conclusões

Neste trabalho foram desenvolvidos, estudados e caracterizados filmes finos de CeO_2 e CeO_2:V_2O_5 para utilização como contra eletrodo e eletrólitos géis poliméricos à base de acetato de celulose, ambos com potencial aplicação em dispositivos eletrocrômicos.

Na primeira parte do trabalho, foram produzidos filmes finos de CeO_2 e de CeO_2 dopados com V_2O_5, preparados pelo processo sol gel e depositados através da técnica de spin coating. Para tal, foi utilizada uma metodologia já estabelecida na literatura, bem como os parâmetros de concentração e proporção dos materiais - filmes de CeO_2 com 3 camadas de deposição e filmes de CeO_2:V_2O_5 com 15% mol de dopagem de V_2O_5 e 5 camadas de deposição.

Foi estudada a influência da temperatura nas propriedades eletroquímicas dos filmes, com variação entre 20 e 80 °C, com salto de 10 °C. Pela técnica de voltametria cíclica, foi possível observar um aumento da área do voltamograma, além de um deslocamento dos picos, conforme a temperatura foi aumentada. Através da cronoamperometria/cronocoulometria foi observada uma diminuição no tempo de resposta, entretanto, a capacidade de inserir íons na camada do material melhorou, subindo de 10 para 12 $mC.cm^{-2}$ e 12 para 40 $mC.cm^{-2}$, para os filmes de CeO_2e CeO_2:V_2O_5 respectivamente, com 60 segundos de aplicação do potencial. Através da técnica de espectroscopia de impedância eletroquímica, foi registrada uma diminuição da resistência, favorecendo assim a condutividade iônica.

Para o estudo da influência do intemperismo, os filmes foram submetidos à uma câmara de intemperismo acelerado durante o período total de 75 dias, período equivalente a 900 dias (2,5 anos) de exposição ao ambiente externo. A cada período pré-estabelecido de tempo (intervalos de 15 dias, equivalentes a 180, 360, 720 e 900 dias), as amostras foram retiradas e submetidas à novas análises eletroquímicas, a fim de acompanhar a influência ao longo do período total equivalente a 2,5 anos. Ao final deste período, foram realizadas também novas análises morfológicas e estruturais, objetivando analisar possíveis variações ocorridas nos filmes.

Através dos perfis obtidos pela voltametria cíclica, ambos os filmes apresentaram picos anódicos e catódicos. Como esperado, o filme dopado apresentou uma maior área que o filme não dopado, e em ambos os casos, não houve mudanças significativas após os 900 dias de incubação. O filme dopado também apresentou um processo mais rápido de inserção, além de maior capacidade de inserção de carga, em todos os cenários testados. Entretanto, para ambos os filmes, o processo de intemperismo revelou uma queda na densidade de carga, mas ainda mantendo resultados promissores para a aplicação proposta. A curva Nyquist obtida através da técnica de impedância eletroquímica não mostrou diferença significativa, e a angulação próxima à 45° se manteve após os 900 dias, confirmando o processo de difusão de transporte de massa. Em relação à morfologia dos filmes após período de intemperismo, pelas técnicas de MFA e MEV foi observada uma maior degradação, maior porosidade e presença de rachaduras para o filme de CeO_2, enquanto o filme dopado apresentou uma superfície mais uniforme e lisa. A análise estrutural realizada através do DRX não apresentou mudanças na estrutura dos filmes.

Assim, a partir das análises realizadas, é possível afirmar que o material continua um promissor candidato à utilização como contra-eletrodo para aplicação em dispositivos eletrocrômicos mesmo após longos períodos de exposição ao intemperismo, uma vez que suas propriedades se mantiveram promissoras, característica muito importante e desejada para o tipo de material e aplicação proposta.

A segunda parte do trabalho se propôs a preparar e caracterizar eletrólitos géis poliméricos à base de acetato de celulose, com diferentes concentrações de $LiClO_4$, a fim de encontrar a melhor concentração e proporção entre os materiais, visando otimizar os resultados eletroquímicos do mesmo. O gel que apresentou melhores resultados foi o gel contendo 10% em massa de acetato de celulose e 1,4 M de $LiClO_4$. Na escolha do gel, levaram-se em conta também fatores como viscosidade e teor de sal adicionado, além do valor de condutividade.

As análises de impedância eletroquímica em função da temperatura mostraram que esta variação possui influência na condutividade do material de forma não linear. A voltametria cíclica realizada apresentou uma área com a forma esperada para todos os géis testados em todas as diferentes velocidades de varredura. O gel também apresentou uma excelente estabilidade ao apresentar um

pequeno decréscimo na área do voltamograma após 400 ciclos de análise, importante característica para a aplicação proposta de utilização como eletrólito.

A partir do espectro de transmitância obtido, obteve-se uma transparência próxima a 85% na região do visível, valor bastante satisfatório para utilização em dispositivos eletrocrômicos. O gel apresentou uma significativa perda de massa na faixa entre 150 e 250 °C, além de uma estrutura semicristalina, a partir das análises de termogravimetria e difração de raios-X.

É possível afirmar que o gel produzido contendo 10% em massa de acetato de celulose e 1,4 M de LiClO4 apresenta valores e propriedades importantes, sendo um promissor eletrólito a ser utilizado em dispositivos eletrocrômicos.

6 Referências

ABUSHAMMALA, H.; MAO, J. A review of the surface modification of cellulose and nanocellulose using aliphatic and aromatic mono-and di-isocyanates. **Molecules**, v. 24, n. 15, p. 2782, 2019.

AHMAD, M. M. Lithium ionic conduction and relaxation dynamics of spark plasma sintered Li5La3Ta2O12 garnet nanoceramics. **Nanoscale Research Letters**, v. 10, n. 1, p. 1-10, 2015.

AKBARZADEH, E.; SHOCKRAVI, A.; VATANPOUR, V. High performance compatible thiazole-based polymeric blend cellulose acetate membrane as selective CO2 absorbent and molecular sieve. **Carbohydrate Polymers**, v. 252, p. 117215, 2021.

ALVES, J. A. A.; DOS SANTOS, M. D. L.; MORAIS, C. C.; ASCHERI, J. L. R.; SIGNINI, R.; DOS SANTOS, D. M.; BASTOS, S. M. C.; ASCHERI, D. P. R. Sorghum straw: Pulping and bleaching process optimization and synthesis of cellulose acetate. **International journal of biological macromolecules**, v. 135, p. 877-886, 2019.

ANSER, M. K.; HANIF, I.; ALHARTHI, M.; CHAUDHRY, I. S. Impact of fossil fuels, renewable energy consumption and industrial growth on carbon emissions in Latin American and Caribbean economies. **Atmósfera**, v. 33, i. 3, p. 201-213, 2020.

ARYA, A.; SHARMA, A. L. Polymer electrolytes for lithium ion batteries: a critical study. **Ionics**, v. 23, n. 3, p. 497-540, 2017.

ASTM (American Society for Testing and Materials). **Book of Definitions**, W. Conshohocken, 1996.

ASTM (American Society for Testing and Materials). **Standard practice for operating fluorescent light apparatus for UV exposure of nonmetallic materials**, 2006.

AVELLANEDA, C. O.; BERTON, A. C., BULHÕES, L. O. S. Optical and electrochemical properties of CeO2 thin film prepared by an alkoxide route. **Solar Energy Materials & Solar Cells** 92 (2008) 240–244, 2008.

AVELLANEDA, C. O.; BULHÕES, L. O. S. Optical and electrochemical properties of V2O5:Ta Sol–Gel thin films. **Solar Energy Materials and Solar Cells**, v. 90, n. 4, p. 444-451, 2006.

BABU, R. P.; O'CONNOR, K.; SEERAM, R. Current progress on bio-based polymers and their future trends. **Progress in Biomaterials**, v. 2, i. 8, 2013.

BALAKRISHNAN, N.; JOYNER, J. D.; JISHNU, N. S.; DAS, A.; JABEEN FATIMA, M. J.; PRASANTH, R. Electrospun polyacrylonitrile (PAN)-based polymer gel electrolytes for lithium-ion batteries. In: **Electrospinning for Advanced Energy Storage Applications**. Springer, Singapore, 2021. p. 121-152, 2021.

BALBONI, R. D. C.; LEMOS, R. M. J.; MOURA, E. A.; CHOLANT, C. M.; AZEVEDO, C. F.; CALDEIRA, I. M.; GUNDEL, A.; FLORES, W. H.; PAWLICKA, A.; AVELLANEDA, C. O. Electrochemical, UV–Vis, and microscopical characteristics of sol–gel CeO2: V2O5 thin film. **Journal of Materials Science: Materials in Electronics**, v. 29, n. 19, p. 16911-16920, 2018.

BRIMM, E. O.; BRANTLEY, J. C.; LORENZ, J. H.; JELLINEK, M. H. Sodium and Potassium Tungsten Bronzes. **Journal of The American Chemical Society**, v. 73, i. 11, p. 5427-5432, 1951.

BRUNDLAND, G. H. **World commission on environment and development. Our Common Future oxford.** Oxford: Oxford University Press, 1987.

CAI, G.; WANG, J.; LEE, P. S. Next-generation multifunctional electrochromic devices. **Accounts of chemical research**, v. 49, n. 8, p. 1469-1476, 2016.

CALDEIRA, I.; LÜDTKE, A.; TAVARES, F.; CHOLANT, C.; BALBONI, R.; FLORES, W. H.; GALIO, A.; PAWLICKA, A.; AVELLANEDA, C. O. Ecologically friendly xanthan gum-PVA matrix for solid polymeric electrolytes. **Ionics**, v. 24, n. 2, p. 413-420, 2018.

CANNAVALE, A.; COSSARI, P.; EPERON, G. E.; COLELLA, S.; FIORITO, F.; GIGLI, G.; SNAITH, H. J.; LISTORTI, A. Forthcoming perspectives of photoelectrochromic devices: a critical review. **Energy & Environmental Science**, v. 9, n. 9, p. 2682-2719, 2016.

CERQUEIRA, D. A.; FILHO, G. R.; CARVALHO, R. A.; VALENTE, A. J. M. Caracterização de Acetato de Celulose Obtido a partir do Bagaço de Cana-de-Açúcar por H-RMN. **Polímeros**, v.20, n.2, p.85-91, 2010.

CHANG-JIAN, C-W.; CHO, E-C.; YEN, S-C.; HO, B-C.; LEE, K-C.; HUANG, J-H.; HSIAO, Y-S. Facile preparation of WO3/PEDOT:PSS composite for inkjet printed electrochromic window and its performance for heat shielding. **Dyes and Pigments**, v. 148, p. 465-473, 2018.

CHOLANT, C. M.; KRÜGER, L. U.; BALBONI, R. D. C.; RODRIGUES, M. P.; TAVARES, F. C.; PERES, L. L.; FLORES, W. H.; GUNDEL, A.; PAWLICKA, A.; AVELLANEDA, C. O. Synthesis and characterization of solid polymer electrolyte based on poly (vinyl alcohol)/gum Arabic/LiClO4. **Ionics**, v. 26, n. 6, p. 2941-2948, 2020.

CHOLANT, C. M.; RODRIGUES, M. P.; PERES, L. L.; BALBONI, R. D.; KRÜGER, L. U.; PLACIDO, D. N.; FLORES, W. H.; GUNDEL, A.; PAWLICKA, A.; AVELLANEDA, C. O. Study of the conductivity of solid polymeric electrolyte based on PVA/GA blend with addition of acetic acid. **Journal of Solid State Electrochemistry**, v. 24, n. 8, p. 1867-1875, 2020.

COSTA, D. M. A.; SANTOS, A. F.; SILVA, E. D.; SILVA, I. A. Desenvolvimento e caracterização de filmes à base de amido de feijão macáçar (Vigna u nguiculata (L.) Wap). **Holos**, v. 7, p. 2-16, 2017.

CZANDERNA, A. W.; BENSON, D. K.; JORGENSEN, G. J.; ZHANG, J. G.; TRACY, C. E.; DEB, S. K. Durability issues and service lifetime prediction of electrochromic windows for buildings applications. **Solar Energy Materials and Solar Cells**, v. 56, n. 3-4, p. 419-436, 1999.

DEB, S. K. A Novel Electrophotographic System. **Applied Optics**, v. 8, i. S1, p. 192-195, 1969.

DEFOREST, N.; SHEHABI, A.; SELKOWITZ, S.; MILLIRON, D. J. A comparative energy analysis of three electrochromic glazing technologies in commercial and residential buildings. **Applied Energy**, v. 192, p. 95-109, 2017.

DETSI, A., KAVETSOU, E., KOSTOPOULOU, I., PITTEROU, I., PONTILLO, A. R. N., TZANI, A., CHRISTODOULOU, P.; SILIACHLI, A.; ZOUMPOULAKIS, P. Nanosystems for the encapsulation of natural products: The case of chitosan biopolymer as a matrix. **Pharmaceutics**, v. 12, n. 7, p. 669, 2020.

DI CARLO, G.; BIROLI, A. O.; TESSORE, F.; CARAMORI, S.; PIZZOTTI, M. β-Substituted Zn^{II} porphyrins as dyes for DSSC: A possible approach to photovoltaic Windows. **Coordination Chemistry Reviews**, v.358, p.153-177, 2018.

DOS SANTOS, F. H. **Caracterização de Polivinilálcool e Polivinilpirrolidona (PVAl/PVP) Para Reparo de Cartilagem Articular Mandibular.** 2011. Dissertação (Mestrado) – Faculdade de Engenharia Mecânica, Universidade Estadual de Campinas, São Paulo, 2011.

EIA. **Annual energy outlook 2012 with projections to 2035**.Disponível em <http://www.eia.gov>

EPE - EMPRESA DE PESQUISA ENERGÉTICA – **Anuário Estatístico de Energia Elétrica 2020**–Disponível em <http://www.epe.gov.br/>

GERMERSHAUS, O.; LÜHMANN, T.; RYBAK, J.-C.; RITZER, J.; MEINEL, L. Application of natural and semi-synthetic polymers for the delivery of sensitive drugs. **International Materials Reviews**, v. 60, i. 2, p. 101-131, 2015.

GÖKDEMIR, F. P.; SAATCI, A. E.; ÖZDEMIR, O.; KESKIN, B.; KUTLU, K. Structural, optical and electrochromic properties of cerium dioxide thin films prepared by sol–gel dip coating method. **Materials Science in Semi conductor Processing**, v. 38, p. 300-305, 2014.

GRANQVIST, C.G. Recent advances in electrochromics for smart windows applications. **Solar Energy**. v. 63, n. 4, p. 199-216,1998.

GRANQVIST, C. G.; HULTÅKER, A. Transparent and conducting ITO films: new developments and applications. **Thin solid films**, v. 411, n. 1, p. 1-5, 2002.

HAN, T.; DZAKPASU, C. B.; KIM, D.; KIM, S.; JEONG, Y. C.; RYOU, M. H.; LEE, Y. M. Thin and porous polymer membrane-based electrochromic devices. **Journal of Materials Chemistry C**, v. 7, n. 4, p. 1042-1047, 2019.

IEA. **Explore energy data by category, indicator, country or region**. Paris, 2019. Disponível em<http://www.iea.gov>

ISLAM, S. M.; BARILE, C. J. Dual Tinting Dynamic Windows Using Reversible Metal Electrodeposition and Prussian Blue. **ACS applied materials & interfaces**, v. 11, n. 43, p. 40043-40049, 2019.

JAROSZ, T.; GEBKA, K.; STOLARCZYK, A.; DOMAGALA, W. Transparent to black electrochromism—the “holy grail” of organic optoelectronics. **Polymers**, v. 11, n. 2, p. 273, 2019.

JAUHARI, J.; WIRANATA, S.; RAHMA, A.; NAWAWI, Z.; SRIYANTI, I. Polyvinylpyrrolidone/cellulose acetate nanofibers synthesized using electrospinning method and their characteristics. **Materials Research Express**, v. 6, n. 6, p. 064002, 2019.

JIN, X.; YOU, L.; CHEN, Z.; LI, Q. High-efficiency platinum-free quasi-solid-state dye-sensitized solar cells from polyaniline (polypyrrole)-carbon nanotube complex tailored conducting gel electrolytes and counter electrodes. **Electrochimica Acta**, v. 260, p. 905-911, 2018.

JITTIARPORN, P.; BADILESCU, S.; AL SAWAFTA, M. N.; SIKONG, L.; TRUONG, V. V. Electrochromic properties of sol–gel prepared hybrid transition metal oxides–A short review. **Journal of Science: Advanced Materials and Devices**, v. 2, n. 3, p. 286-300, 2017.

KAISER, A.; STARK, W. J.; GRASS, R. N. Rapid production of a porous cellulose acetate membrane for water filtration using readily available chemicals. **Journal of chemical education**, v. 94, n. 4, p. 483-487, 2017.

KAMALISARVESTANI, M.; SAIDUR, R.; MEKHILEF, S.; JAVADI, F.S. Performance, materials and coating technologies of thermochromic thin films on smart windows. **Renewable and Sustainable Energy Reviews**, v.26, p. 353–364, 2013.

KIBERT, Charles J. Establishing principles and a model for sustainable construction: **Proceedings of the first international conference on sustainable construction**. Tampa, Florida, 1994. p. 6-9.

KITAZAWA, Y.; TAKITA, R.; YOSHIDA, K.; MURANAKA, A.; MATSUBARA, S.; UCHIYAMA, M. “Naked” Lithium Cation: Strongly Activated Metal Cations Facilitated by Carborane Anions. **The Journal of Organic Chemistry**, v. 82, n. 4, p. 1931-1935, 2017.

KNOTT, E. P.; CRAIG, M. R.; LIU, D. Y.; BABIARZ, J. E.; DYER, A. L.; REYNOLDS, J. R. A minimally coloured dioxypyrrole polymer as a counter electrode material in polymeric electrochromic window devices. **Journal of Materials Chemistry**, v. 22, p. 4953-4962, 2012.

KORTZ, C.; HEIN, A.; CIOBANU, M.; WALDER, L.; OESTERSCHULZE, E. Complementary hybrid electrodes for high contrast electrochromic devices with fast response. **Nature communications**, v. 10, n. 1, p. 1-7, 2019.

KUMAR, R.; RANWA, S.; KUMAR, G. Biodegradable flexible substrate based on chitosan/PVP blend polymer for disposable electronics device applications. **The Journal of Physical Chemistry B**, v. 124, n. 1, p. 149-155, 2019.

LAU, S.; KAHAR, A. W. M.; YUSRINA, M. D. Effect of glycerol as plasticizer on the tensile properties of chitosan/microcrystalline cellulose films. In: **AIP Conference Proceedings**. AIP Publishing LLC, 2021. p. 020204.

LEE, E. S.; CLAYBAUGH, E. S.; LAFRANCE, M. End user impacts of automated electrochromic windows in a pilot retrofit application. **Energy and Buildings**, v.42, p.267-284, 2012.

LEE, H. J., LEE, C.; SONG, J.; YUN, Y. J.; JUN, Y.; AH, C. S. Electrochromic devices based on ultraviolet-cured poly (methyl methacrylate) gel electrolytes and their utilisation in smart window applications. **Journal of Materials Chemistry C**, v. 8, n. 26, p. 8747-8754, 2020.

LI, M. **Conjugated Polymer-Based Functional Materials for Wearable Electronics: Electrochromism**. 2018. Tese (Doutorado) – University of Connecticut, Connecticut, 2018

LIN, Y-S.; TSAI, C-W.; CHEN, P-W. Electrochromic properties of V2O5-z thin films sputtered onto flexible PET/ITO substrates. **Solid State Ionics**, v.179, i. 7-8, p.290-297, 2008.

LIU, C.; SACCI, R. L.; SAHORE, R.; VEITH, G. M.; DUDNEY, N. J.; CHEN, X. C. Polyacrylonitrile-based electrolytes: How processing and residual solvent affect ion transport and stability. **Journal of Power Sources**, v. 527, p. 231165, 2022.

LIU, Q.; DONG, G.; CHEN Q.; GUO J.; XIAO Y.; DELPLANCKE-OGLETREE, M-P.; RENIERS, F.; DIAO, X. Charge-transfer kinetics and cyclic properties of inorganic all-solid-state electrochromic device with remarkably improved optical memory. **Solar Energy Materials and Solar Cells**, v.174, p.545-553, 2018.

LIU, R.; ZHANG, L.; HUANG, Z.; XU, J. Sequential and alternating RAFT single unit monomer insertion: model trimers as the guide for discrete oligomer synthesis. **Polymer Chemistry**, v. 11, n. 28, p. 4557-4567, 2020.

LIU, Y.; CAI, X.; XIAO, X.; WANG, J.; SHENG, G.; XU, G. Preparation of WO3 gel electrochromic device by simple two-step method. **Materials Today Communications**, v. 30, p. 103090, 2022.

LOI, M. R.; MOURA, E. A.; WESTPHAL, T. M.; BALBONI, R. D.; GÜNDEL, A.; FLORES, W. H.; PEREIRA, M. B.; SANTOS, M. J. L; SANTOS, J. F. L.; PAWLICKA, A.; AVELLANEDA, C. Impact of Zr precursor on the electrochemical properties of V2O5 sol-gel films. **Journal of Electroanalytical Chemistry**, v. 839, p. 67-74, 2019.

LUCON, O.; GOLDEMBERG, J. Crise financeira, energia e sustentabilidade no Brasil. **Estudos Avançados**, v.23, n. 65, p. 121-130, 2009.

MA, K.; TANG, Q.; ZHU, C-R.; LONG, J-F.; GONG, C-B.; FU, X-K.Novel dual-colored 1,1′,1″,1‴-tetrasubstituted (4,4′,4″,4‴-tetrapyridyl) cyclobutane with rapid electrochromic switching. **Electrochimica Acta**, v. 259, p. 986-993, 2018.

MANJUNATHA, H.; DAMLE, R.; PRAVIN, K.; KUMARASWAMY, G. N. Modification in the transport and morphological properties of solid polymer electrolyte system by low-energy ion irradiation. **Ionics**, v. 24, n. 10, p. 3027-3037, 2018.

MARIANO-TORRES, J. A.; LÓPEZ-MARURE, A.; DOMIGUEZ-SÁNCHEZ, M. A. Synthesis and characterization of polymers based on citric acid and glycerol: Its application in non-biodegradable polymers. **Dyna**, v. 82, n. 190, p. 53-59, 2015.

MASTURAH BINTI FAKHRUDDIN, S.; INO, K.; INOUE, K. Y.; NASHIMOTO, Y.; SHIKU, H. Bipolar Electrode-based Electrochromic Devices for Analytical Applications–A Review. **Electroanalysis**, v. 34, n. 2, p. 212-226, 2022.

MATEUS, Ricardo. **Novas Tecnologias Construtivas Com Vista à Sustentabilidade da Construção**. 2004. 224f. Dissertação (Mestrado em Engenharia Civil) – Escola de Engenharia, Universidade do Minho, Minho, 2004.

MATHELA, S.; SANGWAN, B.; DHAPOLA, P. S.; SINGH, P. K.; TOMAR, R. Ionic liquid incorporated poly (ethylene oxide)(PEO) doped with potassium iodide (KI) solid polymer electrolyte for energy device. **Materials Today: Proceedings**, v. 49, p. 3250-3253, 2022.

MEDEIROS, E. S.; OLIVEIRA, J. E.; CONSOLIN-FILHO, N.; PATERNO, L. G.; MATTOSO, L. H. C. Uso de Polímeros Condutores em Sensores. Parte 1: Introdução aos Polímeros Condutores. **Revista Eletrônica de Materiais e Processos**, v.7.2, p.62-77, 2012.

MONISHA, S.; MATHAVAN, T.; SELVASEKARAPANDIAN, S.; BENIAL, A. M. F.; ARISTATIL, G.; MANI, N.; PREMALATHA, M. Investigation of bio polymer electrolyte based on cellulose acetate-ammonium nitrate for potential use in electrochemical devices. **Carbohydrate polymers**, v. 157, p. 38-47, 2017.

MOSER, M. L.; LI, G.; CHEN, M.; BEKYAROVA, E.; ITKIS, M. E.; HADDON, R. C. Fast Electrochromic Device Based on Single-Walled Carbon Nanotube Thin Films. **Nano Letters**, v. 16, i. 9, p. 5386-5393, 2016.

MOSTAFA, N. A.; FARAG, A. A.; ABO-DIEF, H. M.; TAYEB, A. M. Production of biodegradable plastic from agricultural wastes. **Arabian journal of chemistry**, v. 11, n. 4, p. 546-553, 2018.

MOURA, E. A.; CHOLANT, C. M.; BALBONI, R. D. C.; WESTPHAL, T. M.; LEMOS, R. M. J.; AZEVEDO, C. F.; GUNDEL, A.; FLORES, W. H.; GOMEZ, J. A.; ELY, F.; PAWLICKA, A.; AVELLANEDA, C. O. Electrochemical properties of thin films of V2O5 doped with TiO2. **Journal of Physics and Chemistry of Solids**, v. 119, p. 1-8, 2018.

MUTHUKRISHNAN, M.; SHANTHI, C.; SELVASEKARAPANDIAN, S.; MANJULADEVI, R.; PERUMAL, P.; CHRISHTOPHER SELVIN, P. Synthesis and characterization of pectin-based biopolymer electrolyte for electrochemical applications. **Ionics**, v. 25, n. 1, p. 203-214, 2019.

NGAMAROONCHOTE, A.; CHOTSUWAN, C. Performance and reliability of cellulose acetate-based gel electrolyte for electrochromic devices. **Journal of Applied Electrochemistry**, v. 46, p.575-582, 2016.

OMRANY, H.; MARSONO, A. K. Optimization of building energy performance through passive design strategies. **British Journal of Applied Science Technology**, v. 13, i. 6, p. 1-16, 2016.

ONG, M. T.; VERNERS, O.; DRAEGER, E. W.; VAN DUIN, A. C. T.; LORDI, V.; PASK, J. E. Lithium Ion Solvation and Diffusion in Bulk Organic Electrolytes from First-Principles and Classical Reactive Molecular Dynamics. **The Journal of Physical Chemistry B**, v. 119, i. 4, p. 1535-1545, 2015.

ONOZATO, T.; CHO, H. J.; OHTA, H. An oxide-based flexible electrochromic transistor under mechanical stress. **Japanese Journal of Applied Physics**, v. 59, n. 2, p. 024002, 2020.

OREL, B.; LAVRENCIC-STANGAR, U.; PIHLAR, B. Amorphous Nb/Fe-Oxide ion-storage films for counter electrode applications in electrochromic devices. **Journal of Electrochemical Society**, v. 145, n. 5, p. 1607-1614, 1998.

PATHAK, D. K.; CHAUDHARY, A.; TANWAR, M.; GOUTAM, U. K.; KUMAR, R. Nano-cobalt oxide/viologen hybrid solid state device: Electrochromism beyond chemical cell. **Applied Physics Letters**, v. 116, n. 14, p. 141901, 2020.

PICARDI, G.; VARSANO, F.; DECKER, F.; KRASOVEC, U. O.; SURCA, A.; OREL, B. Electrochemical characterization of optically passive CeVO4 counterelectrodes. **Electrochimica Acta**, v. 44, i. 18, p. 3157-3164, 1999.

PLATT, J. Electrochromism, a Possible Change of Color Producible in Dyes by an Electric Field. **The Journal of Chemical Physics**, v. 34, n. 3, p. 862, 1961.

POOSAPATI, A.; NEGRETE, K.; JANG, N.; HU, L.; LAN, Y.; MADAN, D. Wood cellulose-based thin gel electrolyte with enhanced ionic conductivity. **MRS Communications**, v. 9, n. 3, p. 1015-1021, 2019.

PORTO, J. S.; DE FREITAS, J. M. R.; BALBONI, R. D. C.; TREICHEL, S.; DA CUNHA, E. G.; DE MATTOS, R. S.; LEITZKE, R. K.; CHOLANT, C. M.; AVELLANEDA, C. A. O. Thermoenergetic and luminous performance of a office building with the use of electrochromic glasses. **Revista Matéria**, v. 25, n. 3, 2020.

QUINTANA, E.; AGO, M.; VALLS, C.; RONCERO, M. B.; ROJAS, O. J. Alternative chemo-enzymatic treatment for homogeneous and heterogeneous acetylation of wood fibers. **Cellulose**, v. 25, n. 9, p. 5323-5336, 2018.

QUINTANILHA, R. C.; ROCHA, I.; VICHESSI, R. B.; LUCHT, E.; NAIDEK, K.; WINNISCHOFER, H.; VIDOTTI, M. Eletrocromismo: Fundamentos e a aplicação de nanomateriais no desenvolvimento de eletrodos de alto desemprenho. **Química Nova**, v. 37, n. 4, p. 677-688, 2014.

RASIA, G. M. **Síntese e Funcionalização de Hidrogéis de Poli (Álcool Vinílico).** 2014. Dissertação (Mestrado). Universidade Federal do Rio Grande do Sul, Porto Alegre, 2014.

SENEVIRATHNE, A. M. C.; SENEVIRATNE, V. A.; ILEPERUMA, O. A. Use of fumed silica nanoparticles to attain polymer free novel quasi-solid state electrolyte for high-efficiency dye-sensitized solar cells. **Solar Energy**, v. 159, p. 531-537, 2018.

SENNA, André Martins. **Géis de acetato de celulose reticulados: síntese, caracterização e estudos de adsorção de íons Cu^{2+}**. 2011. 83 f. Dissertação (Mestrado em Ciência dos Materiais) - Universidade Federal de São Carlos, Sorocaba, 2011.

SHAHI, A.; ARUNAN, E. Hydrogen bonding, halogen bonding and lithium bonding: an atoms in molecules and natural bond orbital perspective towards conservation of total bond order, inter- and intra-molecular bonding. **Physical Chemistry Chemical Physics**, v. 16, p. 22935-22952, 2014.

SHAKHNOV, V. A.; VLASOV, A. I.; TOKAREV, S. V. Electrochromic thin-film components for information representation systems. **In: IOP Conference series: materials science and Engineering**. IOP Publishing, v. 1, n. 1, p. 012005, 2016.

SHARMA, A.; NAGARKAR, S.; THAKRE, S.; KUMARASWAMY, G. Structure–property relations in regenerated cellulose fibers: comparison of fibers manufactured using viscose and lyocell processes. **Cellulose**, v. 26, n. 6, p. 3655-3669, 2019.

SHEN, D. E.; OSTERHOLM, A. M.; REYNOLDS, J. R. Out of sight but not out of mind: the role of counter electrodes in polymer-based solid-state electrochromic devices. **Journal of Materials Chemistry C**, v. 3, i. 37, p. 9715-9725, 2015.

SHIM, H. B.; KIM, W. Y.; KANG, I-K.; LEE, H. C.; Microstructural Effects on Nickel Oxide Film Properties in an Infrared Electrochromic Window for Shutter-Less Infrared Sensor Application. **IEEE Sensors Journal**, v.17, n.20, p.6522-6528, 2017.

SIM, L. N.; PAWLICKA, A. Polymer Electrolytes for Electrochromic Windows. **Polymer Electrolytes: Characterization Techniques and Energy Applications**, p. 365-389, 2020.

SINGH, A. K.; KIRUTHIKA, S.; MONDAL, I.; KULKARNI, G. U. Fabrication of solar and electrically adjustable large area smart windows for indoor light and heat modulation. **Journal of Materials Chemistry C**, v. 5, p. 5917-5922, 2017.

SMIATEK, J.; HEUER, A.; WINTER, M. Properties of ion complexes and their impact on charge transport in organic solvent-based electrolyte solutions for lithium batteries: insights from a theoretical perspective. **Batteries**, v. 4, n. 4, p. 62, 2018.

SUBBU, C.; RAJENDRAN, S.; KESAVAN, K.; PREMILA, R. The physical and electrochemical properties of poly (vinylidene chloride-co-acrylonitrile)-based polymer electrolytes prepared with different plasticizers. **Ionics**, v. 22, n. 2, p. 229-240, 2016.

SUN, X. G.; FANG, Y.; JIANG, X.; YOSHII, K.; TSUDA, T.; DAI, S. Polymer gel electrolytes for application in aluminum deposition and rechargeable aluminum ion batteries. **Chemical communications**, v. 52, n. 2, p. 292-295, 2016.

SVENSSON, J. S. E. M.; GRANQVIST, C. G. Electrochromic coatings for “smart windows”. **Solar Energy Materials**, v.12, i.6, p.391-402, 1985.

TAVARES, P.F.; GASPAR, A. R.; MARTINS, A. G.; FRONTINI, F. Evaluation of Electrochromic Windows Impact in the Energy Performance of Buildings in Mediterranean Climates. **Energy Policy**, v.67, p. 68-81, 2014.

TIAN, H.; TANG, Z.; ZHUANG, X.; CHEN, X.; JING, X. Biodegradable synthetic polymers: Preparation, functionalization and biomedical application. **Progress in Polymer Science**, v. 37, i. 2, p. 237-280, 2012.

TONG, K.; LI, R.; ZHU, J.; YAO, H.; ZHOU, H.; ZENG, X.; JI, S.; JIN, P. Preparation of VO2/Al-O core-shell structure with enhanced weathering resistance for smart window. **Ceramics International**, v. 43, n. 5, p. 4055-4061, 2017.

UPADHYE, M. C.; KUCHEKAR, M. C.; PUJARI, R. R.; SABLE, N. U. Biopolymers: A comprehensive review. 2022.

UTPALLA, P.; SHARMA, S. K.; SUDARSHAN, K.; SAHU, M.; PUJARI, P. K. Investigation of the free volume characteristics of PEO based solid state polymer electrolyte by means of positron annihilation spectroscopy. **Solid State Ionics**, v. 339, p. 114990, 2019.

VELEVSKA, J.; STOJANOV, N.; PECOVSKA-GJORGJEVICH, M.; NAJDOSKI, M. Electrochromism in tungsten oxide thin films prepared by chemical bath deposition. **Journal of Electrochemical Science and Engineering**, v. 7, n. 1, p. 27-37, 2017.

WANG, R.; YAO, M.; NIU, Z. Smart supercapacitors from materials to devices. **InfoMat**, v. 2, n. 1, p. 113-125, 2020.

WANG, Z.; WANG, X.; CONG, S.; CHEN, J.; SUN, H.; CHEN, Z.; SONG, G.; GENG, F.; CHEN, Q.; ZHAO, Z. Towards full-colour tunability of inorganic electrochromic devices using ultracompact fabry-perot nanocavities. **Nature communications**, v. 11, n. 1, p. 1-9, 2020.

WENDLING, M. **Apostila Série Eletrônica**. SENAI. 2011.

WEY, Y.; WANG, X.; TORAH, R.; TUDOR, J. Dispenser printing of electrochromic display on textiles for creative applications. **Electronics Letters**, v. 53, i. 12, p. 779-781, 2017.

WU, W.; WANG, M.; MA, J.; CAO, Y.; DENG, Y. Electrochromic metal oxides: Recent progress and prospect. **Advanced Electronic Materials**, v. 4, n. 8, p. 1800185, 2018.

XIONG, K.; TORDERA, D.; JONSSON, M. P.; DAHLIN, A. B. Active control of plasmonic colors: emerging display technologies. **Reports on Progress in Physics**, v. 82, n. 2, p. 024501, 2019.

YANEVA, S.; SEMERDZHIEVA, V.; RAYKOVA, R.; MARINKOVA, D.; CHERNEV, G.; ILIEV, I.; YOTOVA, L. Synthesis and investigation of the properties of hybrid materials for enzyme immobilization. **Journal of Chemical Technology & Metallurgy**, v. 53, n. 6, 2018.

YANG, P.; SUN, P.; MAI, W. Electrochromic energy storage devices. **Materials Today**, v. 19, n.7, p. 394-402, 2016.

YUKSEL, R.; COSKUN, S.; GUNBAS, G.; CIRPAN, A.; TOPPARE, L.; UNALAN, H. E. Silver nanowire/conducting polymer nanocomposite electrochromic supercapacitor electrodes. **Journal of The Electrochemical Society**, v. 164, n. 4, p. A721, 2017.

ZHANG, P.; WANG, S.; ZHANG, X.; JING, X. The effect of free dihydroxydiphenylmethanes on the thermal stability of novolac resin. **Polymer Degradation and Stability**, v. 168, p. 108946, 2019.

ZHANG, Q.; DONG, H.; HU, W. Electrochemical polymerization for two-dimensional conjugated polymers. **Journal of Materials Chemistry C**, v. 6, n. 40, p. 10672-10686, 2018.

ZHANG, S.; CHEN, S.; HU, F.; XU, R.; YAN, B.; JIANG, M.; GU, Y.; YANG, F.; CAO, Y. Spray-processable, large-area, patterned and all-solid-state electrochromic device based on silica/polyaniline nanocomposites. **Solar Energy Materials and Solar Cells**, v. 200, p. 109951, 2019.

ZHU, H.; WANG, L. Smart window based on Cu7S4/hydrogel composites with fast photothermal response. **Solar Energy Materials and Solar Cells**, v. 202, p. 110109, 2019.

ANEXO A – Material Suplementar do Artigo 2

SUPPLEMENTARY MATERIAL

Influence of Weathering and Temperature on the Electrochemical and Microscopical Characteristics of CeO2 and CeO2:V2O5 Sol-Gel Thin Films

Raphael D. C. Balboni[1], Camila M. Cholant[1], Luana U. Krüger[1], Elton A. Moura[2], Guilherme K. Maron[1], Wladimir H. Flores[3], André Gündel[3], Darci A. Gatto[1], Agnieszka Pawlicka[4], Cesar A. O. Avellaneda[1], Robson Andreazza[1,]*

[1] Centro de Desenvolvimento Tecnológico, Universidade Federal de Pelotas, Rua Gomes Carneiro, 1, Centro, Pelotas, RS 96010-610, Brazil

[2] Setor de Ciências Exatas, Universidade Federal do Paraná, R. Cel. Francisco Heráclito dos Santos, 100, Jardim das Américas, Curitiba, PR 81531-980, Brazil

[3] Campus Bagé, Universidade Federal de Pampa, Rua Maria A.G. de Godoy n° 1650, Bagé, RS 96413-170, Brazil

[4] IQSC-USP, Av. Trabalhador Sãocarlense 400, São Carlos, SP 13566-590, Brazil

[*] Corresponding author. Phone number: 55 53 3284-1694. e-mail address: robsonandreazza@yahoo.com.br

Table S-1. Electrochemical Impedance Spectroscopy parameters and resistances of the CeO_2 thin films

Temperature	R_s (ohm)	R_{ct} (Ohm)	f_{max} (Hz)	θ_{max} (°)	C_{dc} (F)	σ (S/cm)
20 °C	330.4	340.2	35510	63.7	1.31×10^{-8}	2.70×10^{-8}
30 °C	252.2	256.1	74560	65.2	8.33×10^{-9}	3.59×10^{-8}
40 °C	203.8	206.7	65890	64.1	1.16×10^{-8}	4.45×10^{-8}
50 °C	175.3	178.3	65890	63.1	1.35×10^{-8}	5.16×10^{-8}
60 °C	130.9	133.2	58220	30.6	2.05×10^{-8}	6.90×10^{-8}
70 °C	114.1	116.4	45470	32.8	3.01×10^{-8}	7.90×10^{-8}
80 °C	98.0	100.1	40180	32.6	3.95×10^{-8}	9.19×10^{-8}

R_s: electrode-electrolyte resistance; R_{ct}: polarization resistance; f_{max}: maximum frequency of the depressed arc; C_{dc}: double layer electrical capacitance; σ: ionic conductivity.

Table S-2. Electrochemical Impedance Spectroscopy parameters and resistances of the CeO_2:V_2O_5 thin films

Temperature	R_s (ohm)	R_{ct} (Ohm)	f_{max} (Hz)	θ_{max} (°)	C_{dc} (F)	σ (S/cm)
20 °C	355.6	365.9	11670	56.8	3.72×10^{-8}	8.19×10^{-8}
30 °C	330.0	336.8	31380	56.5	1.50×10^{-8}	8.90×10^{-8}
40 °C	253.2	258.3	45470	55.3	1.35×10^{-8}	1.16×10^{-7}
50 °C	207.6	211.3	51450	55.3	1.46×10^{-8}	1.42×10^{-7}
60 °C	178.9	183.7	19140	54.5	4.52×10^{-8}	1.63×10^{-7}
70 °C	149.5	151.5	58220	54.2	1.80×10^{-8}	1.98×10^{-7}
80 °C	140.5	143.3	21660	54.2	5.12×10^{-8}	2.09×10^{-7}

R_s: electrode-electrolyte resistance; R_{ct}: polarization resistance; f_{max}: maximum frequency of the depressed arc; C_{dc}: double layer electrical capacitance; σ: ionic conductivity.

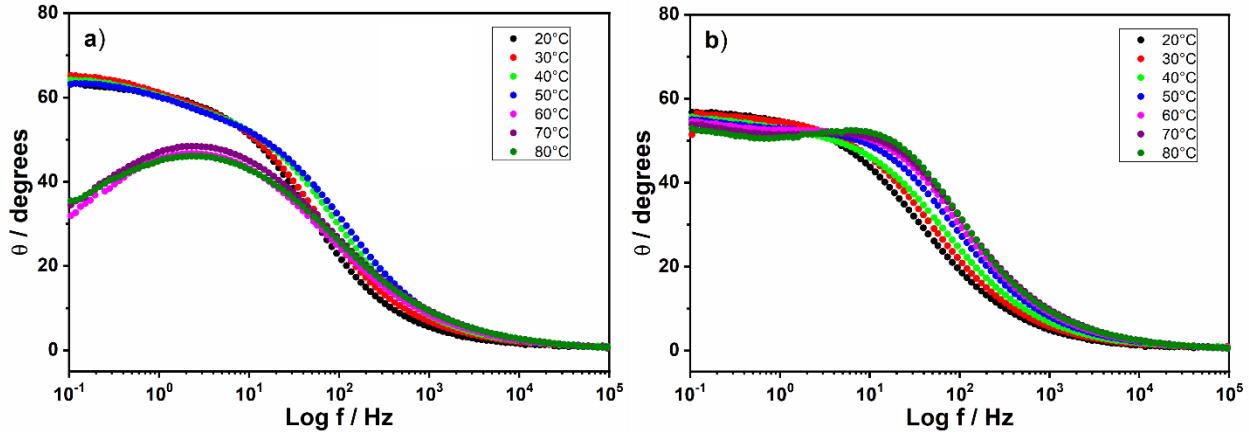

Figure S-1 – Phase angle for the thin films calculated by electrochemical impedance spectroscopy versus frequency log as a function of temperature: **a)** CeO_2; **b)** CeO_2:V_2O_5.

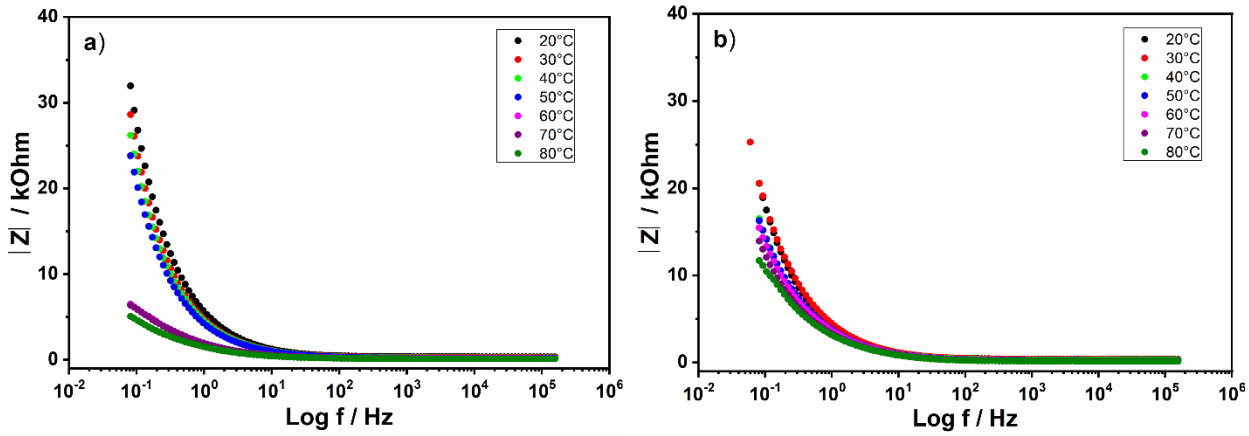

Figure S-2 – Bode diagram for the thin films by electrochemical impedance spectroscopy as a function of temperature: **a)** CeO_2; **b)** CeO_2:V_2O_5.

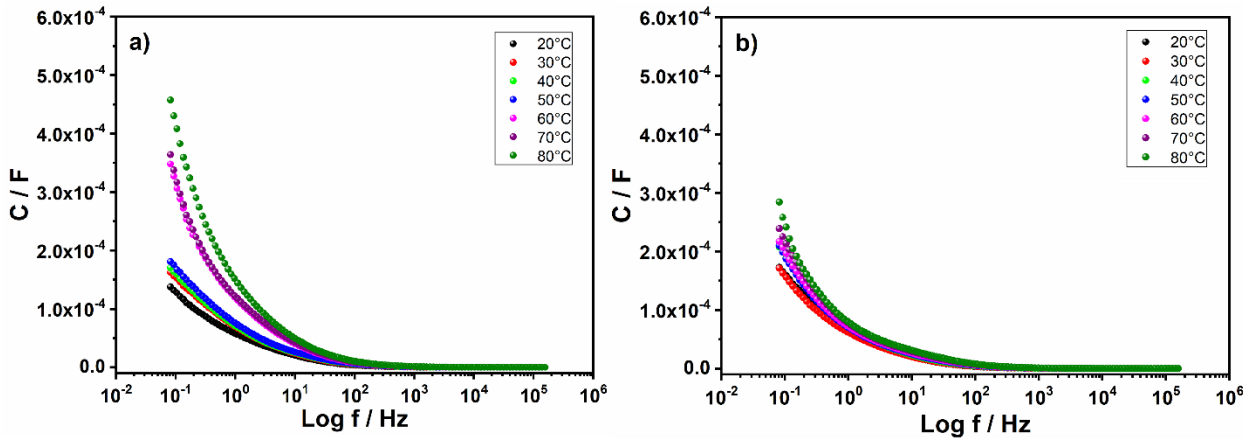

Figure S-3 – Capacitance for the thin films calculated by electrochemical impedance spectroscopy as a function of temperature: **a)** CeO_2; **b)** CeO_2:V_2O_5.

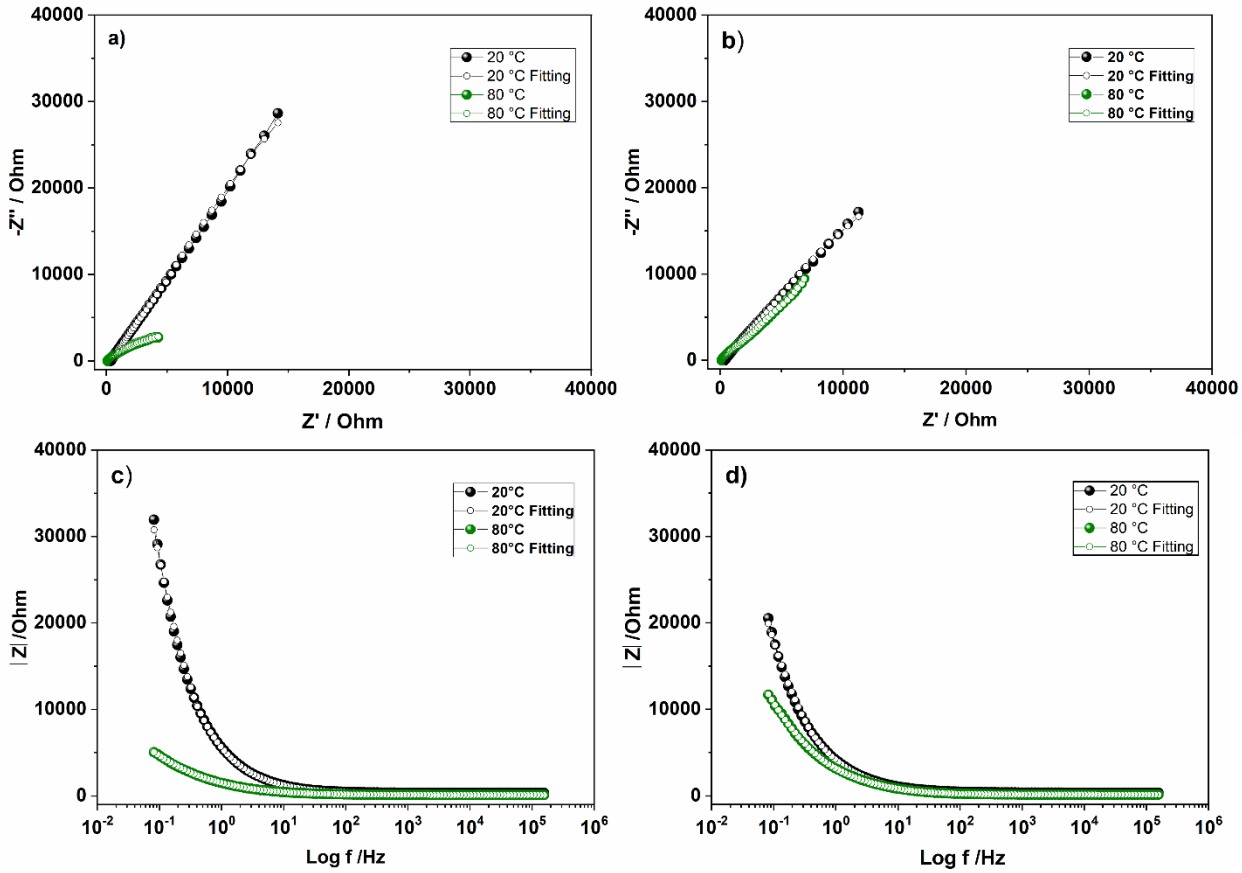

Figure S-4 – Experimental and fitted curves for the thin films: **a)** Nyquist diagram of the CeO_2; **b)** Nyquist diagram of the CeO_2:V_2O_5; **c)** Bode diagram of the CeO_2; **d)** Bode diagram of the CeO_2:V_2O_5.

ANEXO B – Material Suplementar do Artigo 3

SUPPLEMENTARY MATERIAL

Sustainable Biogels Based On Cellulose Acetate For Application In Electrochromic Devices

Raphael D. C. Balboni[1], Camila M. Cholant[1], Rafaela M. J. Lemos[1], Lucas S. Rodrigues[1], Cesar A. O. Avellaneda[1], Robson Andreazza[1]

[1] Centro de Desenvolvimento Tecnológico, Universidade Federal de Pelotas, Rua Gomes Carneiro, 1, Centro, Pelotas, RS 96010-610, Brazil

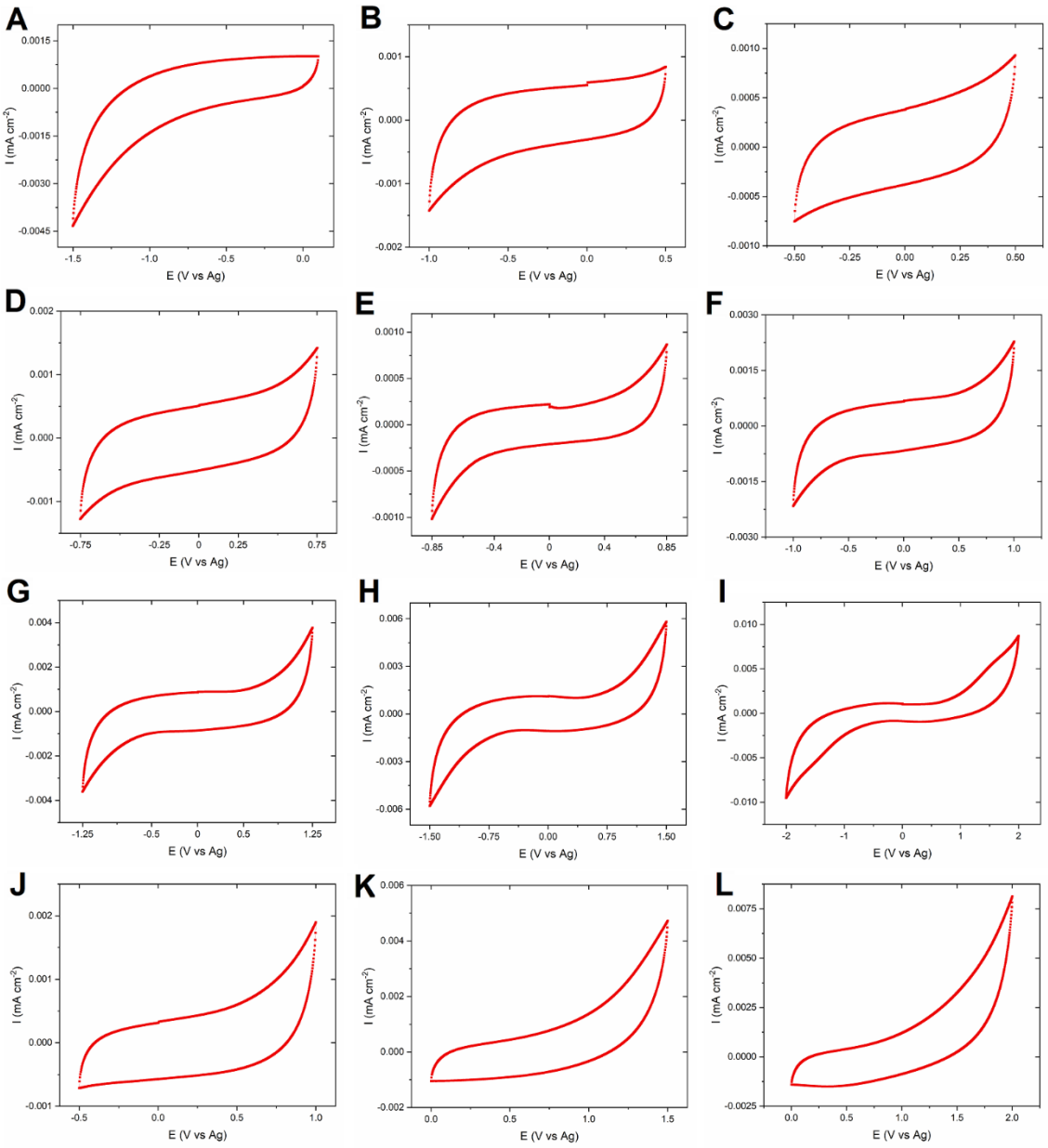

Figure S1 Cyclic voltammetry at different potential windows: a) -1.5/0 V; b) -1.0/+0.5 V; c) -0.5/+0.5 V; d) -0.75/+0.75 V; e) -0.85/+0.85 V; f) -1.0/+1.0 V; g) -1.25/+1.25 V; h) -1.5/+1.5 V; i) -2.0/+2.0 V; j) -0.5/+1.0 V; k) 0/+1.5 V; l) 0/2.0 V.

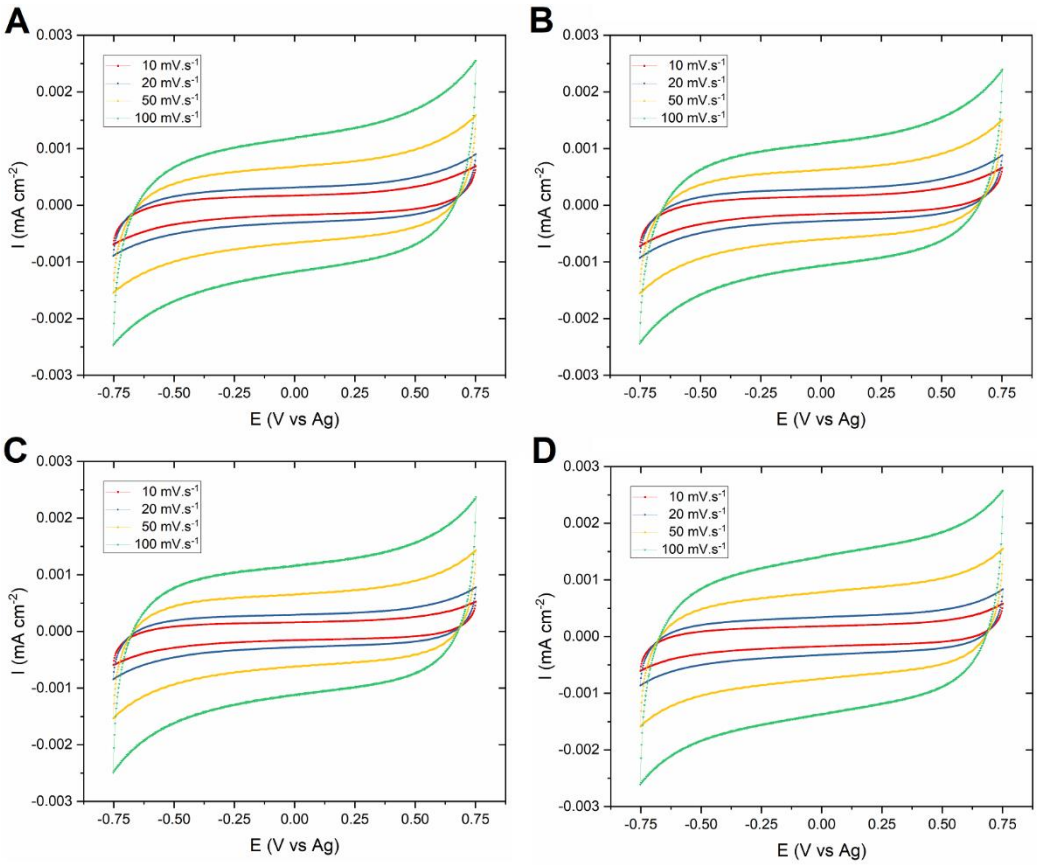

Figure S2 Cyclic voltammetry curves at different scan rates of: a) Gel A (6 wt% of CA; 0.8 M of $LiClO_4$), b) Gel E (14 wt% of CA; 0.8 M of $LiClO_4$), c) Gel F (10 wt% of CA; 0.4 M of $LiClO_4$) and d) Gel M (10 wt% of CA; 1.8 M of $LiClO_4$).

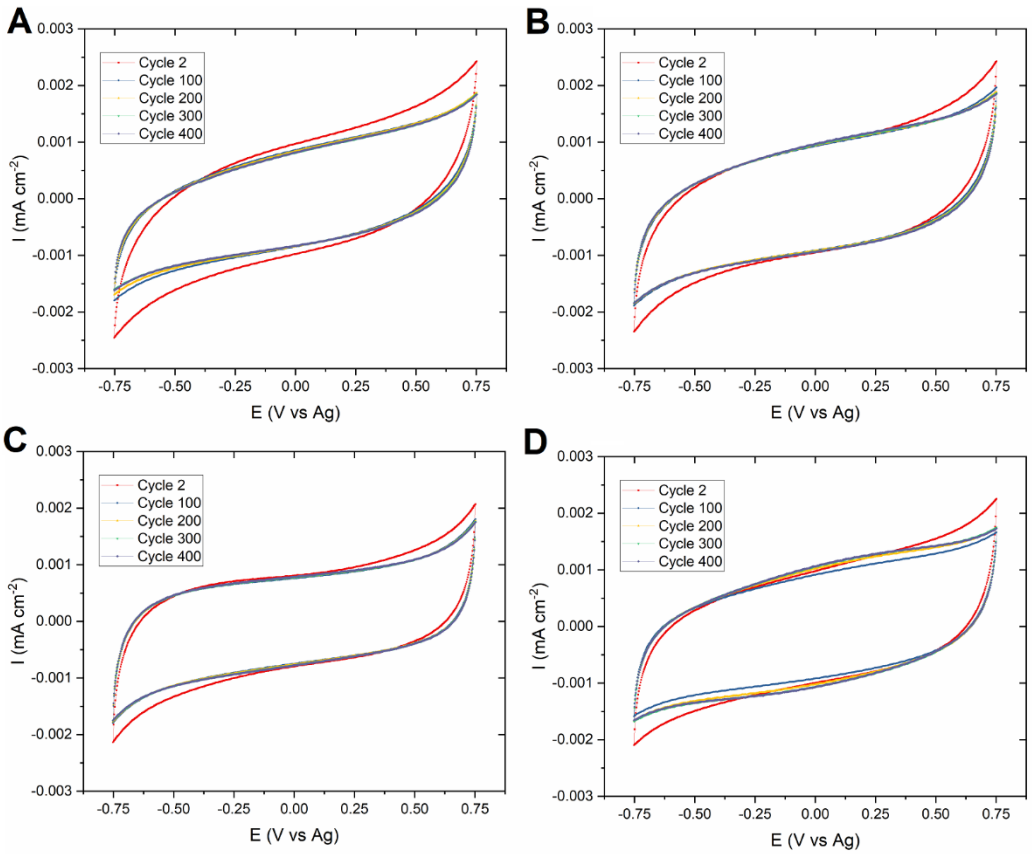

Figure S3 Cyclic voltammetry curves over 400 cycles of: a) Gel A (6 wt% of CA; 0.8 M of $LiClO_4$), b) Gel E (14 wt% of CA; 0.8 M of $LiClO_4$), c) Gel F (10 wt% of CA; 0.4 M of $LiClO_4$) and d) Gel M (10 wt% of CA; 1.8 M of $LiClO_4$).

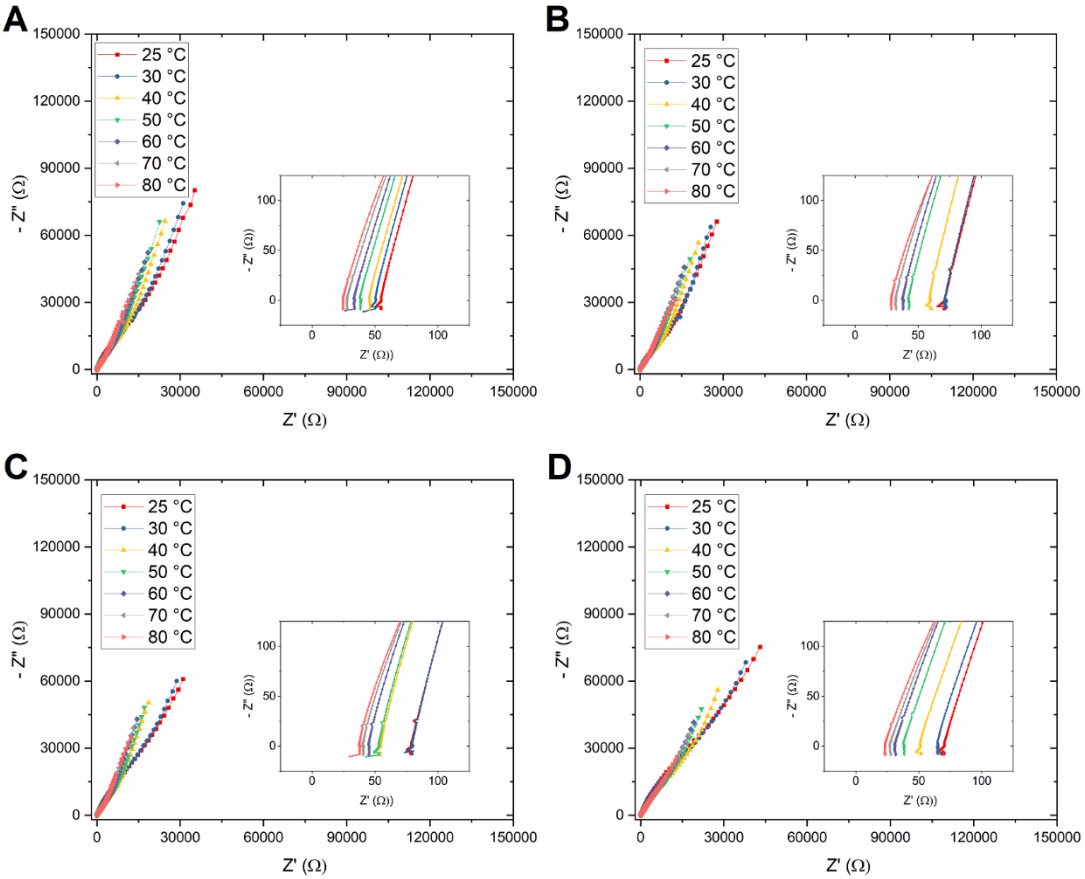

Figure S4 Electrochemical impedance spectroscopy curves from 25 to 80 °C of: a) Gel A (6 wt% of CA; 0.8 M of $LiClO_4$), b) Gel E (14 wt% of CA; 0.8 M of $LiClO_4$), c) Gel F (10 wt% of CA; 0.4 M of $LiClO_4$) and d) Gel M (10 wt% of CA; 1.8 M of $LiClO_4$).

ANEXO C – Material Suplementar do Artigo 4

Supporting Information

Easy to assemble PDMS/CNTs/PANI flexible supercapacitor with high energy-to-power density

Raphael D. C. Balboni,[a] Guilherme K. Maron,[a] Mateus G. Masteghin,[b] Mehmet O. Tas,[b] Lucas S. Rodrigues,[a] Veridiana Gehrke,[a] José H. Alano,[c] Robson Andreazza,[a] Neftali L. V. Carreño[a] and S. Ravi P. Silva*[b]

Experimental

All detailed information about calculation of areal and gravimetric specific capacitances, energy and power densities are described in detail, according to the following equations:

For measurements in three-electrode configuration, the areal specific capacitances (C_{spa}) were calculated according to the equation (1).

$$Cspa = \frac{i\ X\ \Delta t}{A\ X\ \Delta v} \quad (1)$$

Where $Cspa$ is the areal specific capacitance, I is the discharge current, Δt is the discharge time, A is the area of the electrode (0.49 cm^{-2}) and ΔV is the potential range. The gravimetric specific capacitances (C_{spg}) were calculated according to equation (2).

$$Cspg = \frac{i\ X\ \Delta t}{m\ X\ \Delta v} \quad (2)$$

Where m is the mass of polyaniline electrodeposited on the electrode. The gravimetric performances of the electrodes were based on the mass of PANI, since the mass of carbon nanotubes were difficult to reliably measure. Thus, the PDMS and the CNTs poorly contribute to the electrochemical performance of the device.

For measurements performed in the flexible symmetric two-electrode supercapacitors, the C_{spa} and C_{spg} were calculated from GCD curves according to the equation (3) and equation (4), using the area of both electrodes (total of 0.98 cm^2) and the mass of PANI of both electrodes, respectively.

$$Cspa = \frac{2I \int Vdt}{\Delta V^2 A} \quad (3)$$

Where I is the current of charge/discharge, $\int Vdt$ is the area of the discharge curve after the IR drop, ΔV is the voltage window and A is the active area of the electrodes (0.98cm^2)

$$Cspa = \frac{4I \int Vdt}{\Delta V^2 m} \quad (4)$$

The areal and gravimetric energy densities were calculated from the GCD curves at different current densities, according to the equation (3)

$$Et = \frac{Csp \times \Delta v^2}{2 \times 3.6} \quad (5)$$

Where Et is the energy density, C_{sp} is the areal (or gravimetric) specific capacitance and ΔV is the potential range. The power density was calculated according to the equation (4)

$$Pt = \frac{Et}{\Delta t} \times 3600 \quad (6)$$

Where Pt is the power density, Et is the energy density and Δt is the discharge time.

For the cyclic voltammetry tests, the values of areal specific capacitances were obtained from the equation (5)

$$Cspa = \int 2\, idv/\nu\, \Delta E\, A \quad (7)$$

Where idv is the area of the curve, ν is the scan rate, ΔE is the potential range and A is the area of a single electrode.

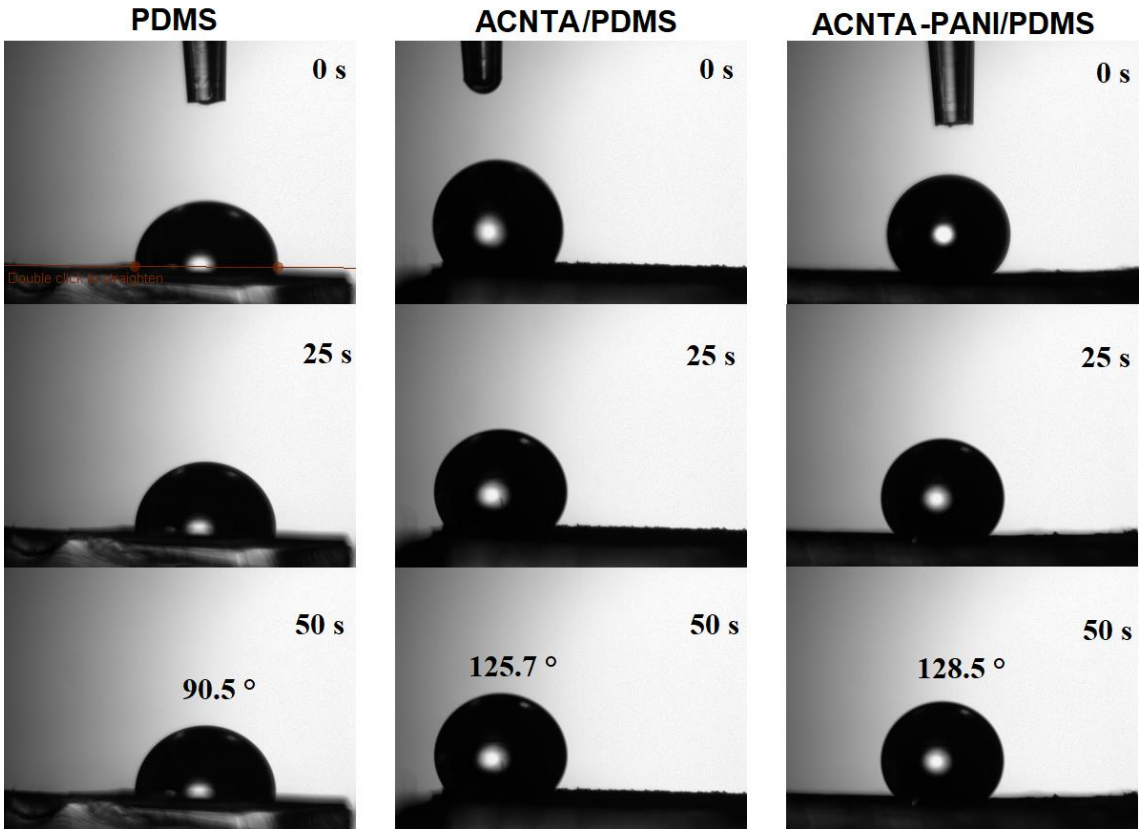

Fig. S1 Contact angle measurements of PDMS, ACNTA/PDMS and ACNTA-PANI/PDMS

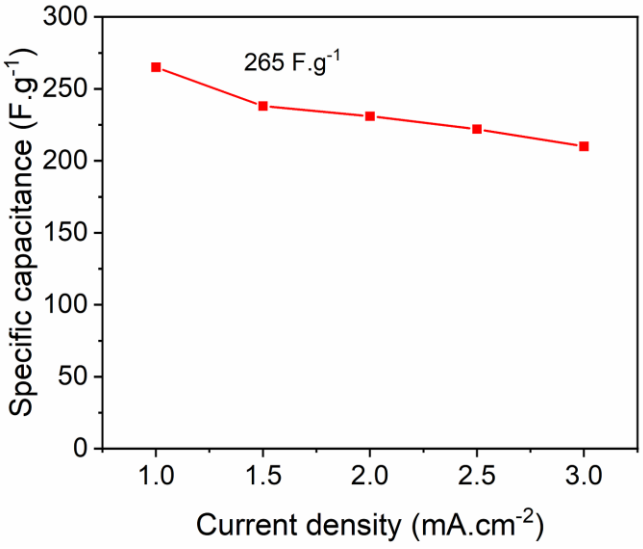

Fig. S2 Gravimetric specific capacitance calculated from GCD curves for the ACNTA-PANI/PDMS measured in three-electrode configuration

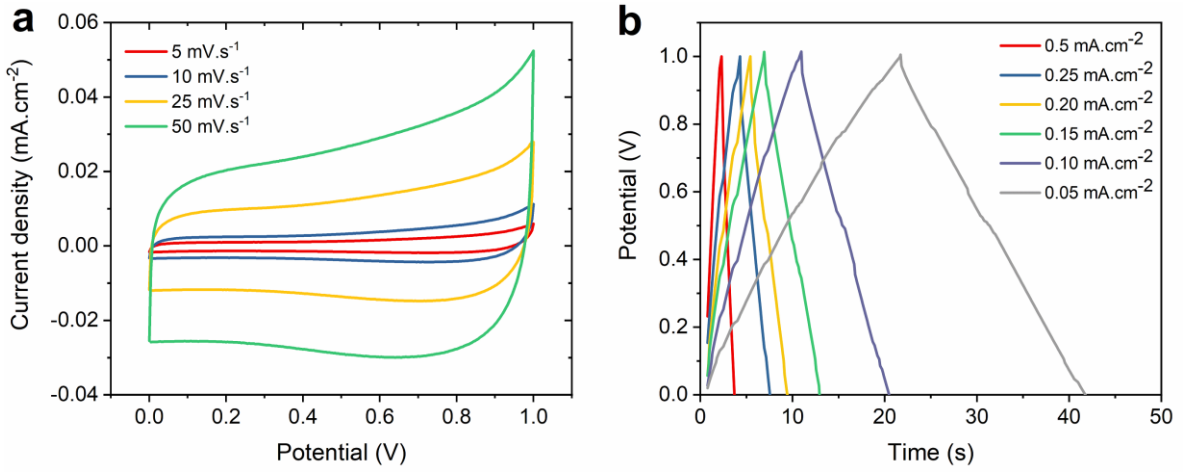

Fig. S3 Electrochemical performance of symmetric two-electrode ACNTA/PDMS supercapacitor. (a) CV curves at scan rates varying between 5 – 50 $mV.s^{-1}$. (b) GCD curves at different current densities

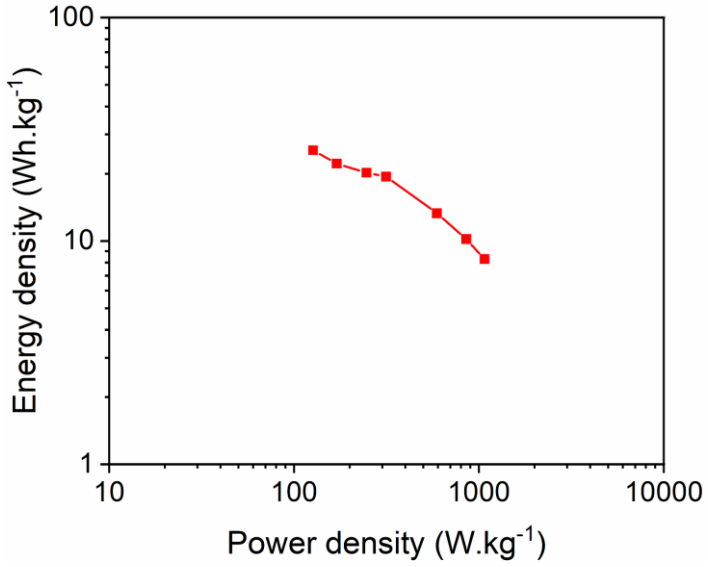

Fig. S4 Ragone plot showing the gravimetric energy and power densities calculated based on the mass of PANI

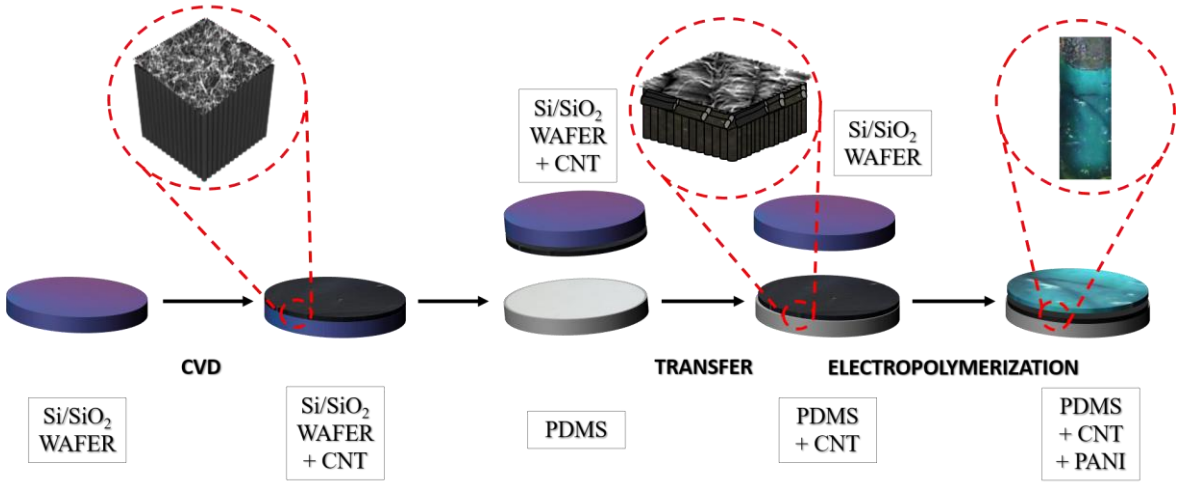

Fig. S5 Illustration of the electrode's fabrication process showing the steps between the initial Si/SiO_2 wafer and the final supercapacitor electrode. The vertically aligned carbon nanotubes (VA-CNTs) are grown at the activated metal catalyst on the surface of the buried oxide, which later is drop-casted facing a mild-cured PDMS, concluding the transfer process. The PDMS+CNT electrode then undergoes a PANI electropolymerization finalizing the fabrication of the flexible SC device

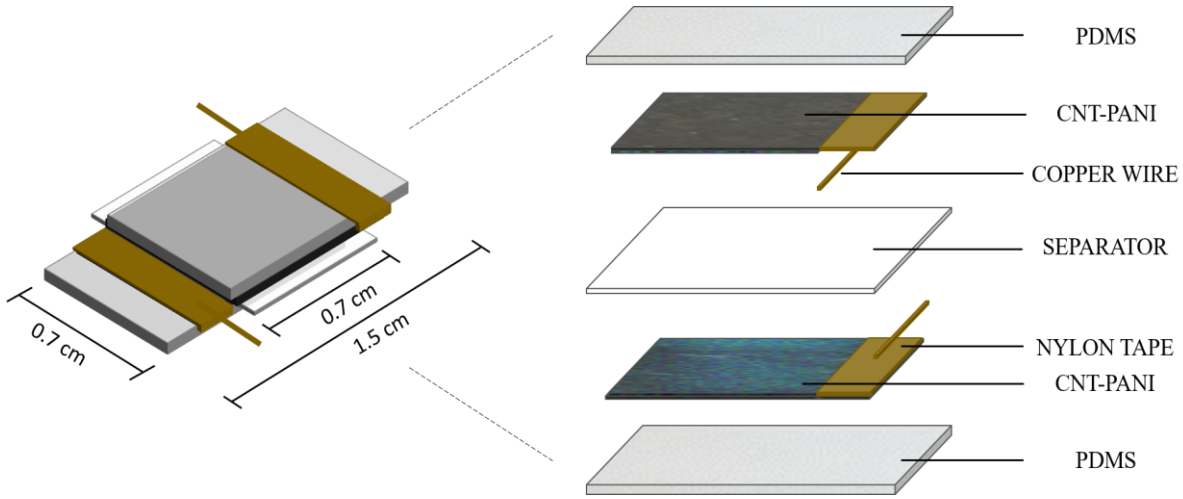

Fig. S6 Illustration of the flexible two-electrode supercapacitor assembly

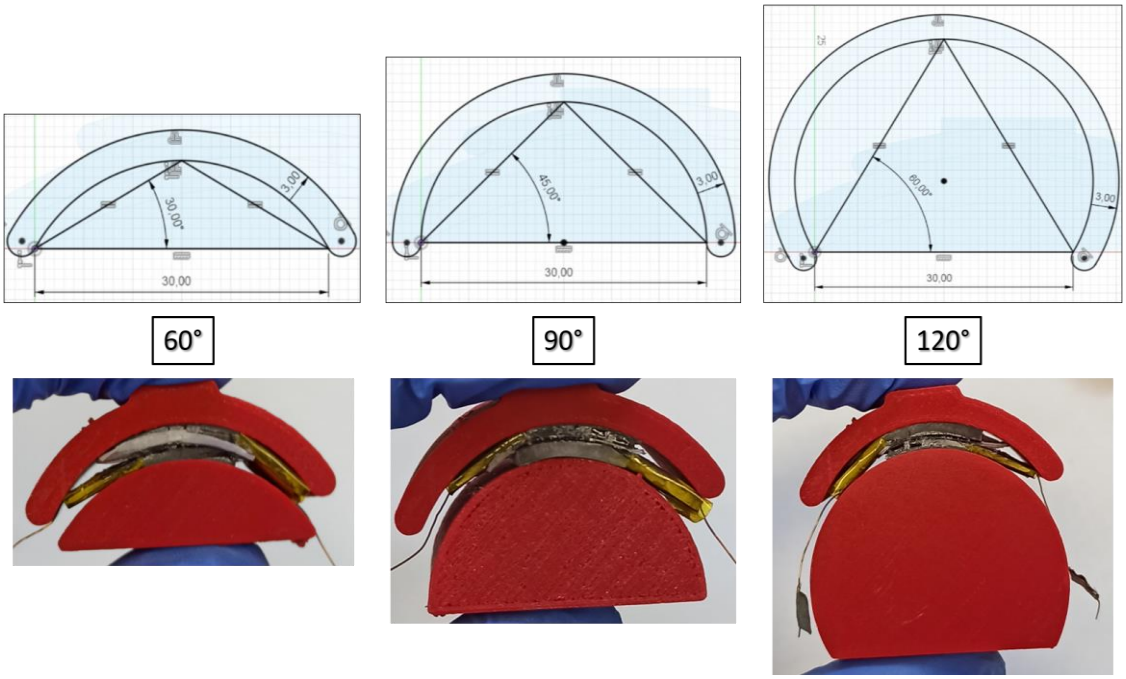

Fig. S7 Scheme illustrating the electrochemical measurements under different bending angles

Table S1 Comparison of areal and gravimetric specific capacitances of this work measured in two and three-electrode configurations with various similar materials for flexible supercapacitor application.

Sample	Measurement configuration	Current density	Scan rate	Csp ($mF.cm^{-2}$)	Csp ($F.g^{-1}$)	Ref
ACNTA-PANI/PDMS	Three-electrode	1 $mA.cm^{-2}$	-	408	265	**This work**
ACNTA-PANI/PDMS	Two- electrode	0.2 $mA.cm^{-2}$	-	40.6	51.6	**This work**
Ti3C2Tx/CF	Three-electrode	-	10 $mV.s^{-1}$		401	1
RuO2/CF	Three-electrode	-	10 $mV.s^{-1}$	-	388	1
a-MWCNT/PANI	Three-electrode	0.25 $A.g^{-1}$	-	-	201	2
PANI/VACNTs	Three-electrode	5 $A.g^{-1}$	-	-	415	3
PANI/MWCNT/PDMS	Three-electrode	-	5 $mV.s^{-1}$	481	-	4
Activated CC	Three-electrode	-	10 $mV.s^{-1}$	88	-	5
CNT@graphene@PANI/PDMS	Three-electrode	0.4 mA	-	588.7	-	6
VACNT-SS – TiO2	Two-electrode	1.67 $mA.cm^{-2}$	-	16.24	-	7
PPy(DBS)/CNTs/PDMS	Two-electrode	-	100 $mV.s^{-1}$	3.6	-	8
graphene/MoS2	Two-electrode	0.3 mA	-	70	-	9
MWCNT/PANI	Two-electrode	1 $A.g^{-1}$	-	-	233	10
CNT/MoS2/PDMS	Two-electrode	0.1 $mA.cm^{-2}$	-	-	10.67	11
PANI/MWCNT/PDMS	Two-electrode	-	5 $mV.s^{-1}$	-	159	4
MWCNTs-PANI-PDMS	Two-electrode	0.2 $mA.cm^{-2}$	-	44.13		12
CNT – PANI - PDMS	Two-electrode	1 $A.g^{-1}$			308.4	13
SWCNT-PDMS	Two-electrode	1 $A.g^{-1}$	-	-	54	12
3D-G/PANI/pdms	Two-electrode	1 $A.g^{-1}$	-	-	140	14
G-PANI	Two-electrode	0.1 $mA.cm^{-2}$	-	23	-	15
NRG//PANI	Two-electrode	0.25 $mA.cm^{-2}$	-	14.5	-	16
MOF/PANI	Two-electrode	0.1 $mA.cm^{-2}$	-	28.1	-	17

Table S2 Parameters obtained from the equivalent electric circuit from EIS measurements.

Sample	Rs ($ohm.cm^{-2}$)	C1 ($mF.cm^{-2}$)	R1 ($ohm.cm^{-2}$)	W	C2 ($mF.cm^{-2}$)
ACNTA/PDMS	214	6.99	209.7	7.2	1.04
ACNTA-PANI/PDMS	153.3	8.34	72.46	5.5	20.23

References

1 Q. Jiang, N. Kurra, M. Alhabeb, Y. Gogotsi and H. N. Alshareef, *Adv. Energy Mater.*, 2018, **8**, 1–10.

2 S. Y. Lee, J. Il Kim and S. J. Park, *Energy*, 2014, **78**, 298–303.

3 S. Hussain, E. Kovacevic, R. Amade, J. Berndt, C. Pattyn, A. Dias, C. Boulmer-Leborgne, M. R. Ammar and E. Bertran-Serra, *Electrochim. Acta*, 2018, **268**, 218–225.

4 M. Yu, Y. Zhang, Y. Zeng, M. S. Balogun, K. Mai, Z. Zhang, X. Lu and Y. Tong, *Adv. Mater.*, 2014, **26**, 4724–4729.

5 G. Wang, H. Wang, X. Lu, Y. Ling, M. Yu, T. Zhai, Y. Tong and Y. Li, *Adv. Mater.*, 2014, **26**, 2676–2682.

6 X. Liang, L. Zhao, Q. Wang, Y. Ma and D. Zhang, *Nanoscale*, 2018, **10**, 22329–22334.

7 P. Avasthi, A. Kumar and V. Balakrishnan, *ACS Appl. Nano Mater.*, 2019, **2**, 1484–1495.

8 R. Zhang, K. Yan, A. Palumbo, J. Xu, S. Fu and E.-H. Yang, *Nanotechnology*, 2019, **30**, 95401.

9 N. Li, T. Lv, Y. Yao, H. Li, K. Liu and T. Chen, *J. Mater. Chem. A*, 2017, **5**, 3267–3273.

10 H. Lin, L. Li, J. Ren, Z. Cai, L. Qiu, Z. Yang and H. Peng, *Sci. Rep.*, 2013, **3**, 1–6.

11 T. Lv, Y. Yao, N. Li and T. Chen, *Angew. Chemie - Int. Ed.*, 2016, **55**, 9191–9195.

12 L. Li, Z. Lou, W. Han, D. Chen, K. Jiang and G. Shen, *Adv. Mater. Technol.*, , DOI:10.1002/admt.201600282.

13 X. Chen, H. Lin, P. Chen, G. Guan, J. Deng and H. Peng, *Adv. Mater.*, 2014, **26**, 4444–4449.

14 K. Li, Y. Huang, J. Liu, M. Sarfraz, P. O. Agboola, I. Shakir and Y. Xu, *J. Mater. Chem. A*, 2018, **6**, 1802–1808.

15 X. Zang, X. Li, M. Zhu, X. Li, Z. Zhen, Y. He, K. Wang, J. Wei, F. Kang and H. Zhu, *Nanoscale*, 2015, **7**, 7318–7322.

16 L. Zhang, X. Qing, Z. Chen, J. Wang, G. Yang, Y. Qian, D. Liu, C. Chen, L. Wang and W. Lei, *ACS Appl. Energy Mater.*, 2020, **3**, 6845–6852.

17 A. P. M. Udayan, O. Sadak and S. Gunasekaran, *ACS Appl. Energy Mater.*, 2020, **3**, 12368–12377.